

**A first approach to seawater gallium-aluminium
systematics throughout Earth's history**

by

David M. Ernst

a Thesis submitted in partial fulfilment
of the requirements for the degree of

**Doctor of Philosophy
in Geosciences**

Approved Dissertation Committee

Prof. Dr. Michael Bau
Chair, Constructor University

Prof. Dr. Andrea Koschinsky
Constructor University

Dr. Dieter Garbe-Schönberg
Christian-Albrechts-Universität zu Kiel

Prof. Dr. Bertus Smith
University of Johannesburg

Date of Defense: 17.07.2023
School of Science

Statutory Declaration

Family Name, Given/First Name	
Matriculationnumber	
What kind of thesis are you submitting: Bachelor-, Master- or PhD-Thesis	

English: Declaration of Authorship

I hereby declare that the thesis submitted was created and written solely by myself without any external support. Any sources, direct or indirect, are marked as such. I am aware of the fact that the contents of the thesis in digital form may be revised with regard to usage of unauthorized aid as well as whether the whole or parts of it may be identified as plagiarism. I do agree my work to be entered into a database for it to be compared with existing sources, where it will remain in order to enable further comparisons with future theses. This does not grant any rights of reproduction and usage, however.

The Thesis has been written independently and has not been submitted at any other university for the conferral of a PhD degree; neither has the thesis been previously published in full.

German: Erklärung der Autorenschaft (Urheberschaft)

Ich erkläre hiermit, dass die vorliegende Arbeit ohne fremde Hilfe ausschließlich von mir erstellt und geschrieben worden ist. Jedwede verwendeten Quellen, direkter oder indirekter Art, sind als solche kenntlich gemacht worden. Mir ist die Tatsache bewusst, dass der Inhalt der Thesis in digitaler Form geprüft werden kann im Hinblick darauf, ob es sich ganz oder in Teilen um ein Plagiat handelt. Ich bin damit einverstanden, dass meine Arbeit in einer Datenbank eingegeben werden kann, um mit bereits bestehenden Quellen verglichen zu werden und dort auch verbleibt, um mit zukünftigen Arbeiten verglichen werden zu können. Dies berechtigt jedoch nicht zur Verwendung oder Vervielfältigung.

Diese Arbeit wurde in der vorliegenden Form weder einer anderen Prüfungsbehörde vorgelegt noch wurde das Gesamtdokument bisher veröffentlicht.

.....
Date, Signature

Abstract

Marine chemical sedimentary rocks, like banded iron formations (BIFs), ferromanganese (Fe-Mn) crusts and nodules, marine carbonates or cherts, are of great scientific interest because they can preserve primary information on the physico-chemical conditions of ambient seawater. Especially for research on the Precambrian, marine chemical sedimentary rocks are invaluable archives as they are the only remaining access point to the geochemical conditions of the Archaean and Palaeoproterozoic marine environment.

This PhD thesis investigates the geochemical partner couples of gallium, aluminium (Ga-Al), germanium, and silicon (Ge-Si). Those two couples show mostly coherent geochemical behaviour in igneous and clastic sedimentary processes. However, in (low-temperature) aqueous environments, both partners decouple from each other. This thesis aims to investigate the behaviour of Ga-Al and Ge-Si during the precipitation of Fe (oxyhydr)oxides in the natural environment and to elaborate on whether characteristic distributions of Ga/Al and Ge/Si ratios in marine chemical sedimentary rocks can be applied as geochemical proxies.

Applying Ga/Al and Ge/Si ratios as geochemical proxies requires sound knowledge and understanding of their geochemical behaviours in the natural environment. Few studies have been published on the coupled or decoupled geochemical behaviour of Ga-Al and Ge-Si. These studies focus on the distribution between solid and fluid phases of Ga-Al and Ge-Si during rock weathering, soil formation, in riverine and estuarine processes, and within the seawater column. However, an investigation of Ga-Al and Ge-Si during the formation of Fe-rich precipitates was missing. While BIFs are absent in the modern system, hydrogenetic Fe-Mn crusts (and nodules) might come closest to some kind of “*BIF-analogue*”. Although the geochemical characteristics of BIFs and Fe-Mn crusts clearly differ, both contain Fe (oxyhydr)oxides as a major phase. The comparison of Ga-Al (PhD thesis of Katharina Schier, see below) and Ge-Si (this thesis) systematics in seawater and hydrogenetic Fe-Mn crusts shows fractionation of both couples during scavenging by Fe (oxyhydr)oxides. Hydrogenetic Fe-Mn crusts from the Pacific and Atlantic show lower Ga/Al but higher Ge/Si ratios than ambient seawater, indicating preferred scavenging of Al and Ge, respectively. This observation is in accordance with data from the existing studies on Ga-Al and Ge-Si behaviour in the natural environment. It is commonly attributed to the higher particle reactivity of Al and Ge compared to Ga and Si, respectively. Particle reactivity, in general, should not have been very different during the Precambrian. Nevertheless, in the modern environment, large amounts of particles are of organic origin and metal complexation by organic ligands might also influence the behaviour of Ga, Al, Ge and Si. During the Archaean and Palaeoproterozoic, however, organic particles and ligands were probably almost absent and negligible for particle and complexation reactions in the natural systems.

Banded iron formations may preserve primary trace element signals from ambient seawater, which in turn can give insights into the contemporaneous physico-chemical conditions of the atmosphere and hydrosphere. However, essential prerequisites are purity and pristineness of the investigated BIF samples, which also applies to geochemical archives in general. The rare earth elements (REE) and yttrium (REY) are a powerful

tool commonly used to assess potential detrital contamination and post-depositional alteration of marine chemical sediments. Many geochemical studies on BIFs have been conducted throughout the past decades, and many BIFs are already well-characterised. Nevertheless, there are still unstudied BIFs like the Mt. Ruker BIF from East Antarctica. The first geochemical study conducted on an Antarctic BIF shows that the ~ 2.5 Ga old Mt. Ruker BIF is pure, pristine, and, therefore, a promising target for further geochemical investigations. An in-depth investigation of individual Fe oxide and metachert bands shows that the Mt. Ruker BIF preserved not only a general seawater-like REY distribution (with the BIF-typical exceptions of Ce and Eu) but also the very subtle W-type lanthanide tetrad effect (LTE). This W-type LTE is a characteristic feature of (modern) seawater and indicates, unfractionated incorporation of REY into BIFs. Furthermore, the presence of W-type LTE and uniform Y/Ho ratios in BIF Fe oxide and metachert bands clearly argue for a primary origin of BIF banding. Lab experiments have shown that a diagenetic separation from a previously homogeneous Fe-Si gel would have caused Y-Ho fractionation and the opposite M-type LTE.

A compilation of published BIF REY data shows that also the 2.7 Ga Temagami BIF from Ontario, Canada, preserved the W-type LTE. The Temagami BIF is one of the most studied BIFs, and it is considered to be extremely pure and pristine. It is frequently used as a benchmark test for applying newly developed proxies and, therefore, was chosen for the first study on Ga-Al systematics in BIFs. However, the determination of Ga and Al in BIFs is challenging due to extremely low mass fractions, especially in (meta)chert bands, and due to multiple mass-interferences on Ga when measured with inductively coupled plasma mass spectrometry (ICP-MS). Therefore, comparative analyses with solution-based sector-field (SF-)ICP-MS, ICP-MS/MS and laser-ablation (LA-)ICP-MS and a two-component mixing experiment were conducted to ensure analytical quality. The high-quality Ga-Al data show that the Ga/Al ratios in Temagami BIF are below those of modern seawater but, surprisingly, comparable to those of modern Fe-Mn crusts and nodules.

Furthermore, Temagami Fe oxide and metachert bands show similar Ga/Al ratios, regardless of mineralogy. This indicates that finely dispersed Fe-oxide particles most likely dominate the Ga and Al content in metachert bands. Additional measurements of BIFs of different ages also show Ga/Al ratios similar to those of Temagami BIF, arguing for a rather uniform Ga/Al ratio range in Precambrian BIFs. At the current stage, two explanations for the observed BIF Ga/Al ratios are conceivable: (i) Precambrian seawater had lower Ga/Al ratios than modern seawater given that BIFs incorporated Ga and Al without fractionations, or (ii) Ga and Al were fractionated during BIF formation, diagenesis and/or metamorphic alteration. Future research on the Ga-Al systematics of other BIFs, but also of marine carbonates and cherts, might solve this question.

First author publications

1. Ernst, D.M., Bau, M. (2021). Banded iron formation from Antarctica: The 2.5 Ga old Mt. Ruker BIF and the antiquity of lanthanide tetrad effect and super-chondritic Y/Ho ratio in seawater. *Gondwana Research* 91, 97–111. <https://doi.org/10.1016/j.gr.2020.11.011>
2. Ernst, D.M., Schier, K., Garbe-Schönberg, D., Bau, M. (2022). Fractionation of germanium and silicon during scavenging from seawater by marine Fe (oxy)hydroxides: Evidence from hydrogenetic ferromanganese crusts and nodules. *Chemical Geology* 595. <https://doi.org/10.1016/j.chemgeo.2022.120791>
3. Ernst, D.M., Garbe-Schönberg, D., Kraemer, D., Bau, M., 2023. A first look at the gallium-aluminium systematics of Early Earth's seawater: Evidence from Neoproterozoic banded iron formation. *Geochimica et Cosmochimica Acta* 355, 48–61. <https://doi.org/10.1016/j.gca.2023.06.019>

Co-author publications

5. Schier, K., Ernst, D.M., de Sousa, I.M.C., Garbe-Schönberg, D., Kuhn, T., Hein, J.R., Bau, M. (2021). Gallium-aluminum systematics of marine hydrogenetic ferromanganese crusts: Inter-oceanic differences and fractionation during scavenging. *Geochimica et Cosmochimica Acta* 310, 187–204. <https://doi.org/10.1016/j.gca.2021.05.019>
6. Kraemer, D., Frei, R., Ernst, D.M., Bau, M., Melchiorre, E. (2021). Serpentinization in the Archaean and Early Phanerozoic – Insights from chromium isotope and REY systematics of the Mg Cr hydroxycarbonate stichtite and associated host serpentinites. *Chemical Geology* 565, 120055. <https://doi.org/10.1016/j.chemgeo.2020.120055>

Acknowledgements

I would like to thank my supervisor, Michael Bau, and my PhD committee members, Andrea Koschinsky, Dieter Garbe-Schönberg and Bertus Smith, for their support throughout the last years.

Thank you, Michael, for giving me the opportunity to conduct a PhD with this challenging but exciting research project. Thank you for all the support, all the discussions and all the inspiration you have given me over the years. I know I can always speak openly with you, and that is invaluable. Your great experience and willingness to share your knowledge with others make you a role model for every professor. Thank you for being my teacher and becoming a friend!

Thank you, Andrea, for giving me the opportunity to conduct my first research project even though you didn't know me. Without you, I probably would never have found my way to beautiful Bremen Nord and into academia. You guided me in my first steps in academia and supported me whenever needed.

Thank you, Dieter, for all the effort you put into our challenging analytical work. I learned a lot from your great experience in analytical geochemistry. You have taught me how important it is to carefully choose and consider analytical methods to produce reliable data. Thank you for hosting me in Kiel, letting me work in your lab and all the fruitful discussions.

Thank you, Bertus, for making my visit to South Africa one of the greatest experiences in my life, which I will never forget! I fell in love with your country because of you, your family and friends. Thank you for all the time you and Tam took to show me Joburg and our field trip to Hotazel. You showed me my first proper BIF in the wild, and I learned so much from your great geological experience. Thank you for all your help, support and the unbelievable *lekker* time in South Africa!

I would also like to thank the sadly recently deceased Nic Beukes, who took me on a field trip to the Barberton Greenstone Belt. Thank you, Nic, for sharing your incredible knowledge of geology and South African history. It was such a great pleasure to spend some time with you.

Also, I would like to thank Eva and Tony in St. Andrews, who hosted us for a very short-notice visit and spent their time with us. Thank you, Eva, for introducing me to the field of nitrogen and carbon isotopy and the lab work we conducted together. Thank you, Tony, for the great trip to the Scottish Highlands and for sharing your knowledge of geology, Whisky and Scottish history.

Furthermore, I would like to thank my exceptionally great colleagues for all the support you gave me and all the fun we had together. Thank you, Patrick! You are one of my very first colleagues and became such a dear friend. Thank you for guiding me to Clausthal and the remarkably great time we had. Although several people left and joined our JUB research group, it was always a great bunch of people. Thank you, Kathy and Timmu, for sharing an office with me and putting up with my nonsense so many times. Thank you, Kathy, for writing the project proposal for my PhD project, for all the lab work we conducted together, all the discussions we had and all the support you gave me. Without you, this PhD thesis would not exist. Thank you, Timmu, for your extraordinary and

great sense of humour. Thank you for helping me out with lab work, especially in the final phase of my thesis writing. Thank you, Franzi and Anna, for helping me in the lab many times. Getting a coffee and chatting with you is always a great distraction. Whenever I had a complaint, it was always a good idea to first talk to you as you could calm me down in many cases. I do not know if I really want to thank you, Franzi, for introducing me to Skyjo. This card game obviously has a hidden rule: "David always loses". Thank you, Dennis, for being one of the most caring people I know. Working with you always went extremely smoothly, and you showed me how to work efficiently. But not only the way you work but also your incredibly calm and friendly character impressed me a lot. Thank you, Fumi, for your help and expertise in the fabulous field of Early Earth. Because of your "not-so-calm" character, our field trip to Norway was just *leiwand*.

Ich möchte mich auch ganz herzlich bei meinen Freunden außerhalb der Arbeit und meiner Familie bedanken. Ihr habt mich mein Leben lang geprägt. Vielen Dank an meine Eltern Sandra und Holger, meine beiden Lieblingsschwestern Anne und Lea und meine Großeltern Renate, Renate, Peter und Winfried für eine wundervolle und unbeschwerte Kindheit und eure stetige Unterstützung. Wenn man sich Familie aussuchen könnte, dann würde ich euch auswählen. Auch möchte ich mich ganz herzlich bei meinen beiden besten Freunden Malte und Malte bedanken. Ihr seid schon so lange ein wichtiger Teil meines Lebens und nicht mehr wegzudenken. Vielen Dank für all die großartigen Erlebnisse, die wir gemeinsam hatten und auch noch in Zukunft zusammen haben werden. Na zakończenie chciałbym ci, Claudia, podziękować. Dziękuję, że wspierasz mnie we wszystkim i że zawsze mogę na ciebie liczyć. Ja również tak wiele się od Ciebie nauczyłem i jestem szczęśliwy, że możemy razem dzielić życie. Dziękuję bardzo!

Contents

1	Objectives and structure of this thesis	1
1.1	References	4
2	Introduction	7
2.1	Nomenclature	7
2.2	Early Earth	7
2.2.1	Hadean (4.5 – 4.0 Ga)	8
2.2.2	Archaean (4.0 – 2.5 Ga)	8
2.2.3	Proterozoic (2.5 – 0.542 Ga)	11
2.3	Banded iron formations	13
2.4	Gallium and aluminium	18
2.4.1	Gallium and aluminium literature data	18
2.4.2	Gallium and aluminium in igneous rocks	21
2.4.3	Gallium and aluminium in clastic sedimentary rocks	25
2.4.4	Gallium and aluminium in chemical sedimentary and carbonate rocks	28
2.4.5	Particle reactivity	33
2.4.6	Gallium-aluminium cycle – from crustal rocks to seawater back to chemical sedimentary rocks	34
2.5	Germanium and silicon	43
2.5.1	Germanium and silicon during weathering	46
2.5.2	Germanium and silicon in seawater	47
2.6	Rare earth elements and yttrium	47
2.7	References	48
3	Methods and Materials	65
3.1	Samples	65
3.1.1	Mt. Ruker BIF	65
3.1.2	Hydrogenetic Fe-Mn crusts	67
3.1.3	Temagami BIF	67
3.1.4	Two-component mixing experiment	69
3.2	Wet chemistry	69
3.2.1	High-pressure acid digestion	69
3.2.2	ICP-OES measurements	70
3.2.3	ICP-MS measurements	70
3.2.4	SF-ICP-MS and ICP-MS/MS measurements	71

3.3	Laser-ablation ICP-MS	72
3.3.1	LA-ICP-MS sample preparation	72
3.3.2	LA-ICP-MS measurements	72
3.3.3	Raw data processing and elemental ratio evaluation	73
3.3.4	Fe-Mn crusts	73
3.3.5	Temagami BIF	74
3.3.6	Additional BIFs	75
3.3.7	Challenges of LA-ICP-MS	75
3.4	References	79
4	Germanium-silicon systematics in hydrogenetic ferromanganese crusts	85
4.1	Abstract	85
4.2	Introduction	86
4.2.1	Germanium and silicon	86
4.2.2	Hydrogenetic ferromanganese crusts	88
4.2.3	Aims of this study	89
4.3	Samples and methods	89
4.3.1	Samples	89
4.3.2	Methods	89
4.4	Results	93
4.4.1	Reference materials NOD-P1, NOD-A1 and JMn-1	93
4.4.2	Hydrogenetic Fe-Mn crusts	94
4.5	Discussion	98
4.5.1	Sample purity	98
4.5.2	Fractionation of Ge and Si during formation of hydrogenetic Fe-Mn crusts and nodules	100
4.5.3	Comparison of Ge-Si and Ga-Al relationships in Fe-Mn crusts	105
4.5.4	Are hydrogenetic Fe-Mn crusts an important marine Ge sink?	106
4.6	Conclusion	108
4.7	Declaration of Competing Interest	109
4.8	Acknowledgements	109
4.9	Appendix A. Supplementary data	109
4.9.1	Supplementary figures	110
4.9.2	Supplementary tables	111
4.10	References	112
5	Mt. Ruker BIF, East Antarctica	121
5.1	Abstract	121
5.2	Introduction	122
5.2.1	Geological background	123
5.3	Samples and methods	127
5.4	Results	131
5.5	Discussion	136
5.5.1	Nickel and Zirconium	136

5.5.2	Barium and Strontium	138
5.5.3	Rare earth elements and Yttrium	138
5.5.4	Thorium and Uranium	144
5.6	Conclusion	145
5.7	Declaration of Competing Interest	146
5.8	Acknowledgements	146
5.9	References	147
6	Gallium-aluminium systematics in the Temagami BIF	159
6.1	Abstract	159
6.2	Introduction	160
6.3	Materials and Methods	166
6.3.1	Wet chemistry and solution ICP-OES and ICP-MS for major and trace elements	166
6.3.2	Solution SF- and ICP-MS/MS of Ga and Al	167
6.3.3	Two-component mixing experiment with IF-G and pure SiO ₂ sand	169
6.3.4	Laser ablation SF-ICP-MS of Ga and Al	170
6.3.5	LA-ICP-MS data evaluation	171
6.4	Results	171
6.4.1	Iron	173
6.4.2	Gallium and aluminium – A comparison of SF-ICP-MS and ICP-MS/MS data sets	173
6.4.3	Analytical quality of Ga-Al data as evaluated from the two-component mixing experiment	174
6.4.4	Gallium and aluminium – comparison of solution and laser-ablation ICP-MS	177
6.5	Discussion	177
6.5.1	Ga/Al ratios determined with LA-ICP-MS	177
6.5.2	Solution ICP-MS: Uniform Ga/Al in Fe oxide and metachert bands	178
6.5.3	Fe oxide control on the Ga-Al distribution in BIFs	181
6.5.4	Comparison with the modern marine system and implications for the Temagami seas	182
6.6	Conclusion	185
6.7	Declaration of Competing Interest	186
6.8	Acknowledgements	187
6.9	Appendix A. Supplementary Material	187
6.9.1	Supplementary Tables	187
6.10	Acknowledgements	198
6.11	References	198
7	Unpublished work	209
7.1	Ga/Al in Archaean and Palaeoproterozoic BIFs	209
7.2	References	214

8	Review of applied LA-ICP-MS	215
8.1	References	221
9	Concluding remarks	223
9.1	Relationship between Ga-Al and Ge-Si systematics in BIFs	225
9.2	Immediate implications	229
9.3	References	230
10	Appendix	231
10.1	Supplementary Figures	231
10.2	Supplementary Tables	236

List of Figures

2.1	Formation models for BIFs	17
2.2	Compilation of published Ga/Al ratios in natural systems	20
2.3	Ga/Al ratios in igneous rocks from the EarthChem database	23
2.4	Ga/Al ratios in different igneous rock types	24
2.5	Ga/Al ratios in ultramafic to felsic igneous rocks	24
2.6	Ga/Al ratios in siliciclastic rocks from the SGP database	26
2.7	Ga/Al ratios in different siliciclastic rock types	27
2.8	Ga/Al ratios in carbonate rocks from the SGP database	29
2.9	Ga/Al ratios in different carbonate rock types	30
2.10	Ga/Al ratios in chemical sedimentary rocks from the SGP database	31
2.11	Ga/Al ratios in chemical sedimentary rock types	32
2.12	Ga/Al ratios in boreal rivers, NW Russia	37
2.13	Ga/Al ratios in laterites from western Cameroon and eastern Brazil	38
2.14	Gallium and aluminium in seawater profiles	41
2.15	Ge/Si ratios in igneous rocks from the EarthChem database	44
2.16	Ge/Si ratios in sedimentary rocks from the SGP database	45
3.1	Mt. Ruker BIF sample	66
3.2	Temagami BIF samples	68
3.3	Number of publications using LA-ICP-MS	76
3.4	General LA-ICP-MS setup	77
4.1	Ge/Si reference materials NOD-P1, NOD-A1 and JMn-1	92
4.2	Ge/Si vs Fe/Mn ratios of SO66 Fe-Mn crust samples	99
4.3	Ge/Si ratios vs Si content of SO66 Fe-Mn crust samples	101
4.4	Si and Ge content vs Fe content of SO66 Fe-Mn crust samples	102
4.5	Ge/Si ratios vs Fe content of SO66 Fe-Mn crust samples	104
4.6	Ga vs Ge content of SO66 Fe-Mn crust samples	107
4.7	$^{72}\text{Ge}/^{74}\text{Ge}$ raw signal data of all individual measurements	110
5.1	Map of Antarctica and the Prince Charles Mountain area	125
5.2	Regional stratigraphy of Southern Prince Charles Mountains	126
5.3	Mt. Ruker BIF specimen	128
5.4	Major and trace element distribution in Mt. Ruker BIF samples	132
5.5	REY distribution and W-type LTE in Mt. Ruker BIF samples	134
5.6	SEM images of Mt. Ruker BIF samples	135
5.7	Ba/Sr ratios in Mt. Ruker and Temagami BIF	139
5.8	Y/Ho ratios in Mt. Ruker BIF samples	140

List of Figures

5.9	Y/Ho ratios in BIFs throughout Earth's history	142
5.10	W-type LTE in Precambrian BIFs	144
6.1	Ga/Al in crustal rocks, soils, river waters, seawaters, hydrothermal fluids and Fe-Mn crusts	161
6.2	Ga/Al in igneous and sedimentary rocks	162
6.3	Temagami BIF specimens TM1, TM2, TM3 and TM4	168
6.4	Linear calibrations for Ga/Al ratios determined with IF-G and FeR-4 RMs	173
6.5	Comparison of Ga/Al ratios determined with solution-based SF-ICP-MS, ICP-MS/MS and laser-ablation ICP-MS	175
6.6	Ga and Al content and Ga/Al ratios of solid mixing samples	177
6.7	Ga/Al ratios vs Fe content of Temagami BIF samples	179
7.1	Comparison of usable and unusable LA-ICP-MS measurement signal . . .	210
7.2	Ga/Al in further BIFs determined with LA-ICP-MS	211
7.3	Ga/Al ratios in BIFs throughout Earth's history	212
8.1	Comparison of LA-ICP-MS and solution-based ICP-MS Ga/Al ratios of Temagami BIF samples	216
8.2	Laser-ablation fractionation factors	220
9.1	Ga/Ge ratios vs Fe content of Temagami BIF samples	227
9.2	Ambiguous LA-ICP-MS measurement signal calibration for Ge/Si ratios .	228
10.1	LA-ICP-MS calibration for Isua BIF	231
10.2	LA-ICP-MS calibration for Marra Mamba BIF	232
10.3	LA-ICP-MS calibration for Hotazel IF (GHEX drill core)	233
10.4	LA-ICP-MS calibration for Mt. Ruker and Kuruman BIF	234
10.5	Correlative plots of Ga with trace elements in Temagami BIF	235

List of Tables

2.1	Ionic radii of Ga, Al and Fe	22
4.1	Major and trace element data of SO66 Fe-Mn crust samples	96
4.2	Ge/Si ratios of SO66 Fe-Mn crusts	97
4.3	Determined Ge/Si ratios for the RMs NOD-P1, NOD-A1 and JMn-1 . . .	111
5.1	Major and trace element content of Mt. Ruker BIF samples	129
5.2	Correlation matrix for major and trace elements of Mt. Ruker BIF samples	137
6.1	Fe, Ga and Al content and Ga/Al ratios of Temagami BIF samples . . .	172
6.2	Ga and Al content and Ga/Al ratios of solid mixing samples	176
6.3	Ga/Al ratio raw data and evaluated data for TM3 NP tablets	178
6.4	Major and trace element data of Temagami BIF samples	188
6.5	Ga and Al measured in RMs with SF-ICP-MS and ICP-MS/MS	194
6.6	Individual LA-ICP-MS measurements of Temagami BIF NP tablet samples	195
6.7	Individual LA-ICP-MS measurements of the RM NP tablet samples . . .	196
10.1	Ga/Al and Fe/Si ratios of Isua BIF samples	236
10.2	Ga/Al and Fe/Si ratios of Marra Mamba BIF samples	237
10.3	Ga/Al and Fe/Si ratios of Hotazel and Dales Gorge BIF samples	238
10.4	Ga/Al and Fe/Si ratios of Mt. Ruker and Kuruman BIF samples	240

”The marine geochemical cycles of dissolved Ga and Al are similar, yet different in many ways.”

*Kristin J. Orians & Kenneth W. Bruland
1988*

*"The Road goes ever on and on,
Down from the door where it began.
Now far ahead the Road has gone,
And I must follow, if I can,
Pursuing it with eager feet,
Until it joins some larger way
Where many paths and errands meet.
And whither then? I cannot say."*

*Bilbo Baggins
T.A. 3001 — S.R. 1401*

"For sure, sometimes I don't know what I am doing."

Kimi Raikkonen

1 Objectives and structure of this thesis

The overarching theme of this PhD thesis are geochemical couples and groups of elements that can provide information on the physico-chemical conditions in the marine environment throughout Earth's history. Focus was put on Archaean and Palaeoproterozoic banded iron formations (BIFs) and the two couples of gallium – aluminium (Ga-Al) and germanium – silicon (Ge-Si). These two couples are each considered geochemical partners due to their coherent behaviour in igneous and clastic sedimentary rock-forming processes, i.e., igneous and clastic sedimentary rocks show uniform Ga/Al and Ge/Si ratios. In the past, Ge/Si ratios were used as a source proxy for iron and silica in BIFs (Hamade et al., 2003; Alibert and Kinsley, 2016; Bau et al., 2022). Iron oxide bands in BIFs show elevated Ge/Si ratios compared to (meta)chert bands which were either interpreted to reflect hydrothermal and continental sources, respectively, or to result from the diagenetic separation of a formerly homogeneous Fe-Si gel. Within this PhD thesis, the behaviour of Ga-Al in the context of Ge-Si was investigated to elucidate whether the Ga-Al couple is a suitable geochemical (source) proxy for the Archaean and Palaeoproterozoic marine environment.

This cumulative PhD thesis consists of nine chapters and an Appendix (Chapter 10). Chapter 2 is an introductory and provides background information on the evolution of Earth's marine environments throughout Precambrian, banded iron formations, the chemical behaviour of Ga-Al, Ge-Si and the REY. In Chapter 3 follows a description of the investigated samples and conducted analytical methods.

Although there are no real modern analogues of BIFs, it is still important to understand the behaviour of Ga-Al and Ge-Si in the modern environment to interpret their chemical distributions in Precambrian marine rocks. Modern marine hydrogenetic ferromanganese (Fe-Mn) crusts and nodules might come closest to some kind of “*BIF-analogue*”, although they reveal severe differences with regard to trace metal fractionation (e.g., Bau et al., 1996, 2014; Bau and Koschinsky, 2009). Nevertheless, current knowledge on the coupled natural behaviour of Ga-Al and Ge-Si is small and mainly restricted to river waters and seawater (e.g., Froelich et al., 1985; Orians and Bruland, 1988; Pokrovsky and Schott,

1 Objectives and structure of this thesis

2002; Hammond et al., 2004). Therefore, in the published article of Chapter 4 the behaviours of Ge and Si during scavenging by Fe and Mn (oxyhydr)oxides in the modern marine environment were investigated. Germanium/silicon ratios were determined in Pacific hydrogenetic Fe-Mn crusts, that were previously already investigated for their Ga-Al systematics (Schier, 2020; Schier et al., 2021). The results reveal clear fractionation of the Ge-Si couple compared to the seawater source. The measured Ge/Si ratios are discussed in detail and interpreted in context of their (potential) sources, fractionation processes, Fe-Mn systematics and the Ga-Al systematics (Schier et al., 2021). The results provide valuable insights into the decoupling of Ge-Si in the modern marine environment.

Marine chemical sedimentary rocks, like BIFs, Fe-Mn crusts, manganese formations (MnF) or marine carbonates, bear great potential because they are potential archives that preserve information from (past) ambient seawater. However, a recurring issue is to verify the purity and pristineness of the investigated samples, i.e., if they are free of detritus and only underwent negligible changes during diagenesis, metamorphism, and weathering. A commonly used and powerful tool are the rare earth elements (REE) and yttrium (REY), which show coherent behaviour in geochemical processes due to physical similarities. Seawater-like REY distribution in BIFs and marine carbonates is a strong indicator for the preservation of a primary signal and negligible detrital contamination. Chapter 5 consists of the published article on the first geochemical study of an Antarctic BIF (Mt. Ruker, East Antarctica). Apart from a general geochemical characterisation via major and trace elements, focus is a thorough investigation of the REY systematics as proxies for the samples' purity and pristineness. The general REY distributions in all samples show preservation of a seawater signal. Furthermore, a detailed consideration and interpretation of the W-type lanthanide tetrad effect in the Mt. Ruker BIF samples and previously published data of other BIFs is provided. The Mt. Ruker BIF study shows that the W-type lanthanide tetrad effect is a sensitive and suitable seawater proxy for Archaean and Palaeoproterozoic BIFs as it is only preserved in the purest samples.

Once sample purity and pristineness are ensured, further in-depth geochemical studies can be conducted, like the here targeted Ga-Al systematics in BIFs. Chapter 6 consists of the published article on the Ga-Al systematics in the Archaean Temagami BIF (Ontario, Canada). The Temagami BIF was chosen as a first benchmark test because it is already well studied and considered one of the purest and most pristine BIFs (e.g., Viehmann et al., 2014; Diekrup, 2019; Schulz et al., 2021; Bau et al., 2022; Mundl-Petermeier et al., 2022). Major challenges of Ga and Al determination in BIFs arise from their extremely small mass fractions, especially in (meta)chert bands, and numerous

mass-interferences when analysed with inductively coupled plasma mass spectrometry (ICP-MS). Furthermore, reliable Ga data in suitable reference materials are rather rare. Therefore, three comparative analytical approaches (solution-based SF-ICP-MS, ICP-MS/MS and laser-ablation SF-ICP-MS), and a two-component mixing experiment were conducted. The obtained high-quality Ga and Al data show that Fe oxide and (meta)chert bands of Temagami BIF have uniform but lower Ga/Al ratios than modern seawater. In the course of Chapter 6 these results are considered in context of BIF band mineralogy, Ge-Si systematics and further geochemical proxies, previously applied to BIFs. Furthermore, potential explanations for the observed Ga-Al distribution are also discussed. This study of Ga/Al ratios in the Temagami BIF is the first approach to decipher the geochemical behaviour of the geochemical Ga-Al couple in Archaean and Palaeoproterozoic critical zones.

After analytical methods were set and data quality was ensured, further Archaean and Palaeoproterozoic BIFs were investigated for their Ga-Al systematics. In Chapter 7 these results are described and discussed considering Precambrian marine conditions and the behaviour of Ga and Al in the natural environment.

Chapter 8 gives a review of the conducted LA-ICP-MS and discusses potential reasons for differences in Ga/Al ratios in BIF (meta)chert bands between solution-based and laser-ablation ICP-MS measurements.

Chapter 9 summarises the results of previous chapters, puts them into context with each other and highlights potential future research questions.

1.1 References

- Alibert C. and Kinsley L. (2016) Ge/Si in Hamersley BIF as tracer of hydrothermal Si and Ge inputs to the Paleoproterozoic ocean. *Geochimica et Cosmochimica Acta* 184, 329–343.
- Bau M., Frei R., Garbe-Schönberg D. and Viehmann S. (2022) High-resolution Ge-Si-Fe, Cr isotope and Th-U data for the Neoproterozoic Temagami BIF, Canada, suggest primary origin of BIF bands and oxidative terrestrial weathering 2.7 Ga ago. *Earth and Planetary Science Letters* 589, 117579.
- Bau M. and Koschinsky A. (2009) Oxidative scavenging of cerium on hydrous Fe oxide: Evidence from the distribution of rare earth elements and yttrium between Fe oxides and Mn oxides in hydrogenetic ferromanganese crusts. *Geochem. J.* 43, 37–47.
- Bau M., Koschinsky A., Dulski P. and Hein J. R. (1996) Comparison of the partitioning behaviours of yttrium, rare earth elements, and titanium between hydrogenetic marine ferromanganese crusts and seawater. *Geochimica et Cosmochimica Acta* 60, 1709–1725.
- Bau M., Schmidt K., Koschinsky A., Hein J., Kuhn T. and Usui A. (2014) Discriminating between different genetic types of marine ferro-manganese crusts and nodules based on rare earth elements and yttrium. *Chemical Geology*, 9.
- Diekrup D. (2019) Depositional Pathways and the Post-Depositional History of the Neoproterozoic Algoma-Type BIF in Temagami, ON. University of Ottawa.
- Froelich P. N., Hambrick G. A., Andreae M. O., Mortlock R. A. and Edmond J. M. (1985) The geochemistry of inorganic germanium in natural waters. *J. Geophys. Res.* 90, 1133.
- Hamade T., Konhauser K. O., Raiswell R., Goldsmith S. and Morris R. C. (2003) Using Ge/Si ratios to decouple iron and silica fluxes in Precambrian banded iron formations. *Geology* 31, 35–38.
- Hammond D. E., McManus J. and Berelson W. M. (2004) Oceanic germanium/silicon ratios: Evaluation of the potential overprint of temperature on weathering signals. *Paleoceanography* 19, 11.
- Mundl-Petermeier A., Viehmann S., Tusch J., Bau M., Kurzweil F. and Münker C. (2022) Earth's geodynamic evolution constrained by 182W in Archean seawater. *Nat Commun* 13, 2701.
- Orians K. J. and Bruland K. W. (1988) The marine geochemistry of dissolved gallium: A comparison with dissolved aluminum. *Geochimica et Cosmochimica Acta* 52, 2955–2962.
- Pokrovsky O. S. and Schott J. (2002) Iron colloids/organic matter associated transport of major and trace elements in small boreal rivers and their estuaries (NW Russia). *Chemical Geology* 190, 141–179.
- Schier K. (2020) Trace elements and their application as geochemical proxies in marine chemical sediments. Jacobs University Bremen.
- Schier K., Ernst D. M., de Sousa I. M. C., Garbe-Schönberg D., Kuhn T., Hein J. R. and Bau M. (2021) Gallium-aluminum systematics of marine hydrogenetic ferromanganese

- crusts: Inter-oceanic differences and fractionation during scavenging. *Geochimica et Cosmochimica Acta* 310, 187–204.
- Schulz T., Viehmann S., Hezel D. C., Koeberl C. and Bau M. (2021) Highly Siderophile Elements and Coupled Fe-Os Isotope Signatures in the Temagami Iron Formation, Canada: Possible Signatures of Neoproterozoic Seawater Chemistry and Earth's Oxygenation History. *Astrobiology* 21, 16.
- Viehmann S., Hoffmann J. E., Münker C. and Bau M. (2014) Decoupled Hf-Nd isotopes in Neoproterozoic seawater reveal weathering of emerged continents. *Geology* 42, 115–118.

2 Introduction

2.1 Nomenclature

For the following thesis, certain definitions regarding terminology and usage of units are made here.

The content of elements within solid materials is defined as mass fraction and either given as mass ratios in % (m/m) or in mg/kg (ppm). The content of elements within fluids is defined as concentration and is also given in mg/kg (ppm). Furthermore, elemental concentrations may additionally be given as mol/mol. However, since this thesis focuses on solid rock samples, fluid concentrations from the literature are transformed into mg/kg. Thereby, for simplicity, always a fluid density of 1 g/cm³ is assumed.

Elemental ratios (e.g., Ga/Al) are given as mass ratios, always using the same magnitude in numerator and denominator. Molar ratios from the literature are also transferred into mass ratios. Additionally, molar ratios may be given if appropriate.

2.2 Early Earth

As the name implies, the Precambrian is the period before the Cambrian 0.542 Ga (542 Ma) ago. The Precambrian is subdivided into three aeons: Hadean (4.5 – 4.0 Ga), Archaean (4.0 – 2.5 Ga), and Proterozoic (2.5 – 0.542 Ga). The Precambrian is also sometimes referred to as the "*Early Earth*" because the Earth's interior, surface and atmosphere differed in part drastically from the modern Earth. Since this thesis focuses on banded iron formations (BIFs; see below), the following introduction focuses on the evolution of the Earth's oceans throughout the Precambrian.

In the past, extensive research on the evolution of the Earth's surface systems has been done, and numerous outstanding articles and books have been published. For an in-depth introduction to the evolution of the Earth's atmosphere and oceans, the reader is referred to the according book by *Heinrich "Dick" D. Holland "The Chemical Evolution of the Atmosphere and Oceans"* (Princeton University Press, 1984). Review

articles summarising the knowledge at their time were, for example, prepared by Holland (2003) and Lowenstein et al. (2014).

2.2.1 Hadean (4.5 – 4.0 Ga)

The Hadean is the oldest aeon, but to current knowledge, no rocks from the Hadean are preserved on Earth's surface (Bowring and Williams, 1999). The only remnants of the Hadean are detrital zircons like those from Jack Hills, Western Australia (Harrison, 2009).

2.2.2 Archaean (4.0 – 2.5 Ga)

The Archaean is subdivided into the three eras of the Palaeoarchaeon, Mesoarchaeon and Neoarchaeon. Ocean chemistry during the Archaean differed from today, especially regarding redox conditions. Nowadays, it is commonly accepted that atmospheric and oceanic oxygen levels during the Archaean were negligibly small (e.g., Holland, 2003). Some older studies argued in favour of an oxidising Archaean atmosphere (Ohmoto, 1997). Since the evolution of life is tightly coupled to the presence of free O₂, one of the major research questions is: When did the Earth's atmosphere and hydrosphere become oxidised? Modern Earth surface processes are heavily controlled by the presence of O₂ and, therefore, can differ strongly from surface processes in the Archaean.

The probably best preserved, although highly metamorphosed, Palaeoarchean (4.0 – 3.7 Ga) crust older than 3.6 Ga is the Itsaq Gneiss Complex (3.9 – 3.6 Ga) in southern West Greenland (Nutman et al., 1996). As part of the Itsaq Gneiss Complex, the Isua supracrustal belt contains various deep-sea chemical sedimentary rocks, among others, the oldest known BIF. The earliest indications for carbon of potentially biogenic origin are found in the metasedimentary rocks of the Isua supracrustal belt. Schidlowski (1988) attributed measured variations in $\delta^{13}\text{C}$ values to the existence of photoautotrophic organisms 3.8 Ga ago. Further evidence for the presence of planktonic organisms comes from negative $\delta^{13}\text{C}$ values in graphite globules in approx. 3.7 Ga turbiditic and pelagic sediments of the Isua supracrustal belt (Rosing, 1999). An even older indication for biological activities was proposed by Mojzsis et al. (1996), who investigated $\delta^{13}\text{C}$ in graphite inclusions in 3.85 Ga old rocks from Akilia Island (southwest Greenland). However, it is questionable if those rocks truly are of sedimentary origin (Mojzsis and Harrison, 2002; Palin, 2002; Fedo and Whitehouse, 2002). It is also unclear to what extent the "*late heavy bombardment*" restricted the evolution of life on Earth's surface

before 3.8 Ga (Maher and Stevenson, 1988; Sleep et al., 1989; Hartmann et al., 2000). The $\delta^{13}\text{C}$ data of the 3.7 Ga Isua sedimentary rocks (Rosing, 1999) is corroborated by Pb isotope data and supplemented by originally elevated U/Th ratios that indicate active oxygenic photosynthesis and at least temporarily and locally elevated oxygen levels, respectively (Rosing and Frei, 2004). Since U is mobile under oxic conditions, elevated U/Th ratios argue for at least slightly oxidising surface conditions during the time of rock formation. However, whether the elevated U/Th ratios are a primary or secondary feature remains unclear (Buick, 2008). Overall, the preserved rock record of the Palaeoarchaeon (4.0 – 3.7 Ga) is relatively small and subject to ongoing discussions.

A much larger rock record is preserved from the Mesoarchaeon (3.7 – 3.0 Ga), like the Pilbara craton in Australia and the Barberton Greenstone Belt in South Africa. In the Mesoarchaeon first occurrences of stromatolitic structures in the 3.43 Ga Strelley Pool Chert formation, Pilbara craton Australia (Allwood et al., 2006), and contemporaneous microbial mats in the 3.42 Ga Buck Reef Chert, Barberton Greenstone Belt, are documented (Tice and Lowe, 2004). Although those structures probably do not originate from oxygenic microbial communities, they at least indicate biological activity in shallow waters.

Sulphur isotope data in sulphide and sulphate minerals give the strongest evidence for low atmospheric oxygen levels throughout the whole Archaean. Archaean rocks preserved mass-independent fractionation of sulphur isotopes (MIF-S) that is expressed by large variations in $\delta^{33}\text{S}$ values. The δ notation indicates the deviation of the respective isotope composition from the mass-dependent fractionation array of a reference material; in the case of S, e.g., Canyon Diablo Troilite (Farquhar et al., 2000a). The MIF-S signal in Precambrian rocks was first described by Farquhar et al. (2000a) but multiple studies subsequently complemented the data set (Pavlov and Kasting, 2002; Bekker et al., 2004; Farquhar et al., 2007; Guo et al., 2009; Johnston, 2011). All studies show a large spread of $\delta^{33}\text{S}$ values (MIF-S) in rocks >2.45 Ga, minor variations of $\delta^{33}\text{S}$ between 2.45 and 2.09 Ga and almost no deviations from $\delta^{33}\text{S} = 0$ in rocks younger than 2.09 Ga. The MIF-S signal originates from the photochemical oxidation of S by UV radiation in an anoxic environment (Farquhar et al., 2000b, a). Positive $\delta^{33}\text{S}$ values in barites and cherts >2.09 Ga and negative $\delta^{33}\text{S}$ values in classic sedimentary rocks argue for the development of two reservoirs: (i) a water-soluble sulphate reservoir with negative $\delta^{33}\text{S}$ values, and (ii) an insoluble sulphur reservoir with positive $\delta^{33}\text{S}$ values (Farquhar et al., 2000a). With the onset of oxidative weathering after the "Great Oxidation Event" (GOE; Holland, 2002), the two reservoirs were re-homogenised, and the MIF-S signal disappeared from the rock

2 Introduction

record (Farquhar et al., 2000a). Therefore, the disappearance of the MIF-S signal around 2.45 Ga is probably the best estimate of when the Earth’s atmosphere contained excess $O_2 > 10^{-5}$ PAL (present atmospheric level). Opposite to MIF-S, the mass-dependent fractionation of sulphur isotopes only became pronounced after 2.7 Ga. Mass-dependent sulphur fractionation predominantly originates from microbial sulphate reduction, which was negligible before 2.7 Ga (e.g., Holland, 2003). $\delta^{34}S$ data of pre-GOE rocks indicate generally low sulphate concentrations, corroborating the absence of oxidative weathering in an anoxic atmosphere (Canfield and Raiswell, 1999; Canfield et al., 2000; Habicht et al., 2002).

Further evidence for low atmospheric O_2 levels in the Archaean and Early Proterozoic comes from detrital redox-sensitive minerals like uraninite (UO_2), siderite ($FeCO_3$) or pyrite (FeS_2). All three minerals are only stable under low oxygen conditions. Their occurrence as detrital grains in rocks older than 2.3 Ga (Rasmussen and Buick, 1999; Phillips et al., 2001; Young et al., 2001; Hofmann et al., 2009; Hazen et al., 2009; Sverjensky and Lee, 2010) indicate low oxygen levels during the time of sedimentary rock formation. Elevated Fe(II) and Mn(II) mass fractions in Archaean limestones and dolostones (Veizer et al., 1989), compared to Phanerozoic ones, also indicate much lower oxygen levels in the Archaean.

Shortly after the end of the Neoarchaeon (3.0 – 2.5 Ga), atmospheric oxygen levels rose to approx. 10^{-5} PAL in the course of the GOE (e.g., Farquhar et al., 2000a; Pavlov and Kasting, 2002; Holland, 2003). While the name GOE might indicate that the increase of atmospheric oxygen levels was a single *event*, it was more likely a transition *period* between 2.4 and 2.1 Ga. Multiple studies found evidence for spatially and temporarily limited occurrences of slightly elevated O_2 levels – “*whiffs of oxygen*” (Anbar et al., 2007) or “*oxygen oases*” (Kendall et al., 2010) – in the Neoarchaeon. The redox-sensitive transition metals molybdenum (Mo) and rhenium (Re) are immobile under low-oxygen conditions, which limited their abundance in Archaean seawater and contemporaneous sedimentary rocks (Holland, 2003 and references therein). Anbar et al. (2007), however, found relative enrichments of Mo and Re in the 2.5 Ga Mt. McRae shale, Hammersley Basin, Australia, arguing for at least slightly increased oxygen levels during formation time. A subsequent study by Kendall et al. (2010) found similar evidence in 2.6 – 2.5 Ga black shales of the Campbellrand-Malmani carbonate platform in South Africa. Further evidence for *oxygen whiffs* hundreds of million years before the GOE come from Mo, Fe, S, Cr isotopy, and Fe speciation data (Kaufman et al., 2007; Wille et al., 2007; Frei et al., 2009; Reinhard et al., 2009; Voegelin et al., 2010; Zerkle et al., 2012; Czaja et al., 2012).

Even earlier indications of free oxygen are reported (e.g., Kato et al., 2009; Hoashi et al., 2009; Kerrich and Said, 2011), but those could also originate from weathering during late Phanerozoic (Lowenstein et al., 2014, and references therein).

Evidence from O and Si isotopes in cherts indicate that Archaean oceans were rather mild in temperature, probably below 35 °C (Shields and Kasting, 2007; Hren et al., 2009; Blake et al., 2010). Earlier studies have suggested elevated temperatures around 85 °C (Ohmoto and Felder, 1987; Knauth, 2005; Robert and Chaussidon, 2006).

2.2.3 Proterozoic (2.5 – 0.542 Ga)

In the Proterozoic modern-style plate tectonics evolved, and the continental crust reached a volume comparable to today (Dhuime et al., 2012; Moyen and van Hunen, 2012; Næraa et al., 2012). The biogeochemical carbon cycle underwent severe changes, oxygen accumulated in the atmosphere and hydrosphere, and BIFs disappeared from the rock record.

The Palaeoproterozoic (2.5 – 1.8 Ga) is characterized by the accumulation of atmospheric oxygen to levels between 0.1 % and 10 % PAL at the end of the GOE (e.g., Holland, 2003). The subsequent onset of oxidative weathering caused severe changes in the geochemical cycles of various elements. Mass-dependent sulphur fractionation replaced MIF-S (see above), redox-sensitive elements like Mo and Cr became more enriched in black shales and iron formations (Scott et al., 2008; Konhauser et al., 2011), red beds, paleosols and shales with ferric iron (Fe(III)), and large scale Mn deposits formed (Farquhar et al., 2011; Bekker and Holland, 2012). Marine carbonates between 2.4 and 2.06 show large excursions in $\delta^{13}\text{C}$ values indicating massive burial of organic carbon and extensive production of excess O_2 (Karhu and Holland, 1996; Melezhik and Fallick, 1996; Buick et al., 1998; Bekker et al., 2001, 2005; Guo et al., 2009). Contemporaneous to the $\delta^{13}\text{C}$ excursions, the first occurrences of large-scale marine sulphate evaporites and phosphorites are documented (Bekker et al., 2003, 2006; Melezhik et al., 2005; Schröder et al., 2008; Papineau, 2010; Maheshwari et al., 2010; Reuschel et al., 2012). Sulphate and phosphorite deposits could only form after the onset of oxidative weathering. Under oxic conditions, sulphide minerals dissolve, leading to an increased riverine influx of sulphur to the oceans. Acidic fluids that form during sulphide mineral dissolution, in turn, dissolve silicate rocks causing an elevated phosphorous flux into the oceans. The increase in phosphorous supply and other nutrients due to oxidative weathering probably triggered an increase in oceanic primary production that led to elevated organic carbon burial rates (Holland, 2002; Papineau, 2010; Bekker and Holland, 2012).

2 Introduction

Apart from large-scale sulphate and phosphate deposits, the largest known manganese deposit formed in the Early Palaeoproterozoic: the 2.4–2.22 Ga Hotazel Formation. Manganese requires higher oxygen levels to get oxidized to insoluble Mn(IV) than the oxidation of Fe(II) to Fe(III). Negative cerium anomalies – a typical feature of modern, oxidized seawater (see Chapter 5) – within the upper stratigraphy of the Hotazel Formation further indicate elevated oxygen levels during Hotazel deposition (Tsikos and Moore, 1997; Schier et al., 2020).

All these observations point towards a common cause: accumulation of free oxygen in the atmosphere and hydrosphere and the subsequent onset of oxidative weathering. However, it should be noted that the deep oceans probably remained anoxic for the time being and that only shallow waters were initially oxidized. Evidence for anoxic oceanic deep waters comes from BIFs which only disappeared around 1.7 Ga and not directly after the GOE (e.g., Holland, 2003). It was also suggested that Proterozoic oceans were stratified into ferruginous, euxinic and oxidized layers (see, e.g., Canfield, 1998; Poulton et al., 2004 — for a further discussion, see Lowenstein et al., 2014 and references therein).

The commonly accepted cause of the GOE is oxygen production by cyanobacteria (e.g., Cloud, 1973). Since cyanobacteria most likely already evolved around 2.7 Ga (Brocks et al., 2003, 2005; Canfield, 2005; Buick, 2008), the pervasive oxidation of Earth's atmosphere and shallow waters was delayed by approximately 400 Ma. During those 400 Ma, near-surface sinks consumed the produced oxygen, e.g., oxidation of reduced minerals and organic carbon (François and Gérard, 1986; Holland, 2002; Goldblatt et al., 2006; Buick, 2008; Saito, 2009; Pufahl and Hiatt, 2012; Lyons et al., 2014). Occurrences of pre-GOE oxygen whiffs indicate locally and temporarily enhanced O₂ production or saturation of oxygen sinks.

Alternative or more likely complementary processes of atmosphere oxygenation were the loss of hydrogen into the interplanetary space, a subsequent increase of Earth's overall oxidation state and increasing oxygen concentrations in volcanic gases (Kasting et al., 1979; Kump et al., 2001; Catling et al., 2001; Holland, 2003), and a decline on atmospheric methane concentrations (Zahnle et al., 2006; Konhauser, 2009).

At around 2.06 Ga, the O₂ levels stabilized between 0.1 % and 10 % PAL (Bekker and Holland, 2012) and only minor variations in $\delta^{13}\text{C}$ values are observed (Buick et al., 1995; Brasier and Lindsay, 1998). Ratios of ferric Fe to total Fe remained constant in Late Palaeoproterozoic and Mesoproterozoic (Bekker and Holland, 2012). The Mesoproterozoic (1.8 – 1.2 Ga) and the Early Neoproterozoic (1.2 – 0.542 Ga) are considered the "*boring billion*" (1.85 – 0.85 Ga; Holland, 2006) due to rather stable conditions on the Earth's

surface.

Full oxygenation of deep oceans was only attained in Late Neoproterozoic approx. 580 Ma ago (Canfield, 2005; Holland, 2006; Canfield et al., 2007; Narbonne, 2010; Pufahl and Hiatt, 2012). A second large oxidation event ("*Neoproterozoic Oxidation Event*" – NOE) further increased the atmospheric oxygen to levels above 10 % PAL (e.g., Och and Shields-Zhou, 2012). The NOE was accompanied by positive $\delta^{13}\text{C}$ excursions in marine carbonates between 800 Ma and 500 Ma (Knoll et al., 1986; Derry et al., 1992; Jacobsen and Kaufman, 1999), similar to those in the Palaeoproterozoic. During that period, BIFs re-occur in the rock record but are, in most cases, associated with global glaciations (e.g., Klein and Beukes, 1993).

The Precambrian ends with the Ediacaran Period (0.635 – 0.542 Ga), characterized by the development of complex metazoans and full oxygenation of the deep oceans. It took almost 3.3 Ga from the first appearance of simple organisms around (3.8 Ga) to the first appearance of oxygen-producing cyanobacteria (2.7 Ga), the GOE (2.4 – 2.3 Ga), the NOE (0.58 Ga) and finally the complete oxidation of atmosphere and hydrosphere to modern oxygen levels at the end of Neoproterozoic (0.542 Ga).

Large knowledge progress on those drastic changes and their causes was made by the investigation of marine chemical sedimentary rocks like (banded) iron formations, manganese formations, cherts, and carbonates. Those types of rocks are geochemical archives that can preserve invaluable information on the physico-chemical conditions of ambient seawater and the contemporaneous atmosphere. This thesis focuses on marine banded iron formations, which are discussed in more detail below.

2.3 Banded iron formations

Extensive research was conducted on banded iron formations during the past decades. For detailed summaries, the reader is referred to the comprehensive reviews of, e.g. Bekker et al. (2010) and Konhauser et al. (2017).

Banded iron formations (BIFs), sometimes referred to only as iron formations (IFs), are chemical sedimentary rocks formed in oceanic environments during the Archaean and Palaeoproterozoic. While there is a reoccurrence of BIFs in the Neoproterozoic, no BIFs were formed during the Phanerozoic and, hence, there is no modern analogue of BIFs (e.g., Bekker et al., 2010). James (1954) defined iron formations as "*... a chemical sediment, typically thin-bedded or laminated, containing 15 per cent or more iron of sedimentary origin, commonly but not necessarily containing layers of chert...*".

2 Introduction

Furthermore, James (1954) separated iron formations into four different facies based on their mineralogical compositions: (i) silicate, (ii) carbonate, (iii) sulphide, and (iv) oxide facies. The predominant mineralogy of each facies comprises (i) stilpnomelane, minnesotaite, greenalite and riebeckite; (ii) siderite, ankerite, calcite and dolomite; (iii) pyrite and pyrrhotite; (iv) magnetite and hematite (see Konhauser et al., 2017 and references therein). However, it is important to note that none of the minerals in BIFs are considered truly primary (Klein, 2005). The mineralogy is a product of syn- and post-depositional diagenetic and metamorphic processes. The facies classification by James (1954), is still used. However, nowadays, sulphide-facies IFs are not necessarily considered actual IFs anymore (e.g., Bekker et al., 2010). In the following, only oxide facies BIFs will be considered as those were the subject of this thesis. The characteristic banding in BIFs occurs on various scales from mm- and sub-mm-scale microbanding over cm-scale mesobanding to m-scale macrobanding. Early studies suggested an annual cycle for the deposition of individual bands (e.g., Morris, 1993), which, however, nowadays is generally considered rather unlikely.

A different classification, based on the depositional setting, was introduced by Gross (1980) who separated Archaean and Palaeoproterozoic BIFs into Algoma and Superior-type BIFs. Algoma-type BIFs are associated with volcano-sedimentary rock successions in greenstone belts (Goodwin, 1973; James, 1983; Isley and Abbott, 1999; Huston and Logan, 2004). All known BIFs older than 3.0 Ga are Algoma-type BIFs. Generally, Algoma-type BIFs show smaller lateral extents and are thinner than Superior-type BIFs, although this might also result from much stronger deformation and folding in the greenstone belts (Gole and Klein, 1981; Huston and Logan, 2004). Due to their stratigraphic association with igneous and volcanoclastic rocks, Algoma-type BIFs are considered to have formed in the vicinity of volcanic centres in partially closed basins strongly influenced by submarine exhalative processes (Goodwin, 1962; Gross, 1980, 1983; Gourcerol et al., 2016). Therefore, Algoma-type BIFs might rather reflect local than global seawater conditions (Gourcerol et al., 2016). Superior-type BIFs are stratigraphically associated with clastic and chemical sedimentary rocks. They are considered to have formed on or along passive margins (e.g., Bekker et al., 2010; Konhauser et al., 2017) and are larger than Algoma-type BIFs (Isley, 1995; Bekker et al., 2010). The later occurrence of Superior-type compared to Algoma-type BIFs is explained by the prior absence of stable continental shelves. Although associated with passive margins, Algoma-type BIFs were deposited in deep water below the storm and fair weather wave base since respective sedimentary features are entirely lacking (Simonson and Hassler, 1996; Trendall, 2002;

Krapež et al., 2003). Granular iron formations (GIFs) do show sedimentary features of shallow water deposition but are not considered in this study.

The peak of BIF formation was between 2.8 Ga and 1.85 Ga (e.g., Bekker et al., 2010), interestingly outlasting the GOE. In early studies on the Archaean atmosphere and hydrosphere, BIFs were used as indicators for anoxic conditions (Cloud, 1973; Holland, 1973, 1984). The vast amount of Fe in BIFs required transport and dissolved ferrous Fe(II) accumulation within the water column. This was only possible under reducing and low sulphur conditions because ferric Fe(III) is water-insoluble (Bekker et al., 2004). Based on $\delta^{56}\text{Fe}$ data, there is a consensus that the main Fe source were submarine hydrothermal fluids (Holland, 1973; Jacobsen and Pimentel-Klose, 1988; Derry and Jacobsen, 1990; Beukes and Klein, 1990; Alibert and McCulloch, 1993; Bau et al., 1997; Kump and Seyfried, 2005; Konhauser et al., 2017) although some BIFs also contain portions of continental Fe indicated by their Nd isotopic composition (e.g., Alexander et al., 2008; Haugaard et al., 2013; Li et al., 2015; Viehmann et al., 2015). Several studies indicate that the formation of BIFs often coincides with episodes of enhanced magmatic activities and the formation of, e.g., large igneous provinces (Isley and Abbott, 1999; Barley et al., 2005; Bekker et al., 2010; Lowenstein et al., 2014). An alternative "benthic iron shuttle" was proposed by Anderson and Raiswell (2004) and Severmann et al. (2008). Dissolved Fe(II) derived from continental landmasses is transported within the porewater of shelf sediments into deeper water masses. Although there might be support for this model from Kuruman IF $\delta^{56}\text{Fe}$ data (Heimann et al., 2010), the correlated Brockman IF (Konhauser et al., 2017) shows a different $\delta^{56}\text{Fe}$ distribution (Beukes and Gutzmer, 2008). The Si source is less frequently considered, partly due to extremely low trace element mass fractions in (meta)chert bands. However, recent studies indicate continental influx as the main origin (e.g., Bau et al., 2022).

The deposition process of BIFs is still heavily debated and is the subject of ongoing research. Disagreement prevails about both the process of Fe oxidation and the origin of the banding. The three most commonly discussed models are (i) abiotic photooxidation of Fe(II) by UV radiation (Fig. 2.1A), (ii) indirect oxidation of Fe(II) by photosynthetically produced oxygen (Fig. 2.1B), and (iii) direct metabolic iron oxidation (Fig. 2.1C). Model (i) is based on the presumably much higher UV radiation during Precambrian due to a missing protective ozone layer (Cairns-Smith, 1978). Experimental data has shown that UV radiation with wavelengths between 217 to 406 nm can oxidise Fe(II) in reasonable quantities (Braterman et al., 1983; François and Gérard, 1986; Braterman and Cairns-Smith, 1987). However, a more recent study by Konhauser et al. (2007) argues

2 Introduction

that UV photooxidation is negligible compared to the abiotic formation of Fe silicates and Fe carbonates. Model (ii) is considered traditional and involves oxygen-producing cyanobacteria (Cloud, 1973). Although the "smoking gun" evidence (Bekker et al., 2010) for an early evolution of oxygenic photosynthesis is missing, there is evidence for the pre-GOE evolution of cyanobacteria as described above. Cyanobacteria, living in the near-shore photic zone, produced oxygen that, in turn, oxidized the dissolved Fe(II). Under the assumption of pre-GOE oxygen oases (see above), this model might also explain the formation of pre-GOE BIFs. Model (iii) also involves microorganisms, but in this approach, Fe(II) is used as an electron donor in the metabolism of "iron bacteria" (e.g., *Gaillionella*) or phototrophic bacteria (Harder, 1919; Ehrenreich and Widdel, 1994; Konhauser et al., 2002; Kappler et al., 2005). Therefore, no freely available oxygen was required. The "waste" products of this metabolism are Fe oxyhydroxides. It might also well be that not just one but multiple mechanisms were responsible for Fe(II) oxidation. Bekker et al. (2010) noted that the Fe oxidation process probably differed during pre and post-GOE times.

As mentioned above, BIF mineralogy is considered to be entirely secondary, and no primary mineral phases were preserved. The two most prominent models are that the primary formed phases were either Fe(III) oxyhydroxides (Konhauser et al., 2002; Kappler et al., 2005; Posth et al., 2014; Sun et al., 2015) or a Fe(III)-Si gel (Percak-Dennett et al., 2011; Zheng et al., 2016). During subsequent diagenesis and metamorphism, hematite, magnetite and various Fe silicate minerals (e.g., greenalite and stilpnomelane) formed (e.g., Ayres, 1972; Ewers and Morris, 1981; Beukes and Gutzmer, 2008; Johnson et al., 2008; Li et al., 2013). The assumption of a primary Fe(III)-Si gel phase infers that the banding developed during the diagenetic separation of Fe and Si phases (Krapež et al., 2003; Rasmussen et al., 2013; Alibert and Kinsley, 2016). However, rare earth element and yttrium data strongly argue against a diagenetic origin of BIF banding, as discussed in Chapter 5. Therefore, the banding might more likely resulted from alternating episodes dominated by Fe-rich and Si-rich water masses (Klein and Beukes, 1989; Morris, 1993; Krapež et al., 2003; Fischer and Knoll, 2009).

Banded iron formations were intensively studied in the past decades but are still not fully understood. Nevertheless, BIFs provided invaluable insights into the evolution of Earth's atmosphere and hydrosphere and will provide even more information as analytical technologies continuously evolve.

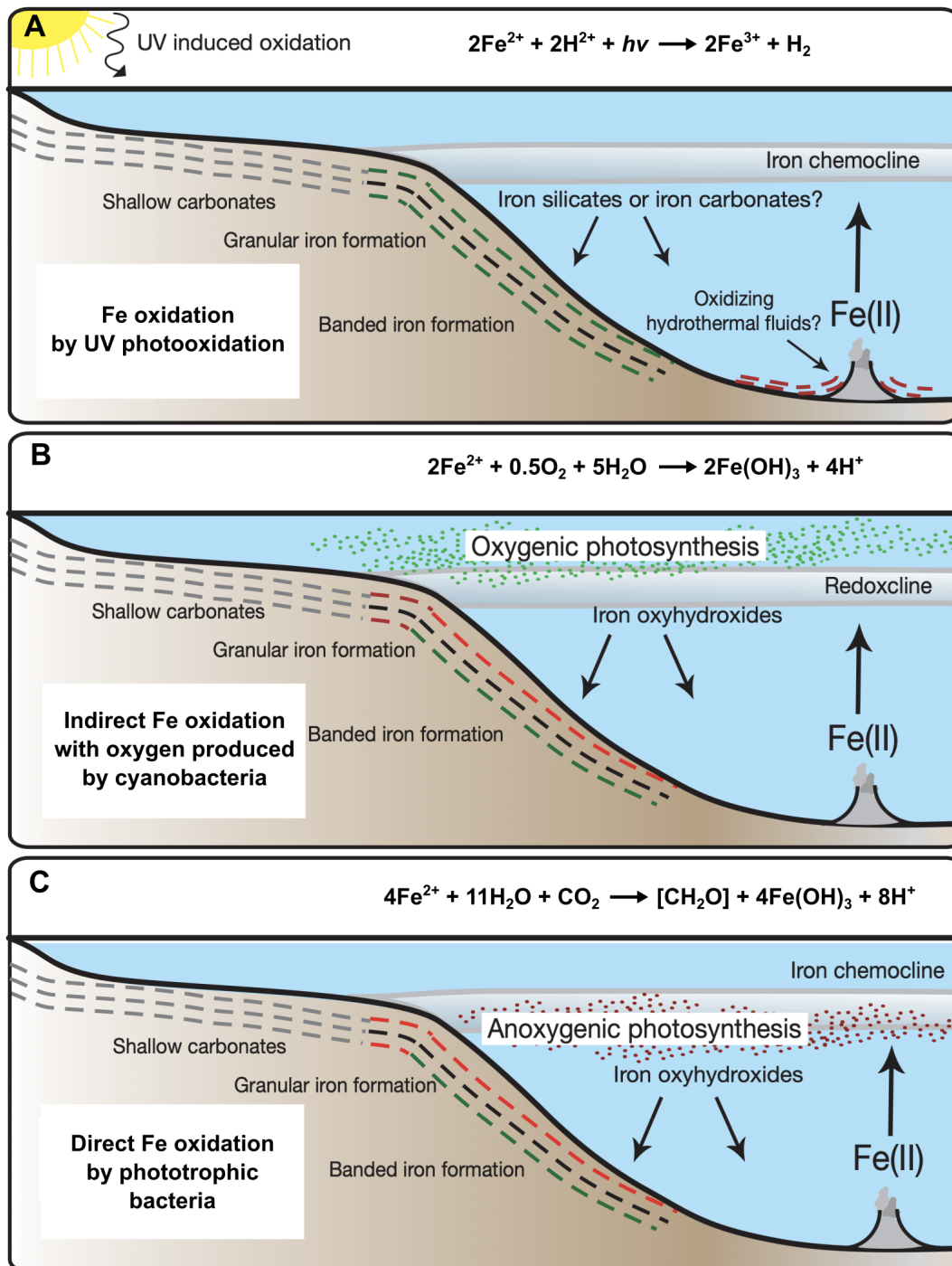


Figure 2.1: Formation models for BIFs. (A) Abiotic photooxidation of Fe(II) by UV radiation. (B) Indirect oxidation of Fe(II) by photosynthetically produced oxygen. (C) Direct metabolic iron oxidation. Modified after Bekker et al. (2010).

2.4 Gallium and aluminium

While aluminium (Al) is the most abundant metal and the third most abundant element in the Earth's crust, after oxygen and silicon (Rudnick and Gao, 2003), gallium (Ga) only occurs in trace amounts. Nevertheless, Ga and Al have similar properties and are located one above the other in the 13th group of the periodic table: Both elements naturally occur in a trivalent state and are not redox-sensitive like, for example, Fe, Ce or Eu. Furthermore, Ga and Al have similar atomic radii of 2.33 Å and 2.39 Å (Rahm et al., 2016). Therefore, it can be expected that Ga and Al show coherent behaviour in geochemical processes that are controlled by charge and radius, similar to the "CHARAC" behaviour of the geochemical twins Y-Ho or Zr-Hf (Bau, 1996). Gallium and aluminium are thus considered *geochemical partner* similar to germanium and silicon — the term *geochemical twins* is avoided here because Al can be a major element while Ga is almost always a minor or trace element in geological samples. There is a vast amount of studies that have investigated the behaviour of Al in various geochemical processes throughout the last decades (e.g., Hydes and Liss, 1977; Van Bennekom and Jager, 1978; Hydes, 1983; Kremling, 1985; Orians and Bruland, 1985; Morris et al., 1986; van den Berg et al., 1994; Middag et al., 2009, 2011). Also, numerous geochemical publications are already available that at least partially deal with Ga (e.g., Vincent and Nightingale, 1974; Persson et al., 2006; Breiter et al., 2013; Løvik et al., 2015; Yuan et al., 2018). However, despite being geochemical partners, only a few studies have been published on the coupled Ga-Al behaviour (see below).

While the geochemical behaviour of Ga and Al is still not fully understood, there are even more unsolved questions about their coupled or decoupled geochemical behaviour. Reliable geochemical data for Ga and Al in the same samples are scarce; therefore, precise predictions on their relative behaviour in natural systems are complicated. The following describes the (relative) geochemical behaviour of Ga and Al throughout their transport from source rocks towards the oceans based on the currently available literature. However, it must be noted that these descriptions and conclusions cannot be considered as generally valid or irrefutable. They should instead be seen as the basis for the working hypothesis of this thesis.

2.4.1 Gallium and aluminium literature data

For a proper discussion of the current scientific knowledge, literature data are of great importance. They can be used to compare element behaviour in different geochemical

processes and to develop models to predict the behaviour under certain conditions. However, if elements of interest are considered rather exotic, either in general or for the sample type of interest, only a small amount of literature data is available. Furthermore, validating published data's quality can be anything from challenging to impossible. While Ga is quite commonly included in geochemical analyses of igneous rocks (e.g., over 19,000 entries for igneous rocks in the EarthChem database; www.earthchem.org/petdb), there is only a very limited amount of Ga concentration data in chemical sedimentary rocks. Even fewer publications contain both Ga and Al data, and only very few studies properly discuss their data quality (e.g., Blokhin et al., 2014; Zhang et al., 2021).

In the following, two types of published data will be used: (i) data from individual published articles as compiled in Figure 2.2 and (ii) data from two geochemical databases that are focused on igneous (EarthChem) and sedimentary (SGP; Sedimentary Geochemistry and Palaeoenvironments Project; Farrell et al., 2021) rocks. While the published articles typically contain information on the analytical methods, the database data was used without a manual quality screening. However, it was beyond the scope of this PhD thesis to compute a satisfactory quality assessment of database data (also see Section 9.2). The database data was "only" used to gain an overview of published Ga-Al data in various rocks.

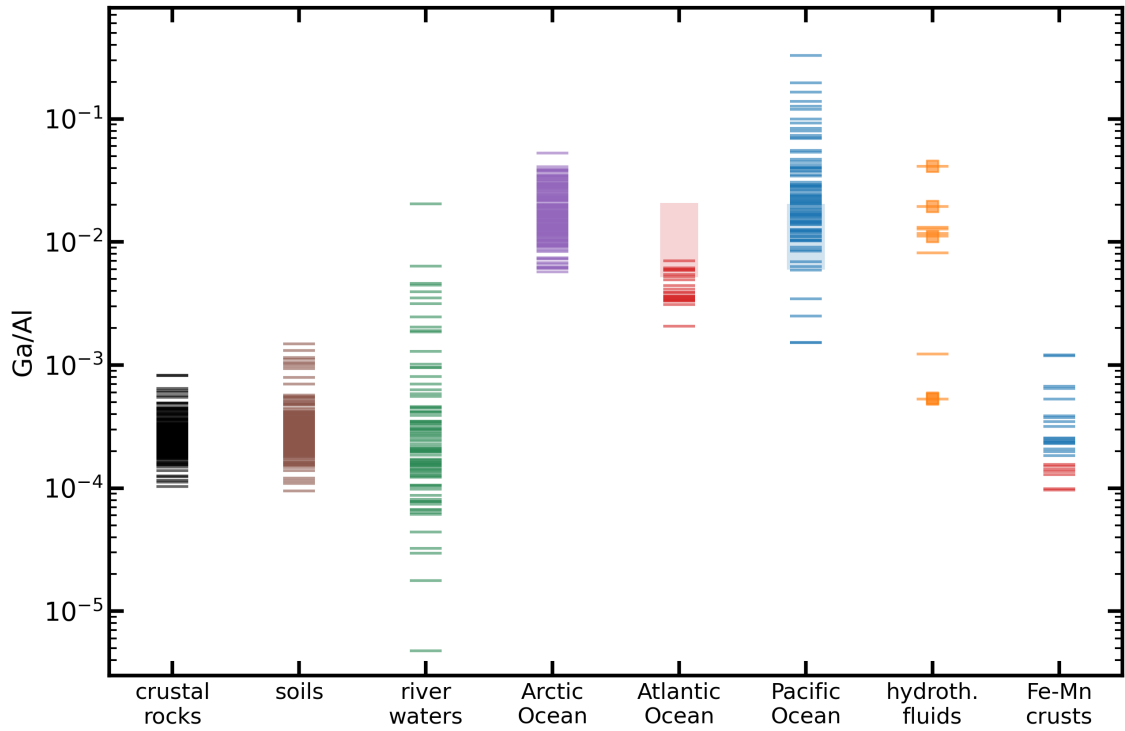


Figure 2.2: Literature data of Ga/Al mass ratios in clastic sedimentary and *igneous rocks* (Goodman, 1972; Tarney et al., 1977, 1979; De Argollo and Schilling, 1978; Cameron and Garrels, 1980; McLennan et al., 1983; Le Roex, 1985; Clarke et al., 1989; Shiller and Frilot, 1996; Fedo et al., 1996; Sanematsu et al., 2011; Amedjoe et al., 2018), *soils* (Shiller and Frilot, 1996; Hieronymus et al., 2001; Chen et al., 2001; Liang et al., 2009; Sanematsu et al., 2011; Yuan et al., 2022), *river water* (Shiller and Frilot, 1996; Pokrovsky and Schott, 2002; Gaillardet et al., 2013), *seawater* (Shiller, 1988, 1998; Orians and Bruland, 1988b; Shiller and Bairamadgi, 2006; Parker et al., 2016; Ho et al., 2019; Charette et al., 2020), *marine hydrothermal fluids* (Schmidt et al., 2017) and *Fe-Mn crusts* (Schiert et al., 2021).

2.4.2 Gallium and aluminium in igneous rocks

Igneous bulk rock measurements show very uniform Ga/Al ratios restricted to a rather narrow range between 1.0×10^{-4} and 8.3×10^{-4} with an average of 2.9×10^{-4} ($n=200$; Goodman, 1972; Tarney et al., 1977; De Argollo and Schilling, 1978; Tarney et al., 1979; Le Roex, 1985; Clarke et al., 1989; Shiller and Frilot, 1996a; Breiter et al., 2013). The average upper continental crust's (UCC) Ga/Al ratio of 2.15×10^{-4} (Rudnick and Gao, 2003) also falls in the range of igneous rock Ga/Al ratios. Therefore, it could be assumed that Ga and Al behave perfectly coherent in igneous rock-forming processes. Goodman (1972), however, performed a more detailed study on Ga and Al distributions in basic volcanic rocks (mainly alkali-basalts and ankaramite) and revealed Ga-Al fractionation between different mineral phases and the groundmass. The groundmass of the investigated rocks shows slightly elevated and more narrow Ga/Al ratios (2.04×10^{-4} to 3.43×10^{-4}) compared to the whole rock samples (1.67×10^{-4} to 3.08×10^{-4}). Goodman (1972) argued that this Ga-Al fractionation between groundmass and crystallised minerals is due to the preference of Ga for tetrahedral sites, which are provided in the liquid phase during fractional crystallisation. This is supported by the observation that the investigated clinopyroxenes, which offer octahedrally coordinated sites, show very low Ga concentrations. In contrast, the plagioclases show elevated Ga concentrations but, nevertheless, also the lowest Ga/Al ratios. Overall, Goodman (1972) concluded that Ga clearly prefers tetrahedrally coordinated sites, and if tetrahedral Fe(III) and Al(III) sites are available, Ga prefers the larger Fe(III) site. The ionic radii given by Shannon (1976) confirm that the effective ionic size of Ga(III) is even closer to that of Fe(III) than to Al(III), both in tetrahedral and octahedral coordination (see Tab. 2.1). Furthermore, the much larger ionic radii of Fe(II) (Tab. 2.1) explain why Ga concentrations in igneous magnetites (contains Fe(III)) are much higher compared to those of ilmenite (Fe(II)) in the same samples (Vincent and Nightingale, 1974). Relatively low Ga concentrations for ilmenite and haematite were already reported earlier by Burton et al. (1959). Vincent and Nightingale (1974) conclude that the liquid phase's Ga concentration increases throughout magma fractionation and that increasing Ga contents in different magnetites is due to a later crystallisation from a more Ga-enriched magma. Nevertheless, those highly effective inter-mineral fractionations of Ga and Al during fractional crystallisation must be spatially limited and occur relative to the whole magma body in a closed system because igneous bulk rock studies show very uniform Ga/Al ratios. Otherwise, igneous rocks with different degrees of fractionation should also show different Ga/Al ratios.

2 Introduction

Table 2.1: Ionic radii of Ga, Al and Fe in tetrahedral and octahedral coordination. Data from Shannon (1976).

Element	Tetrahedral coordination	Octahedral coordination
	Ionic radius [\AA]	
Ga(III)	0.47	0.620
Al(III)	0.39	0.535
Fe(III)	0.49	0.645
Fe(II)	0.63	0.780

A large data compilation from the EarthChem database (www.earthchem.org/petdb; Dec. 9th, 2022) of all entries that contain Ga and Al data (n=17,798) shows a very uniform Ga/Al ratio distribution in all kinds of volcanic, plutonic and volcanoclastic rocks (Fig. 2.3). The Ga/Al ratio distribution of all these samples is restricted to a narrow range from 1.4×10^{-4} to 4.2×10^{-4} (5 % to 95 % per centile) with a median of 2.2×10^{-4} . Although this dataset was not screened for its analytical quality, especially with regard to Ga, the vast amount of concordant entries gives a good constraint on Ga/Al ratios in Earth's igneous rocks.

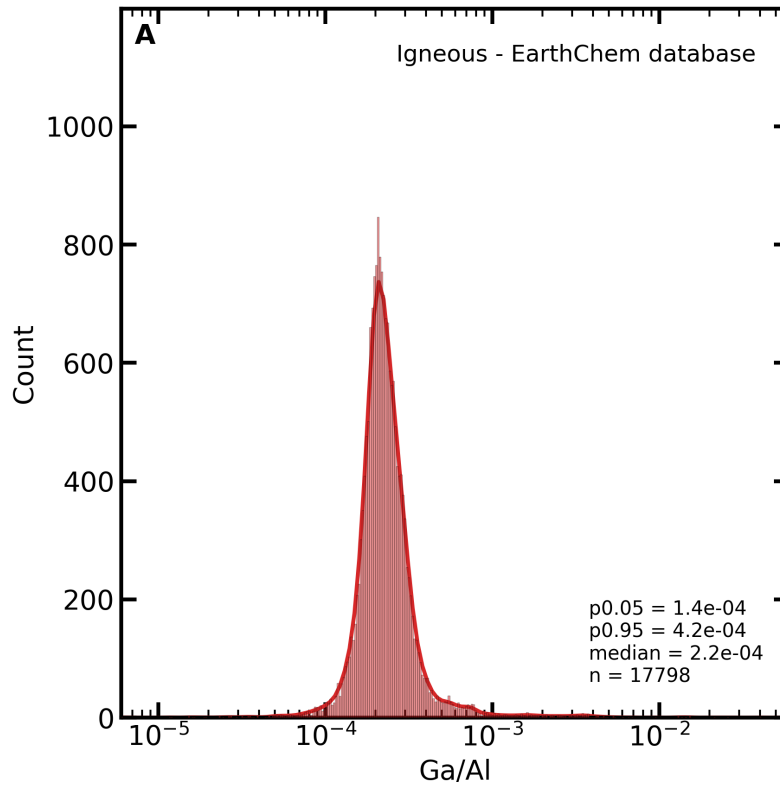


Figure 2.3: Histogram of Ga/Al ratios in *igneous* rocks from the EarthChem database for all entries that contain Ga and Al data. The solid line indicates the probability density. The dataset was compiled on the Dec. 9th, 2022 from the EarthChem database webpage: www.earthchem.org/petdb. Ga/Al ratios predominantly (90 %) range between 1.4×10^{-4} (5 % per centile) and 4.2×10^{-4} (95 % per centile) with a median of 2.2×10^{-4} .

2 Introduction

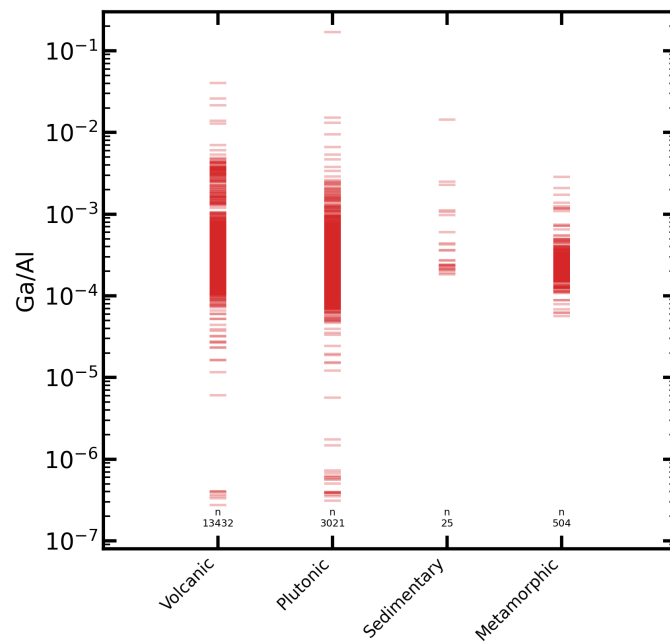


Figure 2.4: Ga/Al ratios for *volcanic*, *plutonic*, *igneous sedimentary* and *metamorphic* rocks from the EarthChem dataset (see Fig. 2.3).

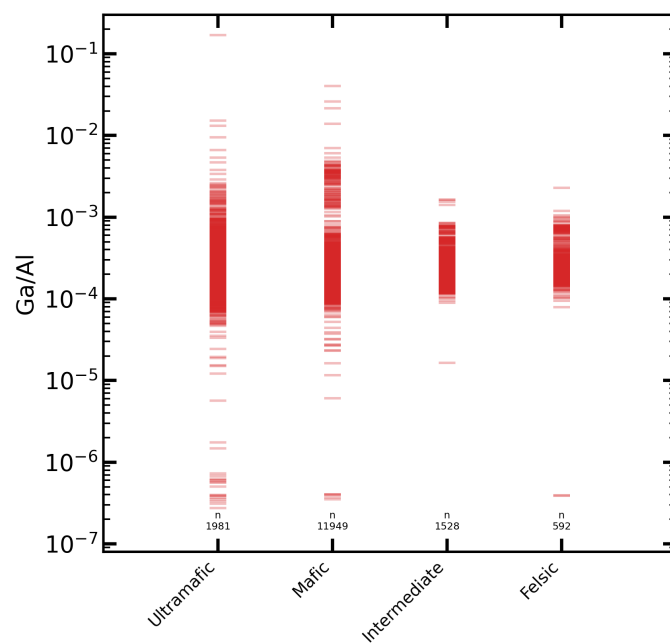


Figure 2.5: Ga/Al ratios for *ultramafic*, *mafic*, *intermediate* and *felsic* igneous rocks from the EarthChem dataset (see Fig. 2.3).

2.4.3 Gallium and aluminium in clastic sedimentary rocks

Despite the wide variety of sedimentary rocks, most of the exposed sedimentary rocks on Earth are comprised of sandstones and shales, with 26.2 % and 25.4 % total share, respectively (Amiotte Suchet et al., 2003). Sandstones and shales account for 79 % of clastic sedimentary rocks, while carbonates constitute 21 %. This distribution is also mirrored in published data on sedimentary rocks.

Clastic sedimentary rock measurements show very uniform Ga/Al ratios that are similarly restricted to a rather narrow range like igneous rocks (Fig. 2.2 included as "crustal rocks"). A manual search for published Ga/Al ratios in shales, mudstones, siltstones and sandstones yielded Ga/Al ratios between 1.2×10^{-4} and 4.0×10^{-4} , with an average of 2.3×10^{-4} ($n=86$; Cameron and Garrels, 1980; McLennan et al., 1983; Shiller and Frilot, 1996a; Fedo et al., 1996; Sanematsu et al., 2011). An unscreened data compilation of 16,885 siliciclastic rock entries (shale, siltstone, mudstone, sandstone, conglomerate, oil shale, arkose, argillite, quartzite, slate, greywacke, pelite, claystone, metapelite) from the SGP database (Farrell et al., 2021) yields a median Ga/Al of 2.5×10^{-4} with 90 % of the data (5 % to 95 % per centile) ranging between 1.5×10^{-4} and 5.0×10^{-4} (Fig. 2.6). The sedimentary rock dataset (SGP) exhibits a more irregular distribution in the histogram compared to the igneous rocks (EarthChem). This could originate from the generally lower Ga (and Al) concentrations in sedimentary compared to igneous rocks and, consequently, larger uncertainties in the analytical data of the former. The dataset was compiled on Dec 6th, 2022, via the SGP database webpage (<https://sgp-search.io/>), and all sample entries at least containing 1 ppm Ga were included. "Metamorphic" samples were excluded. Although this data compilation was not specifically screened for its data quality, geological setting, exact petrology or potential outliers, its Ga/Al ratio distribution coincides with the manual literature data search. The predominant role of shales, shale-like rocks, and sandstone is also visible in the SGP data set, in which (oil) shales, siltstones, mudstones, and sandstones make up 93 % of all entries. Nevertheless, the SGP dataset also includes some less mature clastic sedimentary rocks like conglomerates or arkoses. However, both show a similar Ga/Al distribution, and a fractionation of Ga-Al during the maturing process is not recognisable (Fig. 2.7). Since the majority of the Earth's surface rocks are clastic sedimentary and igneous rocks (Amiotte Suchet et al., 2003), these are also the source rocks for new clastic sedimentary rocks. The uniformity of Ga/Al ratios in clastic sedimentary and igneous rocks further corroborates that Ga and Al do not fractionate during clastic sedimentary processes.

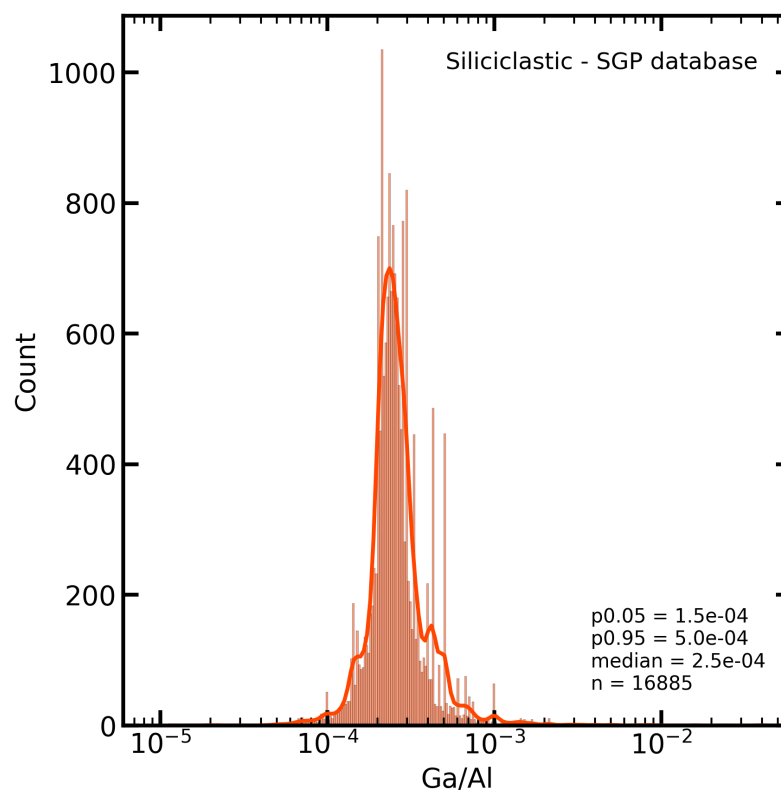


Figure 2.6: Histogram of Ga/Al ratios in clastic sedimentary (*siliciclastic*) rocks from the SGP database (Farrell et al., 2021) for all entries that contain Ga and Al data. The solid line indicates the probability density. The dataset was compiled on Dec. 6th, 2022 from the SGP database webpage: <https://sgp-search.io/>. Ga/Al ratios predominantly (90 %) range between 1.5×10^{-4} (5 % per centile) and 5.0×10^{-4} (95 % per centile) with a median of 2.5×10^{-4} .

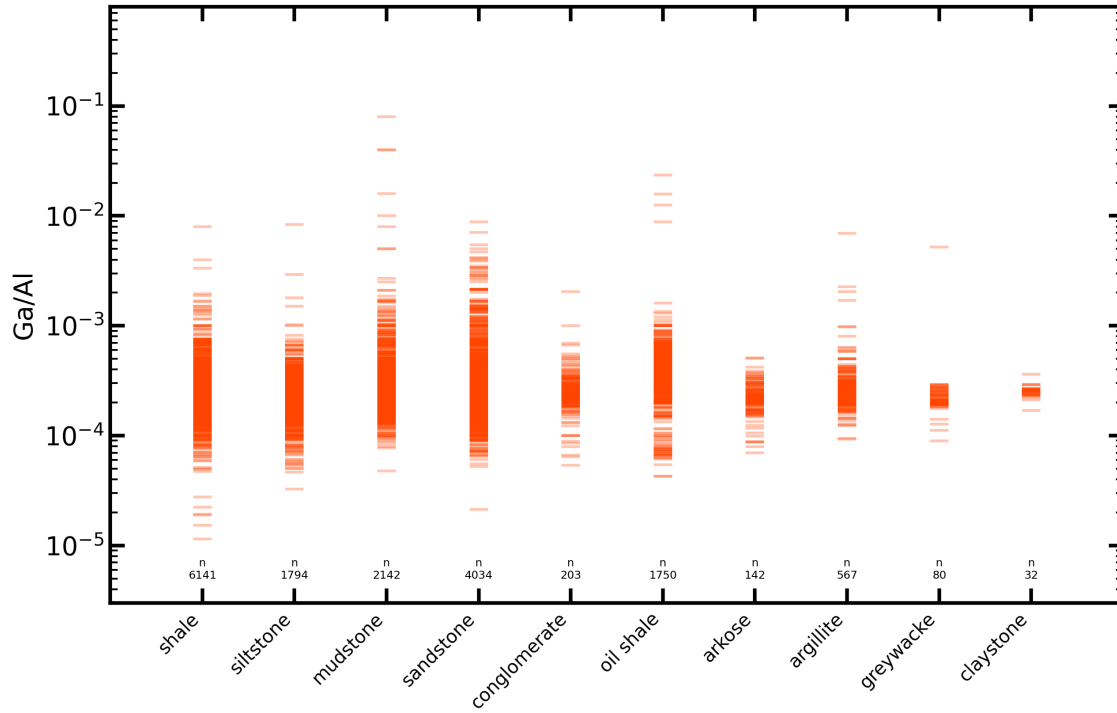


Figure 2.7: Ga/Al ratios for *siliciclastic* rocks from the SGP dataset (see Fig. 2.6). The lithologies listed here were taken from the SGP database. *Shales*, shale-like rocks (*siltstone* and *mudstone*) and *sandstone* account for the largest part of sample entries.

2.4.4 Gallium and aluminium in chemical sedimentary and carbonate rocks

A manual literature search for Ga and Al concentrations, or Ga/Al ratios, in chemical sedimentary rocks like cherts, phosphorites and carbonate rocks is even more challenging than for clastic sedimentary rocks. This also becomes visible by the much smaller amount of SGP entries that contain Ga and Al data for cherts (n=205), phosphorites (n=839) and carbonates (n=904) compared to the siliciclastic rocks.

In the category of carbonates, the vast majority of sample entries are characterised as limestones (n=562) or simply as carbonate (n=180; Fig. 2.8). Unfortunately, it is unclear whether the carbonates' origins are clastic, chemical or biological. However, all carbonate entries cover a rather narrow Ga/Al ratio range from 1.6×10^{-4} (5 % per centile) to 8.3×10^{-4} (95 % per centile) and a median of 2.6×10^{-4} (Fig. 2.9).

The chemical sedimentary rocks in the SGP database cover a Ga/Al ratio range from 1.7×10^{-4} to 1.0×10^{-3} (5 % to 95 % per centile) with a median of 3.1×10^{-4} (Fig. 2.10). The larger spread in Ga/Al ratios compared to previously mentioned rocks, originates from the phosphorite samples (n=839; Fig. 2.11). However, the cherts (n=205) cover a much narrower Ga/Al range from 2.0×10^{-4} to 4.0×10^{-4} (5 % to 95 % per centile) with a median of 2.7×10^{-4} .

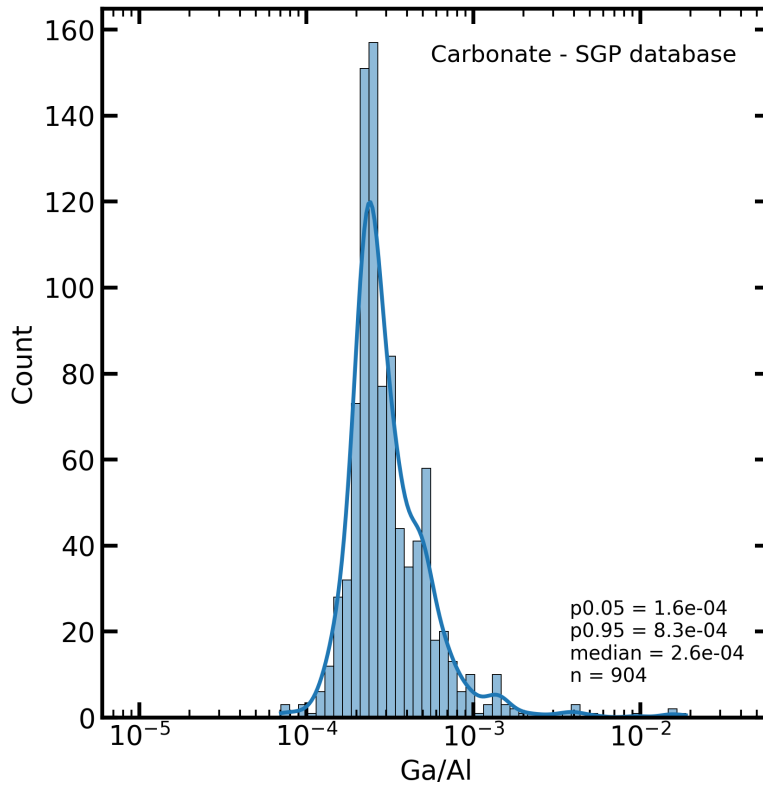


Figure 2.8: Histogram of Ga/Al ratios in *carbonate* rocks from the SGP database (Farrell et al., 2021) for all entries that contain Ga and Al data. The solid line indicates the probability density. The dataset was compiled on Dec. 6th, 2022 from the SGP database webpage: <https://sgp-search.io/>. Ga/Al ratios predominantly (90 %) range between 1.6×10^{-4} (5 % per centile) and 8.3×10^{-4} (95 % per centile) with a median of 2.6×10^{-4} .

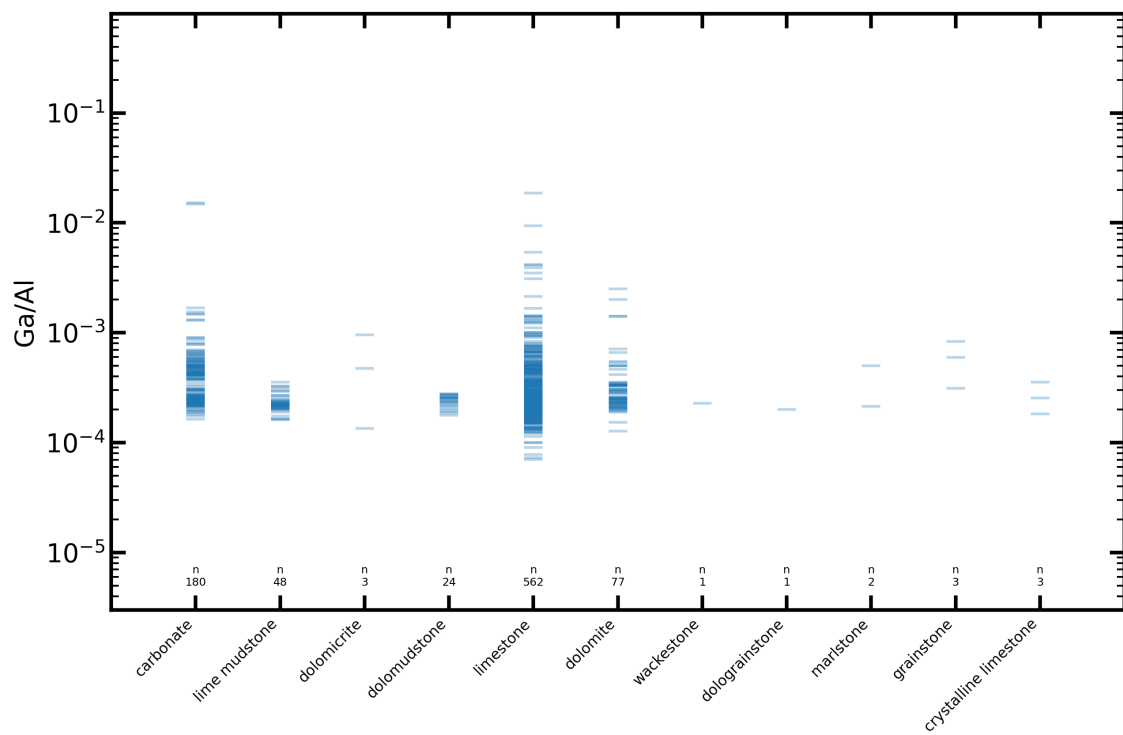


Figure 2.9: Ga/Al ratios for *carbonate* rocks from the SGP dataset (see Fig. 2.8). The lithologies listed here were taken from the SGP database.

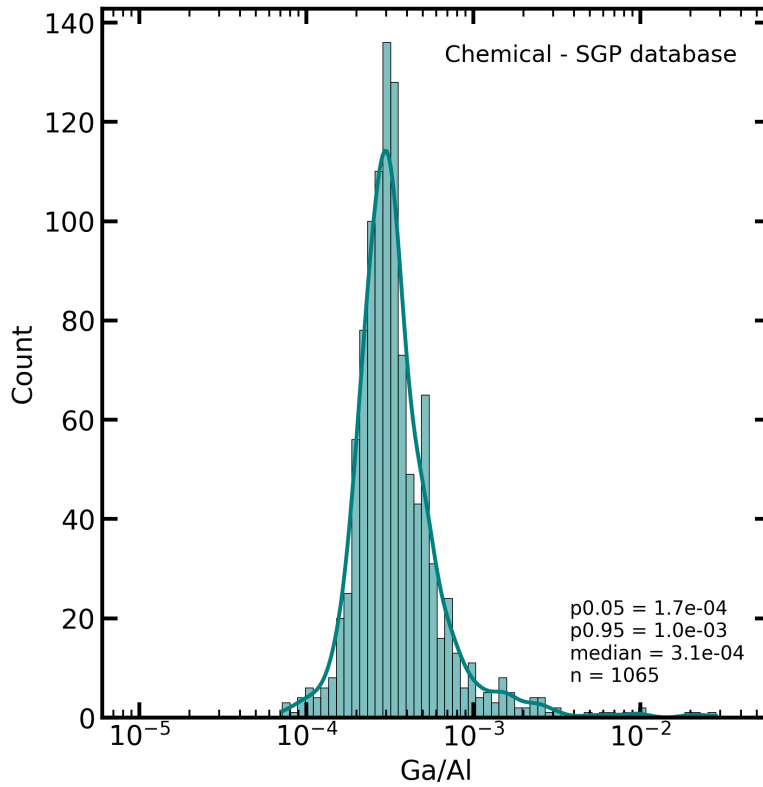


Figure 2.10: Histogram of Ga/Al ratios in *chemical* rocks from the SGP database (Farrell et al., 2021) for all entries that contain Ga and Al data. The solid line indicates the probability density. The dataset was compiled on Dec. 6th, 2022 from the SGP database webpage: <https://sgp-search.io/>. Ga/Al ratios predominantly (90 %) range between 1.7×10^{-4} (5 % per centile) and 1.0×10^{-3} (95 % per centile) with a median of 3.1×10^{-4} .

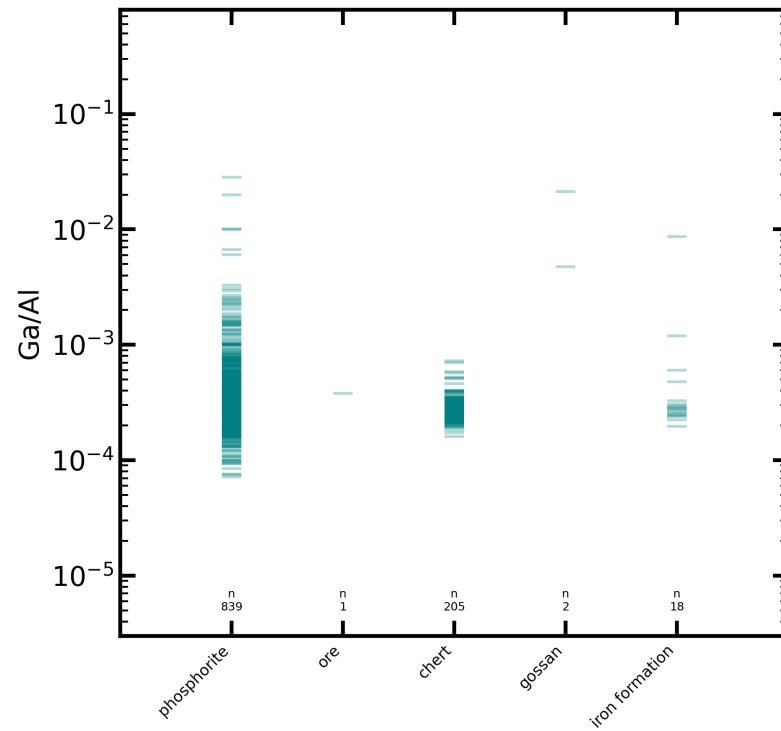


Figure 2.11: Ga/Al ratios for *chemical* rocks from the SGP dataset (see Fig. 2.10). The lithologies listed here were taken from the SGP database.

2.4.5 Particle reactivity

In order to properly describe and discuss the transport of Ga and Al from the continental land masses into the oceans, the term "*particle reactivity*" should be clarified first:

Particle reactivity is often referred to as the reason for the different behaviour of Ga and Al in aqueous environments (Orians and Bruland, 1988a, b; Shiller, 1988; Parker et al., 2016; Ho et al., 2019). Particle reactivity qualitatively describes the likelihood of an element being adsorbed onto a particle surface. Elements with a relatively higher particle reactivity are preferably adsorbed. In the case of Ga and Al, the latter is considered to have the higher particle reactivity resulting in elevated Ga/Al ratios in the remaining dissolved phase. Although particle reactivity cannot be measured directly, other elemental properties can be representative of particle reactivity. Gallium has a slightly larger ionic radius than Al (Ga: 0.47 Å, Al: 0.39 Å; Shannon, 1976). Furthermore, the Ga-O bond length is longer and, therefore, more covalent than the Al-O bond length. The larger radius and the more covalent (i.e., weaker) bonding suggest that Ga is more easily leached from solids than Al (Shiller, 1988; Shiller and Bairamadgi, 2006; Ho et al., 2019). A different approach is the comparison of hydrolysis formation constants. However, with respect to these two contradicting argumentations can be found in literature: (i) Orians and Bruland (1988a) argue that hydrolysis-dominated elements, like Ga and Al, show an increasing particle reactivity with an increasing hydrolysis formation constant ($\log \alpha_M, OH$). Since Ga has a higher hydrolysis formation constant (Smith and Martell, 1976; Byrne, 2010), it should be more particle reactive than Al. This is, however, at odds with observations in the natural aqueous systems as not only reported by the authors themselves (Orians and Bruland, 1988a) but also by all other publications (Shiller, 1988; Orians and Bruland, 1988; Shiller and Bairamadgi, 2006; Parker et al., 2016; Ho et al., 2019). (ii) Shiller (1988), on the opposite, argues that based on the hydrolysis constants given by Smith and Martell (1976), $Al(OH)^{4-}$ should be preferably adsorbed compared to $Ga(OH)^{4-}$. While the hydrolysis constants of Ga and Al can be determined quantitatively, their interpretations seem not to be uniform. This could also originate from the non-uniform reporting of hydrolysis constants ($\log \alpha$, $\log \beta$ or $\log K$ values).

Regardless of the interpretation of hydrolysis constants, the aforementioned published studies all agree that their inorganic speciation controls the particle reactivity of Ga and Al in natural aqueous environments. Under natural river water and seawater pH conditions (pH 6–8), the dominant Ga speciation is $Ga(OH)^{4-}$ while Al is present as $Al(OH)_3^0$ and partly as $Al(OH)^{4-}$ (Byrne, 2002). Most particle surfaces, both inorganic and organic, are negatively charged (Neihof and Loeb, 1972) — an exception are, for example, the slightly

positively charged surfaces of Fe (oxy)hydroxides. While neutral $\text{Al}(\text{OH})_3^0$ complexes might also associate with negatively charged particle surfaces, $\text{Ga}(\text{OH})^4-$ is repelled (Orians and Bruland, 1988a; Shiller and Frilot, 1996a; Parker et al., 2016; Ho et al., 2019). One important aspect here is that hydrolysis constants are determined under lab conditions for the reaction of cationic elements and OH groups. However, in natural waters, cationic Ga(III) and Al(III) are almost non-existent. Therefore, even if the higher hydrolysis constants of Ga would facilitate a stronger binding of Ga onto particle surfaces, its predominant speciation of $\text{Ga}(\text{OH})^4-$ prohibits docking onto negatively charged particle surfaces in the first place.

In summary, it can be said that the rather descriptive and qualitative expression of a "*higher particle reactivity of Al compared to Ga*" is caused by their predominant speciations in natural aqueous environments. Different pH conditions, however, change the dominant speciations, and therefore pH can strongly influence the particle reactivity and fractionation of Ga and Al.

2.4.6 Gallium-aluminium cycle – from crustal rocks to seawater back to chemical sedimentary rocks

The previous sections on Ga-Al distributions in different rock types show that major crustal rocks, regardless of their lithology, cover a rather narrow Ga/Al ratio range with medians between 2×10^{-4} and 3×10^{-4} . Although metamorphic rocks were not specifically discussed here, 504 entries of low-grade to high-grade metamorphic rocks are included in the used EarthChem dataset. These metamorphic rocks show identical Ga/Al ratios to the igneous rocks (Fig. 2.4). Therefore, the UCC Ga/Al ratio of 2.15×10^{-4} given by Rudnick and Gao (2003) is a good approximation of a continental Ga/Al ratio source signal.

Only little is known about the coupled behaviour of Ga and Al during continental weathering. First studies by Shiller (1988) and Shiller and Frilot (1996) investigated Ga and Al in river waters and their distribution between source rocks, residual phases (soils and streambeds) and river waters. Shiller (1988) provided the first Ga and Al data for five rivers (pH 7.1 to 7.7) from the U.S. Their samples were filtered through $0.4 \mu\text{m}$ filters and, therefore, still contain the colloidal fraction. The five rivers show Ga/Al ratios ranging from 7.8×10^{-5} to 2.7×10^{-3} (0.03 to 1.06 mmol/mol), covering one and a half orders of magnitude. Shiller and Frilot (1996) investigated 15 river systems. They compared Ga and Al in $0.4 \mu\text{m}$ filtered river water samples with the respective source

rocks and the supposed residual phases of weathering, streambed sediments and topsoils. While they could not find significant differences in Ga/Al ratios between the source rocks (1.6×10^{-4} to 3.9×10^{-4} , one sample 8.8×10^{-4}) and residual phases (1.3×10^{-4} to 3.4×10^{-4} in stream bed sediments; 1.6×10^{-4} to 2.6×10^{-4} in top soils), the river water samples show elevated Ga/Al between 1.6×10^{-4} and 1.7×10^{-2} (0.06 mmol/mol to 1.78 mmol/mol), covering two orders of magnitude. In both studies (Shiller, 1988; Shiller and Frilot, 1996), the authors conclude that the Ga/Al ratios in river water are controlled by the differences in particle reactivity. Shiller (1988) assumed that river water Ga/Al ratios result from the prevailing speciation of Ga and Al, which is pH-dependent. Therefore, Shiller (1988) assumed that the Ga/Al ratios in river water must be controlled by pH and the amount of organic particles. Shiller and Frilot (1996) could not find good correlations of pH with Ga or Al concentrations. However, the two rivers with the highest dissolved organic carbon (DOC) amount show lower Ga/Al ratios than Shiller and Frilot (1996) expected, based on weathering intensity in those areas. Therefore, Shiller and Frilot (1996) concluded that Al is complexed by DOC and kept in the "dissolved" phase, which reduces the Ga/Al ratio. However, it must be noted that in both studies (Shiller, 1988; Shiller and Frilot, 1996a), the samples were filtered with $0.4 \mu\text{m}$ filters and therefore do not represent the truly dissolved phase. Nowadays, it is known that there can be plenty of organic and inorganic nano-particles and colloids in the $<0.4 \mu\text{m}$ fraction (Merschel et al., 2017). Therefore, it is more likely that the lower Ga/Al ratios in the two high-DOC rivers are due to surface adsorption of Al onto organic colloids ($<0.4 \mu\text{m}$) rather than complexation. Furthermore, the relatively large filter size of $0.4 \mu\text{m}$ could also explain the spread of Ga/Al ratios over two orders of magnitude. If particle reactivity is the driving control on riverine Ga/Al ratios, different particle size distributions in the investigated rivers lead to different amounts of particles in the filtered samples, leading to a large spread in Ga/Al ratios.

A more recent study on boreal rivers by Pokrovsky and Schott (2002) corroborates the assumption that riverine Ga and Al behaviour is controlled by particles. The authors investigated two rivers, one with lower organic carbon (OC) content but higher discharge (Kalga River, NW Russia) and another one with elevated OC content but lower discharge (Unduksa River, NW Russia). Both rivers mainly cover a neutral pH range from 6 to 7, with only a few exceptions (pH 5.5 to 7.9) in the OC-rich river. Pokrovsky and Schott (2002) performed stepwise filtration ($5 \mu\text{m}$, $0.8 \mu\text{m}$, $0.2 \mu\text{m}$) and even ultra-filtration (100 kD, 10 kD, 1 kD). They found that Ga and Al are mainly associated with Fe colloids ($>100 \text{kD}$) and that there is only, if at all, a weak correlation between Ga and Al with

2 Introduction

OC. The Ga/Al ratios throughout stepwise filtration remain rather constant (Fig. 2.12). This, however, seems to be at odds with the different particle reactivities of Ga and Al. It would be expected that samples with a high particle load should have lower Ga/Al ratios compared to the ultra-filtered samples.

Studies that focus on the Ga-Al distribution in weathering residual phases were conducted by Hieronymus et al. (2001), Richardson et al. (2022) and Yuan et al., (2022). Hieronymus et al. (2001) investigated Ga/Al variations during the formation of laterites in Cameroon and Brazil. They found that the Cameroon laterites, considered by the authors as "common laterites", show rather constant Ga/Al ratios along the weathering profiles (Fig. 2.13). The Brazilian laterites, however, exhibit pronounced variations in Ga/Al ratios (Fig. 2.13). Hieronymus et al. (2001) conclude that simple lateritisation does not fractionate Ga and Al. The decoupling of Ga and Al in the Brazilian laterites occurred in a second weathering phase, during which the previously formed kaolinite and gibbsite (lateritisation) were dissolved. During this second dissolution process, the more soluble Ga was either removed from the system or partly scavenged and accumulated by Fe (oxyhydr)oxides. The less mobile Al, on the other hand, was only partly mobilised and migrated downwards in the weathering profiles. Therefore, the Brazilian laterite does not show a correlation between Ga and Al, but they do show a positive linear correlation of Ga and Fe. Yuan et al. (2022) investigated a basalt weathering profile in South China. They found that while the Ga and Al mass fractions increased with increasing weathering, the Ga/Al ratios remained rather constant and only varied by a factor of approx. 1.5. These results are comparable to the Cameroon laterite profile by Hieronymus et al. (2001). Richardson et al. (2022) investigated grey shale weathering profiles in central New York and eastern Tennessee, USA. They stated that their samples also show rather constant Ga/Al ratios regardless of their weathering degree. However, they only provide figures with Ga and Al mass fractions along the profiles but no data tables. Therefore, a proper quantification of the Ga/Al ratio variation is impossible for the reader. Nevertheless, their results also match those of Yuan et al. (2022) and those of the Cameroon laterite from Hieronymus et al. (2001). Richardson et al. (2022) also performed batch-leaching experiments with their soil samples to simulate different weathering conditions. They found that the released Ga/Al ratio (of the solution) is lowest under oxic and acidic conditions. Therefore, Richardson et al. (2022) argue that weathering of aluminosilicates under oxic, acidic conditions should generate soil with elevated Ga/Al ratios.

A few more studies provide data for Ga and Al in soils and weathering profiles (see

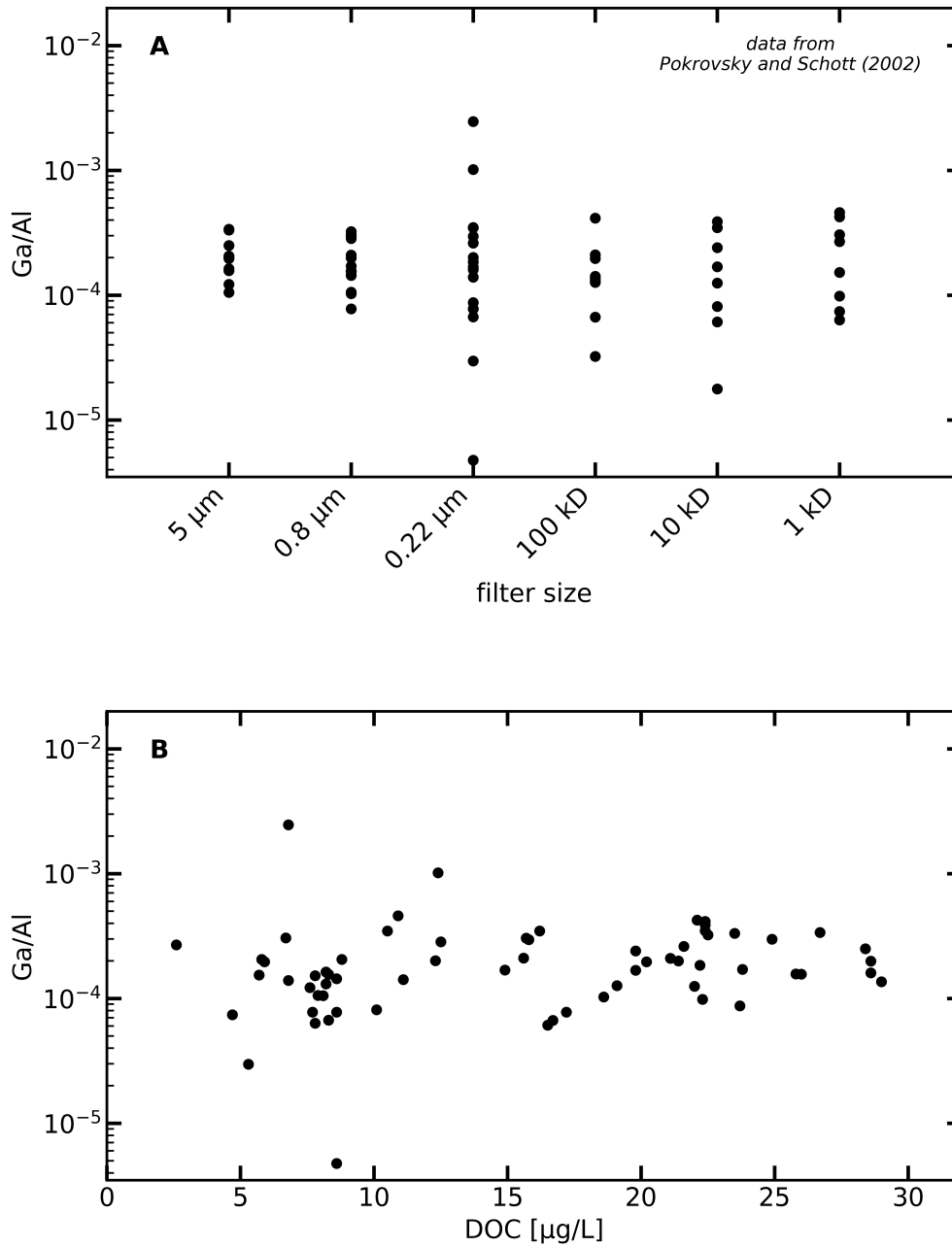


Figure 2.12: Ga/Al ratios in boreal rivers, NW Russia, from Pokrovsky and Schott (2002). A) Ga/Al ratios in different size fractions. B) Ga/Al ratios against dissolved organic carbon (DOC) content.

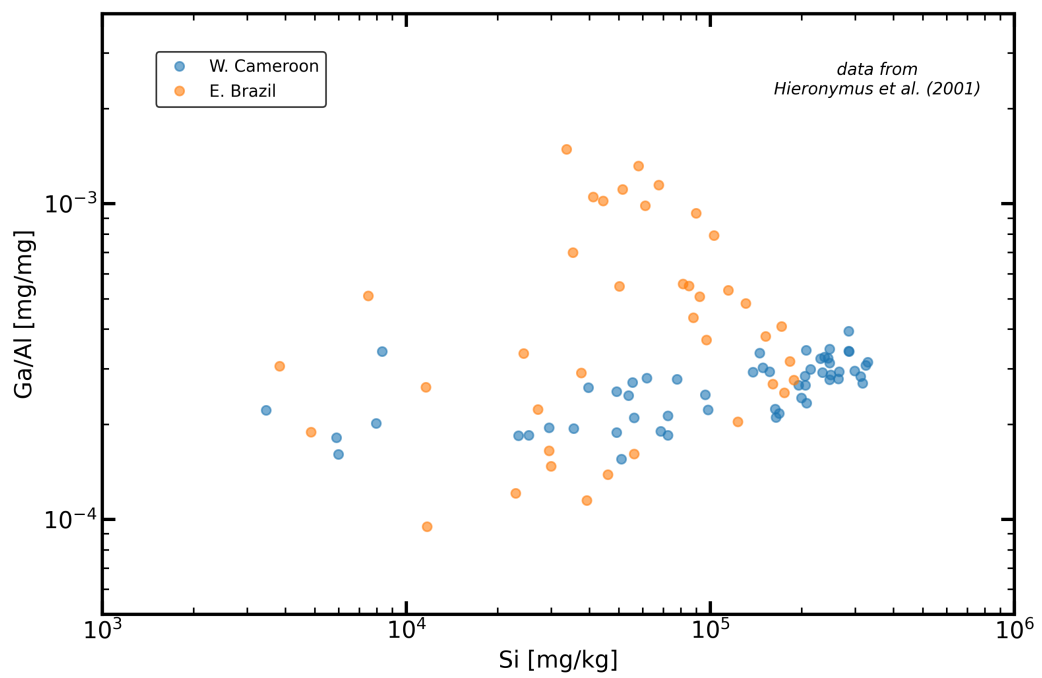


Figure 2.13: Ga/Al ratios in laterites from western Cameroon and eastern Brazil. Data from Hieronymus et al. (2001). Silicon on the x-axis is used as a rough indicator for the degree of weathering: The less Si the higher the degree of weathering.

Fig. 2.2) but, they are not focused on coupled Ga-Al systematics. The current database (Fig. 2.2) indicates that Ga and Al rather remain coupled during soil formation compared to potential source rocks. However, the strong Ga/Al ratio variation in the Brazilian laterite profile (Hieronymus et al., 2001) clearly shows that more research is needed to understand the processes that control the behaviour of Ga and Al during weathering and soil formation.

The transport of Ga and Al in river waters, as described above, is controlled by particle surface adsorption processes. Estuarine processes, however, are almost entirely unstudied. Pokrovsky and Schott (2002) provide Ga and Al data for two estuaries, but the amount of samples is small, and the resolution in the low salinity range is not sufficient. Especially because seawater shows clearly elevated Ga/Al ratios (see below) compared to crustal rocks and river waters, more research on the estuarine behaviour of Ga and Al is urgently needed.

First studies on the coupled behaviour of Ga and Al in seawater were conducted in the late 80s, especially by Orians and Bruland (Orians and Bruland, 1985, 1986, 1988a, b) but also by Shiller (1988). Those studies, and subsequent ones, investigated the distribution of dissolved and sometimes particular Ga and Al along transects and depth profiles in the Pacific and Atlantic Oceans. Already in their first study Orians and Bruland (1985) indicated that the major Al source for the modern ocean system is aeolian dust influx. This observation was later confirmed, also for Ga, due to clear correlations of elevated dissolved Ga and Al concentration in regions with high dust influx (Orians and Bruland, 1986, 1988a, b; Shiller, 1988; Shiller and Bairamadgi, 2006; Ho et al., 2019). Although riverine influxes can also be important metal sources to the oceans, there is a large consensus that the vast majority of riverine Ga and Al is removed within the estuaries upon mixing of fresh and saltwater similar to what is known for the rare earth elements and yttrium (REY; e.g., Tepe and Bau, 2016, Merschel et al., 2017). However, it remains unclear if and to which extent Ga and Al are fractionated in estuaries. Nevertheless, the original Ga/Al influx ratio of aeolian dust and river waters should not be too different (Fig. 2.2).

Some general distribution patterns for Ga and Al in seawater have been described over the past decades. The Atlantic Ocean shows higher Ga and Al concentrations than the Pacific ocean due to enhanced influxes from the surrounding landmasses (e.g., Shiller and Bairamadgi, 2006). Likewise, certain areas with locally high dust influxes, e.g., the East Atlantic at latitudes of the Sahara desert, show clearly elevated Ga and Al concentrations in the surface waters (Orians and Bruland, 1988a, b). Areas with only

2 Introduction

minor dust influx, like the Southern Oceans, show clearly lower Ga and Al concentrations in the surface waters (e.g., Shiller and Bairamadgi, 2006). The distribution of Ga and Al within the water column depends on the present water masses and their origin. For example, the Antarctic Bottom Water (AABW) and Antarctic Intermediate Water (AAIW) both originate from the dust-poor Southern Oceans and, therefore, have lower Ga and Al concentrations compared to water masses from high dust influx areas like the Mediterranean Outflow Water (Shiller and Bairamadgi, 2006; Ho et al., 2019). Therefore, local minima and maxima of Ga and Al concentrations in the water column can occur due to advection (Orians and Bruland, 1988a; Shiller, 1998; Shiller and Bairamadgi, 2006; Ho et al., 2019). Also, temporal extrema are possible, as described by Ho et al. (2019), who found a small "patch" of elevated Al concentrations on their East Pacific Zonal Transect and interpreted it as a remnant of an intense "dust event". Typically, oceanic surface waters show elevated Ga and Al concentrations resulting from the dissolution of dust particles. In the intermediate water masses, Ga and Al concentrations are usually lower than at the surface but more or less constant and only increase towards the bottom close to the water-sediment boundary (Fig. 2.14). The decrease in Ga and Al concentrations below the water surface is attributed to particle adsorption (scavenging), while remobilisation, sediment resuspension and pore waters are suggested to be deep water sources for Ga and Al (e.g., Orians and Bruland, 1985, 1988a; Ho et al., 2019). Gallium and aluminium are generally considered particle-reactive elements like Th or Pb (Orians and Bruland, 1986) and do not show a nutrient-type behaviour like, for example, Fe. Although Shiller and Bairamadgi (2006) found a correlation between Ga/Al ratios and *chlorophyll a* concentration, indicating a preferred biological scavenging of Al, this could not be confirmed in a later study by Ho et al. (2019). However, even if there is a positive correlation between Ga and Al content with organic substances in certain areas, this is most likely due to surface adsorption onto organic particles and not due to active uptake by organic organisms.

Besides these general commonalities, Ga and Al do show rather differing behaviours in seawater, i.e., they fractionate from each other. As nicely stated by Orians and Bruland (1988b): "*The marine geochemical cycles of dissolved Ga and Al are similar, yet different in many ways.*". Probably the most striking feature is that the Ga/Al ratios of oceanic surface waters are typically one to two orders of magnitude higher than that of their major source, aeolian dust (e.g., Orians and Bruland, 1988a, b; Shiller, 1988). Gallium's slightly larger ionic radius (Ga 0.47 Å, Al 0.39 Å; Shannon, 1976) and the longer and, therefore, more covalent (i.e. weaker) bonds of Ga-O compared to Al-O are most likely

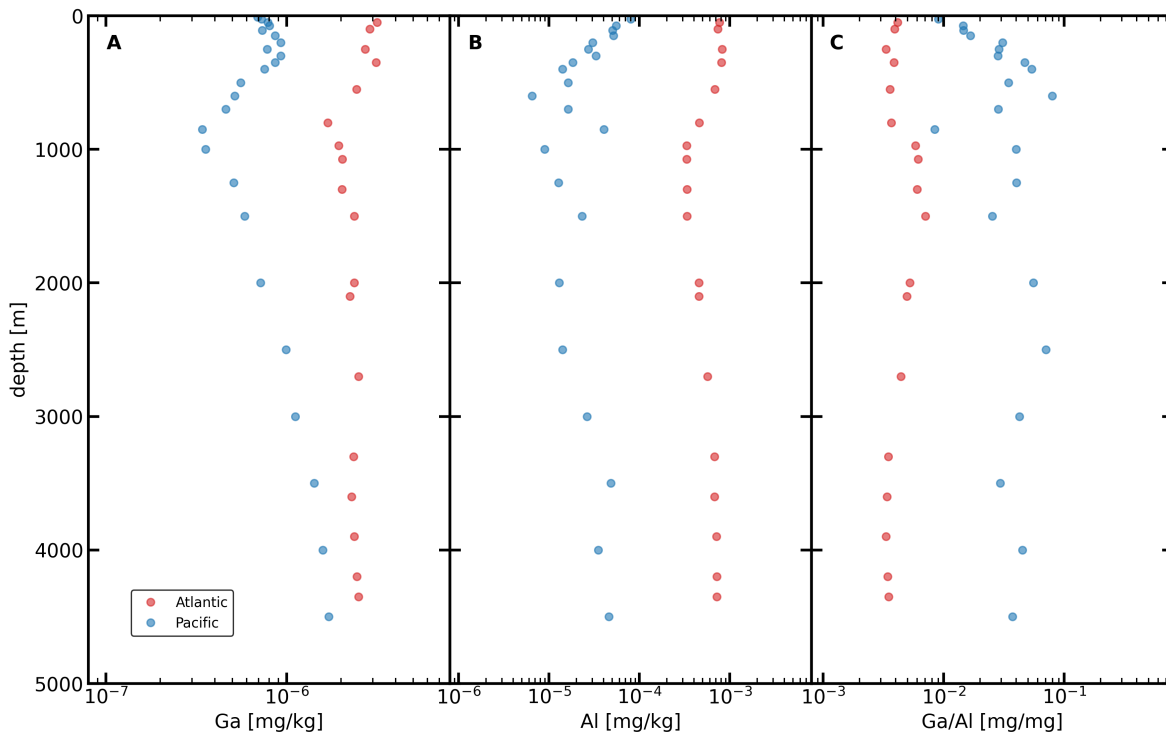


Figure 2.14: Gallium (A) and aluminium (B) concentrations and Ga/Al ratios (C) along a profile in the North West Atlantic (BATS stations) and North East Pacific (SAFE stations). Data from Parker et al. (2016).

2 Introduction

the reasons for the preferred leaching of Ga from particles.

Especially, surface waters in areas with low aeolian input can show strongly elevated but also spatially highly variable Ga/Al ratios as described for the East Pacific Zonal Transect by Ho et al. (2019). However, not only oceanic surface waters but the entire water column is characterised by elevated Ga/Al ratios compared to continental Ga/Al ratios. Figure 2.2 shows published data (references in figure caption) for the Arctic, Atlantic and Pacific oceans which all show elevated Ga/Al ratios compared to the crustal Ga/Al ratio range. The published Ga-Al data suggest that the Atlantic has slightly lower Ga/Al ratios compared to the Pacific and Arctic Oceans, although the elemental concentrations in the Atlantic are higher. Therefore, the residence times of Ga and Al must be smaller than the oceanic mixing time of approx. 1500 years (Broecker and Peng, 1982). While the North Atlantic deep-seawater is relatively young compared to the North Pacific deep water (e.g., Orions and Bruland, 1985), this further means that the residence time of Al must be shorter than that of Ga leading to elevated Ga/Al ratios in the more mature Pacific seawater. Larger inter-oceanic or inter-basin variations for Al than for Ga also indicate shorter residence times and higher particle reactivity for Al (Ho et al., 2019). These observations are further corroborated by the modelled deep water residence times for Ga of approx. 750 years (Orions and Bruland, 1988a) and for Al, between 50 to 200 years (Orions and Bruland, 1985, 1986). Aluminium's surface water residence time is even shorter and is estimated to be between 4 weeks and 4 years (Orions and Bruland, 1988a).

The seawater of the Earth's oceans is source to marine chemical sedimentary rocks. A first study on the behaviour of Ga and Al during the formation of marine ferromanganese (Fe-Mn) crusts and nodules was conducted by Schier et al. (2021). It was shown that modern Fe-Mn crusts and nodules fractionate Ga and Al during scavenging from seawater, resulting in decreased Ga/Al ratios compared to the ambient seawater (Fig. 2.2). Thereby, the Fe-Mn crusts from the Atlantic and Pacific preserved the slight difference in Ga/Al ratios of their respective ocean basins. Possible causes for the Ga-Al fractionation upon scavenging could be the higher particle reactivity of Al but also preferred solution complexation of Ga by organic ligands and, therefore, preferential retention of Ga in solution relative to Al.

2.5 Germanium and silicon

Germanium (Ge) and Silicon (Si) are metalloids of the same group (14) in the periodic table. In an early version of the periodic table, Mendeleev called Ge "ekasilicon" due to its presumed chemical similarities to silicon. Indeed, Ge and Si have similar properties in the natural environment: (i) they have similar atomic radii of 2.34 Å (Ge) and 2.32 Å (Si; Rahm et al., 2016) and, therefore, also rather similar tetrahedral bond lengths of 1.75 Å (Ge-O) and 1.64 Å (Si-O; Martin et al., 1996). (ii) Furthermore, both are tetravalent under natural conditions. Therefore, Ge and Si show coherent behaviour in magmatic and clastic sedimentary processes expressed by rather uniform Ge/Si ratios of various plutonic, volcanic and clastic sedimentary rocks (oceanic crust Ge/Si: 6.5×10^{-6} , continental crust Ge/Si: 4.7×10^{-6} , marine deep-sea-clay Ge/Si: $5.4 \times 10^{-6} - 8.1 \times 10^{-6}$; Rouxel et al., 2006). The upper continental crust (UCC) average concentrations are 1.4 mg/kg Ge and 31,1425 mg/kg Si (66.62 % SiO₂; Rudnick and Gao, 2003), yielding a Ge/Si ratio of $\sim 4.50 \times 10^{-6}$. A data compilation of Ge/Si ratios in igneous (EarthChem database; www.earthchem.org/petdb; Feb. 1st, 2023) and sedimentary rocks (SGP database; Farrell et al., 2021; <https://sgp-search.io/>; Feb. 1st, 2023) shows that Ge/Si ratios in major rocks cover a narrow range with median Ge/Si ratios of 6.6×10^{-6} (Fig. 2.15) and 7.1×10^{-6} (Fig. 2.16), respectively. Due to their chemical similarities and their coupled geochemical behaviour, Ge and Si are also considered geochemical partners.

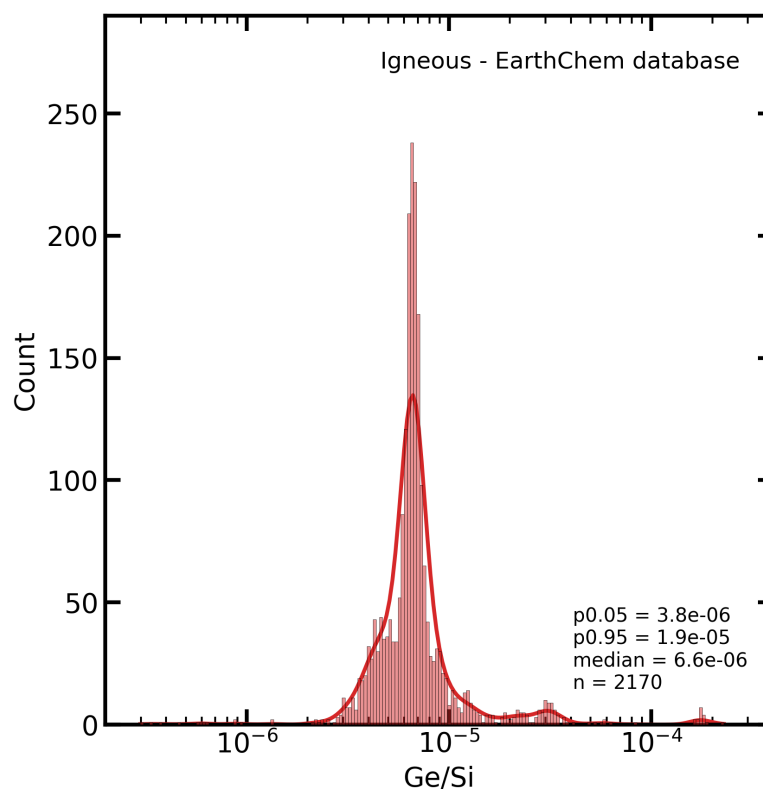


Figure 2.15: Histogram of Ge/Si ratios in *igneous* rocks from the EarthChem database for all entries that contain Ge and Si data. The solid line indicates the probability density. The dataset was compiled on Feb. 1st, 2023 from the EarthChem database webpage: www.earthchem.org/petdb. Ge/Si ratios predominantly (90 %) range between 3.8×10^{-6} (5 % per centile) and 1.9×10^{-5} (95 % per centile) with a median of 6.6×10^{-6} .

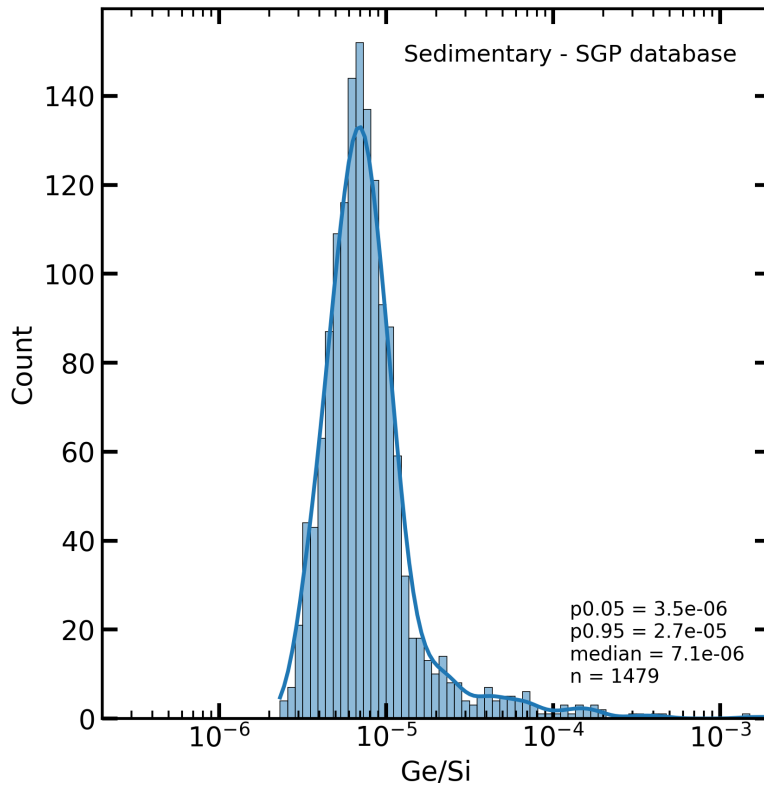


Figure 2.16: Histogram of Ge/Si ratios in *sedimentary* rocks from the SGP database (Farrell et al., 2021) for all entries that contain Ge and Si data. The solid line indicates the probability density. The dataset was compiled on Feb. 1st, 2023 from the SGP database webpage: <https://sgp-search.io/>. Ga/Al ratios predominantly (90 %) range between 3.5×10^{-6} (5 % per centile) and 2.7×10^{-5} (95 % per centile) with a median of 7.1×10^{-6} .

2.5.1 Germanium and silicon during weathering

Despite their geochemical-partner character, Ge and Si behave differently in aqueous environments, i.e., they fractionate. Their fractionation begins during weathering process of rocks at the Earth's surface and shallow subsurface. Sunlight, temperature variations, wind and especially rainwater, soil solutions, groundwater and river water alter solid rocks and remove the more mobile constituents. The more immobile components remain in secondary minerals that form, during these processes, like, e.g., clays and aluminosilicates. Regarding Ge and Si, Froelich et al. (1992) proposed a schematic model in which an initial unweathered rock Ge/Si ratio of $\sim 1.5 \times 10^{-6}$ is altered during incongruent weathering leading to a Ge/Si ratio of $\sim 3.75 \times 10^{-6}$ in secondary clays and a Ge/Si ratio of $\sim 0.35 \times 10^{-6}$ in the solute. Incongruent weathering partially dissolves primary (aluminium-)silicates in the source rocks, leaving residual phases like kaolinite (e.g., Colman, 1981). Therefore, rivers that drain regions of incongruent weathering should exhibit lower Ge/Si ratios than the ambient source rocks. Incongruent weathering appears in areas where physical transport exceeds weathering rates, e.g., in mountain ranges with steep terrain (Murnane and Stallard, 1990; Froelich et al., 1992). Under congruent weathering conditions, the whole source rock is dissolved homogeneously, and even previously formed secondary clays dissolve. During congruent weathering, the Ge/Si ratio is not changed upon transfer from the solid into soil solutions and the draining river water. Congruent weathering occurs in areas where weathering rates exceed physical transport capacities, e.g., flat peneplains (Froelich et al., 1992). Seasonal variations and climatic changes can shift the weathering from incongruent to congruent and vice versa, changing the Ge/Si transported via the rivers into the ocean (Murnane and Stallard, 1990). Furthermore, the mineralogical composition of the weathered rock also influences the Ge/Si ratio in draining rivers. For example, biotite has elevated Ge/Si ratios. Anders et al. (2003) concluded that biotite-rich source rocks strongly influenced some of their samples that show elevated Ge/Si ratios. Nevertheless, Anders et al. (2003) could confirm in their periglacial samples that incongruent weathering results in lower river Ge/Si ratios than the Ge/Si ratio of the respective source rock. Kurtz et al. (2002) also showed that intensely weathered (≥ 20 ka) Hawaiian soils have elevated Ge/Si ratios (1.6×10^{-5} to 6.3×10^{-5}) compared to the basalt source rocks (6.5×10^{-6}) — relatively young soils (0.3 – 2.1 ka) did not show Ge-Si fractionation yet. Furthermore, Kurtz et al. (2002) conducted sequential leaching experiments on the Hawaiian soil samples and showed that the soil Ge is mainly associated with secondary silicates (e.g., allophane).

2.5.2 Germanium and silicon in seawater

The sources of Ge and Si to seawater are very similar to those of Ga and Al. Coastal waters receive Ge and Si mainly from riverine influx showing an average Ge/Si ratio of 1.6×10^{-6} (Mortlock and Froelich, 1987). The second major source is aeolian dust influx that shows Ge/Si ratios between 2.2×10^{-6} and 3.6×10^{-6} (Mortlock and Froelich, 1987). Within the water column, Ge and Si show a coupled behaviour with increasing concentrations from surface towards bottom waters, probably due to continuous dissolution from particles (Sutton et al., 2010; Guillermic et al., 2017). The oceanic Ge/Si ratio is approx. 1.7×10^{-6} (Mortlock and Froelich, 1987) and, therefore, rather similar to the Ge/Si ratios of fluvial and aeolian influxes indicating only slight fractionation of Ge/Si in the marine environment.

2.6 Rare earth elements and yttrium

The rare earth elements (REE) comprise the series of lanthanides, lanthanum (La) to lutetium (Lu), in group IIIa of the periodic table. Their atomic number increases from 57 to 71, which is accompanied by a subsequent filling of the 4f orbital – La starts with an empty 4f orbital – leading to an increasing electromagnetic attraction between the ionic core and the orbital electrons and therefore decreasing ionic radii (Goldschmidt, 1925). In the natural environment, all REE, with two potential exceptions, occur in a trivalent state and therefore show coherent geochemical behaviours. Commonly yttrium (Y) is included (REY, rare earths and yttrium) between dysprosium (Dy) and holmium (Ho) due to its similar ionic radius compared to the latter. Rare earth element and yttrium data are usually visualised in normalised distribution plots. Normalisation to a reference material is necessary to compete for large concentration (or mass fraction) differences between REY with even and odd atomic numbers (Oddo-Harkins rule). Common normalisation materials comprise chondrite (REY_{CN} ; e.g., C1 chondrite after Barrat et al., 2012), representing primordial earth, and shales (REY_{SN} ; e.g., PAAS = Post Archaean Australian Shale after Taylor and McLennan, 1985; McLennan, 1989 or EUS = European Shale after Bau et al., 2018) representing the upper continental crust. Fractionation of neighbouring REY is usually rather small, but significant deviations can occur between the groups of light REY (LREY, La – Nd), middle REY (MREY, Sm – Dy) and heavy REY (HREY, Ho – La). Furthermore, Ce and Eu are redox-sensitive and can be oxidized to Ce(IV) and reduced to Eu(II), respectively. Due to very different ionic radii in these non-trivalent oxidation states, the geochemical behaviour of Ce(IV)

and Eu(II) can differ severely from the remaining REY(III), resulting in decoupling and formation of anomalies in normalised plots.

The REY distribution of a geoscientific sample can contain valuable information about the prevailing physico-chemical conditions. A more detailed description of REY behaviour in modern seawater and general REY characteristics of BIF are given in Chapter 5. Furthermore, profound and comprehensive explanations about REY sources and their behaviour in various natural environments can be found in the dissertation theses of Tepe (2016), Viehmann (2016) and Merschel (2017).

2.7 References

- Alexander B. W., Bau M., Andersson P. and Dulski P. (2008) Continentally-derived solutes in shallow Archaean seawater: Rare earth element and Nd isotope evidence in iron formation from the 2.9Ga Pongola Supergroup, South Africa. *Geochimica et Cosmochimica Acta* 72, 378–394.
- Alibert C. and Kinsley L. (2016) Ge/Si in Hamersley BIF as tracer of hydrothermal Si and Ge inputs to the Paleoproterozoic ocean. *Geochimica et Cosmochimica Acta* 184, 329–343.
- Alibert C. and McCulloch M. T. (1993) Rare earth element and neodymium isotopic compositions of the banded iron-formations and associated shales from Hamersley, western Australia. *Geochimica et Cosmochimica Acta* 57, 187–204.
- Allwood A. C., Walter M. R., Kamber B. S., Marshall C. P. and Burch I. W. (2006) Stromatolite reef from the Early Archaean era of Australia. *Nature* 441, 714–718.
- Amedjoe C. G., Gawu S. K. Y., Ali B., Aseidu D. K. and Nude P. M. (2018) Geochemical compositions of Neoproterozoic to Lower Palaeozoic (?) shales and siltstones in the Volta Basin (Ghana): Constraints on provenance and tectonic setting. *Sedimentary Geology* 368, 114–131.
- Amiotte Suchet P., Probst J.-L. and Ludwig W. (2003) Worldwide distribution of continental rock lithology: Implications for the atmospheric/soil CO₂ uptake by continental weathering and alkalinity river transport to the oceans. *Global Biogeochem. Cycles* 17.
- Anbar A. D., Duan Y., Lyons T. W., Arnold G. L., Kendall B., Creaser R. A., Kaufman A. J., Gordon G. W., Scott C., Garvin J. and Buick R. (2007) A Whiff of Oxygen Before the Great Oxidation Event? *Science* 317, 1903–1906.
- Anders A. M., Sletten R. S., Derry L. A. and Hallet B. (2003) Germanium/silicon ratios in the Copper River Basin, Alaska: Weathering and partitioning in periglacial versus glacial environments. *Journal of Geophysical Research* 108.
- Anderson T. F. and Raiswell R. (2004) Sources and mechanisms for the enrichment of highly reactive iron in euxinic Black Sea sediments. *American Journal of Science* 304, 203–233.

- Ayres D. E. (1972) Genesis of Iron-bearing Minerals in Banded Iron Formation Mesobands in The Dales Gorge Member, Hamersley Group, Western Australia. *Economic Geology* 67, 1214–1233.
- Barley M., Bekker A. and Krapez B. (2005) Late Archaean to Early Paleoproterozoic global tectonics, environmental change and the rise of atmospheric oxygen. *Earth and Planetary Science Letters* 238, 156–171.
- Barrat J. A., Zanda B., Moynier F., Bollinger C., Liorzou C. and Bayon G. (2012) Geochemistry of CI chondrites: Major and trace elements, and Cu and Zn Isotopes. *Geochimica et Cosmochimica Acta*, 79–92.
- Bau M. (1996) Controls on the fractionation of isovalent trace elements in magmatic and aqueous systems: evidence from Y/Ho, Zr/Hf, and lanthanide tetrad effect. *Contributions to Mineralogy and Petrology* 123, 323–333.
- Bau M., Frei R., Garbe-Schönberg D. and Viehmann S. (2022) High-resolution Ge-Si-Fe, Cr isotope and Th-U data for the Neoproterozoic Temagami BIF, Canada, suggest primary origin of BIF bands and oxidative terrestrial weathering 2.7 Ga ago. *Earth and Planetary Science Letters* 589, 117579.
- Bau M., Höhndorf A., Dulski P. and Beukes N. J. (1997) Sources of Rare-Earth Elements and Iron in Paleoproterozoic Iron-Formations from the Transvaal Supergroup, South Africa: Evidence from Neodymium Isotopes. *The Journal of Geology* 105, 121–129.
- Bau M., Schmidt K., Pack A., Bendel V. and Kraemer D. (2018) The European Shale: An improved data set for normalisation of rare earth element and yttrium concentrations in environmental and biological samples from Europe. *Applied Geochemistry* 90, 142–149.
- Bekker A. and Holland H. D. (2012) Oxygen overshoot and recovery during the early Paleoproterozoic. *Earth and Planetary Science Letters* 317–318, 295–304.
- Bekker A., Holland H. D., Wang P.-L., Rumble D., Stein H. J., Hannah J. L., Coetzee L. L. and Beukes N. J. (2004) Dating the rise of atmospheric oxygen. *Nature* 427, 117–120.
- Bekker A., Karhu J. A., Eriksson K. A. and Kaufman A. J. (2003) Chemostratigraphy of Paleoproterozoic carbonate successions of the Wyoming Craton: tectonic forcing of biogeochemical change? *Precambrian Research* 120, 279–325.
- Bekker A., Karhu J. A. and Kaufman A. J. (2006) Carbon isotope record for the onset of the Lomagundi carbon isotope excursion in the Great Lakes area, North America. *Precambrian Research* 148, 145–180.
- Bekker A., Kaufman A. J., Karhu J. A., Beukes N. J., Swart Q. D., Coetzee L. L. and Eriksson K. A. (2001) Chemostratigraphy of the Paleoproterozoic Duitschland Formation, South Africa: implications for coupled climate change and carbon cycling. *American Journal of Science* 301, 261–285.
- Bekker A., Kaufman A., Karhu J. and Eriksson K. (2005) Evidence for Paleoproterozoic cap carbonates in North America. *Precambrian Research* 137, 167–206.
- Bekker A., Slack J. F., Planavsky N., Krapež B., Hofmann A., Konhauser K. O. and Rouxel O. J. (2010) Iron Formation: The Sedimentary Product of a Complex Interplay among Mantle, Tectonic, Oceanic, and Biospheric Processes. *Economic Geology* 105, 467–508.

2 Introduction

- van den Berg C. M. G., Boussemart M., Yokoi K., Prartono T. and Campos M. L. A. M. (1994) Speciation of aluminium, chromium and titanium in the NW Mediterranean. *Marine Chemistry* 45, 267–282.
- Beukes N. J. and Gutzmer J. (2008) Origin and Paleoenvironmental Significance of Major Iron Formations at the Archaean-Paleoproterozoic Boundary. In *Banded Iron Formation-Related High-Grade Iron Ore Society of Economic Geologists*.
- Beukes N. J. and Klein C. (1990) Geochemistry and sedimentology of a facies transition — from microbanded to granular iron-formation — in the early Proterozoic Transvaal Supergroup, South Africa. *Precambrian Research* 47, 99–139.
- Blake R. E., Chang S. J. and Lepland A. (2010) Phosphate oxygen isotopic evidence for a temperate and biologically active Archaean ocean. *Nature* 464, 1029–1032.
- Blokhin M. G., Zarubina N. V. and Mikhailyk P. E. (2014) Inductively coupled plasma mass spectrometric measurement of gallium in ferromanganese crusts from the Sea of Japan. *J Anal Chem* 69, 1237–1244.
- Bowring S. A. and Williams I. S. (1999) Priscoan (4.00–4.03 Ga) orthogneisses from northwestern Canada. *Contributions to Mineralogy and Petrology* 134, 3–16.
- Brasier M. D. and Lindsay J. F. (1998) A billion years of environmental stability and the emergence of eukaryotes: New data from northern Australia. *Geol* 26, 555.
- Braterman P. S. and Cairns-Smith A. G. (1987) Photoprecipitation and the banded iron-formations — Some quantitative aspects. *Origins Life Evol Biosphere* 17, 221–228.
- Braterman P. S., Cairns-Smith A. G. and Sloper R. W. (1983) Photo-oxidation of hydrated Fe²⁺—significance for banded iron formations. *Nature* 303, 163–164.
- Breiter K., Gardenová N., Kanický V. and Vaculovič T. (2013) Gallium and germanium geochemistry during magmatic fractionation and post-magmatic alteration in different types of granitoids: a case study from the Bohemian Massif (Czech Republic). *Geologica Carpathica* 64, 171–180b.
- Brocks J. J., Buick R., Summons R. E. and Logan G. A. (2003) A reconstruction of Archaean biological diversity based on molecular fossils from the 2.78 to 2.45 billion-year-old Mount Bruce Supergroup, Hamersley Basin, Western Australia. *Geochimica et Cosmochimica Acta* 67, 4321–4335.
- Brocks J. J., Love G. D., Summons R. E., Knoll A. H., Logan G. A. and Bowden S. A. (2005) Biomarker evidence for green and purple sulphur bacteria in a stratified Palaeoproterozoic sea. *Nature* 437, 866–870.
- Broecker W. S. and Peng T. H. (1982) *Tracers in the Sea*. New York., Eldigio Press.
- Buick I. S., Uken R., Gibson R. L. and Wallmach T. (1998) High- $\delta^{13}\text{C}$ Paleoproterozoic carbonates from the Transvaal Supergroup, South Africa. *Geol* 26, 875.
- Buick R. (2008) When did oxygenic photosynthesis evolve? *Phil. Trans. R. Soc. B* 363, 2731–2743.
- Buick R., Des Marais D. J. and Knoll A. H. (1995) Stable isotopic compositions of carbonates from the Mesoproterozoic Bangemall group, northwestern Australia. *Chemical Geology* 123, 153–171.
- Burton J. D., Culkin F. and Riley J. P. (1959) The abundances of gallium and germanium in terrestrial materials. *Geochimica et Cosmochimica Acta* 16, 151–180.

- Byrne R. H. (2010) Comparative carbonate and hydroxide complexation of cations in seawater. *Geochimica et Cosmochimica Acta* 74, 4312–4321.
- Byrne R. H. (2002) Inorganic speciation of dissolved elements in seawater: the influence of pH on concentration ratios. *Geochem Trans* 3, 11.
- Cairns-Smith A. G. (1978) Precambrian solution photochemistry, inverse segregation, and banded iron formations. *Nature* 276, 807–808.
- Cameron E. M. and Garrels R. M. (1980) Geochemical compositions of some Precambrian shales from the Canadian Shield. *Chemical Geology* 28, 181–197.
- Canfield D. E. (1998) A new model for Proterozoic ocean chemistry. *Nature* 396, 450–452.
- Canfield D. E. (2005) THE EARLY HISTORY OF ATMOSPHERIC OXYGEN: Homage to Robert M. Garrels. *Annu. Rev. Earth Planet. Sci.* 33, 1–36.
- Canfield D. E., Habicht K. S. and Thamdrup B. (2000) The Archaean Sulfur Cycle and the Early History of Atmospheric Oxygen. *Science* 288, 658–661.
- Canfield D. E., Poulton S. W. and Narbonne G. M. (2007) Late-Neoproterozoic Deep-Ocean Oxygenation and the Rise of Animal Life. *Science* 315, 92–95.
- Canfield D. E. and Raiswell R. (1999) The evolution of the sulfur cycle. *American Journal of Science* 299, 697–723.
- Catling D. C., Zahnle K. J. and McKay C. P. (2001) Biogenic Methane, Hydrogen Escape, and the Irreversible Oxidation of Early Earth. *Science* 293, 839–843.
- Charette M. A., Kipp L. E., Jensen L. T., Dabrowski J. S., Whitmore L. M., Fitzsimmons J. N., Williford T., Ulfsbo A., Jones E., Bundy R. M., Vivancos S. M., Pahnke K., John S. G., Xiang Y., Hatta M., Petrova M. V., Heimbürger-Boavida L., Bauch D., Newton R., Pasqualini A., Agather A. M., Amon R. M. W., Anderson R. F., Andersson P. S., Benner R., Bowman K. L., Edwards R. L., Gdaniec S., Gerringa L. J. A., González A. G., Granskog M., Haley B., Hammerschmidt C. R., Hansell D. A., Henderson P. B., Kadko D. C., Kaiser K., Laan P., Lam P. J., Lamborg C. H., Levier M., Li X., Margolin A. R., Measures C., Middag R., Millero F. J., Moore W. S., Paffrath R., Planquette H., Rabe B., Reader H., Rember R., Rijkenberg M. J. A., Roy-Barman M., Rutgers van der Loeff M., Saito M., Schauer U., Schlosser P., Sherrell R. M., Shiller A. M., Slagter H., Sonke J. E., Stedmon C., Woosley R. J., Valk O., Ooijen J. and Zhang R. (2020) The Transpolar Drift as a Source of Riverine and Shelf-Derived Trace Elements to the Central Arctic Ocean. *J. Geophys. Res. Oceans* 125.
- Chen J., An Z., Liu L., Ji J., Yang J. and Chen Y. (2001) Variations in chemical compositions of the eolian dust in Chinese Loess Plateau over the past 2.5 Ma and chemical weathering in the Asian inland. *Sci. China Ser. D-Earth Sci.* 44, 403–413.
- Clarke D. B., Cameron B. I., Muecke G. K. and Bates J. L. (1989) Early Tertiary basalts from the Labrador Sea floor and Davis Strait region. *Can. J. Earth Sci.* 26, 956–968.
- Cloud P. (1973) Paleocological Significance of the Banded Iron-Formation. *Economic Geology* 68, 1135–1143.
- Colman S. M. (1981) Rock-Weathering Rates as Functions of Time. *Quaternary Research* 15, 250–264.
- Czaja A. D., Johnson C. M., Roden E. E., Beard B. L., Voegelin A. R., Nägler T. F., Beukes N. J. and Wille M. (2012) Evidence for free oxygen in the Neoproterozoic. *Science* 335, 1606–1609.

- ocean based on coupled iron–molybdenum isotope fractionation. *Geochimica et Cosmochimica Acta* 86, 118–137.
- De Argollo R. M. and Schilling J.-G. (1978) Ge/Si and Ga/Al variations along the Reykjanes Ridge and Iceland. *Nature* 276, 24–28.
- Derry L. A. and Jacobsen S. B. (1990) The chemical evolution of Precambrian seawater: Evidence from REEs in banded iron formations. *Geochimica et Cosmochimica Acta* 54, 2965–2977.
- Derry L. A., Kaufman A. J. and Jacobsen S. B. (1992) Sedimentary cycling and environmental change in the Late Proterozoic: Evidence from stable and radiogenic isotopes. *Geochimica et Cosmochimica Acta* 56, 1317–1329.
- Dhuime B., Hawkesworth C. J., Cawood P. A. and Storey C. D. (2012) A Change in the Geodynamics of Continental Growth 3 Billion Years Ago. *Science* 335, 1334–1336.
- Ehrenreich A. and Widdel F. (1994) Anaerobic oxidation of ferrous iron by purple bacteria, a new type of phototrophic metabolism. *Appl Environ Microbiol* 60, 4517–4526.
- Ewers W. E. and Morris R. C. (1981) Studies of the Dales Gorge Member of the Brockman Iron Formation, Western Australia. *Economic Geology* 76, 1929–1953.
- Farquhar J., Bao H. and Thiemens M. (2000a) Atmospheric Influence of Earth’s Earliest Sulfur Cycle. *Science* 289, 756–758.
- Farquhar J., Peters M., Johnston D. T., Strauss H., Masterson A., Wiechert U. and Kaufman A. J. (2007) Isotopic evidence for Mesoarchaeon anoxia and changing atmospheric sulphur chemistry. *Nature* 449, 706–709.
- Farquhar J., Savarino J., Jackson T. L. and Thiemens M. H. (2000b) Evidence of atmospheric sulphur in the martian regolith from sulphur isotopes in meteorites. *Nature* 404, 50–52.
- Farquhar J., Zerkle A. L. and Bekker A. (2011) Geological constraints on the origin of oxygenic photosynthesis. *Photosynth Res* 107, 11–36.
- Farrell Ú. C., Samawi R., Anjanappa S., Klykov R., Adeboye O. O., Agic H., Ahm A. C., Boag T. H., Bowyer F., Brocks J. J., Brunoir T. N., Canfield D. E., Chen X., Cheng M., Clarkson M. O., Cole D. B., Cordie D. R., Crockford P. W., Cui H., Dahl T. W., Mouro L. D., Dewing K., Dornbos S. Q., Drabon N., Dumoulin J. A., Emmings J. F., Endriga C. R., Fraser T. A., Gaines R. R., Gaschnig R. M., Gibson T. M., Gilleaudeau G. J., Gill B. C., Goldberg K., Guilbaud R., Halverson G. P., Hammarlund E. U., Hantsoo K. G., Henderson M. A., Hodgskiss M. S. W., Horner T. J., Husson J. M., Johnson B., Kabanov P., Brenhin Keller C., Kimmig J., Kipp M. A., Knoll A. H., Kreitsmann T., Kunzmann M., Kurzweil F., LeRoy M. A., Li C., Lipp A. G., Loydell D. K., Lu X., Macdonald F. A., Magnall J. M., Mänd K., Mehra A., Melchin M. J., Miller A. J., Mills N. T., Mwinde C. N., O’Connell B., Och L. M., Ossa Ossa F., Pagès A., Paiste K., Partin C. A., Peters S. E., Petrov P., Playter T. L., Plaza-Torres S., Porter S. M., Poulton S. W., Pruss S. B., Richoz S., Ritzler S. R., Rooney A. D., Sahoo S. K., Schoepfer S. D., Sclafani J. A., Shen Y., Shorttle O., Slotznick S. P., Smith E. F., Spinks S., Stockey R. G., Strauss J. V., Stüeken E. E., Tecklenburg S., Thomson D., Tosca N. J., Uhlein G. J., Vizcaíno M. N., Wang H., White T., Wilby P. R., Woltz C. R., Wood R. A., Xiang L., Yurchenko I. A., Zhang T., Planavsky N. J., Lau K. V., Johnston D. T. and Sperling E. A. (2021) The

- Sedimentary Geochemistry and Paleoenvironments Project. *Geobiology* 19, 545–556.
- Fedo C. M., Eriksson K. A. and Krogstad E. J. (1996) Geochemistry of shales from the Archaean (3.0 Ga) Buhwa Greenstone Belt, Zimbabwe: Implications for provenance and source-area weathering. *Geochimica et Cosmochimica Acta* 60, 1751–1763.
- Fedo C. M. and Whitehouse M. J. (2002) Metasomatic Origin of Quartz-Pyroxene Rock, Akilia, Greenland, and Implications for Earth's Earliest Life. *Science* 296, 1448–1452.
- Fischer W. W. and Knoll A. H. (2009) An iron shuttle for deepwater silica in Late Archaean and early Paleoproterozoic iron formation. *Geological Society of America Bulletin*, 14.
- François L. M. and Gérard J.-C. (1986) Reducing power of ferrous iron in the Archaean Ocean, 1. Contribution of photosynthetic oxygen. *Paleoceanography* 1, 355–368.
- Frei R., Gaucher C., Poulton S. W. and Canfield Don. E. (2009) Fluctuations in Precambrian atmospheric oxygenation recorded by chromium isotopes. *Nature* 461, 250–254.
- Froelich P. N., Blanc V., Mortlock R. A., Chillrud S. N., Dunstan W., Udomkit A. and Peng T.-H. (1992) River Fluxes of Dissolved Silica to the Ocean Were Higher during Glacials: Ge/Si In Diatoms, Rivers, and Oceans. *Paleoceanography* 7, 739–767.
- Gaillardet J., Viers J. and Dupré B. (2013) Trace Elements in River Waters. In *Treatise on Geochemistry* Elsevier. pp. 195–235.
- Goldblatt C., Lenton T. M. and Watson A. J. (2006) Bistability of atmospheric oxygen and the Great Oxidation. *Nature* 443, 683–686.
- Goldschmidt V. M. (1925) Isomorphie und Polymorphie der Sesquioxide. Die Lanthaniden-Kontraktion und Ihre Konsequenzen. In *Geochemische Verteilungsgesetze der Elemente* Oslo.
- Gole M. J. and Klein C. (1981) Banded Iron-Formations through much of Precambrian time. *Journal of Geology* 89, 169–183.
- Goodman R. J. (1972) The distribution of Ga and Rb in coexisting groundmass and phenocryst phases of some basic volcanic rocks. *Geochimica et Cosmochimica Acta* 36, 303–317.
- Goodwin A. M. (1973) Archaean Iron-Formations and Tectonic basins of the Canadian Shield. *Economic Geology* 68, 915–933.
- Goodwin A. M. (1962) Structure, Stratigraphy, and Origin of Iron Formations, Michipicoten Area, Algoma District, Ontario, Canada. *Geological Society of America Bulletin* 73, 561–586.
- Gourcerol B., Thurston P. C., Kontak D. J., Côte-Mantha O. and Biczok J. (2016) Depositional setting of Algoma-type banded iron formation. *Precambrian Research* 281, 47–79.
- Gross G. A. (1980) A classification of iron formations based on depositional environments. *Canadian Mineralogist* 18, 215–222.
- Gross G. A. (1983) Tectonic Systems and the deposition of iron-formation. *Precambrian Research* 20, 171–187.
- Guillermic M., Lalonde S. V., Hendry K. R. and Rouxel O. J. (2017) The isotope composition of inorganic germanium in seawater and deep-sea sponges. *Geochimica et Cosmochimica Acta* 212, 99–118.

2 Introduction

- Guo Q., Strauss H., Kaufman A. J., Schröder S., Gutzmer J., Wing B., Baker M. A., Bekker A., Jin Q., Kim S.-T. and Farquhar J. (2009) Reconstructing Earth's surface oxidation across the Archaean-Proterozoic transition. *Geology* 37, 399–402.
- Habicht K. S., Gade M., Thamdrup B., Berg P. and Canfield D. E. (2002) Calibration of Sulfate Levels in the Archaean Ocean. *Science* 298, 2372–2374.
- Harder E. C. (1919) Iron-depositing bacteria and their geological relations. U.S. Geological Survey Professional Paper 113.
- Hartmann W. K., Ryder G., Dones L. and Grinspoon D. (2000) The Time-Dependent Intense Bombardment of the Primordial Earth/Moon System. In *Origin of the earth and moon* University of Arizona Press, Tucson. pp. 493–512.
- Haugaard R., Frei R., Stendal H. and Konhauser K. (2013) Petrology and geochemistry of the ~2.9 Ga Itilliarsuk banded iron formation and associated supracrustal rocks, West Greenland: Source characteristics and depositional environment. *Precambrian Research* 229, 150–176.
- Hazen R. M., Ewing R. C. and Sverjensky D. A. (2009) Evolution of uranium and thorium minerals. *American Mineralogist* 94, 1293–1311.
- Heimann A., Johnson C. M., Beard B. L., Valley J. W., Roden E. E., Spicuzza M. J. and Beukes N. J. (2010) Fe, C, and O isotope compositions of banded iron formation carbonates demonstrate a major role for dissimilatory iron reduction in 2.5Ga marine environments. *Earth and Planetary Science Letters* 294, 8–18.
- Hieronimus B., Kotschoubey B. and BouleÁgue J. (2001) Gallium behaviour in some contrasting lateritic profiles from Cameroon and Brazil. *Journal of Geochemical Exploration* 72, 147–163.
- Ho P., Resing J. A. and Shiller A. M. (2019) Processes controlling the distribution of dissolved Al and Ga along the U.S. GEOTRACES East Pacific Zonal Transect (GP16). *Deep Sea Research Part I: Oceanographic Research Papers* 147, 128–145.
- Hoashi M., Bevacqua D. C., Otake T., Watanabe Y., Hickman A. H., Utsunomiya S. and Ohmoto H. (2009) Primary haematite formation in an oxygenated sea 3.46 billion years ago. *Nature Geosci* 2, 301–306.
- Hofmann A., Bekker A., Rouxel O., Rumble D. and Master S. (2009) Multiple sulphur and iron isotope composition of detrital pyrite in Archaean sedimentary rocks: A new tool for provenance analysis. *Earth and Planetary Science Letters* 286, 436–445.
- Holland H. D. (1984) *The Chemical Evolution of the Atmosphere and Oceans.*, Princeton University Press, Princeton, NJ.
- Holland H. D. (2003) The Geologic History of Seawater. In *Treatise on Geochemistry* 6. Elsevier. pp. 583–625.
- Holland H. D. (1973) The Oceans; A Possible Source of Iron in Iron-Formations. *Economic Geology* 68, 1169–1172.
- Holland H. D. (2006) The oxygenation of the atmosphere and oceans. *Phil. Trans. R. Soc. B* 361, 903–915.
- Holland H. D. (2002) Volcanic gases, black smokers, and the great oxidation event. *Geochimica et Cosmochimica Acta* 66, 3811–3826.
- Hren M. T., Tice M. M. and Chamberlain C. P. (2009) Oxygen and hydrogen isotope evidence for a temperate climate 3.42 billion years ago. *Nature* 462, 205–208.

- Huston D. L. and Logan G. A. (2004) Barite, BIFs and bugs: evidence for the evolution of the Earth's early hydrosphere. *Earth and Planetary Science Letters* 220, 41–55.
- Hydes D. J. (1983) Distribution of aluminium in waters of the North East Atlantic 25°N to 35°N. *Geochimica et Cosmochimica Acta* 47, 967–973.
- Hydes D. J. and Liss P. S. (1977) The Behaviour of Dissolved Aluminium in Estuarine and Coastal Waters. *Estuarine and Coastal Marine Science* 5, 755–769.
- Isley A. E. (1995) Hydrothermal Plumes and the Delivery of Iron to Banded Iron Formation. *The Journal of Geology* 103, 169–185.
- Isley A. E. and Abbott D. H. (1999) Plume-related mafic volcanism and the deposition of banded iron formation. *J. Geophys. Res.* 104, 15461–15477.
- Jacobsen S. B. and Kaufman A. J. (1999) The Sr, C and O isotopic evolution of Neoproterozoic seawater. *Chemical Geology* 161, 37–57.
- Jacobsen S. B. and Pimentel-Klose M. R. (1988) Nd isotopic variations in Precambrian banded iron formations. *Geophys. Res. Lett.* 15, 393–396.
- James H. L. (1983) Chapter 12 Distribution of Banded Iron-Formation in Space and Time. In *Developments in Precambrian Geology* Elsevier. pp. 471–490.
- James H. L. (1954) Sedimentary Facies of Iron-Formation. *Economic Geology* 49, 235–293.
- Johnson C. M., Beard B. L. and Roden E. E. (2008) The Iron Isotope Fingerprints of Redox and Biogeochemical Cycling in Modern and Ancient Earth. *Annu. Rev. Earth Planet. Sci.* 36, 457–493.
- Johnston D. T. (2011) Multiple sulfur isotopes and the evolution of Earth's surface sulfur cycle. *Earth-Science Reviews* 106, 161–183.
- Kappler A., Pasquero C., Konhauser K. O. and Newman D. K. (2005) Deposition of banded iron formations by anoxygenic phototrophic Fe(II)-oxidizing bacteria. *Geol* 33, 865.
- Karhu J. A. and Holland H. D. (1996) Carbon isotopes and the rise of atmospheric oxygen. *Geol* 24, 867.
- Kasting J. F., Liu S. C. and Donahue T. M. (1979) Oxygen levels in the prebiological atmosphere. *J. Geophys. Res.* 84, 3097.
- Kato Y., Suzuki K., Nakamura K., Hickman A., Nedachi M., Kusakabe M., Bevacqua D. and Ohmoto H. (2009) Hematite formation by oxygenated groundwater more than 2.76 billion years ago. *Earth and Planetary Science Letters* 278, 40–49.
- Kaufman A. J., Corsetti F. A. and Varni M. A. (2007) The effect of rising atmospheric oxygen on carbon and sulfur isotope anomalies in the Neoproterozoic Johnnie Formation, Death Valley, USA. *Chemical Geology* 237, 47–63.
- Kendall B., Reinhard C. T., Lyons T. W., Kaufman A. J., Poulton S. W. and Anbar A. D. (2010) Pervasive oxygenation along late Archaean ocean margins. *Nature Geosci* 3, 647–652.
- Kerrick R. and Said N. (2011) Extreme positive Ce-anomalies in a 3.0Ga submarine volcanic sequence, Murchison Province: Oxygenated marine bottom waters. *Chemical Geology* 280, 232–241.
- Klein C. (2005) Some Precambrian banded iron-formations (BIFs) from around the world: Their age, geologic setting, mineralogy, metamorphism, geochemistry, and origins. *American Mineralogist* 90, 1473–1499.

2 Introduction

- Klein C. and Beukes N. J. (1989) Geochemistry and Sedimentology of a Facies Transition from Limestone to Iron-Formation Deposition in the Early Proterozoic Transvaal Supergroup, South Africa. *Economic Geology* 84, 1733–1774.
- Klein C. and Beukes N. J. (1993) Sedimentology and Geochemistry of the Glaciogenic Late Proterozoic Rapitan Iron-Formation in Canada. *Economic Geology* 88, 542–565.
- Knauth L. P. (2005) Temperature and salinity history of the Precambrian ocean: implications for the course of microbial evolution. *Palaeogeography, Palaeoclimatology, Palaeoecology* 219, 53–69.
- Knoll A. H., Hayes J. M., Kaufman A. J., Swett K. and Lambert I. B. (1986) Secular variation in carbon isotope ratios from Upper Proterozoic successions of Svalbard and East Greenland. *Nature* 321, 832–838.
- Konhauser K. O. (2009) Oceanic nickel depletion and a methanogen famine before the Great Oxidation Event. 458, 5.
- Konhauser K. O., Amskold L., Lalonde S. V., Posth N. R., Kappler A. and Anbar A. (2007) Decoupling photochemical Fe(II) oxidation from shallow-water BIF deposition. *Earth and Planetary Science Letters* 258, 87–100.
- Konhauser K. O., Hamade T., Raiswell R., Morris R. C., Grant Ferris F., Southam G. and Canfield D. E. (2002) Could bacteria have formed the Precambrian banded iron formations? *Geol* 30, 1079.
- Konhauser K. O., Lalonde S. V., Planavsky N. J., Pecoits E., Lyons T. W., Mojzsis S. J., Rouxel O. J., Barley M. E., Rosière C., Fralick P. W., Kump L. R. and Bekker A. (2011) Aerobic bacterial pyrite oxidation and acid rock drainage during the Great Oxidation Event. *Nature* 478, 369–373.
- Konhauser K. O., Planavsky N. J., Hardisty D. S., Robbins L. J., Warchola T. J., Haugaard R., Lalonde S. V., Partin C. A., Oonk P. B. H., Tsikos H., Lyons T. W., Bekker A. and Johnson C. M. (2017) Iron formations: A global record of Neoproterozoic to Palaeoproterozoic environmental history. *Earth-Science Reviews* 172, 140–177.
- Krapež B., Barley M. E. and Pickard A. L. (2003) Hydrothermal and resedimented origins of the precursor sediments to banded iron formation: sedimentological evidence from the Early Palaeoproterozoic Brockman Supersequence of Western Australia: Resedimented origins of banded iron formation. *Sedimentology* 50, 979–1011.
- Kremling K. (1985) The distribution of cadmium, copper, nickel, manganese, and aluminium in surface waters of the open Atlantic and European shelf area. *Deep Sea Research Part A. Oceanographic Research Papers* 32, 531–555.
- Kump L. R., Kasting J. F. and Barley M. E. (2001) Rise of atmospheric oxygen and the “upside-down” Archaean mantle: RESEARCH LETTER. *Geochem. Geophys. Geosyst.* 2.
- Kump L. R. and Seyfried W. E. (2005) Hydrothermal Fe fluxes during the Precambrian: Effect of low oceanic sulfate concentrations and low hydrostatic pressure on the composition of black smokers. *Earth and Planetary Science Letters* 235, 654–662.
- Kurtz A. C., Derry L. A. and Chadwick O. A. (2002) Germanium-silicon fractionation in the weathering environment. *Geochimica et Cosmochimica Acta* 66, 1525–1537.
- Le Roex A. P. (1985) Geochemistry, Mineralogy and Magmatic Evolution of the Basaltic and Trachytic Lavas from Gough Island, South Atlantic. *Journal of Petrology* 26,

- 149–186.
- Li W., Beard B. L. and Johnson C. M. (2015) Biologically recycled continental iron is a major component in banded iron formations. *Proc. Natl. Acad. Sci. U.S.A.* 112, 8193–8198.
- Li Y.-L., Konhauser K. O., Kappler A. and Hao X.-L. (2013) Experimental low-grade alteration of biogenic magnetite indicates microbial involvement in generation of banded iron formations. *Earth and Planetary Science Letters* 361, 229–237.
- Liang M., Guo Z., Kahmann A. J. and Oldfield F. (2009) Geochemical characteristics of the Miocene eolian deposits in China: Their provenance and climate implications. *Geochem. Geophys. Geosyst.* 10, 16.
- Løvik A. N., Restrepo E. and Müller D. B. (2015) The Global Anthropogenic Gallium System: Determinants of Demand, Supply and Efficiency Improvements. *Environ. Sci. Technol.* 49, 5704–5712.
- Lowenstein T. K., Kendall B. and Anbar A. D. (2014) The Geologic History of Seawater. In *Treatise on Geochemistry* Elsevier. pp. 569–622.
- Lyons T. W., Reinhard C. T. and Planavsky N. J. (2014) The rise of oxygen in Earth's early ocean and atmosphere. *Nature* 506, 307–315.
- Maher K. A. and Stevenson D. J. (1988) Impact frustration of the origin of life. *Nature* 331, 612–614.
- Maheshwari A., Sial A. N., Gaucher C., Bossi J., Bekker A., Ferreira V. P. and Romano A. W. (2010) Global nature of the Paleoproterozoic Lomagundi carbon isotope excursion: A review of occurrences in Brazil, India, and Uruguay. *Precambrian Research* 182, 274–299.
- Martin F., Ildefones P., Hazemann J.-L., Petit S., Grauby O. and Decarreau A. (1996) Random distribution of Ge and Si in synthetic talc and EXAFS and FTIR study. *European Journal of Mineralogy* 8, 289–299.
- McLennan S. M. (1989) Rare earth elements in sedimentary rocks: influence of provenance and sedimentary processes. In *Geochemistry and Mineralogy of Rare Earth Elements* De Gruyter, Berlin, Boston. pp. 169–200.
- McLennan S. M., Taylor S. R. and Kröner A. (1983) Geochemical evolution of Archaean shales from South Africa. I. The Swaziland and Pongola Supergroups. *Precambrian Research* 22, 93–124.
- Melezhik V. A. and Fallick A. E. (1996) A widespread positive $\delta^{13}\text{C}_{\text{carb}}$ anomaly at around 2.33–2.06 Ga on the Fennoscandian Shield: a paradox?. *Terra Research* 8, 141–157.
- Melezhik V. A., Fallick A. E., Rychanchik D. V. and Kuznetsov A. B. (2005) Palaeoproterozoic evaporites in Fennoscandia: implications for seawater sulphate, the rise of atmospheric oxygen and local amplification of the $\delta^{13}\text{C}$ excursion: Palaeoproterozoic evaporates in Fennoscandia. *Terra Nova* 17, 141–148.
- Merschel G. (2017) Trace Element and Isotope Geochemistry of Particle- Reactive Elements in River Waters of the Amazon River Basin. Jacobs University Bremen.
- Merschel G., Bau M. and Dantas E. L. (2017) Contrasting impact of organic and inorganic nanoparticles and colloids on the behavior of particle-reactive elements in tropical estuaries: An experimental study. *Geochimica et Cosmochimica Acta* 197, 1–13.

2 Introduction

- Middag R., de Baar H. J. W., Laan P. and Bakker K. (2009) Dissolved aluminium and the silicon cycle in the Arctic Ocean. *Marine Chemistry* 115, 176–195.
- Middag R., van Slooten C., de Baar H. J. W. and Laan P. (2011) Dissolved aluminium in the Southern Ocean. *Deep Sea Research Part II: Topical Studies in Oceanography* 58, 2647–2660.
- Mojzsis S. J., Arrhenius G., McKeegan K. D., Harrison T. M., Nutman A. P. and Friend C. R. L. (1996) Evidence for life on Earth before 3,800 million years ago. *Nature* 384, 55–59.
- Mojzsis S. J. and Harrison T. M. (2002) Origin and Significance of Archaean Quartzose Rocks at Akilia, Greenland. *Science* 298, 917–917.
- Morris A. W., Howland R. J. M. and Bale A. J. (1986) Dissolved aluminium in the Tamar Estuary, southwest England. *Geochimica et Cosmochimica Acta* 50, 189–197.
- Morris R. C. (1993) Genetic modelling for banded iron-formation of the Hamersley Group, Pilbara Craton, Western Australia. *Precambrian Research* 60, 243–286.
- Mortlock R. A. and Froelich P. N. (1987) Continental weathering of germanium: Ge Si in the global river discharge. *Geochimica et Cosmochimica Acta* 51, 2075–2082.
- Moyen J.-F. and van Hunen J. (2012) Short-term episodicity of Archaean plate tectonics. *Geology* 40, 451–454.
- Murnane R. J. and Stallard R. F. (1990) Germanium and silicon in rivers of the Orinoco drainage basin. *Nature* 344, 749–752.
- Næraa T., Scherstén A., Rosing M. T., Kemp A. I. S., Hoffmann J. E., Kokfelt T. F. and Whitehouse M. J. (2012) Hafnium isotope evidence for a transition in the dynamics of continental growth 3.2 Gyr ago. *Nature* 485, 627–630.
- Narbonne G. M. (2010) Ocean Chemistry and Early Animals. *Science* 328, 53–54.
- Neihof R. A. and Loeb G. I. (1972) The surface charge of particulate matter in seawater. *Limnol. Oceanogr.* 17, 7–16.
- Nutman A. P., McGregor V. R., Friend C. R. L., Bennett V. C. and Kinny P. D. (1996) The Itsaq Gneiss Complex of southern West Greenland; the world's most extensive record of early crustal evolution (3900–3600 Ma). *Precambrian Research* 78, 1–39.
- Och L. M. and Shields-Zhou G. A. (2012) The Neoproterozoic oxygenation event: Environmental perturbations and biogeochemical cycling. *Earth-Science Reviews* 110, 26–57.
- Ohmoto H. (1997) When did the Earth's atmosphere become oxic? *Geochem. News* 93, 26–27.
- Ohmoto H. and Felder R. P. (1987) Bacterial activity in the warmer, sulphate-bearing, Archaean oceans. *Nature* 328, 244–246.
- Orians K. J. and Bruland K. W. (1985) Dissolved aluminium in the central North Pacific. *Nature* 316, 427–429.
- Orians K. J. and Bruland K. W. (1988a) Dissolved gallium in the open ocean. *Nature* 332, 717–719.
- Orians K. J. and Bruland K. W. (1986) The biogeochemistry of aluminum in the Pacific Ocean. *Earth and Planetary Science Letters* 78, 397–410.
- Orians K. J. and Bruland K. W. (1988b) The marine geochemistry of dissolved gallium: A comparison with dissolved aluminum. *Geochimica et Cosmochimica Acta* 52,

- 2955–2962.
- Palin J. M. (2002) The Origin of a Most Contentious Rock. *Science* 298, 961–962.
- Papineau D. (2010) Global Biogeochemical Changes at Both Ends of the Proterozoic: Insights from Phosphorites. *Astrobiology* 10, 165–181.
- Parker C. E., Brown M. T. and Bruland K. W. (2016) Scandium in the open ocean: A comparison with other group 3 trivalent metals. *Geophys. Res. Lett.* 43, 2758–2764.
- Pavlov A. A. and Kasting F. (2002) Mass-Independent Fractionation of Sulfur Isotopes in Archaean Sediments: Strong Evidence for an Anoxic Archaean Atmosphere. *Astrobiology*, 27–41.
- Percak-Dennett E. M., Beard B. L., Xu H., Konishi H., Johnson C. M. and Roden E. E. (2011) Iron isotope fractionation during microbial dissimilatory iron oxide reduction in simulated Archaean seawater: Iron isotope fraction during Fe(III) oxide-silica reduction. *Geobiology* 9, 205–220.
- Persson P., Zivkovic K. and Sjöberg S. (2006) Quantitative Adsorption and Local Structures of Gallium(III) at the Water- α -FeOOH Interface. *Langmuir* 22, 2096–2104.
- Phillips G. N., Law J. D. M. and Myers R. E. (2001) Is the redox state of the Archaean atmosphere constrained? *SEG Discovery* 47, 1–18.
- Pokrovsky O. S. and Schott J. (2002) Iron colloids/organic matter associated transport of major and trace elements in small boreal rivers and their estuaries (NW Russia). *Chemical Geology* 190, 141–179.
- Posth N. R., Canfield D. E. and Kappler A. (2014) Biogenic Fe(III) minerals: From formation to diagenesis and preservation in the rock record. *Earth-Science Reviews* 135, 103–121.
- Poulton S. W., Fralick P. W. and Canfield D. E. (2004) The transition to a sulphidic ocean ~1.84 billion years ago. *Nature* 431, 173–177.
- Pufahl P. K. and Hiatt E. E. (2012) Oxygenation of the Earth’s atmosphere–ocean system: A review of physical and chemical sedimentologic responses. *Marine and Petroleum Geology* 32, 1–20.
- Rahm M., Hoffmann R. and Ashcroft N. W. (2016) Atomic and Ionic Radii of Elements 1–96. *Chem. Eur. J.* 22, 14625–14632.
- Rasmussen B. and Buick R. (1999) Redox state of the Archaean atmosphere: Evidence from detrital heavy minerals in ca. 3250–2750 Ma sandstones from the Pilbara Craton, Australia. *Geol* 27, 115–118.
- Rasmussen B., Meier D. B., Krapež B. and Muhling J. R. (2013) Iron silicate microgranules as precursor sediments to 2.5-billion-year-old banded iron formations. *Geology* 41, 435–438.
- Reinhard C. T., Raiswell R., Scott C., Anbar A. D. and Lyons T. W. (2009) A Late Archaean Sulfidic Sea Stimulated by Early Oxidative Weathering of the Continents. *Science* 326, 713–716.
- Reuschel M., Melezhik V. A., Whitehouse M. J., Lepland A., Fallick A. E. and Strauss H. (2012) Isotopic evidence for a sizeable seawater sulfate reservoir at 2.1Ga. *Precambrian Research* 192–195, 78–88.
- Richardson J. B., Mischenko I. C., Mackowiak T. J. and Perdrial N. (2022) Trace metals and metalloids and Ga/Al ratios in grey shale weathering profiles along a climate

- gradient and in batch reactors. *Geoderma* 405, 115431.
- Robert F. and Chaussidon M. (2006) A palaeotemperature curve for the Precambrian oceans based on silicon isotopes in cherts. *Nature* 443, 969–972.
- Rosing M. T. (1999) ^{13}C -Depleted Carbon Microparticles in >3700 -Ma Sea-Floor Sedimentary Rocks from West Greenland. *Science* 283, 674–676.
- Rosing M. T. and Frei R. (2004) U-rich Archaean sea-floor sediments from Greenland – indications of >3700 Ma oxygenic photosynthesis. *Earth and Planetary Science Letters* 217, 237–244.
- Rouxel O., Galy A. and Elderfield H. (2006) Germanium isotopic variations in igneous rocks and marine sediments. , 14.
- Rudnick R. L. and Gao S. (2003) 3.01 Composition of the Continental Crust. In *Treatise on Geochemistry* Elsevier. pp. 1–64.
- Saito M. A. (2009) Less nickel for more oxygen. *Nature* 458, 714–715.
- Sanematsu K., Moriyama T., Laochou S. and Watanabe Y. (2011) Laterization of basalts and sandstone associated with the enrichment of Al, Ga and Sc in the Bolaven Plateau, southern Laos. *Bull. Geol. Surv. Japan* 62, 105–129.
- Schidlowski M. (1988) A 3,800-million-year isotopic record of life from carbon in sedimentary rocks. *Nature* 333, 313–318.
- Schier K., Bau M., Smith A. J. B., Beukes N. J., Coetzee L. L. and Viehmann S. (2020) Chemical evolution of seawater in the Transvaal Ocean between 2426 Ma (Ongeluk Large Igneous Province) and 2413 Ma ago (Kalahari Manganese Field). *Gondwana Research* 88, 373–388.
- Schier K., Ernst D. M., de Sousa I. M. C., Garbe-Schönberg D., Kuhn T., Hein J. R. and Bau M. (2021) Gallium-aluminum systematics of marine hydrogenetic ferromanganese crusts: Inter-oceanic differences and fractionation during scavenging. *Geochimica et Cosmochimica Acta* 310, 187–204.
- Schmidt K., Garbe-Schönberg D., Hannington M. D., Anderson M. O., Bühring B., Haase K., Haruel C., Lupton J. and Koschinsky A. (2017) Boiling vapour-type fluids from the Nifonea vent field (New Hebrides Back-Arc, Vanuatu, SW Pacific): Geochemistry of an early-stage, post-eruptive hydrothermal system. *Geochimica et Cosmochimica Acta* 207, 185–209.
- Schröder S., Bekker A., Beukes N. J., Strauss H. and van Niekerk H. S. (2008) Rise in seawater sulphate concentration associated with the Paleoproterozoic positive carbon isotope excursion: evidence from sulphate evaporites in the ~ 2.2 – 2.1 Gyr shallow-marine Lucknow Formation, South Africa. *Terra Nova* 20, 108–117.
- Scott C., Lyons T. W., Bekker A., Shen Y., Poulton S. W., Chu X. and Anbar A. D. (2008) Tracing the stepwise oxygenation of the Proterozoic ocean. *Nature* 452, 456–459.
- Severmann S., Lyons T. W., Anbar A., McManus J. and Gordon G. (2008) Modern iron isotope perspective on the benthic iron shuttle and the redox evolution of ancient oceans. *Geol* 36, 487.
- Shannon R. D. (1976) Revised effective ionic radii and systematic studies of interatomic distances in halides and chalcogenides. *Acta crystallographica section A* 32, 751–76.

- Shields G. A. and Kasting J. F. (2007) Evidence for hot early oceans? *Nature* 447, E1–E1.
- Shiller A. M. (1998) Dissolved gallium in the Atlantic Ocean. *Marine Chemistry* 61, 87–99.
- Shiller A. M. (1988) Enrichment of dissolved gallium relative to aluminum in natural waters. *Geochimica et Cosmochimica Acta* 52, 1879–1882.
- Shiller A. M. and Bairamadgi G. R. (2006) Dissolved gallium in the northwest Pacific and the south and central Atlantic Oceans: Implications for aeolian Fe input and a reconsideration of profiles. *Geochem. Geophys. Geosyst.* 7, 14.
- Shiller A. M. and Frilot D. M. (1996) The geochemistry of gallium relative to aluminum in Californian streams. *Geochimica et Cosmochimica Acta* 60, 1323–1328.
- Simonson B. M. and Hassler S. W. (1996) Was the Deposition of Large Precambrian Iron Formations Linked to Major Marine Transgressions? *The Journal of Geology* 104, 665–676.
- Sleep N. H., Zahnle K. J., Kasting J. F. and Morowitz H. J. (1989) Annihilation of ecosystems by large asteroid impacts on the early Earth. *Nature* 342, 139–142.
- Smith R. M. and Martell A. E. (1976) Critical Stability Constants. In *Inorganic Complexes* Plenum Press, New York and London.
- Sun S., Konhauser K. O., Kappler A. and Li Y.-L. (2015) Primary hematite in Neoproterozoic to Paleoproterozoic oceans. *Geological Society of America Bulletin* 127, 850–861.
- Sutton J., Ellwood M. J., Maher W. A. and Croot P. L. (2010) Oceanic distribution of inorganic germanium relative to silicon: Germanium discrimination by diatoms. *Global Biogeochem. Cycles* 24, 13.
- Sverjensky D. A. and Lee N. (2010) The Great Oxidation Event and Mineral Diversification. *Elements* 6, 31–36.
- Tarney J., Saunders A. D. and Weaver S. D. (1977) Geochemistry of volcanic rocks from the island arcs and marginal basins of the Scotia Arc Region. In *Island Arcs, Deep Sea Trenches and Back-Arc basins* American Geophysical Union. pp. 367–377.
- Tarney J., Wood D. A., Varet J., Saunders A. D. and Cann J. R. (1979) Nature of mantle heterogeneity in the North Atlantic: Evidence from Leg 49 basalts. In *Maurice Ewing Series* (eds. M. Talwani, C. G. Harrison, and D. E. Hayes). American Geophysical Union, Washington, D. C. pp. 285–301.
- Taylor S. R. and McLennan S. M. (1985) *The continental crust: Its composition and evolution.*, Blackwell Scientific, Boston.
- Tepe N. (2016) Rare earth elements and Yttrium (REY) in natural waters and the potential impact of polar rivers on the REY distribution in seawater. Jacobs University Bremen.
- Tepe N. and Bau M. (2016) Behavior of rare earth elements and yttrium during simulation of arctic estuarine mixing between glacial-fed river waters and seawater and the impact of inorganic (nano-)particles. *Chemical Geology* 438, 134–145.
- Tice M. M. and Lowe D. R. (2004) Photosynthetic microbial mats in the 3,416-Myr-old ocean. *Nature* 431, 549–552.
- Trendall A. F. (2002) The Significance of Iron-Formation in the Precambrian Stratigraphic Record. In *Precambrian Sedimentary Environments* (eds. W. Altermann and P. L.

- Corcoran). Blackwell Publishing Ltd., Oxford, UK. pp. 33–66.
- Tsikos H. and Moore J. M. (1997) Petrography and geochemistry of the Paleoproterozoic Hotazel Iron-Formation, Kalahari manganese field, South Africa; implications for Precambrian manganese metallogenesis. *Economic Geology* 92, 87–97.
- Van Bennekom A. J. and Jager J. E. (1978) Dissolved aluminium in the Zaire river plume. *Netherlands Journal of Sea Research* 12, 358–367.
- Veizer J., Hoefs J., Lowe D. R. and Thurston P. C. (1989) Geochemistry of Precambrian carbonates: II. Archaean greenstone belts and Archaean sea water. *Geochimica et Cosmochimica Acta* 53, 859–871.
- Viehmann S., Bau M., Böhn B., Dantas E. L., Andrade F. R. D. and Walde D. H. G. (2016) Geochemical characterisation of Neoproterozoic marine habitats: Evidence from trace elements and Nd isotopes in the Urucum iron and manganese formations, Brazil. *Precambrian Research* 282, 74–96.
- Viehmann S., Bau M., Smith A. J. B., Beukes N. J., Dantas E. L. and Böhn B. (2015) The reliability of ~2.9 Ga old Witwatersrand banded iron formations (South Africa) as archives for Mesoarchean seawater: Evidence from REE and Nd isotope systematics. *Journal of African Earth Sciences* 111, 322–334.
- Vincent E. A. and Nightingale G. (1974) Gallium in rocks and minerals of the Skaergaard intrusion. *Chemical Geology* 14, 63–73.
- Voegelin A. R., Nägler T. F., Beukes N. J. and Lacassie J. P. (2010) Molybdenum isotopes in late Archaean carbonate rocks: Implications for early Earth oxygenation. *Precambrian Research* 182, 70–82.
- Wille M., Kramers J. D., Nägler T. F., Beukes N. J., Schröder S., Meisel Th., Lacassie J. P. and Voegelin A. R. (2007) Evidence for a gradual rise of oxygen between 2.6 and 2.5 Ga from Mo isotopes and Re-PGE signatures in shales. *Geochimica et Cosmochimica Acta* 71, 2417–2435.
- Young G. M., Long D. G. F., Fedo C. M. and Nesbitt H. W. (2001) Paleoproterozoic Huronian basin: product of a Wilson cycle punctuated by glaciations and a meteorite impact. *Sedimentary Geology* 141–142, 233–254.
- Yuan W., Gong Y., Chen J., Wang Z., Huang F., Yang X., Chetelat B., Teng H. and Schott J. (2022) Gallium isotope constraints on the intense weathering of basalt. *Geochimica et Cosmochimica Acta* 333, 22–38.
- Yuan W., Saldi G. D., Chen J., Vetuschi Zuccolini M., Birck J.-L., Liu Y. and Schott J. (2018) Gallium isotope fractionation during Ga adsorption on calcite and goethite. *Geochimica et Cosmochimica Acta* 223, 350–363.
- Zahnle K., Claire M. and Catling D. (2006) The loss of mass-independent fractionation in sulfur due to a Palaeoproterozoic collapse of atmospheric methane. *Geobiology* 4, 271–283.
- Zerle A. L., Claire M. W., Domagal-Goldman S. D., Farquhar J. and Poulton S. W. (2012) A bistable organic-rich atmosphere on the Neoproterozoic Earth. *Nature Geosci* 5, 359–363.
- Zhang Y., Liao S., Tao C., Wen H., Fan H., Wen J., Yang W. and Li W. (2021) Ga isotopic fractionation in sulfides from the Yuhuang and Duanqiao hydrothermal fields on the Southwest Indian Ridge. *Geoscience Frontiers* 12, 101137.

Zheng X.-Y., Beard B. L., Reddy T. R., Roden E. E. and Johnson C. M. (2016) Abiologic silicon isotope fractionation between aqueous Si and Fe(III)-Si gel in simulated Archaean seawater: Implications for Si isotope records in Precambrian sedimentary rocks. *Geochimica et Cosmochimica Acta* 187, 102–122.

3 Methods and Materials

3.1 Samples

3.1.1 Mt. Ruker BIF

The Mt. Ruker BIF was sampled in 1973/74 by J. Hoffmann (former professor at Bergakademie TU Freiberg) during the USSR expedition 19.SAE. Prof. Hoffmann generously gave some of the collected BIF samples (Fig. 3.1) to Prof. Michael Bau in the mid-1990s. Therefore, only very little about the sampling procedure is known. However, it can be said with certainty that the Mt. Ruker BIF was sampled from surface outcrops, probably with a common sledgehammer and geological hammer. At Jacobs University's Geochemistry lab, one hand specimen was micro drilled (3 mm diameter) to gain nine subsamples from the five individual Fe-oxide and metachert bands. However, sample ANT5.1 was a very heterogenous micro drillcore and, therefore, excluded from further investigations. The micro-drilled subsamples were crushed and milled by hand in an agate mortar. The mortar and pestle were thoroughly cleaned three times in between each sample with sand ("Sea Sand for analysis" by PanReac AppliChem 121160.1214), methanol and deionised (DI) water.

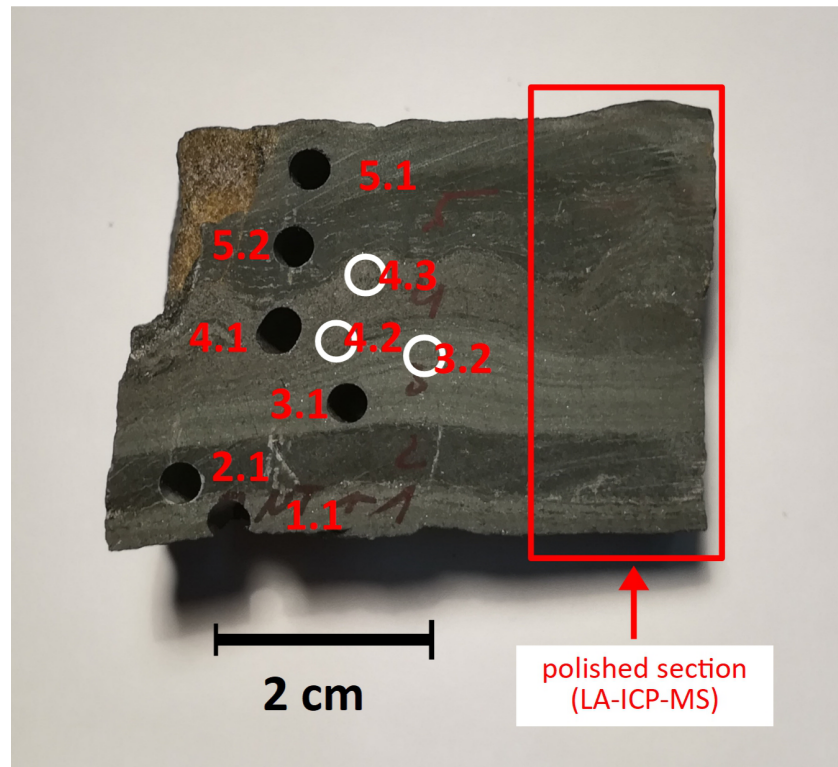


Figure 3.1: Mt. Ruker BIF sample with indications for the micro drillcores on the left side. The right side was used to prepare a polished section for laser-ablation ICP-MS (see Section 3.3).

3.1.2 Hydrogenetic Fe-Mn crusts

The investigated ferromanganese (Fe-Mn) crusts were collected in the Central Pacific during the SO66 research cruise with the German research vessel FS SONNE. During the SO66 cruise, the area between Kiribati, Wallis and Futuna ($0^{\circ} - 10^{\circ}$ S and 175° E – 157° W) was sampled. In 1996, Bau et al. (1996) published the first descriptions and analytical results for 23 of the collected Fe-Mn crust samples.

Due to a more recent study by Bau et al. (2014) on the same samples, already milled sample powders were available for the following digestion.

3.1.3 Temagami BIF

The Temagami BIF samples were collected close to the small town of Temagami (eastern Ontario, Canada) from a roadcut along Highway 11. Each specimen comprises alternating Fe-oxide and metachert bands of cm to dm width (Fig. 3.2). The Fe-oxide bands mainly consist of magnetite with minor haematite. The metachert bands are partly ferruginous. The samples investigated here were already used in previous publications by Bau and Alexander (2009), Viehmann et al. (2014) Schulz et al. (2021) Bau et al. (2022) and Mundl-Petermeier et al. (2022).

The specimens were subsampled by micro drillcores of individual, adjacent bands. Each subsample was crushed and milled afterwards, following the same manual hand milling procedure described above.

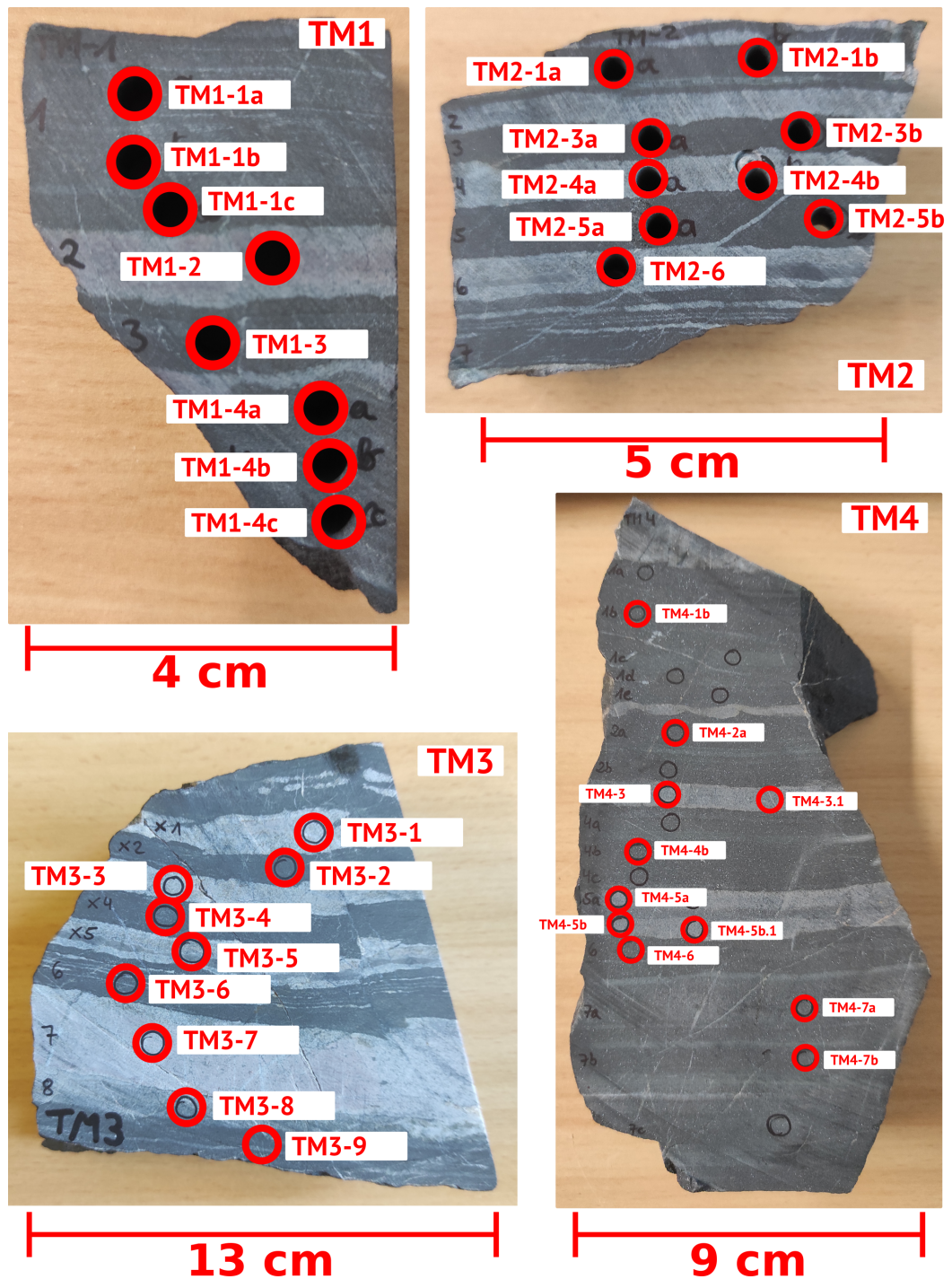


Figure 3.2: All four Temagami BIF hand specimens (*TM1*, *TM2*, *TM3* and *TM4*) with indications for the micro drillcores. Fe-oxide bands are dark coloured while metachert bands are light coloured. Polished sections and nano-particulate pressed powder tablets for LA-ICP-MS were prepared from *TM3* specimen.

3.1.4 Two-component mixing experiment

The two-component mixing experiment comprises the two mixing endmembers IF-G (BIF reference material from Isua, Greenland) and pure quartz sand (99.995 %; Sigma-Aldrich, CAS number 14808-60-7) as well as nine mixed samples with relative IF-G amounts from 10 % to 90 % and SiO₂ amounts from 90 % to 10 %, respectively. The samples' exact proportions were determined gravimetrically. Afterwards, each sample was homogenised and milled manually in an agate mortar. The agate mortar and pestle were cleaned thoroughly (see above) between every sample.

3.2 Wet chemistry

3.2.1 High-pressure acid digestion

High-pressure acid digestion is a standard method to dissolve solid rock material, which can be analysed by solution-based methods (e.g., ICP-OES or ICP-MS, see below) afterwards. The samples must be powdered first (see above) for a complete digestion result. Before digestion, the samples were dried in an oven overnight at 105°C. From each sample, 50 mg or 100 mg was weighed and put into an individual Teflon beaker. The exact weight was noted. The samples were then digested for 18 hours in a PicoTrace DAS Pressure Digestion System at 180°C using a 3-acid digestion protocol with suprapure conc. HCl (3 ml), HNO₃ (1 ml) and HF (1 ml). The next day, the acid mixture was evaporated at approximately 180°C on a hot plate. When reaching incipient dryness, the samples were refilled with 5 ml conc. HCl and evaporated again. This step was repeated a second time. Finally, after the last evaporation, the samples were filled with either 0.5 M HNO₃ or a mixture of 0.5 M HNO₃ and 0.5 % HCl and transferred into acid-cleaned polyethylene (PE) bottles. The dissolved samples were then precisely (determined gravimetrically and noted) filled up to 50 g with 0.5 M HNO₃ or the 0.5 M HNO₃ and 0.5 % HCl mixture. This yields a sample dilution of approx. 500 or 1000. In each digestion run, at least one reference material (RM) was included, and one beaker was left without sample material but was treated the same as a (method) blank. The digested samples were subsequently analysed with ICP-OES and ICP-MS (see below) for major, minor, and trace elements.

3.2.2 ICP-OES measurements

Inductively coupled plasma optical emission spectroscopy (ICP-OES; Spectro Ciros Vision) measurements were performed at Jacobs University Bremen to determine the major element composition in the digested samples. Raw data evaluation of the ICP-OES measurement was computed via linear regression of six multi-element calibration standards with precisely defined and increasing elemental concentrations. These six calibration standards were prepared freshly for each measurement from a regularly renewed stock solution. Depending on the sample matrix, either 0.5 M HNO₃ or 0.5 M HNO₃ and 0.5 % HCl mixture, the six calibration standards were prepared with the same acid(s) to avoid matrix-dependent effects during the measurement. The samples were measured along with a least one RM, method blanks from the digestion and acid blanks containing the 0.5 M HNO₃ (or 0.5 M HNO₃ and 0.5 % HCl mixture) used for sample dilution. The sample and RM dilutions were estimated to match the elemental concentrations of calibration standards three to four. In order to compensate for common machine-dependent fluctuations, e.g., sample intake or ionisation, an internal yttrium standard (10 ppm) was applied to each calibration standard, sample, RM and blank. Every calibration standard, sample, RM and blank was prepared gravimetrically, and the exact weights of internal standard, sample or stock and acid were noted for an exact raw data evaluation. The accuracy and precision were monitored by repetitive measurements of well-defined RMs while the method and acid blanks tracked potential sample contaminations or carry-over.

The respective precision, accuracy and limits of quantification can be found in the individual publications (Chapter 4, 5 and 6).

3.2.3 ICP-MS measurements

Inductively coupled plasma mass spectrometry (ICP-MS; PerkinElmer NexION 350x) measurements were performed at Jacobs University Bremen to determine minor and trace elements in the digested samples. Similar to ICP-OES analyses, the samples were measured along with RM(s), method and acid blanks to monitor accuracy, precision and potential contaminations. ICP-MS raw data evaluation was computed via calibration with a 2 ppm multi-element calibration standard. A second 4 ppm calibration standard was used for cross-checking. The calibration standards, samples, RM, acid and method blanks were gravimetrically prepared for each measurement. The stock solution for the 2 ppm and 4 ppm calibration standards was regularly renewed. Internal standardisation

was also applied, similar to ICP-OES, but with 2 ppm Ru, Re, Rh and Bi. Due to mass-dependent interferences caused by the formation of oxides during ionisation, an oxide correction of the raw data is necessary. Therefore, the ICP-MS was tuned before each measurement for a fixed oxide formation rate ($\text{CeO/Ce} = 2.5\%$). Similarly, the formation rate of doubly charged ions was minimised (Ce^{++}/Ce).

The respective precision, accuracy and limits of quantification can be found in the individual publications (Chapters 4, 5 and 6).

3.2.4 SF-ICP-MS and ICP-MS/MS measurements

Due to several potential polyatomic and doubly-charged interferences on both naturally occurring Ga isotopes (^{69}Ga and ^{71}Ga), Ga and Al in the digested samples were determined with sector-field (SF)-ICP-MS at the University of Kiel and ICP-MS/MS (tandem ICP-MS) at the Federal Institute for Geosciences and Natural Resources (BGR) in Hannover. Gallium is only present in trace amounts (a few ppm) in all investigated samples and, therefore, very susceptible to mass interferences. For ^{69}Ga , potential and sample-relevant interferences could originate from polyatomic $^{29}\text{Si}^{40}\text{Ar}^+$, $^{53}\text{Cr}^{16}\text{O}^+$, $^{67}\text{ZnH}^+$ or $^{57}\text{Fe}^{12}\text{C}^+$ and the doubly-charged $^{138}\text{Ba}^{++}$. Potential interferences on the ^{71}Ga isotope are $^{55}\text{Mn}^{16}\text{O}^+$, $^{70}\text{GeH}^+$, $^{31}\text{P}^{40}\text{Ar}^+$, $^{56}\text{Fe}^{16}\text{OH}^+$ and doubly-charged $^{142}\text{Ce}^{++}$ and $^{142}\text{Nd}^{++}$. For the respective relevance of each interference, see the methods sections in Chapter 6.

The SF-ICP-MS measurements were conducted with a ThermoFisher Element XR in high-resolution mode with a resolving power of 10,000. This resolving power is high enough to determine the pure Ga peak precisely. However, an increase in the resolving power is always accompanied by a loss of signal intensities that must be considered for the sample dilutions. For further information on calibration procedures, see Garbe-Schönberg (1993).

The ICP-MS/MS (ThermoFisher iCAP TQ) utilises an additional quadrupole mass filter that is built-in along the ion beam before the collision/reaction cell. Both the additional quadrupole mass filter and the reaction cell significantly remove polyatomic and doubly charged interferences. Hydrogen (H_2) was used as cell gas in the reaction cell.

Aluminium was always measured along with Ga to ensure an optimal determination of Ga/Al ratios. A combination of multiple analytical methods would cause additional uncertainties.

3.3 Laser-ablation ICP-MS

Mainly for the determination of Ge/Si but also for Ga/Al ratios in Fe-Mn crusts, BIFs, and the solid mixing series, laser-ablation (LA)-ICP-MS measurements were conducted. Germanium and silicon form volatile complexes with fluoride and are almost quantitatively lost in acid digestion during evaporation (Chapman et al., 1949). Laser-ablation ICP-MS, however, combines the advantages of an in situ method with the superior analytical capabilities of, in this case, the SF-ICP-MS (ThermoFisher Element XR). The SF-ICP-MS was also run in high-resolution mode for the laser-ablation measurements. In the following, laser-ablation measurements with the SF-ICP-MS will be abbreviated only as "LA-ICP-MS". The procedure of sample preparation, measurement and data processing are described below.

3.3.1 LA-ICP-MS sample preparation

LA-ICP-MS measurements were conducted on two types of samples: (i) polished sections of banded iron formation samples and (ii) nano-particulate pressed powder tablets (NP tablets) of Fe-Mn crusts, individual Temagami BIF Fe-oxide and metachert bands and the solid mixing series.

The samples for the polished sections were cut with a rock saw and embedded in epoxy resin. After the resin was hardened, the cut side was manually polished on a glass plate with silicon carbide polishing powder in three steps of decreasing grain sizes.

The NP tablets were prepared from 3 to 5 g sample powder, following Garbe-Schönberg and Müller (2014). The sample powders were again dry-milled and thoroughly homogenised, reaching a typical grain size of $d_{50} < 1.5 \mu\text{m}$. Due to this fine grain size and homogenisation, the sample powders can be pressed into tablets without adding any binding substances. Reference materials were also prepared in the same way so that different ablation behaviours (matrix effects) between the samples and RMs are minimised.

3.3.2 LA-ICP-MS measurements

The LA-ICP-MS setup at the University of Kiel consists of a Zurich-type-large-volume ablation cell and a GeoLasProPlusHD (193 nm ArF Excimer laser; Coherent) laser ablation system that was connected to the same SF-ICP-MS (ThermoFisher Element XR) that was also used for solution SF-ICP-MS measurements (see above). The samples,

polished sections or NP tablets, were mounted together with RMs into the Zurich-type-large-volume ablation cell. This cell was constantly flushed with He (ca. 1000 ml/min) as carrier gas and H₂ (ca. 14 ml/min) to increase sensitivity and suppress the formation of oxides. Measurement spots or transects for line scans were selected manually on each sample and RM. For spot measurements, the laser was set to a spot diameter of 160 µm, a fluence of 6 J/cm² and 400 pulses at 10 Hz. Line scans were only conducted for the polished BIF sections along 1,000 µm transects (300 µm on NP RMs). The fluence and laser frequency of line scans were similar to spot measurements (6 J/cm²; 10 Hz), but the laser spot size was set to 120 µm after a faster (100 Hz) pre-ablation of the transect with 160 µm. The laser movement speed along the transects was set to 10 µm/s resulting in a sample measurement time of 100 seconds (30 s for RMs). Before each ablation, a 20 s to 30 s machine background signal was collected. Each ablation was followed by a 20 s to 30 s wash-out before moving the ablation cell to the next measurement spot or transect.

3.3.3 Raw data processing and elemental ratio evaluation

The LA-ICP-MS yields raw counts/seconds (cps) data for short (approx. 4 s) individual time segments. The sequence of these individual time segments results in the total signal for background, sample and wash-out. These time series of each measurement were then processed with LADR (Laser Ablation Data Reduction – Norris Scientific). In the case of the Fe-Mn crust samples, the entire data processing was done with LADR. For the Temagami BIF samples, only the pre-processing was computed with LADR: (i) selection of time intervals for background and sampling signal, and (ii) background signal subtraction. For LA-ICP-MS measurements, only elemental ratios, e.g., Ga/Al or Ge/Si, were evaluated because the used LA-ICP-MS method lacked an internal standard. Therefore, quantifying absolute mass fractions within a reasonable confidence level was impossible. However, if only elemental ratios are determined, this limitation is reduced.

3.3.4 Fe-Mn crusts

The LA-ICP-MS data processing for the Fe-Mn crust samples was computed with the "Quantified Ratios" program of LADR (Laser Ablation Data Reduction), software version 1.1.02. A single RM calibration with the NOD-P1 (Pacific Fe-Mn nodule) RM was applied to quantify Ge/Si ratios. The two ⁷²Ge/²⁸Si and ⁷⁴Ge/²⁸Si ratios were measured and evaluated. The used reference values for NOD-P1 Ge and Si concentrations are 1.09 mg/kg and 64,978 mg/kg, respectively (Smith, 1995; Scribner et al., 2006). Due to

the general similarities between Fe-Mn crusts and nodules and since the NOD-P1 was also prepared as an NP tablet, the matrices of the RM and samples should be almost identical. Therefore, (unidentified) matrix effects are expected to be negligible. Further NP tablet RMs (NOD-A1 and JMn-1) were included for cross-checking and monitoring the analytical accuracy and drift.

The time intervals for the background and sample signals were hand-picked to receive stable signals at high intensities. Major signal fluctuations can occur, albeit very rarely for NP tablet samples, due to irregular ablation of sample material. Time intervals with such outliers should be avoided in the data evaluation as those can affect the result negatively. After selecting the background and sample signals, LADR automatically performs an individual background subtraction for each sample. The background-subtracted signals of $^{72}\text{Ge}/^{28}\text{Si}$ and $^{74}\text{Ge}/^{28}\text{Si}$ were then converted into elemental Ge/Si ratios using the single point calibration of NOD-P1 and application of a natural abundance correction after Anders and Grevesse (1989). An interference correction was not applied because the measurements were performed in high-resolution mode (resolving power of 10,000). Detailed instructions for the usage of LADR can be found in the "LADR Software Manual", which can be downloaded as part of the software package from the official LADR webpage (www.norsci.com/ladr/). A paid licence is not necessary for downloading the software and manual.

3.3.5 Temagami BIF

Only raw data pre-processing was done using LADR (version 1.1.02) for the Temagami BIF NP tablet samples. The two $^{69}\text{Ga}/^{27}\text{Al}$ and $^{71}\text{Ga}/^{27}\text{Al}$ ratios were evaluated. Time intervals of background and sample signals were selected with the graphical user interface of LADR, and background correction (see above) was applied for each sample. Afterwards, the pre-processed data was exported as a CSV file for further manual data evaluation.

Linear calibrations for $^{69}\text{Ga}/^{27}\text{Al}$ and $^{71}\text{Ga}/^{27}\text{Al}$ were computed using the two BIF RMs IF-G (Isua iron formation, Greenland) and FeR-4 (Temagami iron formation, Ontario, Canada): Measured LA-ICP-MS Ga/Al intensity ratios [cps/cps] were matched with reference Ga/Al ratios (7.9×10^{-4} and 2.7×10^{-4}) determined by solution SF-ICP-MS measurements of digested aliquots (see above). For both Ga/Al ratios ($^{69}\text{Ga}/^{27}\text{Al}$ and $^{71}\text{Ga}/^{27}\text{Al}$), an individual calibration was performed so that natural abundance corrections for Ga were not necessary. The IF-G and FeR-4 RMs were chosen for calibration because they match the samples' matrices, as both are BIF RMs and were also prepared as NP tablets. Furthermore, they cover a sample-relevant Ga/Al ratio range, unlike, for

example, the commonly used NIST SRM glasses. In addition to the IF-G and FeR-4, the BIF RM FeR-3 (Temagami iron formation, Ontario, Canada) and the two Fe-Mn nodule RMs NOD-P1 (Pacific) and NOD-A1 (Atlantic) were also analysed for monitoring the measurement accuracy, precision and drift. It should be noted, however, that the matrices and compositions of the NOD-P1 and NOD-A1 RMs differ from the Temagami BIF samples studied, as the Mn concentrations in the former are much higher. Finally, each sample's elemental Ga/Al ratios were computed using the respective calibration equation. For further details on the calibration equation and results of the other RMs, see Chapter 6.3.5.

3.3.6 Additional BIFs

The LA-ICP-MS measurements of the BIF polished sections (Isua, Marra Mamba, GHEX-97, Mt. Ruker, Dales Gorge and Kuruman) were evaluated in the same way as the Temagami BIF described above. The respective calibration equations can be found in Fig. 10.1 to Fig. 10.4.

3.3.7 Challenges of LA-ICP-MS

One part of this PhD research project was to develop and apply a LA-ICP-MS protocol for in situ Ga/Al (and Ge/Si) ratio determination in individual BIF bands. Therefore, a brief summary of the evolution and principles of LA-ICP-MS analysis is given below. For more detailed information, the reader is referred to the increasing amount of review studies on LA-ICP-MS in various scientific fields (e.g., Günther and Hattendorf, 2005; Liu et al., 2008; Shaheen et al., 2012; Luo et al., 2015; Limbeck et al., 2015; Chew et al., 2021).

Although today (2023), the general concept of laser-ablation ICP-MS is already more than 40 years old (Thompson et al., 1981; Carr and Horlick, 1982; Gray, 1985) and its predecessor, the "Laser Microspectrochemical Analysis" (e.g., Moenke and Moenke-Blankenburg, 1973), is even older, it was only in the more recent years that LA-ICP-MS got more established (e.g., Durrant and Ward, 2005; Pozebon et al., 2014 and references therein). Figure 3.3 shows the increasing number of published articles per year that deal with LA-ICP-MS (source Scopus). This development is probably driven by the fast technological evolution of analytical equipment (laser systems and ICP-MS) in the last decades and decreasing acquisition costs. 2021 and 2022 were the first years in which fewer articles on LA-ICP-MS were published than in the previous year. This could be

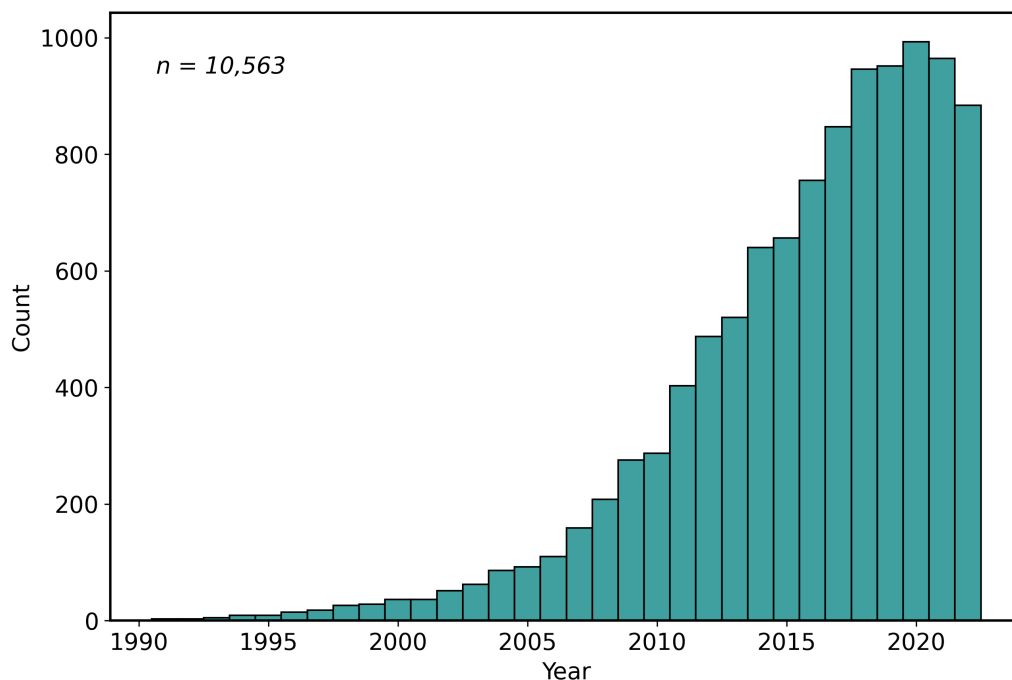


Figure 3.3: Number of published articles per year dealing with LA-ICP-MS. The dataset was compiled from the Scopus webpage on Dec. 27th, 2022 by searching for "LA-ICP-MS". The two main associated subject areas are Earth and Planetary Sciences ($n=8,036$) and Chemistry ($n=1,303$).

attributed to the exceptionally high number of publications during the pandemic years 2020 and 2021 and to the fact that not all publications of 2022 were yet covered in the data set as it was compiled at the end of December 2022.

Although there are nowadays various combinations of different laser-ablation systems with different ICP-MS machines, the general setup of LA-ICP-MS is the same (Fig. 3.4). The major parts are the laser, the ablation cell and the ICP-MS. The solid samples and RMs, e.g., polished sections or pressed powder tablets, are mounted in the ablation cell. The ablation cell is pressure sealed and only has a tube in and outlet attached to the carrier gas supply and the ICP-MS, respectively. The laser beam passes through a small glass window at the top of the ablation cell. These windows are made of special glasses and are adapted to the characteristics of the used laser, mainly wavelength. The ablation cell is constantly flushed with a high-purity carrier gas, typically Ar or He, to transport the ablated material to the ICP-MS and create a small overpressure within the ablation cell. The ablation cell itself is mounted on a movable (X-Y-Z direction) stage. Multiple laser types are used, but they can be grouped into two main categories: (i) nanosecond

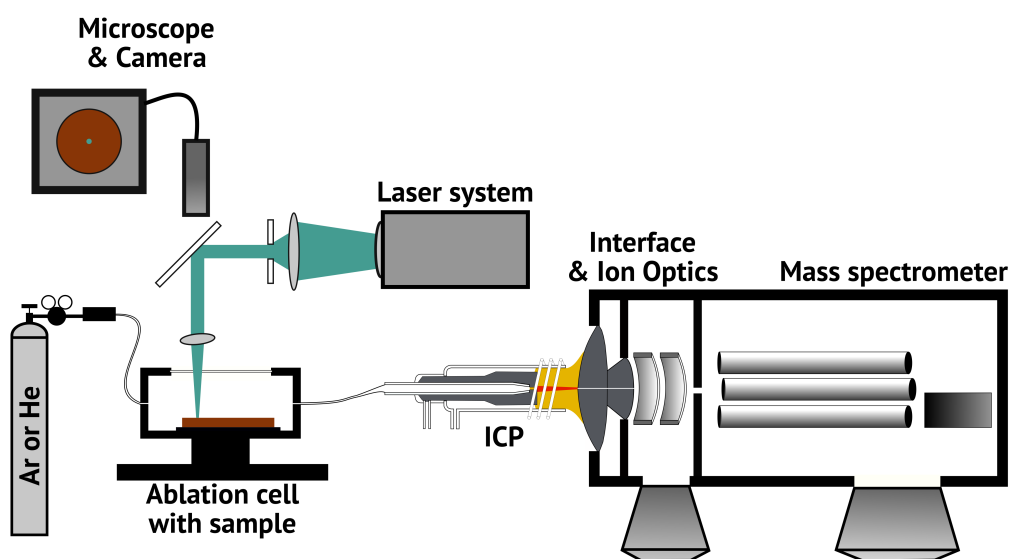


Figure 3.4: General LA-ICP-MS setup, see text for description. Redrawn after Günther and Hattendorf (2005).

(ns) and (ii) femtosecond (fs) lasers. These designations refer to the respective pulse durations, while fs-lasers are much younger and offer certain advantages with respect to ablation behaviour and elemental fractionation (e.g., Günther and Hattendorf, 2005; Shaheen et al., 2012; Limbeck et al., 2015). Nanosecond lasers are still more common and are further grouped into infrared (IR) and ultraviolet (UV) based on the respective wavelength (e.g., Günther and Hattendorf, 2005 and references therein). The generated laser pulses are guided and focused through a number of lenses, mirrors and the inlet window onto the sample surface. A microscope, typically combined with a camera, is attached on top of the ablation cell and in line with the laser beam for observation and measurement point selection. The ablated sample material is flushed into the ICP-MS by the carrier gas, where the particles are atomised and ionised in the plasma and subsequently measured. Most commonly, single-quadrupole ICP-MS is used in LA-ICP-MS setups, but more evolved systems like sector-field (SF-)ICP-MS, ICP-MS/MS or time-of-flight (TOF) ICP-MS can also be attached to the LA system.

Laser ablation ICP-MS, in many cases, offers a time and cost-saving alternative to more conventional solution-based ICP-MS analyses. However, signal calibration is probably the greatest challenge and potential limitation for LA-ICP-MS measurements. The ablation behaviour of different samples strongly depends on the sample matrix and the

3 Methods and Materials

interaction of the laser and sample. Therefore, the amount of ablated material can vary severely for different sample matrices and shift the measured intensities regardless of the sample's actual composition. Two approaches are commonly used to solve this problem (Miliszkiewicz et al., 2015 and references therein): (i) normalisation to 100 % composition and (ii) application of an internal standard – multiple internal standards can be used at once but for ease of reading the singular form is used here. The first approach requires the analysis of all major components. The measured signal intensities of all analytes are then summed up and considered the total (100 %) sample composition. The relative amount of each analyte is then computed based on its individual signal intensity relative to the total signal intensity. However, this method is strongly controlled by major element composition, and slight differences in total signal intensities can cause large effects on the results of minor and trace components.

The second approach, internal standardisation, does not necessarily require the analysis of all major components. However, at least one analyte's absolute concentration has to be known. This can be determined by a different analytical method. Alternatively, quite frequently, the internal standard is calculated based on the sample's stoichiometry. While this approach can yield good results for analysing single minerals or synthetic substances, it is unsuitable for more heterogeneous natural samples like, e.g., bulk rock analyses. In any case, however, a homogeneous distribution of the internal standard within the sample is an important prerequisite.

A review of LA-ICP-MS techniques applied in this PhD project with respect to the investigated sample types and target elements is given at the end of this thesis in Chapter 8.

3.4 References

- Anders E. and Grevesse N. (1989) Abundances of the elements: Meteoric and solar. *Geochimica et Cosmochimica Acta*, 197–214.
- Bau M. and Alexander B. W. (2009) Distribution of high field strength elements (Y, Zr, REE, Hf, Ta, Th, U) in adjacent magnetite and chert bands and in reference standards FeR-3 and FeR-4 from the Temagami iron-formation, Canada, and the redox level of the Neoproterozoic ocean. *Precambrian Research* 174, 337–346.
- Bau M., Frei R., Garbe-Schönberg D. and Viehmann S. (2022) High-resolution Ge-Si-Fe, Cr isotope and Th-U data for the Neoproterozoic Temagami BIF, Canada, suggest primary origin of BIF bands and oxidative terrestrial weathering 2.7 Ga ago. *Earth and Planetary Science Letters* 589, 117579.
- Bau M., Koschinsky A., Dulski P. and Hein J. R. (1996) Comparison of the partitioning behaviours of yttrium, rare earth elements, and titanium between hydrothermal marine ferromanganese crusts and seawater. *Geochimica et Cosmochimica Acta* 60, 1709–1725.
- Bau M., Schmidt K., Koschinsky A., Hein J., Kuhn T. and Usui A. (2014) Discriminating between different genetic types of marine ferro-manganese crusts and nodules based on rare earth elements and yttrium. *Chemical Geology*, 9.
- Carr J. W. and Horlick G. (1982) Laser vaporization of solid metal samples into an inductively coupled plasma. *Spectrochimica Acta Part B: Atomic Spectroscopy* 37, 1–15.
- Chapman F. W., Marvin G. G. and Tyree S. Y. (1949) Volatilization of Elements from Perchloric and Hydrofluoric Acid Solutions. *Anal. Chem.* 21, 700–701.
- Chew D., Drost K., Marsh J. H. and Petrus J. A. (2021) LA-ICP-MS imaging in the geosciences and its applications to geochronology. *Chemical Geology* 559, 119917.
- Durrant S. F. and Ward N. I. (2005) Recent biological and environmental applications of laser ablation inductively coupled plasma mass spectrometry (LA-ICP-MS). *J. Anal. At. Spectrom.* 20, 821.
- Garbe-Schönberg C.-D. (1993) Simultaneous Determination of Thirty-Seven Trace Elements In Twenty-Eight International Standards By ICP-MS. *Geostandards and Geoanalytical Research* 17, 81–97.
- Garbe-Schönberg D. and Müller S. (2014) Nano-particulate pressed powder tablets for LA-ICP-MS. *J. Anal. At. Spectrom.* 29, 990–1000.
- Gray A. L. (1985) Solid sample introduction by laser ablation for inductively coupled plasma source mass spectrometry. *Analyst* 110, 551.
- Günther D. and Hattendorf B. (2005) Solid sample analysis using laser ablation inductively coupled plasma mass spectrometry. *TrAC Trends in Analytical Chemistry* 24, 255–265.
- Limbeck A., Galler P., Bonta M., Bauer G., Nischkauer W. and Vanhaecke F. (2015) Recent advances in quantitative LA-ICP-MS analysis: challenges and solutions in the life sciences and environmental chemistry. *Anal Bioanal Chem* 407, 6593–6617.
- Liu Y., Hu Z., Gao S., Günther D., Xu J., Gao C. and Chen H. (2008) In situ analysis of major and trace elements of anhydrous minerals by LA-ICP-MS without applying an

- internal standard. *Chemical Geology* 257, 34–43.
- Luo T., Wang Y., Hu Z., Günther D., Liu Y., Gao S., Li M. and Hu S. (2015) Further investigation into ICP-induced elemental fractionation in LA-ICP-MS using a local aerosol extraction strategy. *J. Anal. At. Spectrom.* 30, 941–949.
- Miliszkievicz N., Walas S. and Tobiasz A. (2015) Current approaches to calibration of LA-ICP-MS analysis. *J. Anal. At. Spectrom.* 30, 327–338.
- Moenke H. and Moenke-Blankenburg L. (1973) *Laser Microspectrochemical Analysis.*, Adam Hilger Ltd., London.
- Mundl-Petermeier A., Viehmann S., Tusch J., Bau M., Kurzweil F. and Münker C. (2022) Earth’s geodynamic evolution constrained by 182W in Archaean seawater. *Nat Commun* 13, 2701.
- Pozebon D., Scheffler G. L., Dressler V. L. and Nunes M. A. G. (2014) Review of the applications of laser ablation inductively coupled plasma mass spectrometry (LA-ICP-MS) to the analysis of biological samples. *J. Anal. At. Spectrom.* 29, 2204–2228.
- Schulz T., Viehmann S., Hezel D. C., Koeberl C. and Bau M. (2021) Highly Siderophile Elements and Coupled Fe-Os Isotope Signatures in the Temagami Iron Formation, Canada: Possible Signatures of Neoproterozoic Seawater Chemistry and Earth’s Oxygenation History. *Astrobiology* 21, 16.
- Scribner A. M., Kurtz A. C. and Chadwick O. A. (2006) Germanium sequestration by soil: Targeting the roles of secondary clays and Fe-oxyhydroxides. *Earth and Planetary Science Letters* 243, 760–770.
- Shaheen M. E., Gagnon J. E. and Fryer B. J. (2012) Femtosecond (fs) lasers coupled with modern ICP-MS instruments provide new and improved potential for in situ elemental and isotopic analyses in the geosciences. *Chemical Geology* 330–331, 260–273.
- Smith D. B. (1995) USGS Certificate of Analysis Manganese Nodules. NOD-P1., USGS.
- Thompson M., Goulter J. E. and Sieper F. (1981) Laser ablation for the introduction of solid samples into an inductively coupled plasma for atomic-emission spectrometry. *Analyst* 106, 32.
- Viehmann S., Hoffmann J. E., Münker C. and Bau M. (2014) Decoupled Hf-Nd isotopes in Neoproterozoic seawater reveal weathering of emerged continents. *Geology* 42, 115–118.

Fractionation of germanium and silicon during
scavenging from seawater by marine Fe
(oxy)hydroxides: Evidence from hydrogenetic
ferromanganese crusts and nodules

David M. Ernst^{a*}, Katharina Schier^a, Dieter Garbe-Schönberg^{b, a},
Michael Bau^a

^a *Department of Physics and Earth Sciences, Jacobs University Bremen, Campus Ring
1, 28759 Bremen, Germany*

^b *Institute of Geosciences, Kiel University, Ludewig-Meyn-Straße 10, 24118 Kiel,
Germany*

published in

Chemical Geology

Chemical Geology 595 (2022) 120791

* *Corresponding author. Email adress: d.ernst@jacobs-university.de (D. M. Ernst)*

<https://doi.org/10.1016/j.chemgeo.2022.120791>

Received 8 December 2021; Received in revised form 19 February 2022; Accepted 24 February 2022

Available online 27 February 2022

0009-2541/© 2022 Elsevier B.V. All rights reserved.

4 Germanium-silicon systematics in hydrogenetic ferromanganese crusts

4.1 Abstract

Germanium (Ge) and silicon (Si) are an element pair which shows rather coherent behaviour in many geochemical systems. In aqueous systems and in the critical zone, however, Ge and Si may fractionate from each other, leading to slight differences between the Ge/Si ratios of continental crust, river water and seawater. We here show that even stronger fractionation of the Ge-Si couple occurs within seawater during the formation of hydrogenetic ferromanganese (Fe-Mn) crusts and nodules. We determined Ge/Si ratios of hydrogenetic Fe-Mn crusts from the Pacific Ocean following a new analytical approach using laser-ablation ICP-MS on nanoparticulate tablets prepared from the Fe-Mn crust material. Data quality was monitored and demonstrated by repetitive measurements of Fe-Mn nodule reference material (RM) NOD-P1 from the Pacific Ocean ($\text{Ge/Si}_{\text{wt}}: 16.8 \times 10^{-6} \text{ g/g}$; $\text{Ge/Si}_{\text{mol}}: 6.47 \times 10^{-6} \text{ mol/mol}$), which is the only RM for which high-quality Ge-Si reference data are available. We also report Ge/Si ratios for Fe-Mn nodule RMs NOD-A1 from the Atlantic Ocean ($\text{Ge/Si}_{\text{wt}}: 24.9 \times 10^{-6}$; $\text{Ge/Si}_{\text{mol}}: 9.6 \times 10^{-6}$) and for JMn-1 from the Pacific Ocean ($\text{Ge/Si}_{\text{wt}}: 17.9 \times 10^{-6}$; $\text{Ge/Si}_{\text{mol}}: 6.9 \times 10^{-6}$). The Ge/Si_{wt} ratios of the hydrogenetic Fe-Mn crusts from the Pacific Ocean range from 13.2×10^{-6} to 33.5×10^{-6} ($\text{Ge/Si}_{\text{mol}}: 5.1 \times 10^{-6}$ to 13×10^{-6}). The Ge/Si ratios of both Fe-Mn crusts and nodules are significantly higher than those of ambient seawater (ca. $\text{Ge/Si}_{\text{wt}}: 1.7 \times 10^{-6}$; $\text{Ge/Si}_{\text{mol}}: 0.7 \times 10^{-6}$). Their Ge/Si ratios are also well-above those of potential (alumino)silicate detritus. Hence, these high Ge/Si ratios reveal fractionation of Ge and Si during scavenging from seawater by the iron (oxy)hydroxide component in Fe-Mn crusts, and do not result from the presence of detrital material in the chemical precipitate. Their high Ge/Si ratios relative to seawater also suggest that despite higher complexation constants with organic ligands for Ge than Si, dissolved organic ligands do not control marine Ge-Si fractionation via preferential retention of Ge in seawater.

4.2 Introduction

4.2.1 Germanium and silicon

Germanium (Ge) and silicon (Si) are both members of group 13 of the Periodic Table of Elements. In the first drafts of the periodic table by Dmitri Mendeleev Ge was named "eka-silicon" which refers to the position of Ge right below Si and implies some kind of relationship between these two elements. Both elements are predominantly tetravalent in natural systems and have very similar ionic radii (Si: 1.46 Å and Ge: 1.52 Å, in 4-fold coordination) and oxide bond lengths (Si-O: 1.63 Å, Ge-O: 1.64 Å) (Martin et al., 1996). This allows Ge to substitute Si in the crystal lattice of silicates, following the basic principles of Goldschmidt (1958). Therefore, Ge and Si show coherent behaviour during those igneous geochemical processes that are mainly controlled by charge and size of the cations (similar to the "CHARAC" behaviour of the geochemical twins Y-Ho and Zr-Hf; Bau, 1996). This is corroborated by the largely uniform Ge/Si ratios that characterise the vast majority of igneous and clastic sedimentary rocks (oceanic crust: Ge/Si_{wt}: 6.5×10^{-6} , Ge/Si_{mol}: 2.5×10^{-6} ; continental crust: Ge/Si_{wt}: 4.7×10^{-6} , Ge/Si_{mol}: 1.8×10^{-6} ; marine deep-sea clay: Ge/Si_{wt}: $5.4\text{--}8.1 \times 10^{-6}$, Ge/Si_{mol}: $2.1 \times 10^{-6}\text{--}3.1 \times 10^{-6}$ (Rouxel et al., 2006) and upper continental crust: Ge/Si_{wt}: 4.5×10^{-6} , Ge/Si_{mol}: 1.7×10^{-6} (Rudnick and Gao, 2003); note that Ge/Si_{wt} ratios (used for solids) are given as mass ratios [g/g] and Ge/Si_{mol} ratios (used for solutions) are given as molar ratios [mol/mol]). Although there seems to be a slight fractionation of Ge and Si during igneous fractionation processes resulting in higher Ge/Si ratios of mafic as compared to felsic magmas, their ratios are close to the average Ge/Si ratio for the continental crust.

Slight fractionation of the Ge/Si ratio during continental weathering, leading to somewhat lower Ge/Si_{wt} ratios of river waters ($0.8\text{--}3.1 \times 10^{-6}$; Ge/Si_{mol}: $0.3\text{--}1.2 \times 10^{-6}$), had already been described by Mortlock and Froelich (1987) and was more recently confirmed by Aguirre et al. (2017) and Ameijeiras-Mariño et al. (2018). Further work by Murnane and Stallard (1990) and Froelich et al. (1992) suggested that the Ge/Si ratios in river waters depend on the intensity of weathering: (i) low weathering intensities result in incongruent alteration of rocks and the formation of secondary clay minerals with enhanced Ge/Si ratio compared to the source rocks, while the related river waters show lower Ge/Si ratios; (ii) during intense (chemical) weathering, Ge-enriched secondary minerals are re-dissolved, leading to an increase of the Ge/Si ratio in such river waters. These results were later confirmed by Kurtz et al. (2002) who described a high Ge/Si reservoir (Ge/Si_{wt}: $16.0\text{--}42.7 \times 10^{-6}$; Ge/Si_{mol}: $6.2\text{--}16.4 \times 10^{-6}$) in Hawaiian soils, and

argued for retention of Ge in clays during incongruent silicate weathering; they also observed the highest Ge/Si ratios in the oldest soils. Besides inorganic fractionation of the Ge/Si ratio, complexation of Ge and Si by organic ligands can also influence the Ge/Si ratio in aqueous media. Pokrovski and Schott (1998) observed that the complexation of Ge by humic acids may increase the Ge/Si ratio of organic-rich surface waters, because in contrast to Ge, the complexation of Si with such humic acids is minute. This is supported by data from an organic-rich river in Cameroon (Viers et al., 1997), that shows elevated Ge/Si ratios compared to rivers with less organic material. Furthermore, Viers et al. (1997) used stepwise filtration to show that the Ge concentration is directly linked to the dissolved organic carbon (DOC) content, while the Si concentration is not. The enrichment of Ge in coal and other lignitized organic material described by Bernstein (1985), also argues for preferential association of Ge relative to Si with organic ligands.

The modern marine system mainly receives its element inventory from three sources: (i) hydrothermal fluids which predominantly influence the direct vicinity of vent sites and show Ge/Si_{wt} ratios between 10.1×10^{-6} and 134.3×10^{-6} ($\text{Ge/Si}_{\text{mol}}$: $3.9\text{--}51.7 \times 10^{-6}$; e.g., Mortlock et al., 1993; Escoube et al., 2015); (ii) riverine input (avg. Ge/Si_{wt} : 1.6×10^{-6} , $\text{Ge/Si}_{\text{mol}}$: 0.6×10^{-6} ; Mortlock and Froelich, 1987) which is the major source in coastal waters; and (iii) atmospheric dust (Ge/Si_{wt} of loess: $3.6\text{--}3.8 \times 10^{-6}$, $\text{Ge/Si}_{\text{mol}}$: $1.4\text{--}1.5 \times 10^{-6}$; Ge/Si_{wt} of mineral aerosols: $2.2\text{--}6.0 \times 10^{-6}$, $\text{Ge/Si}_{\text{mol}}$: $0.8\text{--}2.3 \times 10^{-6}$; Mortlock and Froelich, 1987) which is of particular importance in pelagic ocean areas at large distance from any coastline. In the marine water column, Ge and Si behave very similar to each other: The dissolved concentrations of both elements in the Pacific, Atlantic and Southern Oceans increase with depth (e.g., Froelich et al., 1985; Sutton et al., 2010), indicating continuous removal of Ge and Si from particles. Dissolved Ge and Si concentrations in the Atlantic are lower compared to those in the South Pacific or the Southern Oceans, while Antarctic Bottom Water (AABW) also shows elevated Ge and Si concentrations. Dissolved Ge/Si ratios, however, are very similar throughout the ocean basins and throughout the water column (Sutton et al., 2010; Guillermic et al., 2017). In general, the correlation between dissolved Ge and Si concentrations in the oceans can be described by a linear equation and only at very low Si concentrations ($<10 \mu\text{mol/L}$; $\sim 0.28 \text{ mg/kg}$) the relationship between Ge and Si is better described by a 2nd-order polynomial function (Sutton et al., 2010). Residence times for Ge and Si were estimated to be ~ 8000 years and $15,000\text{--}17,000$ years, respectively (Hammond et al., 2004; Tréguer and De La Rocha, 2013).

As the dominant source of the marine element inventory is derived from the continents via riverine input (e.g., Hammond et al., 2004), the Ge/Si ratios of modern seawater

($\text{Ge}/\text{Si}_{\text{wt}}: 1.7 \times 10^{-6}$, $\text{Ge}/\text{Si}_{\text{mol}}: 0.7 \times 10^{-6}$; Mortlock and Froelich, 1987) which are similar to those of the source rivers, suggest only minor fractionation during estuarine processes. However, although the input of Ge (and Si) into the oceans is rather well understood, this is different for the removal of Ge removal and the apparent mismatch is commonly referred to as the "missing Ge sink" (King et al., 2000).

4.2.2 Hydrogenetic ferromanganese crusts

Hydrogenetic ferromanganese crusts (Fe-Mn crusts) are marine chemical sediments which form encrustations on rocks and other substrates in the deep-sea (400–7000 m; Hein et al., 2000). In contrast to diagenetic and hydrothermal Fe-Mn crusts, the chemical inventory of hydrogenetic crusts is exclusively derived from ambient seawater with small but variable contributions from detrital aluminosilicates (e.g., Bau et al., 2014, and references therein). They mainly consist of Fe and Mn (oxyhydr)oxides and grow at very slow rates of only very few mm/Ma on submarine plateaus and flanks of seamounts, where sedimentation rates are low enough to not exceed these slow growth rates. During their formation, hydrogenetic Fe-Mn crusts very effectively scavenge particle-reactive trace elements from ambient seawater. This results in a strong enrichment of, for example, Rare Earths and Yttrium (REY), Cu, Ni, Co, Bi, Mo, W, Te, Pt, Ti, Zr, Hf, Nb, Ta, Th, and U (e.g., Hein et al., 2013, 2000; Hein and Koschinsky, 2013; Schmidt et al., 2014) compared to their seawater source.

Nanoparticles and colloids of Fe and Mn (oxyhydr)oxides form in the water column wherever oxygen-rich bottom water gets in contact with the water of the metal-enriched oxygen-minimum-zone (e.g., Koschinsky and Halbach, 1995; Hein et al., 2000). The oxidic Fe and Mn nanoparticles may aggregate to colloids and interact with dissolved trace elements. Following a very simplistic "electrostatic model" (e.g., Li, 1991; Koschinsky and Halbach, 1995; for its limitations see, e.g., Bau and Koschinsky, 2009), positively charged dissolved metal cations associate with the negatively charged surface of the Mn oxides, while negatively charged and neutral metal complexes attach to the slightly positively charged surface of the Fe (oxy)hydroxides. This process continues after, eventually, these Fe and Mn colloids are deposited at the sea floor for as long as they are exposed at the sediment/water interface during the slow growth of the Fe-Mn oxide encrustations. Hydrogenetic Fe-Mn crusts are characterized by high porosities and specific surfaces areas of up to 60 % and $\sim 325 \text{ m}^2/\text{g}$, respectively (e.g., Hein et al., 2000).

4.2.3 Aims of this study

Considering the quest for a "missing Ge sink in seawater" (King et al., 2000) combined with the analytical challenges of determining Ge concentrations in Fe-rich sample matrices and the resulting lack of data on Ge concentrations and Ge/Si ratios of marine hydrogenetic Fe-Mn crusts, we investigated the Ge-Si-Fe systematics of these marine chemical sediments. Moreover, Fe-Mn crusts and nodules have become targets of deep-sea mining of unconventional resources (e.g., Koschinsky et al., 2018) for which sound knowledge of their inventory of critical metals such as Ge is a prerequisite. Here we provide the results of the first study on Ge and Ge/Si ratios in marine hydrogenetic Fe-Mn crusts (and also Ge and Ge/Si data for Fe-Mn nodule reference standards).

4.3 Samples and methods

4.3.1 Samples

During the 66th cruise of the German research vessel FS SONNE (SO66) Fe-Mn crusts were sampled in the Central Pacific in an area between Kiribati and Wallis and Futuna (0° – 10° S and 175° E – 175° W). Bau et al. (1996, 2014) described and analysed 23 Fe-Mn crust samples, 14 of which were classified as purely hydrogenetic and nonphosphatized. From those 14 samples, eleven were selected for the reconnaissance study reported here. In addition to these eleven Fe-Mn crust samples, the Fe-Mn nodule RMs USGS NOD-A1 (Atlantic), NOD-P1 (northern Pacific) and JGS JMn-1 (southern Central Pacific) were investigated.

4.3.2 Methods

For bulk analyses of major and trace elements, 50 mg dried (105 °C for 12 h) aliquots of each milled Fe-Mn crust or nodule sample were dissolved in a high-pressure high-temperature digestion system (DAS Picotrace, Bovenden, Germany). An acid mix of 3:1:1 conc. HCl, HNO₃ and HF was added to each digestion beaker. The digestion program ran for 12 h at 180 °C. The dissolved samples were evaporated to incipient dryness twice and redissolved with 5 ml conc. HCl. Eventually, the sample was transferred to acid-cleaned PE bottles and diluted with a mix of 0.5 M HNO₃ and 0.5 % HCl. All acids used were of semiconductorgrade purity.

Subsequent to the digestion, all samples were analysed in the GeochemistryLab at

Jacobs University Bremen for major and trace elements with ICP-OES (Spectro Ciros Vision) and quadrupole ICP-MS (Perkin Elmer NexION 350X), respectively. The analytical quality was controlled using the Fe-Mn nodule reference material (RM) NOD-P1 (Pacific), the method blank and acid blanks which were prepared for each measurement session. For monitoring the digestion routine, a method blank was also included in the sample set. The ICP-OES and ICP-MS analytical procedure follows that described by Alexander (2008).

We emphasize, however, that Ge and Si concentrations cannot be determined by the protocol described above, as Ge and Si form stable complexes with fluoride during the three-acid digestion and then volatilize during the evaporation steps. Hence, Ge and Si concentrations were determined at Kiel University by high-resolution ICP-MS (HR-ICPMS) –ThermoFisher Element XR –in combination with a GeoLasPro PlusHD (Coherent) laser ablation system on different aliquots of the sample powder. For the laser ablation measurements, a nano-particulate pressed powder tablet (for details see Garbe-Schönberg and Müller, 2014) was prepared for each Fe-Mn crust sample and RMs. The SO66 samples together with nanoparticulate tablets of the Fe-Mn nodule RMs NOD-A1 (Atlantic), NOD-P1, and JMn-1 (Pacific) and the glass RM NIST610 were mounted into a Zurich-type-large-volume ablation cell. The ablation cell was permanently flushed with ~ 1 l/min He as carrier gas together with 14 ml/min H_2 for an increase of sensitivity and a reduction of oxide formation. The laser ablation was performed with a constant fluence of 6 J/cm^2 , a spot size of $160 \text{ }\mu\text{m}$ in diameter, and 400 pulses on each measured point at a frequency of 10 Hz. Prior to the ablation, 20 s of background signal were collected for each measured point. Each ablation run was followed by 20 s wash-out before proceeding to the next point. In the beginning and at the end of the measurement session all four RMs were measured three times each. Additionally, after 25 measurements on the samples (five measurements per sample), NIST610, NOD-A1 and NOD-P1 were measured three times each. This repeated measurement of the RMs allows to monitor machine drift. All Ge/Si measurements have been done in high-resolution (HR) mode of the Thermo Element XR High-Resolution ICP-SF-MS, which is around 10,000 RP (resolving power, i.e. the ability of the mass spectrometer to separate two mass peaks or ion species). The mass spectra had been checked for overlap from polyatomic interferences and no spectral interferences were found that could have affected the selected mass regions in HR. The possible interference on ^{72}Ge m/z by $^{56}\text{Fe}^{16}\text{O}$ requires 9250 RP, all other polyatomics (e.g., Ar-based cluster ions; Nd and Sm doubly charged ions) in this mass range require only <5500 RP. Iron (^{56}Fe and ^{57}Fe) was monitored during all

measurements along with Nd and Sm.

Germanium-74 could be affected by an isobar of ^{74}Se (56,950 M/dM) and an interference from $^{56}\text{Fe}^{16}\text{O}$ (12,940 M/dM) both cannot be resolved even in HR mode. However, Se mass fractions are extremely low in these samples and ^{74}Se has a natural abundance of 0.89 %, hence this interference is irrelevant. The natural abundance of ^{58}Fe is also very low with 0.28 % but could cause an interference in samples with high Fe mass fractions. In Fig. 4.1 (A–C) it is shown that the difference between the $^{72}\text{Ge}/^{28}\text{Si}$ and $^{74}\text{Ge}/^{28}\text{Si}$ ratios is only very small (in the range of the standard deviation) even in Fe-rich samples. Furthermore, Fig. A1 in the Appendix shows the $^{72}\text{Ge}/^{74}\text{Ge}$ ratios for each single measurement point. While there are many outliers in the gas blank measurements, all data points used for Ge/Si determination (see below) show the expected natural $^{72}\text{Ge}/^{74}\text{Ge}$ ratio (0.7436; Anders and Grevesse, 1989). This further indicates that the measured Ge signals of both isotopes (^{72}Ge and ^{74}Ge) were not or only to a very minor to negligible extent affected by interferences. A possible interference from NiO would be resolved at 8140 RP and, moreover, Ni is low in these samples. All possible interferences from polyatomic (NN, CO) and doubly charged ions (Fe) in the mass range of Si isotopes can be resolved already in MR mode at 3500 RP and, hence, are not relevant for our analyses in HR mode. We here use the ^{72}Ge to calculate Ge/Si ratios.

The raw data were processed with LADR (Laser Ablation Data Reduction — version 1.1.02, Norris Scientific). Only elemental ratios were evaluated using the "Quantified Ratios" program. The NOD-P1 reference standard was selected for use for the quantification (1.09 mg/kg Ge, Scribner et al., 2006; 64,978 mg/kg Si, Smith, 1995), while the other RMs were analysed to check accuracy and to monitor the machine drift during the measurements. NOD-P1 represents a matrix similar to that of the Fe-Mn crust samples, and was also prepared as a nano-particulate press tablet. Therefore, the ablation behaviour of the NOD-P1 sample and of the SO66 samples should be similar and (unidentified) matrix effects negligible. In the raw data, the time intervals for evaluation were picked by hand in order to catch the most stable signal for all elements. The time intervals for the determination of the gas blank were also picked by hand to avoid irregularities at low signals or outliers. The obtained signal intensities of $^{72}\text{Ge}/^{28}\text{Si}$ and $^{74}\text{Ge}/^{28}\text{Si}$ were both recalculated to an elemental Ge/Si ratio corrected for natural abundance using the isotope's natural abundances as given by Anders and Grevesse (1989). For a more detailed description of the LADR data processing see the "LADR Software Manual", which is included in the LADR software package. The LADR software package can be downloaded without buying a licence at the official LADR webpage

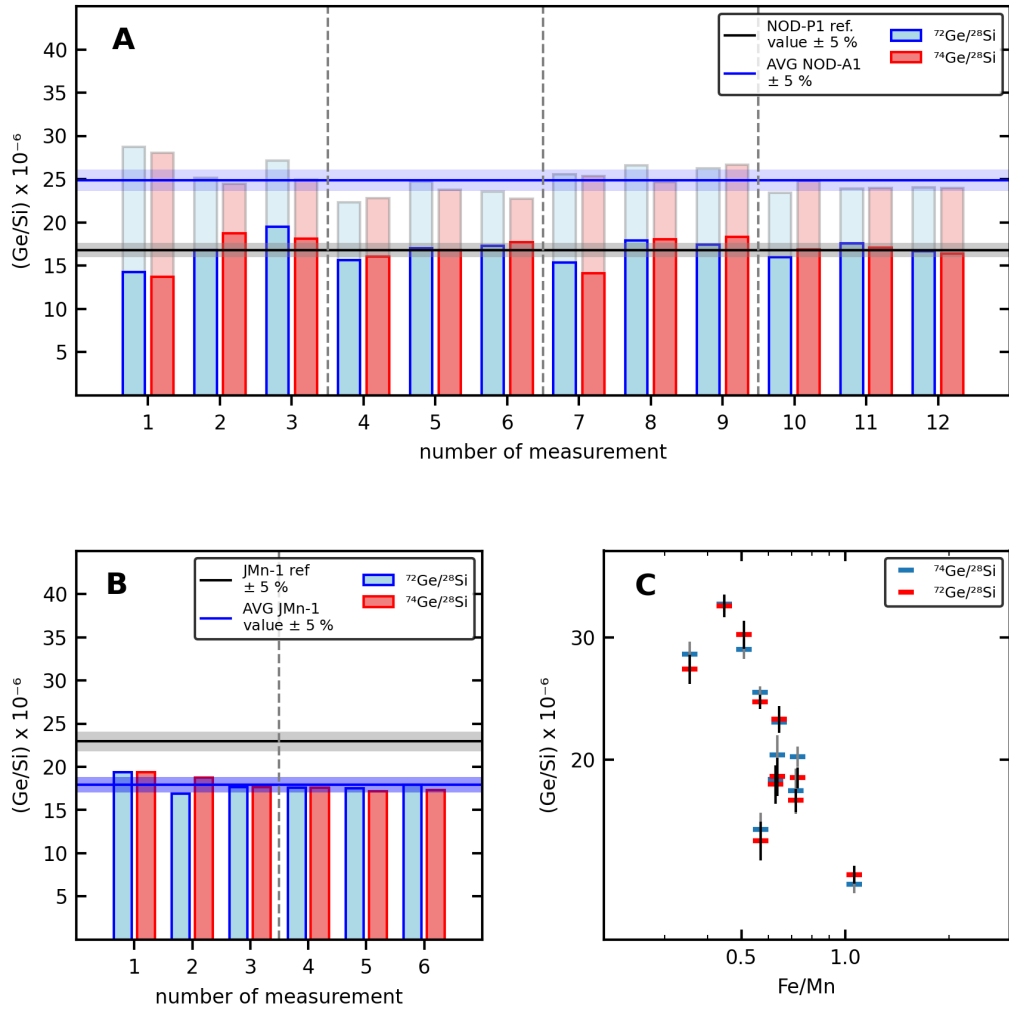


Figure 4.1: Graphs of A) $\text{Ge}/\text{Si}_{\text{wt}}$ ratios for RMs NOD-P1 (solid bars) and NOD-A1 (faded bars) using ^{72}Ge (blue) and ^{74}Ge (red). NOD-P1 reference value indicated by black line; determined average NOD-A1 $\text{Ge}/\text{Si}_{\text{wt}}$ ratio indicated by blue line; B) $\text{Ge}/\text{Si}_{\text{wt}}$ ratios for RM JMn-1 using ^{72}Ge (blue) and ^{74}Ge (red). Reference value (black) and average of $\text{Ge}/\text{Si}_{\text{wt}}$ ratios (blue) determined here indicated by the horizontal lines; C) $\text{Fe}/\text{Mn}_{\text{wt}}$ ratio vs $\text{Ge}/\text{Si}_{\text{wt}}$ ratio for the eleven SO66 Fe-Mn crust samples (blue: ^{74}Ge ; red: ^{72}Ge). Vertical grey and black bars show the respective standard deviation. Reference data for NOD-P1 from Smith (1995) and Scribner et al. (2006), for JMn-1 from Terashima et al. (1995). (For interpretation of the references to colour in this figure legend, the reader is referred to the web version of this article.)

(www.norsci.com/ladr/). During the data processing of this study the current manual version was "LADR Software Manual — Revision 2020C".

4.4 Results

4.4.1 Reference materials NOD-P1, NOD-A1 and JMn-1

Compared to the analysis of many other major and trace elements, analysis of Ge and Si by ICP-MS is rather challenging. During the standard three-acid-digestion (HCl + HNO₃ + HF) Ge and Si evaporate as fluoride complexes. Therefore, published data sets for rock samples and RMs determined by analytical techniques that require sample dissolution often lack Ge and Si data, and the Si data that is reported has often been determined by X-ray fluorescence (XRF). For the RM NOD-P1 there are two Ge reference values given on GeoReM (<http://georem.mpch-mainz.gwdg.de>): (i) Axelsson et al. (2002; Ge: 0.54 mg/kg) used a room temperature digestion without any subsequent evaporation, thereby trying to prevent loss of Ge and Si; (ii) Scribner et al. (2006; Ge: 1.09 mg/kg) used a closed-vessel microwave digestion followed by addition of H₃BO₃ and 15 min heating at 150 °C in order to stabilize the dissolved Ge and Si during the subsequent evaporation. We used the Ge concentration of Scribner et al. (2006) for the determination of the Ge/Si ratio in the RM NOD-P1 together with the Si concentration (64,978 mg/kg) given by Smith (1995).

The measured Ge/Si ratios for the twelve measurements of RM NOD-P1 (Table A.1 in Electronic Annex and Fig. 1 A) show very similar results (RSDEV <5.6 %) regardless of whether ⁷²Ge or ⁷⁴Ge is used, and yield an overall average Ge/Si_{wt} ratio of 16.79 × 10⁻⁶. The relative standard deviation (RSDEV) of 8.5 % based on all 24 individual measurements (twelve measurements with ⁷²Ge and ⁷⁴Ge each) from the reference value (Ge/Si_{wt}^{NOD-P1} = 16.78 × 10⁻⁶; Ge/Si_{mol}^{NOD-P1} = 6.46 × 10⁻⁶; Scribner et al., 2006; Smith, 1995) is also small and indicates only minor machine drift throughout the whole measurement session.

The Ge/Si ratios for the twelve measurements of RM NOD-A1 (Table A.1 and Fig. 1 A) show similar results irrespective of whether they are based on ⁷²Ge or ⁷⁴Ge (RSDEV <4.3 %), and yield an average Ge/Si_{wt} ratio of 24.89 × 10⁻⁶ (Ge/Si_{mol}: 9.59 × 10⁻⁶). The RSDEV (6.5 %) of all 24 individual measurements from the average Ge/Si ratio of NOD-A1 is also low. To the best of our knowledge there are no Ge data published for NOD-A1, hence a comparison of our Ge/Si ratio with a reference value is impossible. The reference value for the Si concentration of NOD-A1 is 17,810 mg/kg (Smith, 1995),

which suggests a calculated Ge concentration of 0.44 mg/kg in NOD-A1, based on the measured average Ge/Si_{wt} ratio of 24.89×10^{-6} . This is only half of the Ge concentration of NOD-P1, but NOD-P1 also shows a much higher Si concentration of 64,978 mg/kg (Smith, 1995), which, in turn, leads to the lower Ge/Si ratios in NOD-P1 compared to NOD-A1. The calculated Ge concentration for NOD-A1 fits to the observations of Axelsson et al. (2002) who suggested a Ge "concentration" in NOD-A1 of " <0.5 mg/kg".

The Ge/Si ratios for the six measurements of RM JMn-1 (Table A.1 and Fig. 4.1 B) show similar results irrespective of whether they are based on ^{72}Ge or ^{74}Ge (RSDEV <5.4 %), and yield an average Ge/Si_{wt} ratio of 17.91×10^{-6} (Ge/Si_{mol}: 6.90×10^{-6}). Reference values given for JMn-1 of Ge = 1.51 mg/kg and Si = 65,819 mg/kg (Terashima et al., 1995) yield a reference Ge/Si_{wt} ratio of 22.94×10^{-6} (Ge/Si_{mol}: 8.83×10^{-6}). Our Ge/Si ratio for JMn-1 from the southern Central Pacific is similar to that of NOD-P1 from the northern Pacific, whereas that derived from the reference values is similar to that of NOD-A1 from the Atlantic Ocean. Moreover, to the best of our knowledge there is only one single Ge concentration published for JMn-1 (Terashima et al., 1995), which is referenced as "unpublished work, K. Govindaraju and G. Mevelle, 1993–1995". In contrast to Ge, the Si concentrations given by Terashima et al. (1995) were confirmed by other studies (see data compilation by Imai et al., 1999). This compiled reference value for the Si concentration of JMn-1 is 65,950 mg/kg (Imai et al., 1999), which would lead to a calculated Ge concentration of 1.18 mg/kg in JMn-1, based on the average Ge/Si_{wt} of 17.91×10^{-6} measured here. This is ~ 22 % less than the reference Ge concentration (1.51 mg/kg) given by Terashima et al. (1995).

Hence, the Ge/Si_{wt} ratios of the three Fe-Mn nodule RMs (which are all of hydrogenetic origin according to the classification scheme of Bau et al., 2014) range between 16.8×10^{-6} and 24.9×10^{-6} , i.e. they all are above the Ge/Si ratio of seawater, and fit perfectly into the range of the SO66 Fe-Mn crust samples reported below. While our Ge/Si ratios for NOD-P1 and NOD-A1 suggest a difference between nodules from the Pacific and Atlantic (similar to what Schier et al. (2021) reported for Ga/Al ratios), this needs to be verified by additional data from a larger sample set.

4.4.2 Hydrogenetic Fe-Mn crusts

The major and trace element composition of the SO66 samples is shown in Table 4.1 (see also Schier et al., 2021). Published Si concentrations determined by X-ray fluorescence for all eleven samples (data from Halbach et al., 1990) are shown for comparison. Absolute germanium concentrations were calculated ("*Ge_{calc}*" in Table 4.1) based on the measured

average Ge/Si ratio (see below) and the published Si concentrations (Halbach et al., 1990).

The Fe and Mn concentrations in the SO66 samples range from 11.5 to 20.3 % (m/m) and from 19.1 to 32.5 % (m/m), respectively, with Fe/Mn ratios between 0.35 and 1.06. The Si concentrations range from 0.84 to 6.03 % (m/m) and those of Ti from 0.82 to 1.48 % (m/m). Zirconium and Hf concentrations are between 347 and 924 mg/kg and between 4.9 and 16.3 mg/kg, respectively, yielding super-chondritic Zr/Hf_{wt} ratios between 50.3 and 77.0.

For a detailed description and discussion of the REY distributions in the SO66 samples see Bau et al. (2014). All samples are classified as purely hydrogenetic Fe-Mn crusts with Nd concentrations >100 mg/kg, positive Ce_{SN} anomalies (SN: shale-normalized; shale is PostArchaean Australian Shale, PAAS, from McLennan, 1989a,b) and sub-chondritic Y/Ho ratios <27, i.e. negative Y_{SN} anomalies.

Ge/Si_{wt} ratios (Table 2) range from 13.7×10^{-6} to 33.3×10^{-6} (Ge/Si_{mol}: 5.3×10^{-6} – 12.8×10^{-6} ; calculated from $^{72}\text{Ge}/^{28}\text{Si}$) and from 13.2×10^{-6} to 33.5×10^{-6} (Ge/Si_{mol}: 5.1×10^{-6} – 12.9×10^{-6} ; calculated from $^{74}\text{Ge}/^{28}\text{Si}$). Both Ge isotopes yield consistent results for each sample, with RSDEV <7.5 %, if all ten data points (five for $^{72}\text{Ge}/^{28}\text{Si}$ and five for $^{74}\text{Ge}/^{28}\text{Si}$) per sample are considered. The $^{74}\text{Ge}/^{28}\text{Si}$ ratio is slightly higher than the $^{72}\text{Ge}/^{28}\text{Si}$ ratio except for samples SO66–522, SO66–531, and SO66–545. We emphasize that the Ge/Si ratios of both sample types investigated, i.e. of hydrogenetic Fe-Mn nodules and of hydrogenetic Fe-Mn crusts are significantly higher than those of upper continental crust and seawater.

Using the Ge/Si ratios determined by Laser Ablation HR-ICP-MS and the Si data from XRF, Ge concentrations in the hydrogenetic Fe-Mn crusts range between 0.2 and 0.8 mg/kg (Table 4.1).

4 Germanium-silicon systematics in hydrogenetic ferromanganese crusts

Table 4.1: Major and trace element data for the eleven SO66 Fe–Mn crust samples. Empty cells indicate values below the LOQ.

SO66	500	503	506	507	513	518	522	524	526	531	545
<i>wt%</i>											
Fe	17.8	15.8	17.2	11.5	17.8	15.4	16.7	16.6	13.2	20.3	15.6
Mn	24.4	27.8	27.0	32.5	24.7	27.2	26.6	25.8	29.6	19.1	30.7
Ca	2.58	2.73	2.66	2.93	2.56	2.63	2.63	3.24	2.61	-	-
Mg	1.05	1.17	1.16	1.32	1.07	1.21	1.16	1.16	1.31	-	-
Si*	3.59	2.61	2.22	0.84	3.11	1.54	2.48	2.36	1.00	6.03	1.30
Al	0.84	0.71	0.39	0.16	0.70	0.30	0.43	0.51	0.23	1.95	0.25
Ti	1.48	1.11	0.95	0.95	0.93	0.92	0.87	0.88	0.82	1.41	0.78
Ni	0.43	0.67	0.57	0.93	0.50	0.58	0.59	0.56	0.66	0.34	0.69
<i>mg/kg</i>											
Rb	5.7	3.7	2.6	3.0	3.2	2.3	2.7	2.6	2.4	6.0	2.7
Sr	1599	1556	1671	1577	1519	1602	1541	1642	1537	1310	1690
Y	187	144	185	125	188	179	198	227	156	154	166
Zr	924	577	480	375	501	418	448	490	347	684	379
Nb	82	66	58	68	49	51	45	47	58	83	53
Cs	0.19	0.04	0.01	0.02	0.03	-	0.03	0.03	-	0.17	0.02
Ba	2035	1764	1366	1721	1307	1214	1232	1308	1231	1588	1623
La	250	180	197	160	222	193	223	222	165	177	175
Ce	964	768	577	892	517	645	539	529	654	780	748
Pr	42.4	28.2	28.6	25.5	34.9	30.0	34.9	34.3	26.6	26.0	27.0
Nd	179	122	129	108	155	135	156	155	117	111	119
Sm	36.0	23.8	25.0	21.3	30.5	26.9	30.3	30.4	23.4	21.3	23.8
Eu	9.2	6.4	6.9	5.7	8.3	7.5	8.3	8.3	6.4	5.7	6.5
Gd	41.1	28.9	33.2	25.0	39.1	34.5	39.2	40.4	29.5	26.8	29.8
Tb	6.4	4.5	5.0	4.0	6.0	5.3	6.0	6.0	4.5	4.1	4.6
Dy	42.4	31.2	36.1	26.8	41.0	35.9	40.7	41.7	31.7	27.3	32.1
Ho	9.4	7.2	8.5	6.1	9.3	8.3	9.3	9.6	7.3	6.4	7.4
Er	28.0	21.6	26.5	18.9	28.2	25.8	28.5	29.8	22.9	19.7	23.2
Tm	4.2	3.3	4.0	2.8	4.2	3.8	4.2	4.3	3.4	2.9	3.5
Yb	28.0	22.0	26.0	18.3	27.9	25.3	27.7	29.5	22.5	19.5	23.1
Lu	4.4	3.4	4.1	2.8	4.3	3.9	4.3	4.5	3.5	3.1	3.7
Hf	16.3	9.3	6.9	6.0	7.1	6.0	5.8	6.5	5.0	13.6	4.9
Ta	0.59	0.66	-	0.21	0.18	-	0.49	-	-	0.91	0.38
W	91	105	110	142	96	112	101	101	127	59	145
Pb	894	1121	1298	1189	1024	1435	1099	1225	1493	899	1436
Th	4.0	2.8	3.1	2.7	3.3	4.5	4.1	3.9	3.9	3.8	3.5
U	11.7	11.4	13.1	9.8	11.9	12.6	11.8	12.7	11.8	9.7	12.5
avg. Ge/Si	1.95×10^{-5}	1.56×10^{-5}	1.96×10^{-5}	2.77×10^{-5}	1.78×10^{-5}	2.46×10^{-5}	1.86×10^{-5}	2.27×10^{-5}	3.34×10^{-5}	1.34×10^{-5}	2.96×10^{-5}
Ge.calc	0.70	0.41	0.44	0.23	0.55	0.38	0.46	0.54	0.33	0.81	0.38
Fe/Mn	0.73	0.57	0.64	0.35	0.72	0.57	0.63	0.64	0.45	1.06	0.51
Zr/Hf	56.7	62.0	69.7	62.5	70.5	70.0	76.9	74.9	69.4	50.3	77.0
Y/Ho	20.0	20.0	21.8	20.5	20.3	21.5	21.3	23.5	21.4	24.3	22.5
Th/U	0.34	0.24	0.24	0.28	0.27	0.36	0.35	0.31	0.33	0.39	0.28
Nd _{SN} /Yb _{SN}	0.53	0.46	0.41	0.49	0.46	0.44	0.46	0.43	0.43	0.47	0.43
La _{SN} /La _{SN} *	1.92	2.25	2.85	2.07	2.47	2.63	2.54	2.70	2.32	2.30	2.44
Ce _{SN} /Ce _{SN} *	3.14	3.89	3.06	4.85	2.20	3.25	2.31	2.35	3.59	4.21	4.06
Eu _{SN} /Eu _{SN} *	1.12	1.15	1.15	1.15	1.15	1.17	1.15	1.15	1.16	1.14	1.16
Gd _{SN} /Gd _{SN} *	1.05	1.07	1.12	1.04	1.09	1.09	1.10	1.13	1.09	1.09	1.08
Pr _{SN} /Pr _{SN} *	0.52	0.45	0.55	0.38	0.67	0.53	0.66	0.65	0.48	0.42	0.44

Table 4.2: Measured Ge/Si ratios for the eleven SO66 Fe-Mn crust samples. ^{72}Ge and ^{74}Ge indicate which isotope was used for the data evaluation.

Sample	Meas. #	Ge/Si x 10 ⁶		AVG Ge/Si x 10 ⁶		RSDEV [%]		AVG Ge/Si x 10 ⁶ combined	RSDEV [%] combined
		^{72}Ge	^{74}Ge	^{72}Ge	^{74}Ge	^{72}Ge	^{74}Ge		
SO66_500	1	19.243	21.038	18.838	20.208	3.5	3.4	19.523	4.9
	2	18.245	20.794						
	3	19.673	20.372						
	4	17.909	19.596						
	5	19.117	19.242						
SO66_503	1	16.840	17.578	15.294	15.845	6.4	5.7	15.570	6.3
	2	15.569	15.396						
	3	15.452	15.860						
	4	14.722	15.131						
	5	13.886	15.263						
SO66_506	1	19.724	19.013	18.924	20.319	6.3	6.7	19.621	7.4
	2	18.681	21.109						
	3	19.623	21.531						
	4	19.896	21.593						
	5	16.695	18.349						
SO66_507	1	29.486	28.454	27.005	28.361	4.8	4.3	27.683	5.2
	2	25.975	26.959						
	3	26.383	29.629						
	4	27.055	29.789						
	5	26.127	26.973						
SO66_513	1	18.318	19.680	17.483	18.050	3.9	7.6	17.766	6.3
	2	17.507	16.837						
	3	18.105	19.438						
	4	16.489	18.047						
	5	16.997	16.246						
SO66_518	1	23.960	24.964	24.228	24.988	2.4	2.1	24.608	2.7
	2	23.230	25.811						
	3	24.414	24.280						
	4	24.651	24.642						
	5	24.887	25.245						
SO66_522	1	17.533	18.363	18.428	18.743	6.4	4.8	18.586	5.7
	2	16.940	17.247						
	3	18.847	18.894						
	4	20.343	19.940						
	5	18.480	19.269						
SO66_524	1	22.553	21.891	22.871	22.627	4.5	2.3	22.749	3.6
	2	24.862	22.684						
	3	22.462	23.150						
	4	22.578	23.193						
	5	21.902	22.215						
SO66_526	1	32.043	34.038	33.336	33.532	3.7	2.7	33.434	3.2
	2	32.927	31.865						
	3	34.384	34.239						
	4	32.179	34.196						
	5	35.148	33.322						
SO66_531	1	13.988	12.974	13.646	13.228	3.0	3.0	13.437	3.3
	2	13.347	13.959						
	3	12.997	12.852						
	4	13.938	13.075						
	5	13.958	13.278						
SO66_545	1	32.643	29.895	30.296	28.844	4.7	3.1	29.570	4.7
	2	29.755	29.965						
	3	29.218	28.166						
	4	31.109	27.940						
	5	28.755	28.252						

4.5 Discussion

4.5.1 Sample purity

For geochemical investigations of chemical sedimentary rocks it is of utmost importance to identify and assess possible "contamination" of the chemical precipitate by detrital material, as trace element concentrations of potential detritus are often significantly higher than those of the chemically precipitated autochthonous component (e.g., Schier et al., 2021a, b; and references therein). In Fe-Mn crusts, detrital contamination could originate from the ubiquitous background sedimentation (e.g., Murray and Renard, 1891; Biscaye, 1965), (sub-)marine volcanism, and/or the substrate rocks. As Fe-Mn crusts are growing on seamounts, their substrate rock is usually basalt or (phosphatized) carbonate. The composition of the marine background sedimentation is best preserved in pelagic clay (Li and Schoonmaker, 2014). However, all these detrital components show much lower Ge/Si ratios compared to those of the SO66 Fe-Mn crust samples (Fig. 4.2) as illustrated by (i) basalt BHVO-2 ($\text{Ge/Si}_{\text{wt}}: 7.0 \times 10^{-6}$, $\text{Ge/Si}_{\text{mol}}: 2.7 \times 10^{-6}$; Jochum et al., 2017), (ii) pelagic clay ($\text{Ge/Si}_{\text{wt}}: 6.4 \times 10^{-6}$, $\text{Ge/Si}_{\text{mol}}: 2.5 \times 10^{-6}$; Li and Schoonmaker, 2014), (iii) loess ($\text{Ge/Si}_{\text{wt}}: 3.6 \times 10^{-6}$ – 3.8×10^{-6} , $\text{Ge/Si}_{\text{mol}}: 1.4 \times 10^{-6}$ – 1.5×10^{-6} ; Mortlock and Froelich, 1987), and (iv) atmospheric dust ($\text{Ge/Si}_{\text{wt}}: 2.2 \times 10^{-6}$ – 6.0×10^{-6} , $\text{Ge/Si}_{\text{mol}}: 0.8 \times 10^{-6}$ – 2.3×10^{-6} ; Mortlock and Froelich, 1987). Langmuir et al. (1978) developed a method to determine potential endmembers in a binary mixing system based on the sample distribution in element-element, element-ratio and ratio-ratio (as in Fig. 4.2) plots. If the Ge/Si ratios in the SO66 Fe-Mn crusts resulted from admixture of detritus to a hydrogenetic endmember, the calculated mixing hyperbola would suggest one endmember with a Ge/Si ratio similar to that of the potential detritus listed above. However, neither the linear regression, calculated for the SO66 Fe-Mn crust samples, nor mixing calculations (upper limit: SO526 + SO524, lower limit: SO507 + SO503) after Langmuir et al. (1978) point towards any of the potential detrital components. Therefore, as the Ge/Si ratios of the hydrogenetic Fe-Mn crusts studied are much higher than those of both potential detritus and of ambient seawater (inset in Fig. 4.2) and since there is no indication for binary mixing with a detrital endmember, a strong impact on or even a control of the Ge-Si systematics of our samples by detrital aluminosilicates can be ruled out.

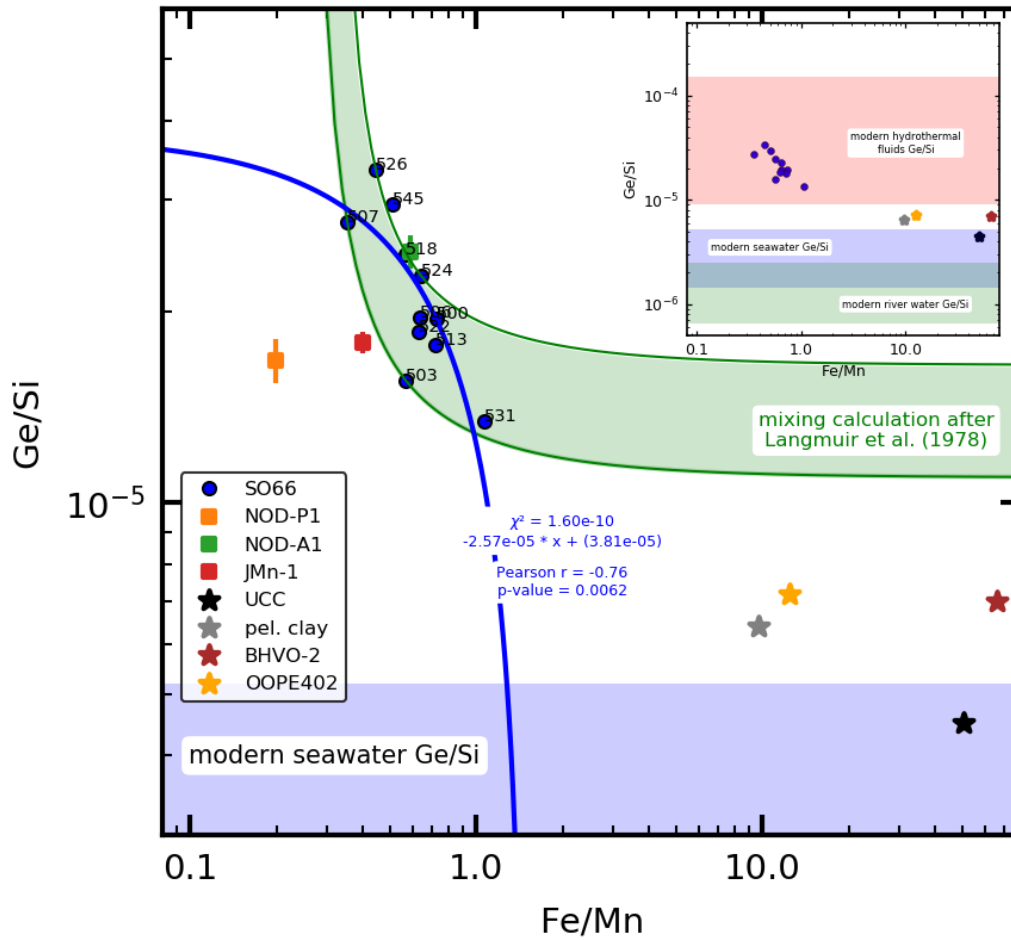


Figure 4.2: Graph of Fe/Mn ratio vs average Ge/Si_{wt} ratio of SO66 Fe-Mn crusts and Fe-Mn nodule RMs NOD-P1, NOD-A1 and JMn-1. Linear regression applied to the SO66 samples is indicated by the solid blue line together with formula, χ -value, Pearson r value and p -value. The green area as bracketed by solid green lines points towards possible endmembers and was calculated after Langmuir et al. (1978) between SO526 and SO524 (upper limit) and between SO507 and SO503 (lower limit). The inset in the upper right shows the same data within a wider Ge/Si_{wt} range on the y-axis shows the elevated Ge/Si_{wt} ratios of the SO66 Fe-Mn crust samples relative to seawater and river water. Reference data: "UCC" (upper continental crust) from Rudnick and Gao (2003); "pel. clay" (pelagic clay) from Li and Schoonmaker (2014); "BHVO-2" (basalt) from Jochum et al. (2017); "OOPE402" (siliceous ooze) from Govindaraju (1994); "modern seawater Ge/Si" from Bruland et al. (2014); "modern river water Ge/Si" from Mortlock and Froelich (1987); "modern hydrothermal fluids Ge/Si" from Mortlock et al. (1993), Escube et al. (2015). (For interpretation of the references to colour in this figure legend, the reader is referred to the web version of this article.)

4.5.2 Fractionation of Ge and Si during formation of hydrogenetic Fe-Mn crusts and nodules

While there are numerous studies on scavenging of various metals by Fe-Mn crusts (e.g., Li, 1991; De Carlo and McMurtry, 1992; Bau et al., 1996; Hein et al., 2013; Mohwinkel et al., 2014; Schmidt et al., 2014; Josso et al., 2017; Lusty et al., 2018; Koschinsky et al., 2020), there are no published results of investigations with a focus on scavenging of Si. Rather, Si is often considered to be mainly of detrital origin (e.g., Hein et al., 2000; Hein et al., 2017; Mizell et al., 2020). However, there is convincing experimental evidence for that considerable amounts of Si can be readily incorporated into or adsorbed onto Fe (oxy)hydroxides (e.g., Schwertmann and Fechter, 1982; Anderson and Benjamin, 1985; Hansen et al., 1994; Taylor, 1995). Hence, it is very likely that dissolved Si from seawater is also sorbed and incorporated onto and into hydrogenetic Fe-Mn crusts and nodules.

The Ge/Si ratios we determined for hydrogenetic Fe-Mn crusts from the Pacific and for hydrogenetic Fe-Mn nodules from the Pacific and Atlantic are about one order of magnitude higher than the Ge/Si ratios of modern seawater (Bruland et al., 2014; Fig. 4.3) and of clastic aluminosilicate detritus. These elevated Ge/Si ratios, therefore, indicate strong fractionation of the Ge-Si couple and preferential Ge removal from seawater by hydrogenetic Fe-Mn crusts. This is fully compatible with experimental results reported and summarized by Pokrovsky et al. (2006) who suggested preferential enrichment of Ge relative to Si on Fe (oxyhydr)oxides based on the higher adsorption of Ge on goethite ($2.5 \mu\text{mol}/\text{m}^2$) compared to Si ($2.2 \mu\text{mol}/\text{m}^2$) at pH 7–8. This is also in agreement with the higher distribution coefficients of Ge relative to Si during co-precipitation with Fe hydroxides ($K_d(\text{Ge}) = 0.9$ vs $K_d(\text{Si}) = 0.4$ in seawater, as reported by Savenko and Volkov, 2003). This may be explained by the ability of Ge to be coordinated 4 and 6-fold, while Si can only be coordinated 4-fold (Pokrovski and Schott, 1998; Pokrovsky et al., 2006).

The two major components of hydrogenetic Fe-Mn crusts and nodules are Fe and Mn (oxyhydr)oxides. In seawater, the surface of the latter is strongly negatively charged, whereas that of the former is neutral to slightly positively charged. The most abundant inorganic dissolved species of Ge and Si in seawater are $\text{Ge}(\text{OH})_4^0$ and $\text{Si}(\text{OH})_4^0$, respectively, while $\text{GeO}(\text{OH})_4^-$ and $\text{GeO}_2(\text{OH})_2^{2-}$ and $\text{SiO}(\text{OH})_3^-$ are significantly less important (<15 %; e.g., Byrne, 2002; Pokrovsky et al., 2006). Thus, these neutral or negatively charged dissolved species may preferentially associate with the Fe (oxy)hydroxide component of marine hydrogenetic Fe-Mn crusts (e.g., Koschinsky and Halbach, 1995) and,

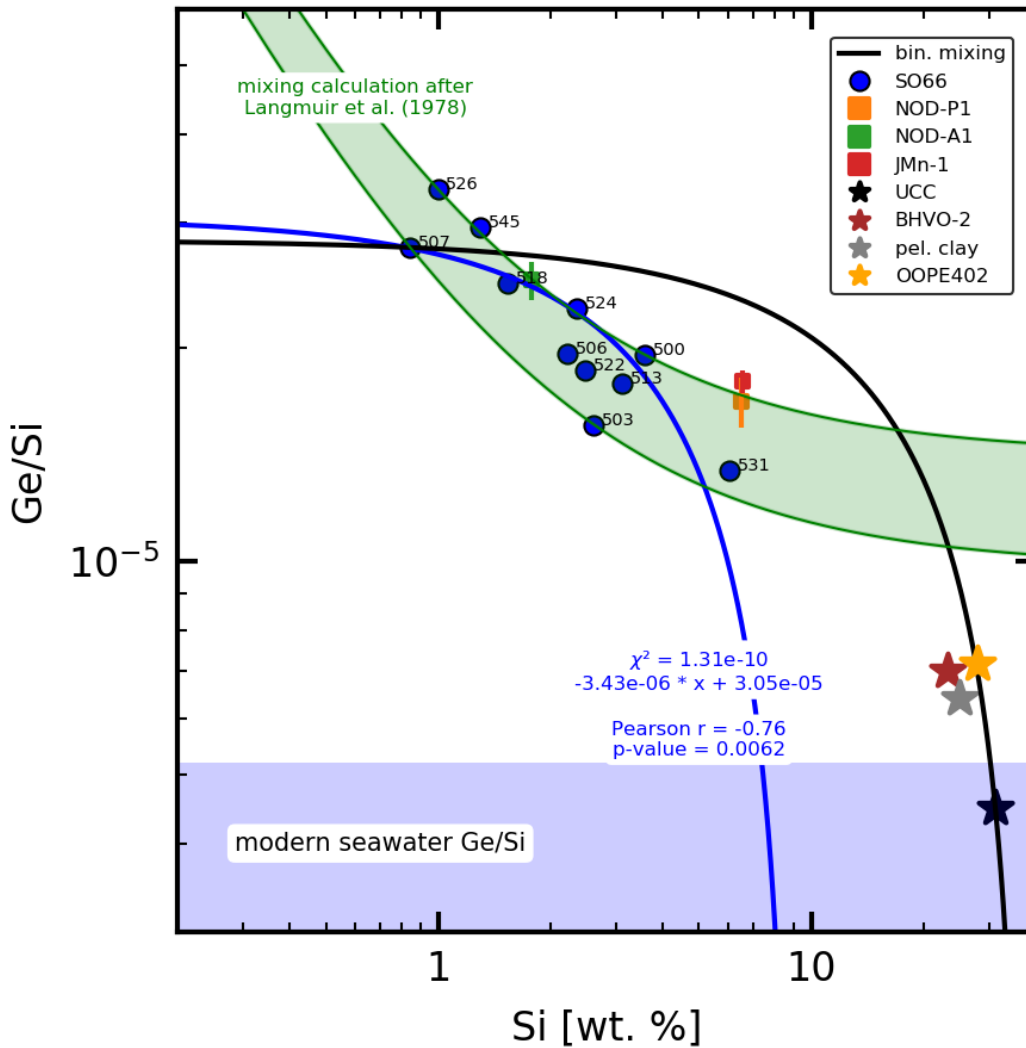


Figure 4.3: Graph of Si concentration (data from Halbach et al., 1990) vs average Ge/Si_{wt} ratio of SO66 Fe-Mn crusts and Fe-Mn nodule RMs. Linear regression applied to these samples is indicated by the solid blue line together with formula, χ^2 -value, Pearson r value and p -value. Binary mixing (solid black line) was calculated using UCC and the SO66_507 sample as endmembers. The green area bracketed by solid green lines points towards possible endmembers, calculated after Langmuir et al. (1978) between SO526 and SO500 (upper limit) and between SO507 and SO503 (lower limit). Reference data: "UCC" (upper continental crust) from Rudnick and Gao (2003); "pel. clay" (pelagic clay) from Li and Schoonmaker (2014); "BHVO-2" (basalt) from Jochum et al. (2017); "OOPE402" (siliceous ooze) from Govindaraju (1994). (For interpretation of the references to colour in this figure legend, the reader is referred to the web version of this article.)

4 Germanium-silicon systematics in hydrogenetic ferromanganese crusts

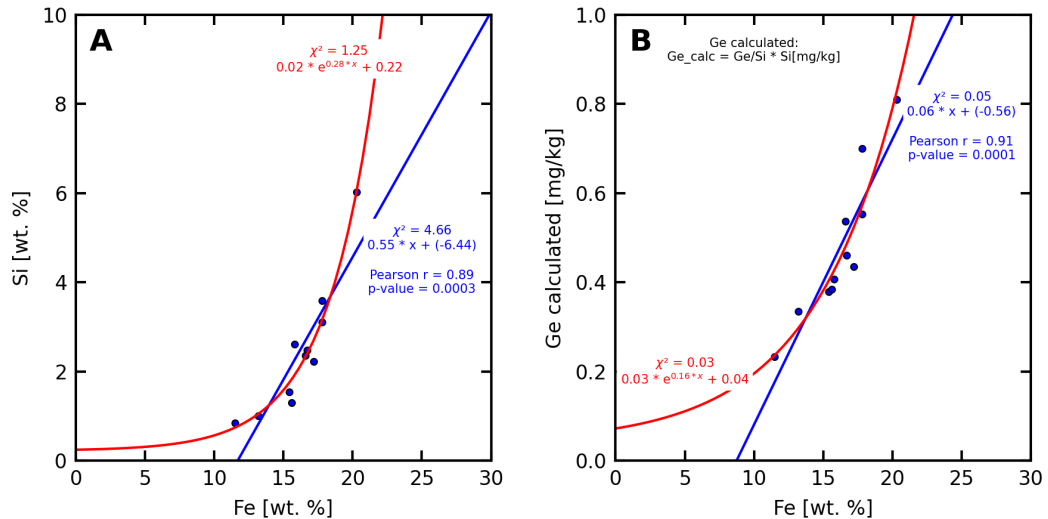


Figure 4.4: A) Graphs of concentrations of Fe vs Si (from Halbach et al., 1990) and B) Fe vs Ge for the SO66 Fe-Mn crusts. Linear regression applied to these samples indicated by the solid blue line together with formula, χ^2 -value, Pearson r value and p -value. Exponential regression applied to these samples indicated by the solid red line together with formula, χ^2 -value. (For interpretation of the references to colour in this figure legend, the reader is referred to the web version of this article.)

indeed, both the Ge and the Si concentrations in the SO66 crusts increase with increasing Fe concentration (Fig. 4.4; note that our data set is too small to decide with confidence whether the positive correlations between Fe and Ge or Si are linear or exponential). This suggests that the Ge and Si concentrations and the Ge/Si ratio of hydrogenetic Fe-Mn crusts are controlled by the Fe (oxy)hydroxides rather than the Mn oxides.

Assuming that the elevated Ge/Si ratios of the SO66 Fe-Mn crusts relative to seawater result from fractionation due to preferential scavenging of Ge by (mostly) the Fe (oxy)hydroxide component of the crusts, the Ge/Si ratios should either (i) increase with decreasing crustal growth rate until an exchange equilibrium between sorbed and dissolved Ge is attained and then remain the same or (ii) it should continuously increase if Ge scavenging occurs via surface-precipitation of Ge. However, as shown in Fig. 4.5, the Ge/Si ratios of the SO66 samples show a linear negative correlation with the Fe concentration (Pearson $r = -0.79$; two-tailed p -value = 0.004). This may suggest the presence of an unknown Fe-poor phase with high Ge/Si ratio, that "dilutes" the Ge/Si signal of the Fe (oxyhydr)oxide component. Inorganic (alumino)silicate detritus was already excluded as a potential mixing phase in Section 4.1 above. However, organic detritus such as radiolarians, diatoms or sponges can also be excluded because they

all show Ge/Si ratios in the range of modern seawater or even somewhat lower (e.g., Tribovillard, 2013; Jochum et al., 2017) and therefore can also be excluded as a solid phase that affects the Ge/Si signal of the bulk Fe-Mn crusts. Unfortunately, our geochemical data does not allow us to conclusively discuss this in any more detail.

Several studies investigated Ge-Si fractionation during continental weathering and Ge-Si behaviour during the formation of secondary silicates/clays (Froelich et al., 1992; Kurtz et al., 2002; Anders et al., 2003; Guillermic et al., 2017). All of these studies showed prominent Ge enrichment in the secondary solid phases (mainly clay minerals) and consistently argue for a preferred sorption of Ge compared to Si onto Fe (oxy)hydroxide or aluminosilicate particles (Mortlock and Froelich, 1987; Kurtz et al., 2002; Pokrovsky et al., 2006). Kurtz et al. (2002) investigated Hawaiian soils which evolved from basalt, and reported increasing Ge enrichment with increasing age of the soils. Rouxel et al. (2006) observed relative Ge enrichment in marine glauconite (an ironbearing phyllosilicate) which showed higher Ge/Si ratios than ambient seawater. All these observations agree with our results on marine hydrogenetic Fe-Mn crusts, pointing towards preferred scavenging of dissolved Ge by solids and preferential retention of Si in solution. However, as indicated by Viers et al. (1997) and Pokrovski and Schott (1998), the enrichment of Ge during soil formation may also be controlled by complexation with organic ligands (especially humic acids) which form stronger chemical complexes with Ge than Si. Pokrovski and Schott (1998), for example, concluded that the relative Ge enrichment in soils is controlled by the preferred sorption of Ge onto Fe (oxy)hydroxides and "organo-mineral colloids". Although only little is known about organic material or biofilms on the surface of hydrogenetic Fe-Mn crusts, it cannot be excluded that the Ge-Si fractionation on Fe-Mn crusts is also affected by Ge interaction with "organo-mineral" surfaces. However, we emphasize that the existence of a uniformly negatively-charged biofilm (Horan and Eccles, 1986; Carlson and Silverstein, 1998) on hydrogenetic Fe-Mn crusts would be in disagreement with the selective distribution of many trace elements between the Fe and the Mn oxides these crusts are comprised of (e.g., Koschinsky and Halbach, 1995; Koschinsky and Hein, 2003). In any case, dissolved organic ligands present in seawater obviously cannot efficiently compete for Ge with functional groups on the surface of Fe-Mn crusts and cannot prevent preferential removal of Ge relative to Si from seawater by hydrogenetic Fe-Mn crusts. Hydrogenetic Fe-Mn crusts, therefore, constitute a marine Ge sink.

A few studies (e.g., Lewis et al., 1988, 1989) have suggested that a relatively large pool of anthropogenic methylated Ge (mGe) exists in the oceans (~ 400 pmol/kg; 2.9×10^{-5} mg/kg), which is often not considered in geochemical studies. However, mGe is

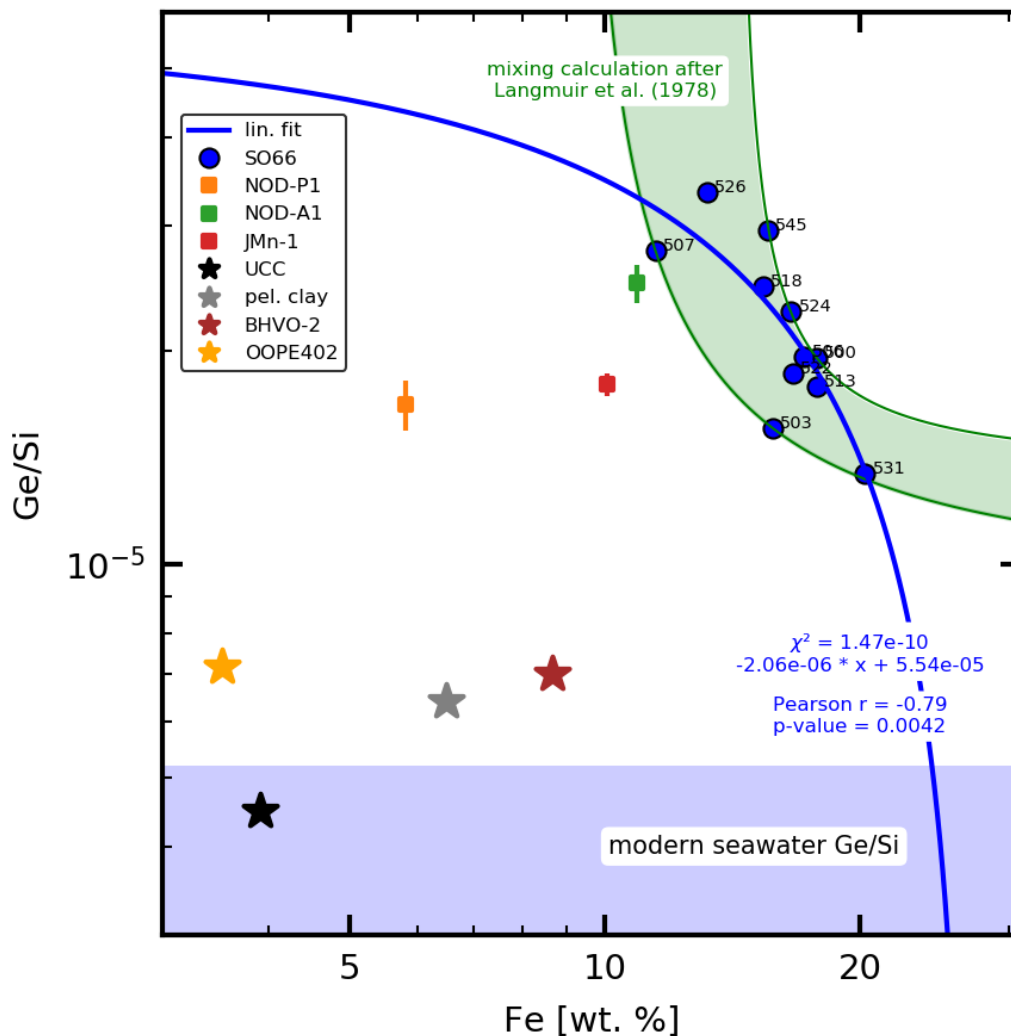


Figure 4.5: Graph of Fe concentration vs average Ge/Si_{wt} ratio for the SO66 Fe-Mn crusts and the Fe-Mn nodule RMs average Ge/Si_{wt} ratios. Linear regression applied to these samples indicated by the solid blue line together with formula, χ^2 -value, Pearson r value and p -value. The green area bracketed by solid green lines points towards possible endmembers, calculated after Langmuir et al. (1978). Reference data: "UCC" (upper continental crust) from Rudnick and Gao (2003); "pel. clay" (pelagic clay) from Li and Schoonmaker (2014); "BHVO-2" (basalt) from Jochum et al. (2017); "OOPE402" (siliceous ooze) from Govindaraju (1994); "modern seawater Ge/Si" from Bruland et al. (2014). (For interpretation of the references to colour in this figure legend, the reader is referred to the web version of this article.)

strongly inert in seawater (Lewis et al., 1988, 1989), suggesting it is no relevant source for the Ge present in Fe-Mn crusts. Considering that these crusts are several millions of years old, any impact of anthropogenic compounds on their bulk composition is a priori very unlikely.

4.5.3 Comparison of Ge-Si and Ga-Al relationships in Fe-Mn crusts

Schier et al. (2021) investigated the fractionation behaviour of Ga and Al during scavenging by Fe-Mn crusts using the same sample set we studied for Ge and Si. A closer comparison of Ga and Ge behaviour may, therefore, provide further evidence for or against a potentially important role of organic ligands for complexation of Ge, Si, Ga and Al in seawater during scavenging by Fe-Mn crusts. Unfortunately, however, straightforward comparison of stability constants of organic Ga and Ge complexes is hampered by the very limited number of ligands for which stability constants for both metals were determined (e.g., Martell and Smith, 1974; 1977; 1982; Smith and Martell, 1975; 1976; 1989). Direct comparison for the $\text{MOHL} + \text{H} \rightarrow \text{ML}$ reaction with EDTA yields stability constants ($\log K$) of 5.64 for Ga and 2.4 for Ge. Hence, Ga forms more stable complexes with EDTA than Ge. If this relationship was typical of organic complexes of Ga and Ge in general, and dissolved organic Ga and Ge complexes controlled the pool of metals available for scavenging onto Fe-Mn crusts, Ge should be enriched in the Fe-Mn crusts compared to Ga. This, however, is the opposite of what is actually observed. Bruland et al. (2014) propose an average $\text{Ga}/\text{Ge}_{\text{wt}}$ ratio of seawater of ~ 0.27 ($\text{Ga}/\text{Ge}_{\text{mol}}$: 0.28; avg. Ga 1.4×10^{-6} mg/kg; avg. Ge 5.1×10^{-6} mg/kg), which is in agreement with results from other studies (e.g., Wheat and McManus, 2008; Guillermic et al., 2017; Whitmore et al., 2020). Schmidt et al. (2017) observed even lower $\text{Ga}/\text{Ge}_{\text{wt}}$ ratios of ~ 0.07 ($\text{Ga}/\text{Ge}_{\text{mol}}$: 0.07) in the western Pacific, possibly linked to the significantly lower Ga concentration in the Pacific as compared to the Atlantic Ocean (for further discussion of inter-oceanic differences see, for example, Schier et al., 2021).

The SO66 Fe-Mn crusts show $\text{Ga}/\text{Ge}_{\text{wt}}$ ratios between 1.64 and 9.23 ($\text{Ga}/\text{Ge}_{\text{mol}}$: 1.72–9.65; Ga data from Schier et al., 2021; Ge data from this study; Fig. 4.6), suggesting an enrichment factor of about 10–100 compared to the oceanic Ga/Ge ratios of Bruland et al. (2014) and Schmidt et al. (2017). Similar behaviour can be observed in the investigated hydrogenetic Fe-Mn nodules (NOD-A1, NOD-P1 and JMn-1). Preferential Ga scavenging relative to Ge by hydrogenetic Fe-Mn crusts and nodules is in disagreement with the assumption that the metal with the stronger affinity for organic ligands (i.e. Ga) is preferentially retained in seawater. This may suggest that Ge and Ga stability constants

with EDTA are not representative of the stability constants of Ge and Ga with organic ligands in the oceans. Alternatively, it may suggest that organic solution-complexation does not control the scavenging behaviour of both Ga and Ge. However, any further in-depth discussion of the marine Ga-Ge systematics has to await Ga and Ge concentration data for seawater from the same sampling locations.

Nevertheless, regardless of the processes that ultimately control Ge scavenging, the Ge-Si couple is, indeed, fractionated by marine Fe (oxyhydr)oxides which preferentially remove Ge from seawater, and hydrogenetic Fe-Mn crusts can be identified as a marine Ge sink.

4.5.4 Are hydrogenetic Fe-Mn crusts an important marine Ge sink?

Due to their very similar geochemical properties, the marine behaviour of Ge and Si are closely related to each other (e.g., Froelich and Andreae, 1981; Froelich et al., 1985; Froelich et al., 1992; Shemesh et al., 1989; Hammond et al., 2000; King et al., 2000; McManus et al., 2003). However, while the mass balance of Si input and output into and out of the oceans are relatively well described and balanced (e.g., Tréguer et al., 2021), there is a missing Ge sink of about 300 t/a (4.1×10^6 mol/a; King et al., 2000). Several studies tried to reconstruct the oceanic Ge cycle and suggested that the excess Ge is sequestered by Fe (oxy)hydroxides in seafloor sediments (e.g., Shemesh et al., 1989; Hammond et al., 2000; King et al., 2000; McManus et al., 2003; Baronas et al., 2017). As shown above, hydrogenetic Fe-Mn crusts remove Ge from seawater and, therefore, one may estimate how significant this specific Ge sink actually is. Using Fe-Mn crust data from Hein et al. (2013, 2017) for seafloor coverage, growth rate and average density, we estimate that an amount of about 24.8×10^6 kg of hydrogenetic Fe-Mn crust material form per year (Eq. (1)):

$$m/a = A * GR * \rho \quad (1)$$

where m/a is the mass of Fe-Mn crust material forming per year, A is the area covered by Fe-Mn crusts (6.35×10^{16} cm²; Hein et al., 2013); GR is the average growth rate (3 mm/Ma) and ρ is the average density (1.3 g/cm³; Hein et al., 2013).

Even at an average Ge concentration of 0.8 mg/kg (which is the maximum Ge concentration observed in our sample set) this suggests that only about 20 kg of Ge per year are removed from seawater by hydrogenetic Fe-Mn crusts. This is surprisingly little, and compared to the missing Ge sink of almost 300,000 kg/a, this amount is negligible and

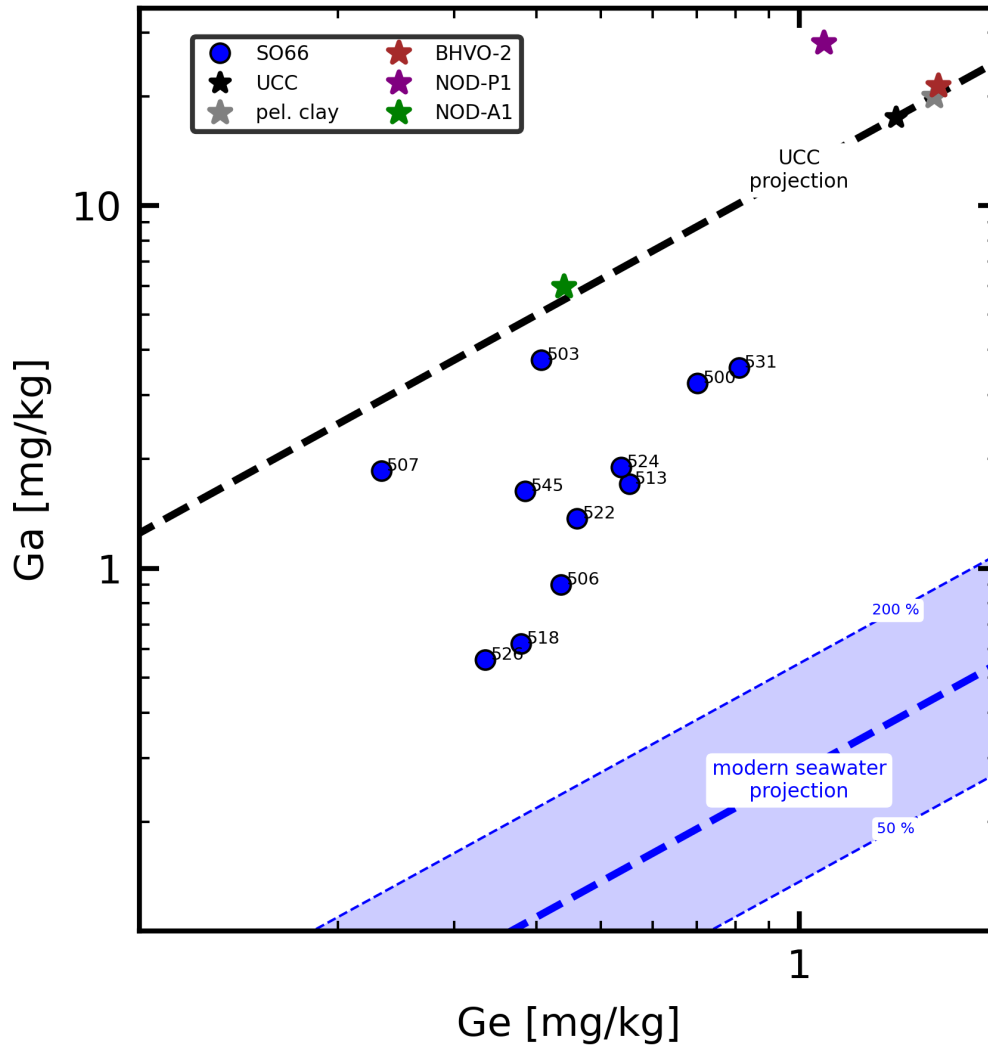


Figure 4.6: Graph of Ge concentration (this study) vs Ga concentration (from Schier et al., 2021, except for NOD-P1) for the SO66 Fe-Mn crusts and the Fe-Mn nodule RMs. The thick dashed blue line indicates the $\text{Ga}/\text{Ge}_{\text{wt}}$ ratio of modern seawater (Bruland et al., 2014) together with the thin dashed blue lines which indicate double avg. seawater $\text{Ga}/\text{Ge}_{\text{wt}}$ and half avg. seawater $\text{Ga}/\text{Ge}_{\text{wt}}$, respectively. The dashed black line indicates the $\text{Ga}/\text{Ge}_{\text{wt}}$ ratio of upper continental crust (UCC from Rudnick and Gao, 2003). Further reference data: "pel. clay" (pelagic clay) from Li and Schoonmaker (2014); "BHVO-2" from Jochum et al. (2017); "NOD-P1" from Scribner et al. (2006) and Axelsson et al. (2002). (For interpretation of the references to colour in this figure legend, the reader is referred to the web version of this article.)

reveals that hydrogenetic Fe-Mn crusts do not represent an important marine Ge sink. Furthermore, their low Ge concentrations also reveal that Fe-Mn crusts do not represent an unconventional resource for the critical metal Ge.

4.6 Conclusion

We here provide for the first time Ge/Si ratios determined by LA-ICP-MS measurements on nano-particulate pellets prepared from marine hydrogenetic Fe-Mn crusts and nodules. Data quality was evaluated and confirmed by comparison of these new data to reference values published for the well-characterized Fe-Mn nodule RM NOD-P1, and attests to the good analytical quality of the results ($\text{Ge/Si}_{\text{wt}} = 16.79 \times 10^{-6}$, $\text{Ge/Si}_{\text{mol}}: 6.47 \times 10^{-6}$; RSDEV of 8.5 % for all 24 conducted measurements). We also report the Ge/Si ratios of Fe-Mn nodule RMs JMn-1 ($\text{Ge/Si} : 17.91 \times 10^{-6}$, $\text{Ge/Si} : 6.90 \times 10^{-6}$) from the southern Central Pacific and NOD-A1 ($\text{Ge/Si}_{\text{wt}}: 24.89 \times 10^{-6}$, $\text{Ge/Si}_{\text{mol}}: 9.59 \times 10^{-6}$) from the Atlantic Ocean. While our results suggest that there may be an inter-oceanic difference between Fe-Mn nodules from the Atlantic (NOD-A1) and the Pacific (NOD-P1 and JMn-1), this needs to be confirmed by additional data. However, the observed difference between the Ge/Si ratios of the Fe-Mn nodules ($(\text{Ge/Si}_{\text{JMn-1}}) / (\text{Ge/Si}_{\text{NOD-A1}}) = 0.7$) is similar to that of the difference between Atlantic and Pacific seawater ($(\text{Ge/Si}_{\text{Atlantic}}) / (\text{Ge/Si}_{\text{Pacific}}) = 0.7\text{--}0.8$) as reported by Sutton et al. (2010).

All hydrogenetic Fe-Mn crusts from cruise SO66 discussed here show elevated Ge/Si ratios ($\text{Ge/Si}_{\text{wt}}: 13.2 \times 10^{-6}\text{--}33.5 \times 10^{-6}$, $\text{Ge/Si}_{\text{mol}}: 5.1 \times 10^{-6}\text{--}12.9 \times 10^{-6}$) compared to modern seawater (ca. $\text{Ge/Si}_{\text{wt}}: 1.7 \times 10^{-6}$, $\text{Ge/Si}_{\text{mol}}: 0.7 \times 10^{-6}$) and potential detritus ($\text{Ge/Si}_{\text{wt}}: 2.2 \times 10^{-6}\text{--}7.0 \times 10^{-6}$, $\text{Ge/Si}_{\text{mol}}: 0.9 \times 10^{-6}\text{--}2.7 \times 10^{-6}$). This rules out any possibility that the high Ge/Si ratios observed result from the presence of a detrital component in the Fe-Mn crusts. Therefore, the measured Ge/Si ratios result from the fractionation of Ge and Si during the formation of hydrogenetic Fe-Mn crusts. Indicated by positive correlations, Ge and Si are associated with the Fe-(oxy)hydroxide phase in the Fe-Mn crusts. This observation is in agreement with the proposed electrostatic model by Koschinsky and Halbach (1995).

Ferromanganese crusts and nodules show elevated Ge/Si ratios in spite of the fact that organic ligands preferably complex Ge relative to Si. This indicates that preferential retention of Ge over Si by organic ligands in seawater cannot prevent its preferential scavenging by Fe (oxy)hydroxides and/or suggests that the amount of organically complexed Ge in seawater is too small to strongly affect Ge-Si behaviour.

Although Fe-Mn crusts remove Ge from seawater, currently available data for their Ge concentrations, growth rates and abundance suggest that hydrogenetic Fe-Mn crusts cannot account for the "missing Ge sink" in seawater. Moreover, at the rather low concentrations of Ge observed in hydrogenetic Fe-Mn crust and nodules, it appears to be very unlikely that such crusts may become an unconventional source of this critical metal in the foreseeable future.

4.7 Declaration of Competing Interest

The authors declare that they have no known competing financial interests or personal relationships that could have appeared to influence the work reported in this paper.

4.8 Acknowledgements

We are grateful to Samuel Müller and Ulrike Westernströer (both CAU Kiel University) who helped with the production of the pressed powder pellets and the operation of the high-resolution LA-ICP-MS, respectively. We acknowledge the many fruitful discussions with colleagues in DFG Priority Program SPP-1833 and appreciate funding from the Deutsche Forschungsgemeinschaft (grant BA-2289/8-1). The reviews of two anonymous reviewers are greatly appreciated and substantially improved the manuscript. Further, Karen Johannesson is gratefully acknowledged for all editorial handling.

4.9 Appendix A. Supplementary data

Supplementary data to this article can be found online at <https://doi.org/10.1016/j.chemgeo.2022.120791>.

4.9.1 Supplementary figures

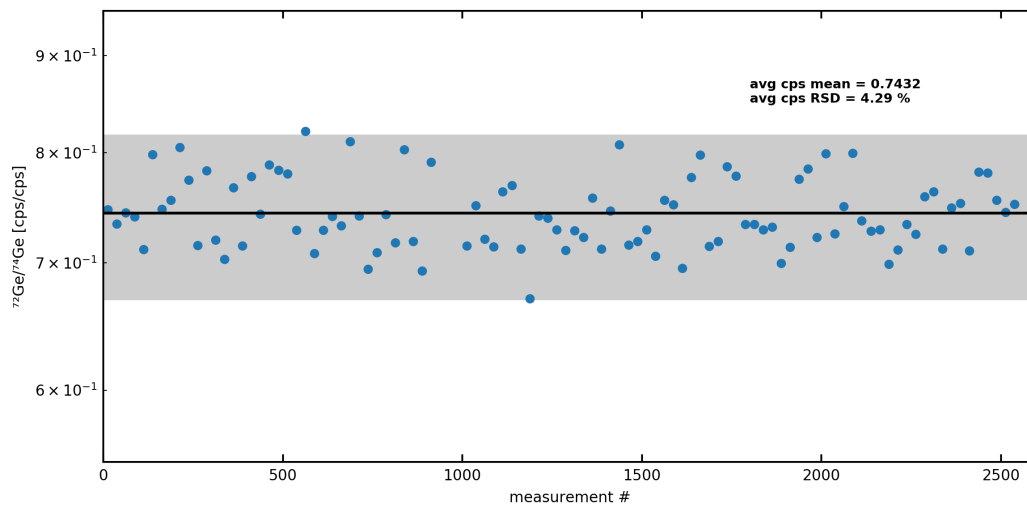


Figure 4.7: Raw data $^{72}\text{Ge}/^{74}\text{Ge}$ ratios of all single measurements. Indicated by the black line: the natural abundance ratio of $^{72}\text{Ge}/^{74}\text{Ge}$ after Anders and Grevesse (1989). The grey bar around the black line indicates $\pm 10\%$ of the natural abundance $^{72}\text{Ge}/^{74}\text{Ge}$ ratio. The blue markers are the average counts/s of each single sample used for evaluation of the final Ge/Si ratios.

4.9.2 Supplementary tables

Table 4.3: Measured Ge/Si ratios for the RMs NOD-P1, NOD-A1 and JMn-1. ^{72}Ge and ^{74}Ge indicate which isotope was used for the data evaluation.

Sample	Meas. #	Ge/Si x 10 ⁶		AVG Ge/Si x 10 ⁶		RSDEV [%]		AVG Ge/Si x 10 ⁶ combined	RSDEV [%] combined
		^{72}Ge	^{74}Ge	^{72}Ge	^{74}Ge	^{72}Ge	^{74}Ge		
NOD-P1	1	14.3	13.7	16.8	16.8	7.8	9.1	16.8	8.4
	2	16.8	18.7						
	3	19.5	18.1						
	4	15.6	16.0						
	5	17.0	16.8						
	6	17.3	17.7						
	7	15.3	14.1						
	8	17.9	18.1						
	9	17.4	18.3						
	10	16.0	16.9						
	11	17.6	17.1						
	12	16.6	16.4						
NOD-A1	1	28.7	28.1	25.1	24.7	6.9	5.9	24.9	6.5
	2	25.1	24.5						
	3	27.1	24.9						
	4	22.3	22.8						
	5	24.7	23.7						
	6	23.6	22.7						
	7	25.6	25.3						
	8	26.6	24.7						
	9	26.2	26.6						
	10	23.4	24.8						
	11	23.9	24.0						
	12	24.0	24.0						
JMn-1	1	19.4	19.4	17.9	18.0	4.3	4.6	17.9	4.5
	2	16.9	18.8						
	3	17.7	17.7						
	4	17.6	17.6						
	5	17.5	17.1						
	6	18.0	17.3						

4.10 References

- Aguirre, A.A., Derry, L.A., Mills, T.J., Anderson, S.P., 2017. Colloidal transport in the Gordon Gulch catchment of the Boulder Creek CZO and its effect on C-Q relationships for silicon. *Water Resour. Res.* 53, 2368–2383.
- Alexander, B.W., 2008. Trace Element Analyses in Geological Materials using Low Resolution Inductively Coupled Plasma Mass Spectrometry (ICPMS) Technical Report No. 18.
- Ameijeiras-Mariño, Yolanda, Opfergelt, Sophie, Derry, Louis A., Robinet, Jérémy, Govers, Gerard, Minella, Jean P.G., Delmelle, Pierre, September 2018. Ge/Si ratios point to increased contribution from deeper mineral weathering to streams after forest conversion to cropland. *Appl. Geochem.* 96, 24–34. [://doi.org/10.1016/j.apgeochem.2018.06.002](https://doi.org/10.1016/j.apgeochem.2018.06.002).
- Anders, E., Grevesse, N., 1989. Abundances of elements: Meteoritic and solar. *Geochim. Cosmochim. Acta* 53, 197–214.
- Anders, A.M., Sletten, R.S., Derry, L.A., Hallet, B., 2003. Germanium/silicon ratios in the Copper River Basin, Alaska: Weathering and partitioning in periglacial versus glacial environments. *J. Geophys. Res.* 108.
- Anderson, P.R., Benjamin, M.M., 1985. Effect of silicon on the crystallization and adsorption properties of ferric oxides. *Environ. Sci. Technol.* 19, 1048–1053.
- Axelsson, M.D., Rodushkin, I., Ingri, J., Öhlander, B., 2002. Multielemental analysis of Mn-Fe nodules by ICP-MS: Optimisation of analytical method. *Analyst* 127, 76–82.
- Baronas, J.J., Hammond, D.E., McManus, J., Wheat, C.G., Siebert, C., 2017. A global Ge isotope budget. *Geochim. Cosmochim. Acta* 203, 265–283.
- Bau, M., 1996. Controls on the fractionation of isovalent trace elements in magmatic and aqueous systems: evidence from Y/Ho, Zr/Hf, and lanthanide tetrad effect. *Contrib. Mineral. Petrol.* 123, 323–333.
- Bau, M., Koschinsky, A., 2009. Oxidative scavenging of cerium on hydrous Fe oxide: evidence from the distribution of rare earth elements and yttrium between Fe oxides and Mn oxides in hydrogenetic ferromanganese crusts. *Geochem. J.* 43, 37–47.
- Bau, M., Koschinsky, A., Dulski, P., Hein, J.R., 1996. Comparison of the partitioning behaviours of yttrium, rare earth elements, and titanium between hydrogenetic marine ferromanganese crusts and seawater. *Geochim. Cosmochim. Acta* 60, 1709–1725.
- Bau, M., Schmidt, K., Koschinsky, A., Hein, J., Kuhn, T., Usui, A., 2014. Discriminating between different genetic types of marine ferro-manganese crusts and nodules based on rare earth elements and yttrium. *Chem. Geol.* 9.
- Bernstein, L.R., 1985. Germanium geochemistry and mineralogy. *Geochim. Cosmochim. Acta* 49 (11), 2409–2422. [https://doi.org/10.1016/0016-7037\(85\)90241-8](https://doi.org/10.1016/0016-7037(85)90241-8).
- Biscaye, P.E., 1965. Mineralogy and Sedimentation of recent Deep-Sea Clay in the Atlantic Ocean and Adjacent Seas and Oceans. *Geol. Soc. Am. Bull.* 76, 803–832.
- Bruland, K.W., Middag, R., Lohan, M.C., 2014. Controls of Trace Metals in Seawater. In: *Treatise on Geochemistry*, Second edition. Elsevier Ltd, pp. 19–51. Available at: <https://doi.org/10.1016/B978-0-08-095975-7.00602-1>.

- Byrne, R.H., 2002. Inorganic speciation of dissolved elements in seawater: the influence of pH on concentration ratios. *Geochem. Trans.* 3, 11–16.
- Carlson, G., Silverstein, J., 1998. Effect of molecular size and charge on biofilm sorption of organic matter. *Water Res.* 32, 1580–1592.
- De Carlo, E.H., McMurtry, G.M., 1992. Rare-earth element geochemistry of ferromanganese crusts from the Hawaiian Archipelago, Central Pacific. *Chem. Geol.* 95, 235–250.
- Escoube, R., Rouxel, O.J., Edwards, K., Glazer, B., Donard, O.F.X., 2015. Coupled Ge/Si and Ge isotope ratios as geochemical tracers of seafloor hydrothermal systems: Case studies at Loihi Seamount and East Pacific rise 9°50'N. *Geochim. Cosmochim. Acta* 167, 93–112.
- Froelich, P.N., Andreae, M.O., 1981. The marine geochemistry of germanium: Ekasilicon. *Science* 213 (4504), 205–207.
- Froelich, P.N., Hambrick, G.A., Andreae, M.O., Mortlock, R.A., 1985. The geochemistry of inorganic germanium. *J. Geophys. Res.* 90, 1133–1141.
- Froelich, P.N., Blanc, V., Mortlock, R.A., Chillrud, S.N., Dunstan, W., Udomkit, A., Peng, T.-H., 1992. River fluxes of dissolved silica to the ocean where higher during glacials: Ge/Si in diatoms, rivers and oceans. *Palaeoceanography* 7 (6), 739–767.
- Garbe-Schönberg, D., Müller, S., 2014. Nano-particulate pressed powder tablets for LAICP-MS. *J. Anal. At. Spectrom.* 29, 990–1000.
- Goldschmidt, M., 1958. *Geochemistry*. Oxford University Press, London, pp. 377–390.
- Govindaraju, K., 1994. 1994 COMPILATION OF WORKING VALUES AND SAMPLE DESCRIPTION FOR 383 GEOSTANDARDS. *Geostand. Geoanal. Res.* 18, 1–158.
- Guillermic, M., Lalonde, S.V., Hendry, K.R., Rouxel, O.J., 2017. The isotope composition of inorganic germanium in seawater and deep-sea sponges. *Geochim. Cosmochim. Acta* 212, 99–118.
- Halbach, P., Koschinsky, A., Sattler, C.-D., Teichmann, F., Wahsner, M., Scho öps, D., Post, J., Hansen, D., Dreßen, P., Bubilek, S., 1990. Technical cruise Report Midpac 4 (SO66): Geoscientific investigations and economic evaluation of Co-rich and Pt-bearing crust deposits in the seamount areas of the Central Pacific south of the equator (Kiribati and Tuvalu) and of massive sulfide occurrences in the North Fiji Basin (Fiji). FS SONNE 1989/90. Technical University of Clausthal, Clausthal-Zellerfeld. Available at: <http://oceanrep.geomar.de/id/eprint/19102>.
- Hammond, D.E., McManus, J., Berelson, W.M., 2004. Oceanic germanium/silicon ratios: Evaluation of the potential overprint of temperature on weathering signals. *Palaeoceanography* 19, 1–11.
- Hammond, D.E., McManus, J., Berelson, W.M., Meredith, C., Klinkhammer, G.P., Coale, K.H., 2000. Diagenetic fractionation of Ge and Si in reducing sediments: the missing Ge sink and a possible mechanism to cause glacial/interglacial variations in oceanic Ge/Si. *Geochim. Cosmochim. Acta* 64, 2453–2465.
- Hansen, H.C.B., Wetche, T.P., Raulund-Rasmussen, K., Borggaard, O.K., 1994. Stability constants for silicate adsorbed to ferrihydrite. *Clay Miner.* 29, 341–350.

- Hein, J.R., Koschinsky, A., 2013. Deep-ocean ferromanganese crusts and nodules. In: Treatise on Geochemistry, Second edition. Published by Elsevier Inc, pp. 273–291. Available at: <https://doi.org/10.1016/B978-0-08-095975-7.01111-6>.
- Hein, J.R., Koschinsky, A., Bau, M., Manheim, F.T., Kang, J.-K., Roberts, L., 2000. Cobalt-rich ferromanganese crusts in the Pacific. In: Cronan, D.S. (Ed.), Handbook of Marine Mineral Deposits. CRC Press, Boca Raton, Florida, pp. 239–279.
- Hein, J.R., Mizell, K., Koschinsky, A., Conrad, T.A., 2013. Deep-ocean mineral deposits as a source of critical metals for high and green-technology applications: Comparison with land-based resources. *Ore Geol. Rev.* 51, 1–14.
- Hein, J.R., Konstantinova, N., Mikesell, M., Mizell, K., Fitzsimmons, J.N., Lam, P.J., Jensen, L.T., Xiang, Y., Gartman, A., Cherkashov, G., Hutchinson, D.R., Till, C.P., 2017. Arctic deep water ferromanganese-oxide deposits reflect the unique characteristics of the Arctic Ocean. *Geochem. Geophys. Geosyst.* 18, 3771–3800.
- Horan, N.J., Eccles, C.R., 1986. Purification and characterization of extracellular polysaccharide from activated sludges. *Water Res.* 20, 1427–1432.
- Imai, N., Terashima, S., Itoh, S., Ando, A., 1999. 1998 compilation of analytical data for five GSJ geochemical reference samples: the "Instrumental Analysis Series". *Geostand. Geoanal. Res.* 23, 223–250.
- Jochum, K.P., Schuessler, J.A., Wang, X.-H., Stoll, B., Weis, U., Müller, W.E.G., Haug, G. H., Andreae, M.O., Froelich, P.N., 2017. Whole-Ocean changes in silica and Ge/Si ratios during the last deglacial deduced from long-lived giant glass sponges. *Geophys. Res. Lett.* 44, 11,555–11,564.
- Josso, P., Pelleter, E., Pourret, O., Fouquet, Y., Etoubleau, J., Cheron, S., Bollinger, C., 2017. A new discrimination scheme for oceanic ferromanganese deposits using high field strength and rare earth elements. *Ore Geol. Rev.* 87, 3–15.
- King, S.L., Froelich, P.N., Jahnke, R.A., 2000. Early diagenesis of germanium in sediments of the Antarctic South Atlantic: in search of the missing Ge sink. *Geochim. Cosmochim. Acta* 64, 1375–1390.
- Koschinsky, A., Halbach, P., 1995. Sequential leaching of marine ferromanganese precipitates: Genetic implications. *Geochim. Cosmochim. Acta* 59, 5113–5132.
- Koschinsky, A., Hein, J.R., 2003. Uptake of elements from seawater by ferromanganese crusts: solid-phase associations and seawater speciation. *Mar. Geol.* 198, 331–351.
- Koschinsky, A., Heinrich, L., Boehnke, K., Cohrs, J.C., Markus, T., Shani, M., Singh, P., Smith, Stegen K., Werner, W., 2018. Deep-sea mining: Interdisciplinary research on potential environmental, legal, economic, and societal implications: Interdisciplinary Review of Deep-sea Mining Impacts. *Integr. Environ. Assess. Manag.* 14, 672–691.
- Koschinsky, A., Hein, J.R., Kraemer, D., Foster, A.L., Kuhn, T., Halbach, P., 2020. Platinum enrichment and phase associations in marine ferromanganese crusts and nodules based on a multi-method approach. *Chem. Geol.* 539, 119426.
- Kurtz, A.C., Derry, L.A., Chadwick, O.A., 2002. Germanium–silicon fractionation in the weathering environment. *Geochim. Cosmochim. Acta* 66 (9), 1525–1537.
- Langmuir, C.H., Vocke, R.D., Hanson, G.N., Hart, S.R., 1978. A General Mixing Equation with Applications to Icelandic Basalts, pp. 380–392.

- Lewis, Brent L., Andreae, Meinrat O., Froelich, Philip N., Mortlock, Richard A., 1988. A review of the biogeochemistry of germanium in natural waters. *Sci. Total Environ.* 73 (Nr. 1–2), 107–120. [https://doi.org/10.1016/0048-9697\(88\)90191-X](https://doi.org/10.1016/0048-9697(88)90191-X).
- Lewis, Brent L., Andreae, Meinrat O., Froelich, Philip N., 1989. Sources and sinks of methylgermanium in natural waters. *Mar. Chem.* 27 (Nr. 3–4), 179–200. [https://doi.org/10.1016/0304-4203\(89\)90047-9](https://doi.org/10.1016/0304-4203(89)90047-9).
- Li, Y.-H., 1991. Distribution patterns of the elements in the ocean: a synthesis. *Geochim. Cosmochim. Acta* 55, 3223–3240.
- Li, Y.-H., Schoonmaker, J.E., 2014. Chemical composition and mineralogy of marine sediments. In: *Treatise on Geochemistry, Second edition*. Elsevier Ltd, pp. 1–32. Available at: <https://doi.org/10.1016/B978-0-08-095975-7.00701-4>.
- Lusty, P.A.J., Hein, J.R., Josso, P., 2018. Formation and occurrence of ferromanganese crusts: Earth's Storehouse for critical metals. *Elements* 14, 313–318. Available at: <https://pubs.geoscienceworld.org/msa/elements/article/14/5/313/559108/Formation-and-Occurrence-of-Ferromanganese-Crusts>.
- Martell E., Arthur, Smith M., Robert, 1974. *Critical Stability Constants Volume 1: Amino Acids*. Plenum Press, New York.
- Martell E., Arthur, Smith M., Robert, 1977. *Critical Stability Constants Volume 3: Other Organic Ligands*. Plenum Press, New York.
- Martell E., Arthur, Smith M., Robert, 1982. *Critical Stability Constants Volume 5: First Supplement*. Plenum Press, New York.
- Martin, F., Ildefonse, P., Hazemann, J.-L., Petit, S., Grauby, O., Decarreau, A., 1996. Random distribution of Ge and Si in synthetic talc: an EXAFS and FTIR study. *Eur. J. Mineral.* 8, 289–300.
- McLennan, S.M., 1989a. In: Lipin, B.R., McKay, G.A. (Eds.), *Geochemistry and Mineralogy of Rare Earth Elements*, 21. *Rev. Miner.*, pp. 169–200.
- McLennan, S.M., 1989b. Rare Earth Elements in Sedimentary Rocks: Influence of Provenance and Sedimentary Processes. In: Lipin, B.R., McKay, G.A. (Eds.), *Geochemistry and mineralogy of rare earth elements*. Mineralogical Society of America *Reviews in Mineralogy*, pp. 169–200.
- McManus, J., Hammond, D.E., Cummins, K., Klinkhammer, G.P., Berelson, W.M., 2003. Diagenetic Ge-Si fractionation in continental margin environments: Further evidence for a nonopal Ge sink. *Geochim. Cosmochim. Acta* 67, 4545–4557.
- Mizell, K., Hein, J.R., Lam, P.J., Koppers, A.A.P., Staudigel, H., 2020. Geographic and oceanographic influences on ferromanganese crust composition along a Pacific Ocean meridional transect, 14N to 14S. *Geochem. Geophys. Geosyst.* 1–19.
- Mohwinkel, D., Kleint, C., Koschinsky, A., 2014. Phase associations and potential selective extraction methods for selected high-tech metals from ferromanganese nodules and crusts with siderophores. *Appl. Geochem.* 43, 13–21.
- Mortlock, R.A., Froelich, P.N., 1987. Continental weathering of germanium: Ge Si in the global river discharge. *Geochim. Cosmochim. Acta* 51 (8), 2075–2082. [https://doi.org/10.1016/0016-7037\(87\)90257-2](https://doi.org/10.1016/0016-7037(87)90257-2).
- Mortlock, R.A., Froelich, P.N., Feely, R.A., Massoth, G.J., Butterfield, D.A., Lupton, J.E., 1993. Silica and germanium in Pacific Ocean hydrothermal vents and plumes. *Earth*

- Planet. Sci. Lett. 119 (3), 365–378. [https://doi.org/10.1016/0012-821X\(93\)90144X](https://doi.org/10.1016/0012-821X(93)90144X).
- Murnane, R.J., Stallard, R.F., 1990. Germanium and silicon in rivers of the Orinoco drainage basin. *Nature* 344, 749–752.
- Murray, J., Renard, A.F., 1891. *Deep-Sea Deposits Based on the Specimens Collected during the Voyage of HMS Challenger in the Years 1872 to 1876*. John Menzies and Co., Edinburgh, United Kingdom. <http://www.vliz.be/nl/open-marien-archief?module=ref&refid=41584>.
- Pokrovski, G.S., Schott, J., 1998. Experimental study of the complexation of silicon and germanium with aqueous organic species: Implications for germanium and silicon transport and Ge/Si ratio in natural waters. *Geochim. Cosmochim. Acta* 62 (21-22), 3413–3428. [https://doi.org/10.1016/s0016-7037\(98\)00249-x](https://doi.org/10.1016/s0016-7037(98)00249-x).
- Pokrovsky, O.S., Pokrovski, G.S., Schott, J., Galy, A., 2006. Experimental study of germanium adsorption on goethite and germanium coprecipitation with iron hydroxide: X-ray absorption fine structure and macroscopic characterization. *Geochim. Cosmochim. Acta* 70, 3325–3341.
- Rouxel, O., Galy, A., Elderfield, H., 2006. Germanium isotopic variations in igneous rocks and marine sediments. *Geochim. Cosmochim. Acta* 70 (13), 3387–3400. <https://doi.org/10.1016/j.gca.2006.04.025>.
- Rudnick, R.L., Gao, S., 2003. Composition of the Continental Crust. *Treat. Geochem.* 3, 1–64.
- Savenko, A.V., Volkov, I.I., 2003. On the abiogenic precipitation of silica in the modern ocean. In: *Geochemistry International* No. 6, pp. 676–680.
- Schier, K., Ernst, D.M., Cordeiro, Moreno, de Sousa, I., Garbe-Schönberg, D., Kuhn, T., Hein, J.R., Bau, M., 2021. Gallium-Aluminum systematics of marine hydrogenetic ferromanganese crusts: Inter-oceanic differences and fractionation during scavenging. *Geochim. Cosmochim. Acta* 310, 187–204.
- Schmidt, K., Bau, M., Hein, J.R., Koschinsky, A., 2014. Fractionation of the geochemical twins Zr-Hf and Nb-Ta during scavenging from seawater by hydrogenetic ferromanganese crusts. *Geochim. Cosmochim. Acta* 140, 468–487. Available at: <https://doi.org/10.1016/j.gca.2014.05.036>.
- Schmidt, K., Garbe-Schönberg, D., Hannington, M.D., Anderson, M.O., Bühring, B., Haase, K., Haruel, C., Lupton, J., Koschinsky, A., 2017. Boiling vapour-type fluids from the Nifonea vent field (New Hebrides Back-Arc, Vanuatu, SW Pacific): Geochemistry of an early-stage, post-eruptive hydrothermal system. *Geochim. Cosmochim. Acta* 207, 185–209.
- Schwertmann, U., Fechter, H., 1982. The point of zero charge of natural and synthetic ferrihydrites and its relation to adsorbed silicate. *Clay Miner.* 17, 471–476.
- Scribner, A.M., Kurtz, A.C., Chadwick, O.A., 2006. Germanium sequestration by soil: Targeting the roles of secondary clays and Fe-oxyhydroxides. *Earth Planet. Sci. Lett.* 243, 760–770.
- Shemesh, A., Mortlock, R.A., Froelich, P.N., 1989. Late Cenozoic Ge/Si record of marine biogenic opal: Implications for variations of riverine fluxes to the ocean. *Palaeoceanography* 4, 221–234.

- Smith, D.B., 1995. USGS Certificate of Analysis Manganese Nodules. NOD-P1. USGS.
- Smith M., Robert, Martell E., Arthur, 1975. *Critical Stability Constants Volume 2: Amines*. Plenum Press, New York.
- Smith M., Robert, Martell E., Arthur, 1976. *Critical Stability Constants Volume 4: Inorganic Complexes*. Plenum Press, New York.
- Smith M., Robert, Martell E., Arthur, 1989. *Critical Stability Constants Volume 6: Second Supplement*. Plenum Press, New York.
- Sutton, J., Ellwood, M.J., Maher, W.A., Croot, P.L., 2010. Oceanic distribution of inorganic germanium relative to silicon: germanium discrimination by diatoms. *Glob. Biogeochem. Cycles* 24, 13.
- Taylor, P., 1995. *Interactions of Silica with Iron Oxides: Effects on Oxide Transformations and Sorption Properties*. Whiteshell Laboratories, Pinawa, Manitoba, Canada.
- Terashima, S., Usui, A., Imai, N., 1995. Two New GSJ Geochemical Reference Samples: Syenite JSy-1 and Manganese Nodule JMn-1. *Geostand. Geoanal. Res.* 19, 221–229.
- Tréguer, P.J., De La Rocha, C.L., 2013. *The World Ocean Silica Cycle*. *Annu. Rev. Mar. Sci.* 5, 477–501.
- Tréguer, P.J., Sutton, J.N., Brzezinski, M., Charette, M.A., Devries, T., Dutkiewicz, S., Ehlert, C., Hawkings, J., Leynaert, A., Liu, S.M., Llopis, Monferrer N., Lo pezAcosta, M., Maldonado, M., Rahman, S., Ran, L., Rouxel, O., 2021. Reviews and syntheses: the biogeochemical cycle of silicon in the modern ocean. *Biogeosciences* 18, 1269–1289.
- Tribovillard, N., 2013. The Ge/Si ratio as a tool to recognize biogenic silica in chert. *Compt. Rendus Geosci.* 345, 160–165.
- Viers, J., Dupré, B., Polvé, M., Schott, J., Dandurand, J.-L., Braun, J.-J., 1997. Chemical weathering in the drainage basin of a tropical watershed (Nsimi-Zoetele site, Cameroon): comparison between organic-poor and organic-rich waters. *Chem. Geol.* 140, 181–206.
- Wheat, C.G., McManus, J., 2008. Germanium in mid-ocean ridge flank hydrothermal fluids: GERMANIUM IN RIDGE FLANK FLUIDS. *Geochem. Geophys. Geosyst.* 9, 16.
- Whitmore, L.M., Pasqualini, A., Newton, R., Shiller, A.M., 2020. Gallium: a new tracer of pacific water in the Arctic Ocean. *J. Geophys. Res. Oceans* 125.

Banded iron formation from Antarctica: The 2.5 Ga
old Mt. Ruker BIF and the antiquity of lanthanide
tetrad effect and super-chondritic Y/Ho ratio in
seawater

David M. Ernst*, Michael Bau

*Department of Physics and Earth Sciences, Jacobs University Bremen, Campus Ring 1,
28759 Bremen, Germany*

published in

Gondwana Research

Gondwana Research 91 (2021) 97–111

** Corresponding author. Email adress: d.ernst@jacobs-university.de (D. M. Ernst)*

<https://doi.org/10.1016/j.gr.2020.11.011>

1342-937X/© 2020 International Association for Gondwana Research. Published by Elsevier B.V. All rights reserved.

5 Geochemical study on the 2.5 Ga Mt. Ruker BIF (East Antarctica) — REY as seawater proxies

5.1 Abstract

Here we report the first detailed geochemical data for Banded Iron-Formation (BIF) from Antarctica. Micro drill cores were taken from adjacent magnetite/haematite and metachert bands from the 2.5 Ga old Mt. Ruker BIF, Prince Charles Mountains, East Antarctica. Low concentrations of Al, Zr, Hf, and Sc reveal the purity of the samples. The chemical composition matches closely that of other early Precambrian BIF, except for an enrichment of Ni, and high Ba/Sr ratios in the metachert. Shale-normalized Rare Earths and Yttrium (REY_{SN}) patterns show all the features of modern seawater such as depletion of light vs heavy REY_{SN} , positive anomalies of La_{SN} , Gd_{SN} , and Y_{SN} (i.e. super-chondritic Y/Ho ratios) and the W-type lanthanide tetrad effect (LTE), but positive Eu_{SN} and no Ce_{SN} anomalies (and no positive Eu anomalies in chondrite-normalized REY patterns). This distribution is fully compatible with that of other pure Early Precambrian BIFs, suggesting high-temperature hydrothermal input of REY into seawater and a redox level of the atmosphere-hydrosphere system too reducing for Ce oxidation. The uniform, super-chondritic Y/Ho ratios in adjacent iron-oxide and metachert BIF bands most strongly suggest that the conspicuous banding does not result from post-depositional separation of an initially homogenous Fe-silicate precipitate, but argues for a primary origin of the banding. The super-chondritic Y/Ho ratios fit well within the range reported for other BIF worldwide, corroborating that positive Y anomalies, although possibly of smaller size than today, have always been a characteristic feature of seawater. The Mt. Ruker BIF further complements the set of Early Precambrian marine chemical sediments in which the W-type LTE has been observed, and demonstrates the antiquity of the LTE in seawater. These subtle features reveal that the distribution of the redox-insensitive

REY in seawater did not change significantly over the almost 4 billion years geological record of seawater. The super-chondritic Y/Ho ratios and W-type LTE in this and other oxide-facies BIF are in marked contrast to the REY distribution in Modern and Cenozoic oxidic hydrogenetic ferromanganese crusts, pointing towards fundamentally different removal mechanisms of REY from Modern vs Early Precambrian seawater.

5.2 Introduction

Precambrian marine chemical sedimentary rocks such as (Banded) Iron-Formations, (B)IF, are of great interest for palaeoenvironmental studies, as they are geological archives for geochemical proxies that provide information on the evolution of the atmosphere-hydrosphere system (e.g., Smith, 2007; Alibert and Kinsley, 2016; Haugaard et al., 2016; Viehmann et al., 2018). Banded Iron-Formations are layered sedimentary rocks comprising of alternating Fe-rich and Si-rich bands of varying thickness (sub-mm to dm). In the traditional classification scheme (James (1954), Fe-rich layers in oxide-facies BIF mainly contain haematite and/or magnetite, while Si-rich bands are predominantly composed of (sometimes ferruginous) chert or quartz. The BIF formed in marine environments throughout the Archaean and Early Proterozoic and during a short period in the Neoproterozoic (e.g., Klein, 2005; Konhauser et al., 2017). However, only a small fraction of these BIF are preserved in the geological record and accessible today in the Early Precambrian cratons. Although many BIF are located in rather remote regions, a wealth of geochemical trace element and isotope data are available for BIF from all continents with the exception of Antarctica. To fill this gap, we here report the results of a pilot study and present the first data set for rare earth elements (REE) and other trace elements in a BIF from Antarctica: The ca. 2.5 Ga old (Phillips et al., 2006) Mt. Ruker BIF which crops out in the Ruker Terrane of the Prince Charles Mountains on the East Antarctic Craton (Kamenev et al., 1993). The Mt. Ruker BIF formed during the transition from the Archaean to the Proterozoic, i.e. during the same period when the large and rather well-studied Superior-type BIFs of the Mt. Bruce and Transvaal supergroups formed on the Pilbara Craton in Western Australia and on the Kaapvaal Craton in South Africa, respectively (Beukes and Gutzmer, 2008). To investigate the chemical composition of adjacent Fe and Si-rich bands, we studied micro drill cores from individual BIF bands.

The distribution of the rare earths and yttrium (REY) in BIF is a well-established proxy in the investigation of BIF (e.g., Fryer, 1977; Danielson et al., 1992; Bau and

Möller, 1993; Bau and Dulski, 1996; Alexander et al., 2008; Viehmann et al., 2015a, 2015b; Alibert, 2016). The REY behave very coherently in natural systems due to their same charge and similar ionic radii which slightly decrease from the light REY (LREY) to the heavy REY (HREY). All REY are exclusively trivalent, except for Ce which can be oxidized to Ce^{4+} in oxic low-temperature systems, and Eu which can be reduced to Eu^{2+} in reducing high-temperature systems. The redox-related fractionation of Ce or Eu from their REY neighbours is commonly used as a geochemical proxy for element sources and redox-conditions (Derry and Jacobsen, 1990; Bau and Möller, 1993; Bau and Dulski, 1996; Webb and Kamber, 2000; Bolhar et al., 2004; Alexander et al., 2008; Viehmann et al., 2015a, 2015b, 2016). For a comprehensive consideration and interpretation of REY behaviour in geochemical samples, the REY are usually normalized either to C1-chondrite, representing the geochemical composition of primordial Earth, or to shale (e.g., Post-Archaeon Australian Shale, PAAS), representing average upper continental crust. Due to the marine origin of BIF, comparison of the shale-normalized REY (REY_{SN}) distribution of Precambrian BIF to that of modern seawater (the REY geochemistry of which is reasonably well understood) has been developed into a very valuable geochemical tool. Based on studies of Early Precambrian well-preserved pure sedimentary carbonates, it is generally agreed that Archaeon to Palaeoproterozoic seawater had very similar REY_{SN} patterns compared to those of modern seawater (e.g., Bau et al., 1999; Kamber and Webb, 2001; Bau and Alexander, 2006; Kamber et al., 2014; Schier et al., 2018, 2020). Exceptions are the redox-sensitive elements Ce and Eu (e.g., Elderfield and Greaves, 1982; Elderfield et al., 1988; Bau, 1991; Piepgras and Jacobsen, 1992; Möller and Bau, 1993). The close similarity between the seawater-like (except for redoxsensitive Ce and Eu) REY_{SN} patterns of pure and pristine Precambrian BIF and pure and pristine sedimentary carbonates most strongly suggests that BIF recorded the REY distribution in ambient seawater and are robust geological archives of marine biogeochemical proxies in spite of diagenesis and/or metamorphism.

5.2.1 Geological background

Mount Ruker is a nunatak (from the Inuit word "nunataq"; a mountain/hill that rises above the ice surface) in the Ruker Terrane in the Prince Charles Mountains, East Antarctica (Fig. 5.1). Despite the remoteness of this area, several authors have investigated the geology of this polyphase Archaeon-Palaeoproterozoic basement and provided rather detailed stratigraphic information (e.g., Kamenev et al., 1993; Phillips et al., 2005; Boger et al., 2006; Mikhalsky et al., 2006; Phillips et al., 2006; Mikhalsky et

al., 2010; Liu et al., 2017; Harley et al., 2013 and references therein). Hence, we here focus on a brief description of the Tingey Complex which hosts the Ruker Group and Mt. Ruker itself. The Ruker Province is comprised of three lithostratigraphic units (see Fig. 5.2; Phillips et al., 2006): the Tingey Complex (3.2 Ga – 2.1 Ga), the Lambert Complex (2.1 Ga–0.95 Ga), and the Sodruzhestvo Group (950 Ma – 500 Ma). The lowest unit of the Tingey Complex is the Mawson orthogneiss which together with other Archaean-Palaeoproterozoic basement rocks further north appears to have provided the source material for the (meta)sediments of the overlying Menzies Group and Stinear Group. This is suggested by the ages of detrital zircons, that overlap with the age of the Mawson orthogneiss (Phillips et al., 2006). The Menzies Group is composed of quartzites, pelitic and calcareous metasediments, and amphibolites (Harley and Kelly, 2007). Mount Ruker itself is part of the Ruker Group (2.5–2.1 Ga) deposited on top of the Stinear Group, and shows BIF at its base and overlying quartzites and agglomerates. The Ruker Group is the youngest group of the Tingey Complex and is itself overlain by the orthogneisses of the Lambert Complex. The Ruker Terrane shows large variations in lithology and metamorphic grade. However, the Ruker Group, including the Mt. Ruker BIF, underwent metamorphism only up to greenschist facies (Mikhalsky et al., 2010), favouring preservation of an original major and trace elemental composition of the Mt. Ruker BIF.

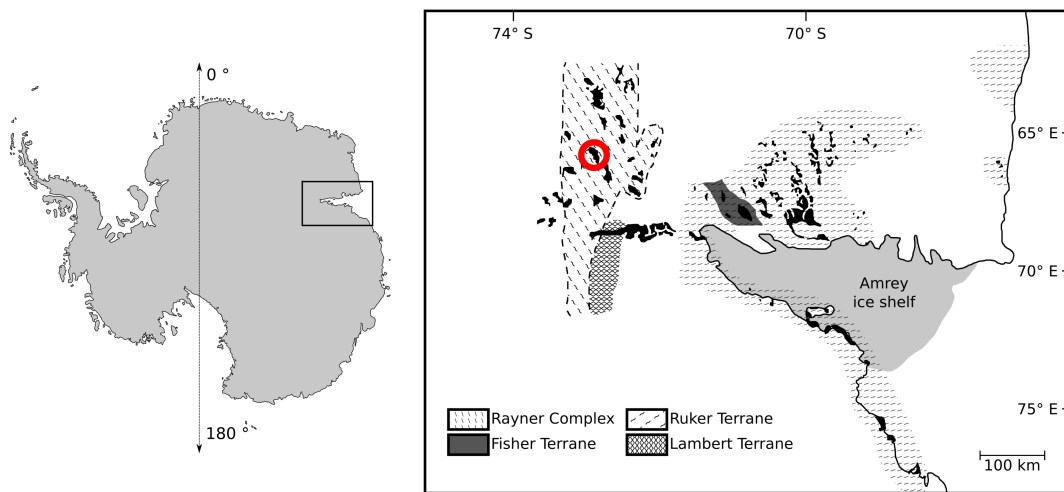


Figure 5.1: Map of Antarctica (left) and schematic geological map of the Prince Charles Mountains, East Antarctica (right). Location of Mt. Ruker marked with red circle. The black areas in the right map are nunataks. Modified after Phillips et al., 2005. (For interpretation of the references to colour in this figure legend, the reader is referred to the web version of this article.)

Southern Prince Charles Mountains Regional stratigraphy and geological events (Phillips et al., 2006)

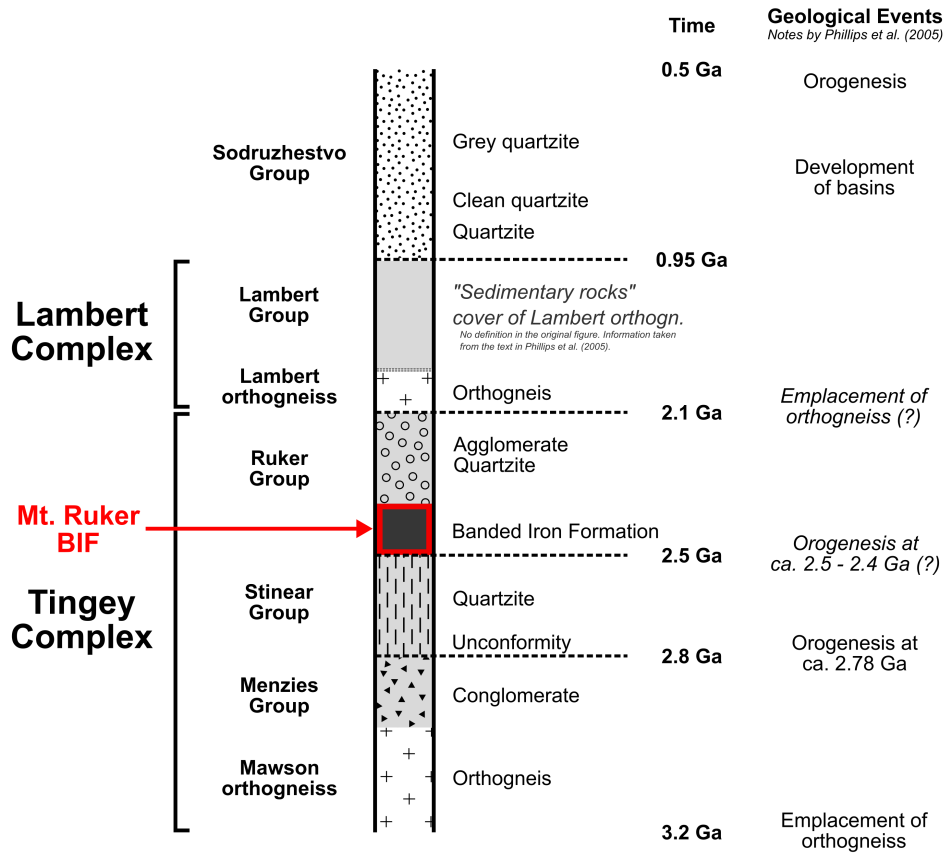


Figure 5.2: Stratigraphic column of the southern Prince Charles Mountains. Modified after Phillips et al. (2006).

5.3 Samples and methods

Banded iron-formation from Mt. Ruker had been sampled by J. Hofmann (retired professor at Bergakademie TU Freiberg) during a USSR expedition (19.SAE) to East Antarctica in 1973/74. At Jacobs University's GeochemistryLab, we drilled nine micro drill cores of 3 mm diameter into five individual adjacent layers of BIF with well-developed microbands from the Mt. Ruker Formation (Fig. 5.3). As sample ANT5.1 was micro drilled into a band which became very heterogeneous with depth, it was excluded from the sample set and will not be addressed any further. The micro drill cores were crushed and milled in an agate mortar, and 50 mg of sample powder were digested at 180 °C following a high-pressure, 3-acid digestion protocol (suprapure conc. HCl, HNO₃ and HF) using a PicoTrace DAS Pressure Digestion System. After evaporation to incipient dryness, the digested samples were diluted in a mixture of 0.5 M HNO₃ and 0.5 % HCl. Major and trace element analyses were performed with inductively coupled plasma optical emission spectroscopy (ICP-OES, SPECTRO CIROS VISION) and quadrupole inductively coupled plasma mass spectroscopy (ICP-MS, PerkinElmer NexION 350X), respectively. A detailed description of the analytical protocol can be found in Dulski (2001) and Alexander et al. (2008). Four digested samples were analysed twice and three times, respectively, by ICP-MS (indicated by "n" in Table 5.1). The relative standard deviations between the measurements of the respective samples were <2.5 % on average. As typical in BIF analysis by ICP-MS following sample decomposition involving HCl, niobium concentrations could not be determined because of strong FeCl⁺ interferences on the monoisotopic ⁹³Nb (Alexander, 2008). Digestion quality as well as analytical performance were monitored by blank samples and by the BIF Certified Reference Materials (CRMs) IF-G and FeR-3. For ICP-MS analysis, BIF CRM IF-G was digested three times in separate digestions and each of these three IF-G aliquots was analysed; for ICP-OES analyses only one IF-G aliquot was used. The major element data in Table 5.1, therefore, are based on one sample, while the trace element data are the average of three IF-G aliquots. Comparison of the IF-G trace element data to earlier publications (Kamber et al., 2004; Viehmann et al., 2016) yields a good agreement and generally <15 % relative deviation from the reference values. For those elements which show deviations >15 %, literature data also do not agree with each other (e.g., for Li, Sc, Ti). These relatively large differences for some elements between different literature data sets are likely caused by the very low trace element concentrations in BIF and highlight the need for additional high precision reference analyses focusing on especially these

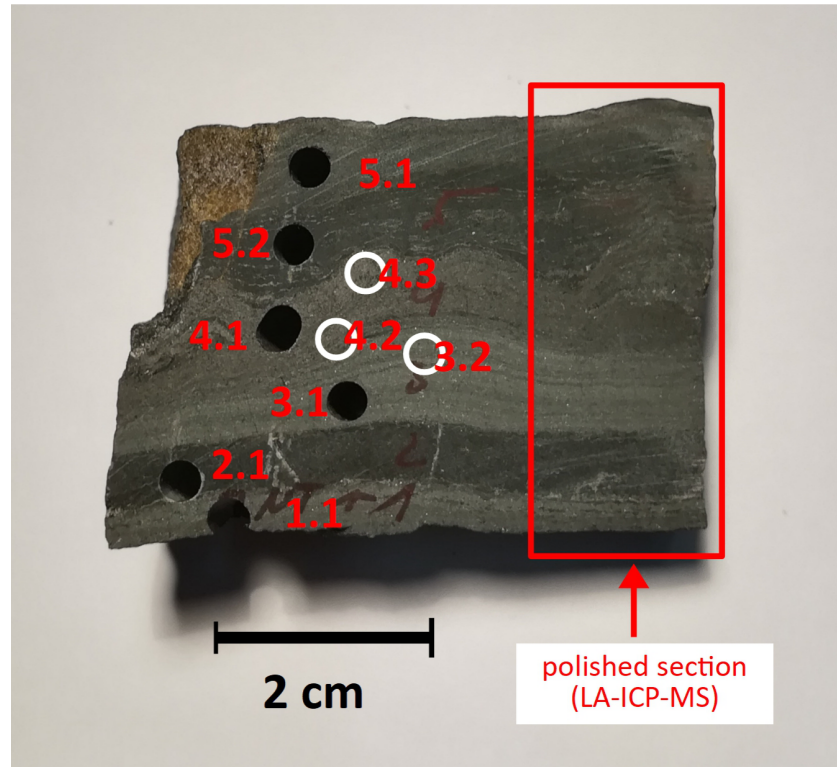


Figure 5.3: Slice of a hand specimen from the Mt. Ruker BIF with labelled microdrill sampling points in individual iron-oxide and metachert bands.

elements.

Anomalies in shale-normalized (subscript SN; Post Archaean Australian Shale (PAAS) from McLennan, 1989a, 1989b) and chondrite-normalized (subscript CN; C1 chondrite from Barrat et al., 2012) REY patterns are quantified by REY_{SN}/REY_{SN}^* and REY_{CN}/REY_{CN}^* ratios, respectively, and are quantified by Eqs. (1) (Bau and Alexander, 2009) and (2) (Bolhar et al., 2004):

$$Pr_{SN}^* = 0.5Ce_{SN} + 0.5Nd_{SN} \quad (1a)$$

$$Eu_{SN}^* = 0.67Sm_{SN} + 0.33Tb_{SN} \quad (1b)$$

$$Eu_{CN}^* = 0.67Sm_{CN} + 0.33Tb_{CN} \quad (1c)$$

$$Gd_{SN}^* = 0.33Sm_{SN} + 0.76Tb_{SN} \quad (1d)$$

$$Ce_{SN}^* = 2Pr_{SN} - 1Nd_{SN} \quad (1e)$$

$$La_{SN}^* = 3Pr_{SN} - 2Nd_{SN} \quad (2)$$

Since PAAS shows a negative Eu anomaly relative to chondrite, the REY data are also

Table 5.1: Element concentrations in Mt. Ruker BIF samples. Some samples were analysed several times for trace elements (ICP-MS), indicated by "n". "FT-1-1" is a sample from the Fig Tree IF.

	ANT1.1	ANT2.1	ANT3.1	ANT3.2	ANT4.1	ANT4.2	ANT4.3	ANT5.2	IF-G	FeR-3	FT-1-1
<i>wt. %</i>											
Al ₂ O ₃	0.17	0.05	0.35	0.18	0.45	0.12	<0.1	<0.05	0.16	0.09	
CaO	1.87	1.21	1.65	1.16	2.06	1.72	0.47	0.03	1.46	0.76	
Cr ₂ O ₃	<0.01	<0.01	<0.01	<0.01	<0.01	<0.01	<0.01	<0.01	<0.01	<0.01	
FeOt	75.96	8.76	73.16	64.53	56.66	62.88	69.24	10.68	52.07	41.72	
Fe ₂ O _{3t}	84.42	9.74	81.30	71.72	62.96	69.88	76.95	11.87	57.87	46.37	
K ₂ O	0.13	<0.07	0.27	<0.2	0.39	<0.2	<0.2	<0.07	<0.2	<0.07	
MgO	0.41	0.55	0.14	0.13	1.57	0.39	0.16	0.22	1.83	0.95	
MnO	0.02	0.06	0.01	0.01	0.19	0.02	0.04	0.01	0.04	0.08	
Na ₂ O	0.31	0.25	0.11	<0.6	0.84	<0.6	<0.6	0.18	<0.6	<0.03	
P ₂ O ₅	1.12	0.47	1.06	<0.7	0.66	<0.7	<0.7	<0.08	<0.7	<0.08	
V ₂ O ₅	<0.01	<0.01	<0.01	<0.01	<0.01	<0.01	<0.01	<0.01	<0.01	<0.01	
ZnO	0.01	0.00	0.01	0.02	0.01	0.03	0.02	0.002	0.02	0.01	
<i>mg/kg</i>	<i>n=3</i>	<i>n=3</i>	<i>n=2</i>		<i>n=2</i>				<i>n=3</i>		
Li	6.27	4.89	2.21	2.20	16.74	6.92	2.19	7.45	0.17	0.41	-
Be	0.66	0.10	0.26	0.28	0.76	0.81	0.88	0.10	4.28	0.44	-
Sc	0.26	0.17	<0.17	<0.5	0.83	<0.5	<0.5	0.33	0.24	0.40	<0.95
Ti	235.88	19.70	243.66	217.74	26.77	29.58	12.37	-	24.74	-	3080.00
Co	0.52	0.15	0.26	0.26	0.98	1.33	1.21	<0.4	3.51	1.44	34.20
Ni	14.59	2.18	9.88	6.21	23.24	315.22	77.52	15.86	23.04	10.84	408.00
Rb	3.89	0.77	7.15	5.19	9.23	3.12	2.96	<0.37	0.25	0.42	6.63
Sr	90.67	59.04	81.93	67.32	94.46	47.63	22.98	14.38	3.42	30.97	4.86
Y	22.97	10.41	26.78	22.29	19.51	16.29	6.12	5.09	8.80	2.57	43.40
Zr	1.23	0.50	1.58	1.50	6.32	2.28	1.95	0.37	0.69	0.80	60.70
Cs	0.26	0.03	0.31	0.31	0.17	0.19	0.21	0.05	0.05	0.22	0.73
Ba	42.50	312.40	30.47	28.26	44.16	17.90	27.96	40.80	1.83	7.25	129.00
La	3.80	1.69	2.96	2.54	2.67	5.90	1.61	0.59	2.58	1.53	41.20
Ce	7.33	3.32	7.09	5.93	5.71	9.15	2.66	1.48	3.84	1.98	75.30
Pr	0.92	0.43	1.08	0.90	0.83	1.06	0.33	0.23	0.41	0.25	8.12
Nd	4.02	1.85	5.58	4.45	4.20	4.53	1.52	1.17	1.68	1.45	31.50
Sm	0.90	0.41	1.43	1.15	1.07	0.95	0.34	0.30	0.38	0.53	5.61
Eu	0.33	0.17	0.61	0.49	0.44	0.40	0.15	0.12	0.36	0.22	2.45
Gd	1.34	0.64	2.24	1.78	1.67	1.41	0.51	0.45	0.67	0.30	5.76
Tb	0.22	0.11	0.36	0.28	0.26	0.22	0.08	0.07	0.11	0.05	0.81
Dy	1.72	0.81	2.58	2.05	1.86	1.52	0.56	0.50	0.81	0.31	5.25
Ho	0.46	0.21	0.63	0.49	0.46	0.38	0.14	0.12	0.20	0.07	1.20
Er	1.56	0.72	1.98	1.62	1.48	1.17	0.44	0.37	0.64	0.21	3.66
Tm	0.23	0.10	0.28	0.22	0.21	0.16	0.06	0.05	0.09	0.03	0.54
Yb	1.50	0.68	1.71	1.38	1.30	1.01	0.40	0.33	0.59	0.19	3.63
Lu	0.23	0.10	0.26	0.21	0.21	0.15	0.06	0.05	0.09	0.03	0.62
Hf	0.04	0.02	<0.3	0.04	0.12	0.07	0.05	<0.3	0.02	<0.3	1.43
W	2.20	<0.17	3.30	2.52	0.58	0.34	<0.17	<0.05	0.61	2.98	6.14
Pb	2.01	1.13	1.88	1.44	2.42	3.97	3.59	<0.4	6.90	5.68	7.75
Th	0.39	0.05	0.40	0.33	0.20	0.42	0.20	0.03	0.04	<0.06	3.17
U	0.23	0.04	0.20	0.17	0.26	0.29	0.34	0.02	0.02	0.14	3.28
Y/Ho	49.76	49.00	42.37	45.74	42.30	43.22	44.62	42.24			
Th/U	1.69	1.36	1.95	1.91	0.77	1.43	0.58	1.47			
Ba/Sr	0.47	5.29	0.37	0.42	0.47	0.38	1.22	2.84			
Nd _{SN} /Yb _{SN}	0.22	0.22	0.27	0.27	0.27	0.38	0.32	0.30			
La _{SN} /La _{SN} *	1.34	1.25	2.06	1.57	2.08	1.65	1.81	1.77			
Ce _{SN} /Ce _{SN} *	1.03	1.00	1.11	1.03	1.13	1.08	1.10	1.07			
Eu _{SN} /Eu _{SN} *	1.49	1.68	1.73	1.76	1.72	1.76	1.83	1.69			
Eu _{CN} /Eu _{CN} *	0.95	1.07	1.10	1.12	1.09	1.11	1.15	1.07			
Gd _{SN} /Gd _{SN} *	1.17	1.19	1.22	1.22	1.25	1.23	1.26	1.22			
Pr _{SN} /Pr _{SN} *	0.99	1.00	0.96	0.99	0.96	0.97	0.96	0.98			

normalized to chondrite (for a detailed discussion see Taylor and McLennan, 1985). An unambiguous Eu anomaly is present in both data sets (PAAS and chondrite-normalized), which is typical of Archaean BIF and caused by profound high-temperature hydrothermal input into Archaean seawater (e.g., Frei and Polat, 2007; Bau and Alexander, 2009; Viehmann et al., 2014).

The mineralogy and petrography of the BIF section was analysed at Bundesanstalt für Geowissenschaften und Rohstoffe (BGR) Hannover, Germany, using a FEI Quanta 650F scanning electron microscope (SEM) equipped with two energy-dispersive X-ray detectors (XFlash Detector 5030, Silicon Drift Detector; Bruker Nano) for semiquantitative element analysis without standardization. The EDX accelerating voltage was 25 kV and the working distance was 10 mm. The mineralogy was identified using energy-dispersive X-ray spectrometry (EDS) combined with backscattered electron (BSE) imaging, which was performed with a low-voltage high-contrast detector (vCD).

5.4 Results

The results of the chemical analyses of the micro drill cores are given in Table 5.1 together with those of the two BIF CRM FeR-3 (Neoproterozoic Temagami BIF, Canada) and IF-G (Eoarchaeon Isua BIF, Greenland). In Fig. 5.4, selected major and trace element concentrations of the Mt. Ruker BIF are compared to PAAS as a representative for potential upper crustal detritus.

Except for Si, the three iron-oxide bands (62.9–84.4 wt % Fe_2O_3) show major and trace element concentrations of up to one order of magnitude higher than the metachert bands (9.74–11.87 wt % Fe_2O_3). Manganese and Al concentrations are low in all samples and range from 0.01–0.19 wt % for MnO_2 and from <0.1–0.45 wt % for Al_2O_3 . Other elements such as CaO (0.03–2.06 wt %) and MgO (0.13–1.57 wt %), are generally low, while concentrations of Cr_2O_3 , K_2O (<0.39 wt %), Na_2O (<0.84 wt %), and P_2O_5 (<1.12 wt %) are often even below the limit of quantification (LOQ). Concentrations of indicators of detrital aluminosilicates such as Zr, are also very low and range from 0.37 to 2.4 mg/kg. Only sample ANT4.1 shows a somewhat elevated Zr concentration of 6.32 mg/kg; this is also the sample with the highest Mn and Al concentrations. Rubidium ranges from 0.77 to 9.23 mg/kg. Three samples (ANT1.1, ANT2.1 and ANT3.2) show elevated Ti concentrations from 218 to 236 mg/kg, while the remaining four samples yield Ti concentrations below 30 mg/kg. Scandium concentrations in the Mt. Ruker BIF samples range from 0.17 to 0.83 mg/kg, Hf from 0.02 to 0.12 mg/kg, and Th from 0.03 to 0.42 mg/kg. Compared to trace element data from other BIF (Dales Gorge Member, Hamersley Basin, Western Australia, ~2.47 Ga; Kuruman IF, Transvaal Supergroup, South Africa, ~2.46 Ga; Carajás BIF, Itacáunas Supergroup, Brazil, ~2.75 Ga; Water Tower IF, Contorted Bed IF, Promise Formation IF, Silverfield Member IF, Witwatersrand Supergroup, South Africa, 2.96 Ga – 2.78 Ga – Bau, 1993; Klein and Beukes, 1989; Klein and Ladeira, 2002; Smith et al., 2013; Viehmann et al., 2015b; Smith and Beukes, 2016, and references therein), these element concentrations are low and indicate only a minor to negligible impact of detrital material on the Mt. Ruker BIF samples. Beside low Th concentrations, the Th/U ratios of the samples range between 0.58 and 1.95, i.e. they are lower and fractionated relative to average continental crust (Th/U: 3.89; Rudnick and Gao, 2003).

One striking feature in Fig. 5.4 is the peak at Ni for the Mt. Ruker samples. All iron-oxide and metachert bands show Zr/Ni ratios well-below unity. However, except for the Pietersburg BIF (Pietersburg greenstone belt, South Africa, ~2.9 Ga; Alexander et

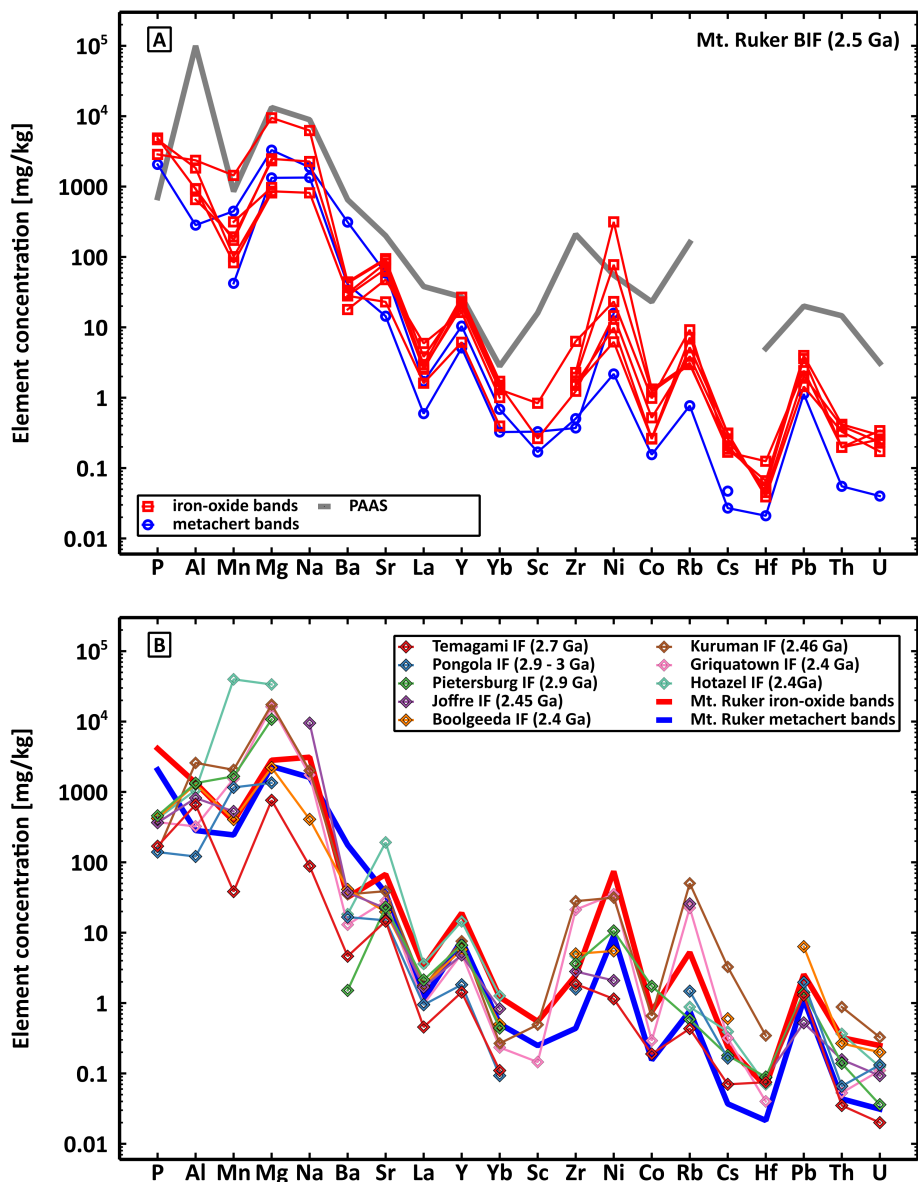


Figure 5.4: (A) Major and trace element distribution in adjacent iron-oxide and metachert bands from the Mt. Ruker BIF (PAAS from Taylor and McLennan (1985) shown for comparison). (B) Comparison of the averages of iron-oxide and metachert bands from the Mt. Ruker BIF with examples of other Algoma-type (Temagami, Pietersburg) and Superior-type (Pongola, Joffre, Boolgeeda, Kuruman, Griquatown, Hotazel) BIF. Literature data from: Bau and Alexander (2009), Alexander et al. (2009), Alexander et al. (2008), Haugaard et al. (2016), Warchola et al. (2018), Beukes and Klein (1990), Schier et al. (2020). Further explanation see text.

al., 2009), most of the other BIF shown in Fig. 5.4B show Zr/Ni ratios close to 1 or even above 1.

Moreover, in Fig. 5.4 the two metachert bands show very similar patterns compared to the iron-oxide bands. However, there is a clear difference in the Ba/Sr ratios between these two types of bands. While the iron-oxide bands show Ba/Sr ratios between 0.37 and 1.22 (average 0.55), the metachert bands show significantly higher Ba/Sr ratios of 5.29 and 2.84.

The Mt. Ruker BIF samples show light REY (LREY) depletion relative to the heavy REY (HREY) with $(\text{Nd}/\text{Yb})_{\text{SN}}$ ratios between 0.22 and 0.38. Indicated by $(\text{La}/\text{La}^*)_{\text{SN}}$ ratios between 1.25 and 2.08, $(\text{Gd}/\text{Gd}^*)_{\text{SN}}$ ratios between 1.17 and 1.26, and superchondritic Y/Ho ratios between 42 and 50, all Mt. Ruker samples display positive La_{SN} , Gd_{SN} , and Y_{SN} anomalies (Fig. 5.5). None of the samples shows a negative Ce_{SN} anomaly ($(\text{Ce}/\text{Ce}^*)_{\text{SN}}$: 1.00–1.13). While the REY distribution shows a positive Eu_{SN} anomaly when normalized to shale ($(\text{Eu}/\text{Eu}^*)_{\text{SN}}$: 1.49–1.83), a positive Eu anomaly cannot be observed in chondrite-normalized patterns ($(\text{Eu}/\text{Eu}^*)_{\text{C1}}$: 0.95–1.15). Except for the redox-sensitive REY, the REY distribution is similar to that of modern seawater.

The chondrite-normalized REE patterns (Fig. 5.4B) most clearly show the lanthanide tetrad effect, in particular the 3rd and the 4th tetrad (Peppard et al., 1969; Masuda and Ikeuchi, 1979; Akagi et al., 1993; Bau, 1996). As usual, the curve of the 2nd tetrad is partly obliterated because of missing data for extinct Pm and the redox-related decoupling of Eu, but can still be identified. The 1st tetrad from La to Nd is also visible in some samples, although it is usually hard to recognize in natural samples (Masuda and Ikeuchi, 1979). The convex shape of the observed tetrads in the REY_{CN} patterns of the Mt. Ruker BIF represents the W-type tetrad effect (following the terminology of Masuda et al., 1987).

In the SEM images (Fig. 5.6), the iron-oxide bands can be identified as very finely intergrown magnetite and haematite. At the transition between iron-oxide and metachert bands, single Fe-oxide crystals (~ 0.05 mm) are intergrown with an Fe-rich Si phase or are embedded in the amorphous Si-phase. The Fe-rich Si phase is typical for the contact zones between iron-oxide and metachert bands and also appears as disseminated grains in the Si phase. The thicknesses of the iron-oxide and metachert bands vary throughout the sample and reach from single mm-scale bands (Fig. 5.6A/B) to very thin (μm to sub- μm) layers (Fig. 5.6C). Beside the Fe oxides and the Si-phase, barite and apatite grains can also be observed (Fig. 5.6A/B).

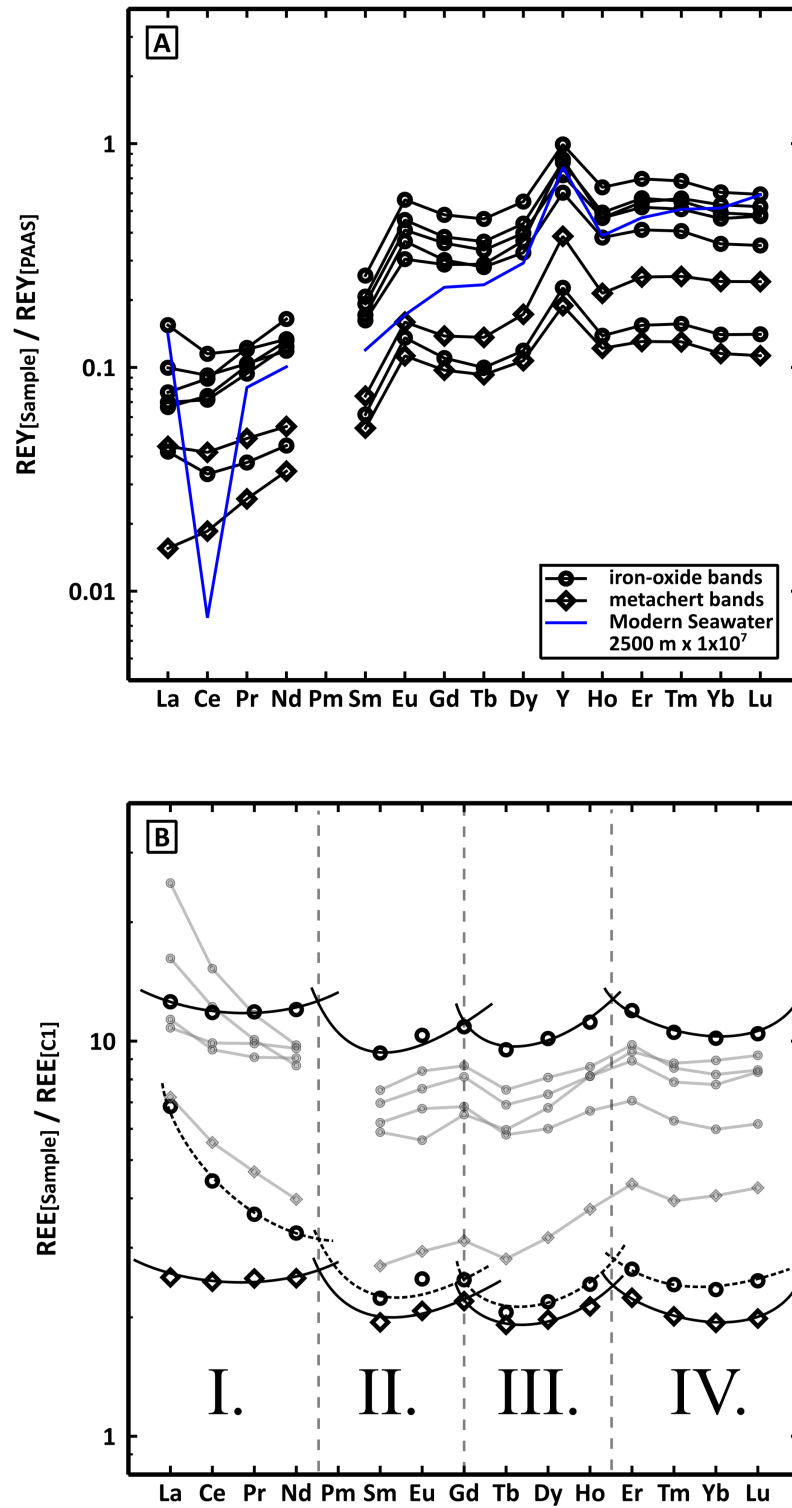


Figure 5.5

Figure 5.5: (A) Shale-normalized REY distribution of adjacent iron-oxide and metachert bands of the Mt. Ruker BIF (modern seawater (blue line; data from Alibo and Nozaki, 1999) shown for comparison). (B) Chondrite-normalized REE distribution of adjacent iron-oxide and metachert bands of the Mt. Ruker BIF with W-type tetrad effect highlighted by black curves (circles: iron-oxide bands, diamonds: metachert bands). The dashed line indicates the tetrad effect with a much steeper course in the first tetrad. (For interpretation of the references to colour in this figure legend, the reader is referred to the web version of this article.)

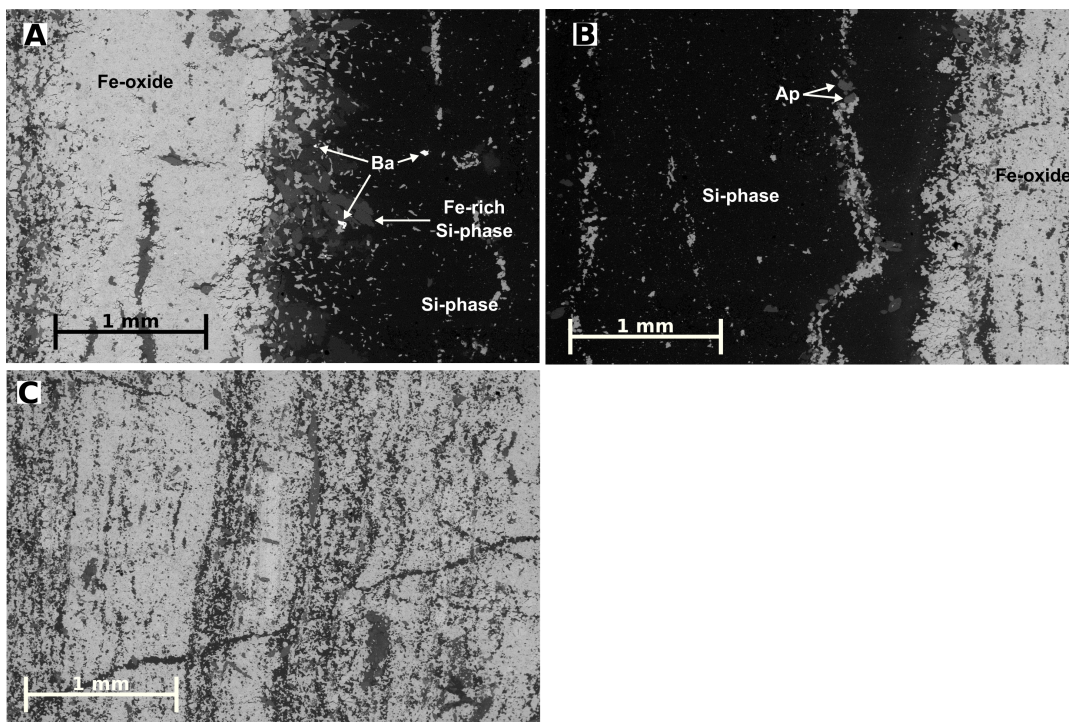


Figure 5.6: SEM images of Mt. Ruker BIF, showing an iron-oxide phase, silicate-phase, barite (Ba) and apatite (Ap).

5.5 Discussion

The conspicuous positive correlation between Al_2O_3 and Sc, Rb, Zr and Hf with correlation factors of 0.98, 0.98, 0.78 and 0.92 (Table 5.2), respectively, strongly suggest a detrital origin of these elements in the Mt. Ruker BIF samples. Titanium, however, which is also commonly known as a detritus-indicator element, does not show any correlation with Al_2O_3 and the other detritus-indicators (Sc, Rb, Zr and Hf), but with P_2O_5 and W (0.97 and 0.96, respectively). However, the remarkably low concentrations of all these high field strength elements compared to those typical of potential detrital material (Fig. 5.4A) and also the other major and trace element concentrations in the Mt. Ruker BIF correspond very well to those of other pure Archaean and Palaeoproterozoic BIF (Fig. 5.4B). Literature data shown in Fig. 5.4B represent average values for each element after samples with high amounts of detritus ($\text{Al} > 2000$ mg/kg; $\text{Zr} > 5$ mg/kg) had been removed from the data set. Except for Ba and Ni, the Mt. Ruker BIF samples show elemental concentrations which fall well-within the range of the averages of pure samples of the Algoma-type Temagami (Temagami greenstone belt, Ontario, Canada; ~ 2.7 Ga; Bau and Alexander, 2009) and Pietersburg and of the Superior-type Pongola (Pongola Supergroup; eastern South Africa, southwestern Swaziland; 2.9 Ga – 3.0 Ga; Alexander et al., 2008), Kuruman, Griquatown (Transvaal Supergroup, South Africa; ~ 2.4 Ga; Pickard, 2003), Hamersley (Joffre and Boolgeeda; Hamersley Basin, Western Australia, 2.6 Ga — 2.4 Ga; Pickard, 2002) and Hotazel IF (Transvaal Supergroup, South Africa; ~ 2.4 Ga; Schier et al., 2020).

5.5.1 Nickel and Zirconium

The iron-oxide and metachert bands in the Mt. Ruker BIF both show elevated Ni concentrations, as illustrated in Fig. 5.4. The ICP-MS analyses were conducted with two nickel cones (sample-cone and skimmer-cone). However, a contamination by the cones is very unlikely because of the very good agreement between the Ni concentrations we determined for CRM IF-G and FeR-3 and literature data. The measured values for IF-G and FeR-3 (23.0 and 10.9 mg/kg, respectively) deviate less than 5 % from literature data by Kamber et al. (2014; IF-G Ni = 22.2 mg/kg) and Sampaio and Enzweiler (2015; FeR-3 Ni = 11.4 mg/kg). Comparison with other BIF in Fig. 5.4B shows that the Kuruman and Griquatown IF have Ni concentrations similar to those of Mt. Ruker. However, Kuruman IF and Griquatown IF show Zr concentrations which are very similar to their Ni concentrations, resulting in Zr/Ni ratios close to unity. In the Mt. Ruker samples,

Table 5.2: Correlation matrix for major and trace elements in Mt. Ruker BIF.

Correlation	Al ₂ O ₃	CaO	FeOt	Fe ₂ O _{3,t}	K ₂ O	MgO	MnO	Na ₂ O	P ₂ O ₅	ZnO	Li	Be	Sc	Ti	Co	Ni	Rb	Sr	Y	Zr	Cs	Ba	ΣREE	Hf	W	Pb	Th	U		
Al ₂ O ₃	1.00																													
CaO	0.65	1.00																												
FeOt	0.46	0.51	1.00																											
Fe ₂ O _{3,t}	0.46	0.51	1.00	1.00																										
K ₂ O	0.99	0.41	-0.90	-0.90	1.00																									
MgO	0.26	0.43	-0.06	-0.06	0.73	1.00																								
MnO	0.61	0.44	-0.02	-0.02	0.81	0.65	1.00																							
Na ₂ O	0.56	0.52	0.18	0.18	0.67	0.99	0.97	1.00																						
P ₂ O ₅	0.22	0.44	0.90	0.90	-0.89	-0.53	-0.57	-0.40	1.00																					
ZnO	-0.18	0.17	0.67	0.67	-0.98	0.00	-0.16	0.24	0.88	1.00																				
Li	0.57	0.32	-0.14	-0.14	0.66	0.31	0.78	0.95	-0.38	-0.32	1.00																			
Be	-0.12	0.17	0.14	0.14	0.14	0.75	0.06	0.76	0.30	0.39	-0.33	1.00																		
Sc	0.98	0.44	0.39	0.39	1.00	0.90	0.88	0.94	-0.11	0.41	1.00	0.67	1.00																	
Ti	0.18	0.24	0.52	0.52	-0.82	-0.49	-0.48	-0.60	0.97	-0.21	-0.24	-0.35	-0.36	1.00																
Co	-0.10	-0.01	0.03	0.03	0.59	0.72	0.05	0.93	-0.03	0.47	-0.23	0.97	0.95	-0.49	1.00															
Ni	-0.25	0.16	0.22	0.22	0.60	-0.13	-0.11	0.69	0.22	0.69	0.09	0.01	0.84	-0.36	0.16	1.00														
Rb	0.90	0.46	0.46	0.46	1.00	-0.05	0.49	0.56	0.27	-0.20	0.62	-0.46	0.97	0.38	-0.45	-0.15	1.00													
Sr	0.54	0.69	0.38	0.38	0.24	-0.11	0.38	0.48	0.57	-0.24	0.47	-0.52	0.43	0.57	-0.76	-0.15	0.75	1.00												
Y	0.56	0.73	0.62	0.62	-0.43	-0.15	0.06	0.12	0.90	0.02	0.13	-0.29	0.36	0.84	-0.54	-0.06	0.71	0.86	1.00											
Zr	0.79	0.52	0.33	0.33	0.87	0.43	0.88	0.93	-0.21	0.12	0.78	-0.08	0.97	-0.25	-0.06	0.13	0.76	0.50	0.32	1.00										
Cs	0.40	0.35	0.84	0.84	-0.60	-0.45	-0.17	-0.03	0.94	0.37	-0.12	-0.34	0.29	0.79	-0.51	0.05	0.62	0.60	0.80	0.22	1.00									
Ba	-0.44	-0.05	-0.65	-0.65	0.06	-0.08	0.13	-0.13	-0.77	-0.56	0.05	-0.33	-0.51	-0.25	-0.41	-0.24	-0.34	0.14	-0.19	-0.23	-0.46	1.00								
ΣREE	0.44	0.80	0.68	0.68	-0.29	-0.09	0.05	0.18	0.86	0.30	0.16	-0.18	0.43	0.63	-0.36	0.32	0.62	0.73	0.92	0.37	0.74	-0.29	1.00							
Hf	0.90	0.49	0.32	0.32	1.00	0.32	0.82	0.99	-0.03	0.02	0.89	-0.20	1.00	-0.22	-0.09	0.19	0.87	0.49	0.33	0.99	0.22	-0.34	0.40	1.00						
W	0.13	-0.31	0.78	0.78	-0.55	-0.71	-0.50	-0.99	0.86	-0.50	-0.42	-0.53	-1.00	0.96	-0.68	-0.53	0.32	0.48	0.83	-0.40	0.86	0.38	0.46	-0.42	1.00					
Pb	-0.13	-0.05	0.09	0.09	0.68	0.64	-0.05	0.65	0.42	0.54	-0.30	0.96	0.82	-0.46	0.99	0.23	-0.47	-0.79	-0.53	-0.12	-0.46	-0.45	-0.33	-0.13	-0.64	1.00				
Th	0.20	0.53	0.79	0.79	-0.83	-0.43	-0.20	-0.07	0.99	0.45	0.00	-0.33	0.12	0.66	-0.47	0.41	0.48	0.62	0.81	0.20	0.88	-0.38	0.89	0.23	0.52	-0.40	1.00			
U	0.46	0.31	0.75	0.75	0.37	-0.28	0.21	0.53	0.62	0.60	0.23	-0.29	0.62	0.06	-0.32	0.47	0.51	0.42	0.38	0.55	0.68	-0.38	0.50	0.58	0.04	-0.27	0.71	1.00		

however, the Zr/Ni ratios are well-below 1. Furthermore, the Temagami, Pongola and Boolgeeda BIF also show Zr/Ni ratios close to unity. Only the Pietersburg IF shows a difference between Zr and Ni concentrations, but not as pronounced as the Mt. Ruker samples. After digestion, all Mt. Ruker samples were stored in a matrix of 0.5 M HNO₃ + 0.5 % HCl with additional 0.01 ml concentrated HF. This should have prevented the adsorption of elements, especially HFSE (like Zr), onto the PE-bottle wall or precipitation in the bottles. The measured Zr concentrations for the CRM IF-G and FeR-3 are 0.69 and 0.8 mg/kg, respectively. The reference values in the literature for IF-G range from 0.602 (Kamber et al., 2004) over 0.802 (Viehmman et al., 2016) to ~1 mg/kg (Fabre et al., 2011; Sampaio and Enzweiler, 2015). For FeR-3, Sampaio and Enzweiler (2014) and Bau and Alexander (2009) give Zr concentrations of 1.2–1.4 and 1.18 mg/kg, respectively. Although there is a difference between the measured Zr values for IF-G and FeR-3 in this study and values from other studies, the quality of the Mt. Ruker Zr data seem to be resilient and the clear difference between the Zr/Ni ratios of Mt. Ruker BIF and the other BIF cannot be explained by a possible loss of Zr during sample preparation for ICP-MS analysis. Konhauser et al. (2009) describe a 2-stage trend of decreasing Ni concentrations in the oceans during Earth’s history, due to decreasing formation of Ni-rich ultramafic rocks. Although the trend of decreasing Ni concentrations with

decreasing age, should also be visible in BIF (Konhauser et al., 2009), the Mt. Ruker BIF samples do not fit into this trend: despite their Neoarchaeon age, they show the highest Ni concentrations of all samples in the compilation of Fig. 5.4B. Additional work and a more detailed comparison of Ni and Zr data from different BIF are needed for an in-depth evaluation of this observation, which is, however, beyond the scope of this study.

5.5.2 Barium and Strontium

The elevated Ba/Sr ratios in the metachert bands are similar to those of PAAS (3.25, Taylor and McLennan, 1985). Direct comparison to the other BIF in Fig. 5.4B is hampered because those are average values of metachert and iron-oxide bands. Therefore, the Temagami BIF micro drill core data from Bau and Alexander (2009) was used for a more detailed comparison (Fig. 5.7). The Mt. Ruker BIF samples show higher Ba/Sr ratios than the Temagami BIF samples. However, in both BIF the iron-oxide bands generally show lower Ba/Sr ratios compared to the metachert bands. With SEM, small grains of barite could be identified, but as shown in Fig. 5.6A, the barite grains are confined to the Si or Fe-rich Si phase in the metachert bands. Although not the whole Mt. Ruker BIF sample set was investigated with SEM, the presence of barite grains in the Si-phase may explain the elevated Ba/Sr ratios. However, it is unclear whether the barite is of primary or secondary origin. A clear correlation of the Ba/Sr ratios with other elements in the BIF (e.g., detritus-indicators like Zr, Hf or Sc; Bau, 1993) is not observed and further investigations is needed for an appropriate discussion of the Ba-Sr systematics of BIF.

5.5.3 Rare earth elements and Yttrium

The REY distribution in marine chemical sedimentary rocks can be a very robust proxy for the physico-chemical conditions in ambient seawater and hence in the atmosphere-hydrosphere system, and for the element sources to seawater at the time and location of deposition (e.g., Kamber and Webb, 2001; Bolhar et al., 2004; Kamber et al., 2004; Bau and Alexander, 2009; Alexander et al., 2009; Viehmann et al., 2014, Viehmann et al., 2015a, 2016; Schier et al., 2018, 2020; and references therein). The close similarity between the chemical composition of the Mt. Ruker BIF and that of other pure and unaltered BIF suggests that the former had not been corrupted during diagenetic and metamorphic processes, but that the Mt. Ruker BIF preserved original geochemical

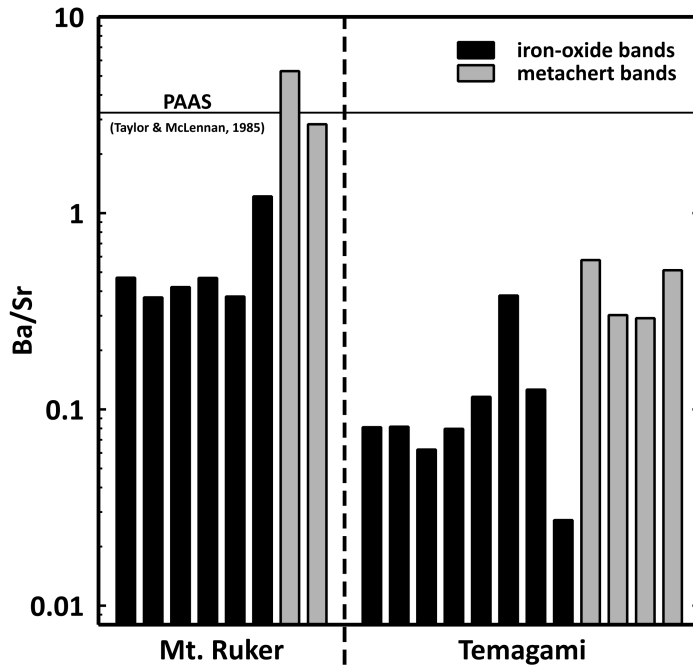


Figure 5.7: Ba/Sr ratios of adjacent iron-oxide and metachert bands of the Mt. Ruker and of the Temagami BIF (Temagami data from Bau and Alexander, 2009).

signals from its marine environment.

Despite the differences in total trace element concentrations between the iron-oxide and the metachert bands, both types of bands show very similar, super-chondritic Y/Ho ratios (Fig. 5.8). As will be discussed in the following, these uniform Y/Ho ratios are a clear indication for the primary origin of the alternating Fe oxide and chert bands in the Mt. Ruker BIF and argue against models which propose a post-depositional origin of the banding of BIF. As shown by numerous experimental studies and by data from natural systems, a distinct fractionation of the geochemical twins Y and Ho occurs during REY scavenging by (modern) Fe and Mn (oxyhydr)oxides (e.g., Bau et al., 1996, 1998, 2014; Bau, 1999; Bau and Koschinsky, 2009, Krämer et al., 2017). Holmium is preferentially scavenged by Fe and Mn (oxyhydr)oxide surfaces relative to Y, leading to a lower Y/Ho ratio of oxidic Fe and Mn precipitates relative to ambient water. This has implications for models that try to explain the formation of the enigmatic banding of BIF by post-depositional processes. If the initial precipitate had indeed been a homogeneous Fe-silicate ooze and the segregation and separation into adjacent Fe (oxyhydr)oxide bands and chert bands occurred during diagenesis (e.g., Krapež et al., 2003; Rasmussen et al., 2013; Alibert and Kinsley, 2016), the Fe (oxyhydr)oxide bands should show

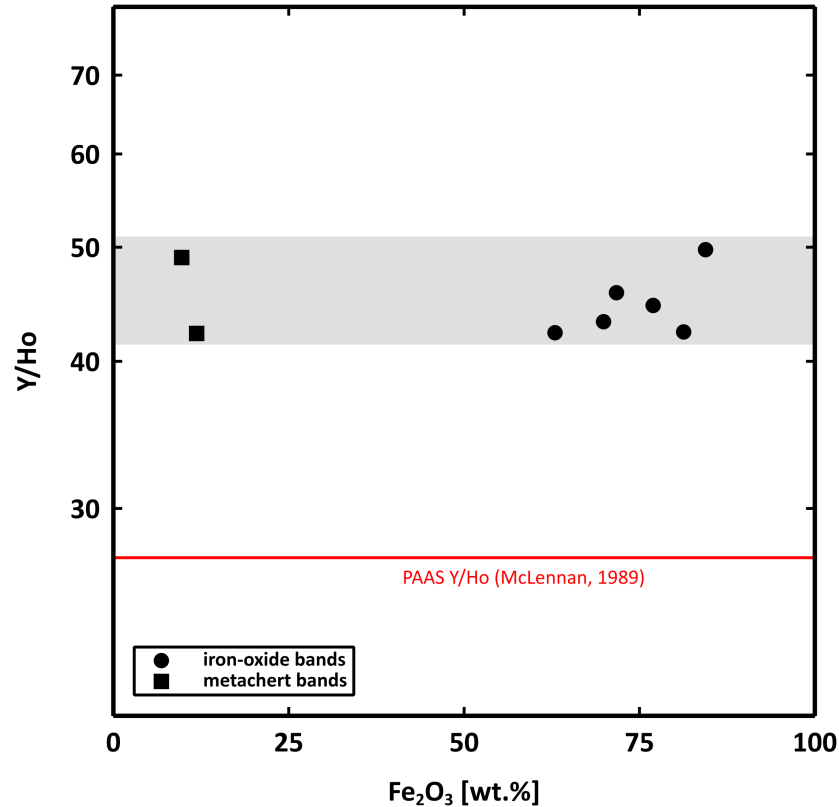


Figure 5.8: Similar super-chondritic Y/Ho ratios in adjacent iron-oxide and metachert bands of the Mt. Ruker BIF, suggesting primary origin of the conspicuous alternating banding of BIF.

systematically lower Y/Ho ratios than the adjacent chert/quartz bands. This, however, is neither observed in the Mt. Ruker BIF samples discussed here (Fig. 5.8) nor in the 2.7 Ga old Temagami IF, Ontario, Canada, (Bau and Alexander, 2009), suggesting that the prominent banding of BIF is usually a primary, i.e. syndepositional, and by no means a post-depositional feature. This does not rule out that Fe silicates were deposited in the Precambrian ocean, but it suggests that this was not the common process eventually resulting in the formation of *banded* IF. A primary origin of the banding in BIF is also supported by the fact that in some BIF, adjacent bands show different Eu_{SN}/Eu_{SN}^* ratios, which is very unlikely to develop in a low-temperature diagenetic environment in which Eu is trivalent (Bau and Dulski, 1992), as decoupling of Eu from its redox-*insensitive* REY neighbours requires elevated temperatures well above 200 °C (e.g., Bau, 1991).

An updated compilation of Bau and Dulski's (1994) Y/Ho data from numerous pure BIF samples plotted against their respective depositional age (Fig. 5.9) corroborates the conclusion that the Earth's oceans were characterized by super-chondritic Y/Ho ratios

since the start of the palaeoceanographic record at Isua, more than 3.8 Ga ago. By far the vast majority of the analysed samples, including those from the Mt. Ruker BIF, show Y/Ho ratios between those of PAAS and other shale averages (McLennan, 1989a, 1989b; Bau et al., 2018) and those of modern seawater. Based on the rather unfractionated scavenging of REY by BIF from seawater, it can be assumed that the Y/Ho ratio in the BIF is similar to that of the ambient water mass during BIF formation. While an alteration of the REY distribution due to metamorphic processes in general is unlikely (Bau, 1993) and the influence of diagenetic and metamorphic processes on Y/Ho ratios are small or even negligible (Bau, 1996), detrital contamination may play a role, as the chondritic Y/Ho ratio of possible detritus (e.g., atmospheric dust or volcanic ash) reduces the super-chondritic ratio of seawater. However, the samples shown in Fig. 5.9 have all been screened for detrital contamination and are thus very pure. The lower Y/Ho ratios of BIF relative to modern seawater, therefore, may rather suggest that Precambrian seawater showed lower (but still super-chondritic) Y/Ho ratios than modern seawater. The lack of any systematically increasing or decreasing trend in a graph of Y/Ho ratios of BIF against depositional age argues strongly for a rather constant super-chondritic Y/Ho ratio of the pure chemically precipitated marine endmember. The above observations made on BIF need to be bolstered by an evaluation of the Y-Ho systematics of other Precambrian marine chemical sediments such as carbonates and phosphates. Preliminary results from such studies (e.g., Bau and Alexander, 2006; Schier et al., 2018, 2020; Kreitsmann et al., 2020) for Precambrian marine sedimentary carbonates, manganese-formations, and phosphorites so far corroborate the omnipresence of superchondritic Y/Ho ratios in seawater. We emphasize that in marked contrast to Precambrian BIFs and manganese formations, modern marine oxidic ferromanganese crusts and nodules which are also mostly composed of Fe and Mn (hydr)oxide minerals, strongly fractionate Y and Ho during REY scavenging from seawater (Bau et al., 1996, 2014) and are characterized by sub-chondritic Y/Ho ratios (Fig. 5.9). This Y-Ho fractionation is accompanied by general REY fractionation during formation of hydrogenetic ferromanganese crusts, the REY distribution of which represents the exchange equilibrium between REY surface and solution-complexes (e.g., Bau et al., 2014; and references therein). This profound difference between the REY patterns of Precambrian and Post-Precambrian marine oxidic Fe and Mn (oxyhydr)oxide precipitates suggests that the respective REY scavenging mechanisms were fundamentally different.

The positive Eu_{SN} anomalies in the Mt. Ruker BIF (Fig. 5.5B) indicate that the input of REY from high-temperature hydrothermal fluids into seawater existed, but was

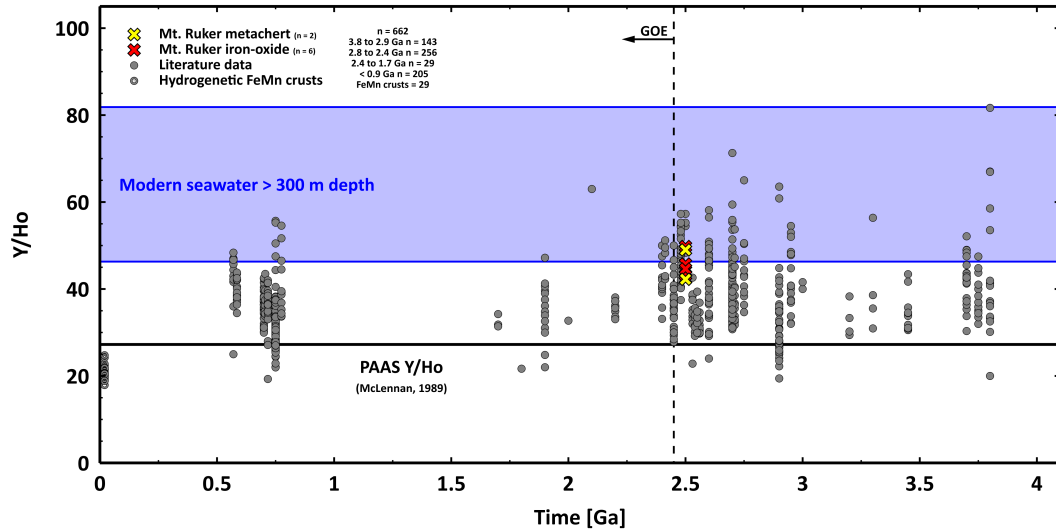


Figure 5.9: Evolution of the Y/Ho ratio of BIF throughout Earth's history. Modern seawater range (Alibo and Nozaki, 1999), PAAS (McLennan, 1989a, 1989b) and modern hydrogenetic Fe/Mn crusts (Bau et al., 1996) shown for comparison. BIF literature data from: Alexander et al. (2008), Alexander et al. (2009), Angerer et al. (2012), Angerer et al. (2016), Aoki et al. (2018), Appel (1983), Baldwin et al. (2012), Basta et al. (2011), Bau and Alexander (2009), Bau and Dulski (1996), Bau et al. (1997), Bolhar et al. (2005a), Bolhar et al. (2005b), Cates and Mojzsis (2009), Delvigne et al. (2012), Døssing et al. (2009), El-Shazly et al. (2019), Fabre et al. (2011), Frei and Polat (2007), Frei et al. (2008), Frei et al. (2009), Frei et al. (2017), Friend et al. (2008), Ghosh and Baidya (2017), Gourcerol et al. (2015), Haugaard et al. (2013), Haugaard et al. (2016), Hou et al. (2014), Kuhn et al. (1998), Lechte and Wallace (2016), Lottermoser and Ashley (2000), Mloszewska et al. (2012), Moon et al. (2017), Peng et al. (2018), Planavsky et al. (2010), Raju (2009), Slack et al. (2009), Smith et al. (2013), Spier et al. (2007), Stern et al. (2013), Toulkeridis et al. (1998), Viehmann et al. (2014), Viehmann et al. (2015b), Viehmann et al. (2016), Le Wang et al. (2014), Wang et al. (2017), Warchola et al. (2018), Zhu et al. (2015). Further explanation see text.

considerably smaller than it used to be during the Archaean. Viehmann et al. (2015b) showed with their compilation of Eu anomalies of numerous BIF throughout Earth's history that the magnitude of the positive Eu anomaly decreased after a strong peak around 2.6 Ga, and that since ca 2.4 Ga ago BIF show only minor Eu anomalies, if any. The 2.5 Ga age of Mt. Ruker BIF is an earliest possible emplacement age, defined by the transition between the older, underlying Stinear Group quartzite and the Ruker Group BIF (Phillips et al., 2006). The Ruker group ends with agglomerates and quartzites at 2.1 Ga. Therefore, an early Palaeoproterozoic formation age of the Mt. Ruker BIF which is characterized by small positive Eu_{SN} but no Eu_{CN} anomalies (Viehmann et al., 2015b), is plausible and in agreement with previous studies.

The lack of Ce anomalies in the Mt. Ruker BIF (Table 5.1 and Fig. 5.5) demonstrates that oxidative fractionation of Ce from its REY neighbours did neither occur in the marine environment where the BIF formed, nor in the terrestrial source region of the REY present in ambient seawater. This is fully compatible with observations elsewhere for pure and pristine marine chemical sediments of early Palaeoproterozoic age (e.g., Schier et al., 2018, 2020).

Apart from redox-sensitive Ce and Eu, the Mt. Ruker BIF shows a REY distribution similar to that of modern seawater (Fig. 5.5A) with positive La, Gd and Y anomalies and enrichment of HREY over LREY. Even the W-type lanthanide tetrad effect can be observed. All this corroborates the interpretation that the Mt. Ruker BIF samples studied are pristine and pure, as aluminosilicate detritus shows chondritic Y/Ho ratios and no REE tetrad effects. The observed W-type tetrad effect is confined to aqueous systems, like seawater or shallow ground water (Masuda and Ikeuchi, 1979; Masuda et al., 1987), whereas the M-type tetrad effect occurs in highly evolved magmatic rocks (Masuda and Akagi, 1989; Bau, 1996) and in Fe oxyhydroxide precipitates (e.g., Bau, 1999). The observation of the W-type tetrad effect in the 2.5 Ga Mt. Ruker BIF is evidence for the presence of the W-type tetrad effect in ambient seawater. Re-evaluation of REY data from other pure BIF (Fig. 5.10) reveals that, similar to super-chondritic Y/Ho ratios, the occurrence of the W-type tetrad effect can be traced as far back as Isua times about 3.8 Ga ago, i.e. the W-type tetrad effect is also an ancient feature of seawater. We emphasize that pure BIF from Mt. Ruker and elsewhere (i.e. oxidic marine Fe precipitates) show the W-type lanthanide tetrad effect (and the super-chondritic Y/Ho ratio) of ambient seawater, and hence scavenged REY from seawater without major fractionation. As for the Y/Ho ratio, this is in marked contrast to what is observed in modern and Cenozoic marine oxidic ferromanganese precipitates and in related scavenging experiments (e.g.,

Bau et al., 2014; and references therein), pointing towards different scavenging processes.

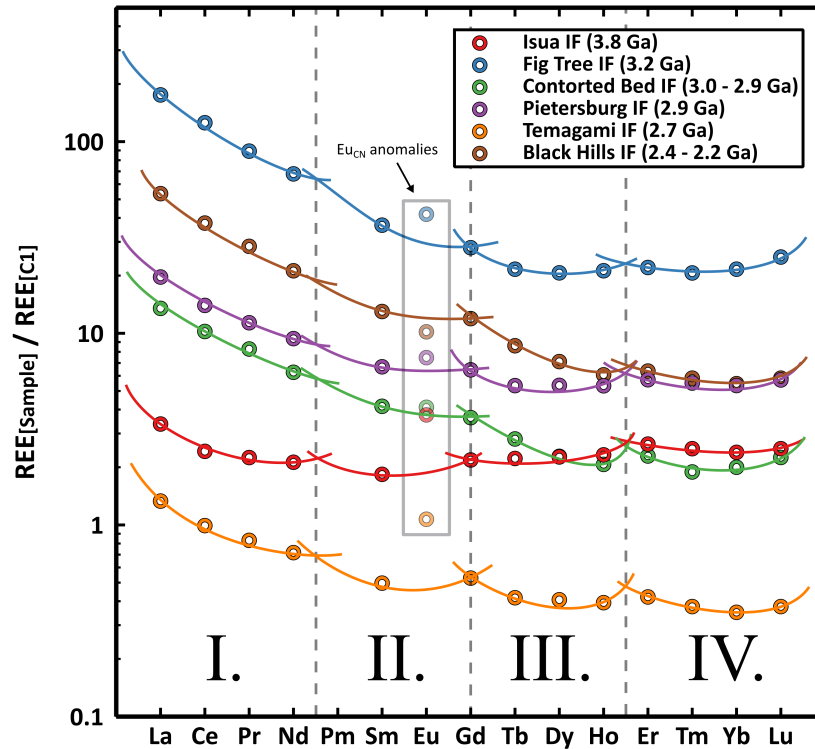


Figure 5.10: The W-type tetrad effect in chondrite-normalized REE data from different BIF, revealing the antiquity of the W-type tetrad effect in seawater. Data from: Isua IF – Frei and Polat, 2007; Fig Tree IF, Barberton Greenstone Belt, South Africa, 3.2 Ga – this study; Contorted Bed IF – Smith et al., 2013; Pietersburg IF – Alexander et al., 2009; Black Hills IF, South Dakota, USA, 2.4–2.2 Ga – Frei et al., 2008; Temagami IF – Bau and Alexander, 2009.

5.5.4 Thorium and Uranium

The Th/U ratios of clastic sedimentary rocks are usually very uniform and close to the continental crustal ratio of 3.9 (Rudnick and Gao, 2003). The Mt. Ruker BIF samples, however, do show distinctively lower Th/U ratios (0.58–1.95), indicating at least minor fractionation of the Th/U pair. The decoupling of Th and U towards lower Th/U ratios is usually due to the oxidation of U^{4+} to U^{6+} in oxidizing environments. During oxidative weathering, for example, the increased mobility of U(VI) relative to Th(IV) and U(IV) compounds produces fractionated below-crustal Th/U ratios in river water and seawater (e.g., Collerson and Kamber, 1999; and references therein). Hence, the rather low Th/U

ratios of the Mt. Ruker BIF may hint at slightly oxidizing conditions in the source area of Th and U during the Mt. Ruker BIF formation. However, the redox level of this surface environment was not high enough to decouple Ce from its REY neighbours to produce Ce anomalies (Fig. 5.5A), as redox-controlled decoupling of Ce from its REY neighbours cannot be observed (Fig. 5.5A). This suggests different redox-sensitivities of the Th/U and Ce/Ce* redox proxies.

The Mt. Ruker BIF, therefore, may be a promising target for further investigations of redox-proxies such as Cr and Mo isotopes.

5.6 Conclusion

We here report results of a geochemical pilot study in which – to the best of our knowledge for the first time – the major and trace element composition of a BIF from Antarctica has been investigated. Individual adjacent metachert and iron-oxide (magnetite/haematite) bands from the 2.5 Ga old Mt. Ruker BIF from the Ruker nunatak in the Prince Charles Mountains, East Antarctica, have been sampled with a micro drill and were analysed with ICP-OES and –MS. These data were compared to those from other Precambrian (B)IF.

The chemical composition of the Mt. Ruker BIF is similar to that of other BIF, but shows an unusual general enrichment of Ni (relative to Zr) and unusually high Ba/Sr ratios in the metachert bands in which barite grains were identified by SEM. It is unclear whether this barite is of primary or secondary (e.g., diagenetic or metamorphic) origin. Low concentrations of elements such as Al, Zr, Hf and Rb indicate the absence of aluminosilicate detritus and reveal the purity of the samples studied.

The REY distribution displays all the features of modern seawater such as enrichment of $LREY_{SN}$ over $HREY_{SN}$, positive La_{SN} , Gd_{SN} and Y_{SN} anomalies, and even the W-type lanthanide tetrad effect. The latter reveals the antiquity of the lanthanide tetrad effect in seawater, as it is the first evidence for the presence of this enigmatic REE feature in early Precambrian seawater.

Small positive Eu_{SN} (but lack of positive Eu_{CN}) anomalies indicate contributions of REY from high-temperature hydrothermal fluids to the REY budget of ambient seawater, and are in full agreement with the general worldwide trend in the evolution of the Eu anomaly in BIFs.

The lack of any Ce anomalies from the REY_{SN} patterns suggests that redox-controlled decoupling of Ce from its REY neighbours was not significant enough to be tracked in

seawater. This is fully compatible with observations in other Early Precambrian (B)IF and suggests that the atmosphere-hydrosphere system during the formation of the Mt. Ruker BIF was less oxic than the modern one.

Super-chondritic Y/Ho ratios in adjacent Fe-oxide and metachert bands reveal the primary origin of the alternating Fe- and Si-rich bands, as diagenetic separation from a homogenous Fe-Si precipitate would have produced lower Y/Ho ratios in the iron-oxide as compared to the metachert bands. The combination of super-chondritic Y/Ho ratios and W-type tetrad effect in pure BIF from Mt. Ruker and elsewhere highlights the fundamental difference between oxidic Fe and Mn precipitates in the Precambrian ocean (i.e. the oxide-facies (B)IF) and oxidic ferromanganese precipitates (i.e. hydrogenetic ferromanganese crusts and nodules) in the Modern and Cenozoic oceans. Comparison of the Y/Ho ratios of the Mt. Ruker BIF to published data show that the Mt. Ruker BIF fits well within the range of Y/Ho ratios shown by pristine and pure (B)IF samples worldwide. Although Y/Ho ratios in the early Precambrian oceans may have been somewhat lower than they are today, positive Y anomalies (i.e. super-chondritic Y/Ho ratios) and the W-type REE tetrad effect obviously have been characteristic features of seawater throughout the entire almost 4 billion years-long geological history of the Earth's oceans.

The results of our pilot study on the Mt. Ruker BIF from East Antarctica strongly suggest that this BIF is a pure, pristine and robust geoarchive and, therefore, a promising target for further investigations of the (bio)geochemical composition of the atmosphere and oceans at the Archaean-Proterozoic boundary, i.e. shortly before the GOE.

5.7 Declaration of Competing Interest

The authors declare that they have no known competing financial interests or personal relationships that could have appeared to influence the work reported in this paper.

5.8 Acknowledgements

We are very grateful to the late Prof. Joachim Hofmann (now retired from Bergakademie TU Freiberg, Germany) who in the mid-1990s generously gave BIF samples from Antarctica to M.B.

We thank Rachid Benaouda (Jacobs University Bremen) for performing the mineralogical SEM analyses and the Mineralogy Department at the Bundesanstalt für

Geowissenschaften und Rohstoffe, Hannover, for access to their facilities. We appreciate the kind assistance of Sebastian Viehmann (University of Vienna) in compiling the Y/Ho data set for BIF. We acknowledge the many fruitful discussions with colleagues in Priority Program SPP-1833 and appreciate funding from the Deutsche Forschungsgemeinschaft (grant BA-2289/8-1).

5.9 References

- Akagi, T., Shabani, M.B., Masuda, A., 1993. Lanthanide tetrad effect in kimuraite [CaY₂(CO₃)₄ · H₂O]: Implication for a new geochemical index. *Geochim. Cosmochim. Acta* 57, 2899–2905.
- Alexander, B., 2008. Trace Element Analyses in Geological Materials using Low Resolution Inductively Coupled Plasma Mass Spectrometry (ICPMS). Jacobs University Technical Report No. 18. p. 73.
- Alexander, B.W., Bau, M., Andersson, P., Dulski, P., 2008. Continentally-derived solutes in shallow Archaean seawater: Rare earth element and Nd isotope evidence in iron formation from the 2.9 Ga Pongola Supergroup, South Africa. *Geochim. Cosmochim. Acta* 72, 378–394.
- Alexander, B.W., Bau, M., Andersson, P., 2009. Neodymium isotopes in Archaean seawater and implications for the marine Nd cycle in Earth's early oceans. *Earth Planet. Sci. Lett.* 283, 144–155.
- Alibert, C., 2016. Rare earth elements in Hamersley BIF minerals. *Geochim. Cosmochim. Acta* 184, 311–328.
- Alibert, C., Kinsley, L., 2016. Ge/Si in Hamersley BIF as tracer of hydrothermal Si and Ge inputs to the Palaeoproterozoic ocean. *Geochim. Cosmochim. Acta* 184, 329–343 Available at. <https://doi.org/10.1016/j.gca.2016.03.027>.
- Alibo, D.S., Nozaki, Y., 1999. Rare earth elements in seawater: Particle association, shalenormalization, and Ce oxidation. *Geochim. Cosmochim. Acta* 63, 363–372.
- Angerer, T., Hagemann, S.G., Danyushevsky, L.V., 2012. Geochemical evolution of the banded iron formation-hosted high-grade iron ore system in the Koolyanobbing greenstone belt, Western Australia. *Econ. Geol.* 107 (4), 599–644.
- Angerer, T., Hagemann, S.G., Walde, D.H.G., Halverson, G.P., Boyce, A.J., 2016. Multiple metal sources in the glaciomarine facies of the Neoproterozoic Jacadigo iron formation in the "Santa Cruz deposit", Corumbá, Brazil. *Precambrian Res.* 275, 369–393.
- Aoki, S., Kabashima, C., Kato, Y., Hirata, T., Komiya, T., 2018. Influence of contamination on banded iron formations in the Isua supracrustal belt, West Greenland: Reevaluation of the Eoarchean seawater compositions. *Geosci. Front.* 9 (4), 1049–1072.
- Appel, P.W.U., 1983. Rare earth elements in the early Archaean Isua iron-formation, West Greenland. *Precambrian Res.* 20 (2–4), 243–258.

- Baldwin, G.J., Turner, E.C., Kamber, B.S., 2012. A new depositional model for glaciogenic neoproterozoic iron formation: Insights from the chemostratigraphy and basin configuration of the rapitan iron formation. *Can. J. Earth Sci.* 49 (2), 455–476.
- Barrat, J.A., Zanda, B., Moynier, F., Bollinger, C., Liorzou, C., Bayon, G., 2012. Geochemistry of CI chondrites: Major and trace elements, and Cu and Zn Isotopes. *Geochim. Cosmochim. Acta* 83, 79–92 Available at: <https://doi.org/10.1016/j.gca.2011.12.011>.
- Basta, F.F., Maurice, A.E., Fontboté, L., Favarger, P.Y., 2011. Petrology and geochemistry of the banded iron formation (BIF) of Wadi Karim and Um Anab, Eastern Desert, Egypt: Implications for the origin of Neoproterozoic BIF. *Precambrian Res.* 187 (3–4), 277–292.
- Bau, M., 1991. Rare-Earth Element Mobility During Hydrothermal and Metamorphic Fluid Rock Interaction and the Significance of the Oxidation-State of Europium. *Chem. Geol.* 93, 219–230.
- Bau, M., 1993. Effects of synand post-depositional processes on the rare-earth element distribution in Precambrian iron-formations. *Eur. J. Mineral.* 5 (2), 257–268.
- Bau, M., 1996. Controls on the fractionation of isovalent trace elements in magmatic and aqueous systems: Evidence from Y/Ho, Zr/Hf, and lanthanide tetrad effect. *Contrib. Mineral. Petrol.* 123, 323–333.
- Bau, M., 1999. Scavenging of dissolved yttrium and rare earths by precipitating iron oxyhydroxide: Experimental evidence for Ce oxidation, Y/Ho fractionation, and lanthanide tetrad effect. *Geochim. Cosmochim. Acta* 63, 67–77.
- Bau, M., Alexander, B., 2006. Preservation of primary REE patterns without Ce anomaly during dolomitization of Mid-Palaeoproterozoic limestone and the potential reestablishment of marine anoxia immediately after the "Great Oxidation Event." *South African J. Geol.* 109, 81–86.
- Bau, M., Alexander, B.W., 2009. Distribution of high field strength elements (Y, Zr, REE, Hf, Ta, Th, U) in adjacent magnetite and chert bands and in reference standards FeR-3 and FeR-4 from the Temagami iron-formation, Canada, and the redox level of the Neoproterozoic ocean. *Precambrian Res.* 174, 337–346.
- Bau, M., Dulski, P., 1992. Small-scale variations of the rare-earth element distribution in Precambrian iron-formations. *Eur. J. Mineral.* 4, 1429–1433.
- Bau, M., Dulski, P., 1994. Evolution of the Yttrium-Holmium Systematics of Seawater Through Time. *Mineral. Mag.* 58A, 61–62.
- Bau, M., Dulski, P., 1996. Distribution of yttrium and rare-earth elements in the Penge and Kuruman iron-formations, Transvaal Supergroup, South Africa. *Precambrian Res.* 79, 37–55.
- Bau, M., Koschinsky, A., 2009. Oxidative scavenging of cerium on hydrous Fe oxide: Evidence from the distribution of rare earth elements and yttrium between Fe oxides and Mn oxides in hydrogenetic ferromanganese crusts. *Geochem. J.* 43, 37–47.
- Bau, M., Möller, P., 1993. Rare earth element systematics of the chemically precipitated component in early precambrian iron formations and the evolution of the terrestrial atmosphere-hydrosphere-lithosphere system. *Geochim. Cosmochim. Acta* 57, 2239–2249.

- Bau, M., Koschinsky, A., Dulski, P., Hein, J.R., 1996. Comparison of the partitioning behaviours of yttrium, rare earth elements, and titanium between hydrogenetic marine ferromanganese crusts and seawater. *Geochim. Cosmochim. Acta* 60, 1709–1725.
- Bau, M., Möller, P., Dulski, P., 1997. Yttrium and lanthanides in eastern Mediterranean seawater and their fractionation during redox-cycling. *Mar. Chem.* 56 (1–2), 123–131.
- Bau, M., Usui, A., Pracejus, B., Mita, N., Kanai, Y., Irber, W., Dulski, P., 1998. Geochemistry of low-temperature water-rock interaction: Evidence from natural waters, andesite, and iron-oxyhydroxide precipitates at Nishiki-numa iron-spring, Hokkaido, Japan. *Chem. Geol.* 151, 293–307.
- Bau, M., Romer, R.L., Lüders, V., Beukes, N.J., 1999. Pb, O, and C isotopes in silicified Mooidraai dolomite (Transvaal Supergroup, South Africa): Implications for the composition of Palaeoproterozoic seawater and "dating" the increase of oxygen in the Precambrian atmosphere. *Earth Planet. Sci. Lett.* 174, 43–57.
- Bau, M., Schmidt, K., Koschinsky, A., Hein, J., Kuhn, T., Usui, A., 2014. Discriminating between different genetic types of marine ferro-manganese crusts and nodules based on rare earth elements and yttrium. *Chem. Geol.* 381, 1–9 Available at. <https://doi.org/10.1016/j.chemgeo.2014.05.004>.
- Bau, M., Schmidt, K., Pack, A., Bendel, V., Kraemer, D., 2018. The European Shale: An improved data set for normalization of rare earth element and yttrium concentrations in environmental and biological samples from Europe. *Appl. Geochem.* 90, 142–149.
- Beukes, N.J., Gutzmer, J., 2008. Origin and paleoenvironmental significance of major iron formations at the Archaean-Palaeoproterozoic boundary. *Rev. Econ. Geol.* 15, 5–47. Beukes, N.J., Klein, C., 1990. Geochemistry and sedimentology of a facies transition from microbanded to granular iron-formation in the early Proterozoic Transvaal Supergroup, South Africa. *Precambrian Res.* 47, 99–139.
- Boger, S.D., Wilson, C.J.L., Fanning, C.M., 2006. An Archaean province in the southern Prince Charles Mountains, East Antarctica: U/Pb zircon evidence for c. 3170 Ma granite plutonism and c. 2780 Ma partial melting and orogenesis. *Precambrian Res.* 145, 207–228.
- Bolhar, R., Kamber, B.S., Moorbath, S., Fedo, C.M., Whitehouse, M.J., 2004. Characterization of early Archaean chemical sediments by trace element signatures. *Earth Planet. Sci. Lett.* 222, 43–60.
- Bolhar, R., Kamber, B.S., Moorbath, S., Whitehouse, M.J., Collerson, K.D., 2005a. Chemical characterization of earth's most ancient clastic metasediments from the Isua Greenstone Belt, southern West Greenland. *Geochim. Cosmochim. Acta* 69 (6), 1555–1573.
- Bolhar, R., Van Kranendonk, M.J., Kamber, B.S., 2005b. A trace element study of sideritejasper banded iron formation in the 3.45 Ga Warrawoona Group, Pilbara Craton Formation from hydrothermal fluids and shallow seawater. *Precambrian Res.* 137 (1–2), 93–114.
- Cates, N.L., Mojzsis, S.J., 2009. Metamorphic zircon, trace elements and Neoproterozoic metamorphism in the ca. 3.75 Ga Nuvvuagittuq supracrustal belt, Québec (Canada). *Chem. Geol.* 261 (1–2), 99–114.
- Collerson, K.D., Kamber, B.S., 1999. Evolution of the continents and the atmosphere

- inferred from Th-U-Nb systematics of the depleted mantle. *Science* (80-). 283, 1519–1522.
- Danielson, A., Möller, P., Dulski, P., 1992. The europium anomalies in banded iron formations and the thermal history of the oceanic crust. *Chem. Geol.* 97 (1–2), 89–100.
- Delvigne, C., Cardinal, D., Hofmann, A., André, L., 2012. Stratigraphic changes of Ge/Si, REE + Y and silicon isotopes as insights into the deposition of a Mesoarchaeon banded iron formation. *Earth Planet. Sci. Lett.* 355–356, 109–118.
- Derry, L.A., Jacobsen, S.B., 1990. The chemical evolution of Precambrian seawater: Evidence from REEs in banded iron formations. *Geochim. Cosmochim. Acta* 54, 2965–2977.
- Døssing, L.N., Frei, R., Stendal, H., Mapeo, R.B.M., 2009. Characterization of enriched lithospheric mantle components in ~2.7 Ga Banded Iron Formations: An example from the Tati Greenstone Belt, Northeastern Botswana. *Precambrian Res.* 172 (3–4), 334–356.
- Dulski, P., 2001. Reference materials for geochemical studies: new analytical data by ICPMS and critical discussion of reference values. *Geostand. Newslett.* 25, 87–125.
- Elderfield, H., Greaves, M.J., 1982. The rare earth elements in seawater. *Nature* 296, 214–219.
- Elderfield, H., Whitfield, M., Burton, J.D., Bacon, M.P., Liss, P.S., 1988. The oceanic chemistry of the rare-earth elements. *Philosophical Transactions of the Royal Society of London. Series A, Math. Phys. Sci.* 325 (1583), 105–126.
- El-Shazly, A.K., Khalil, K.I., Helba, H.A., 2019. Geochemistry of banded iron formations and their host rocks from the Central Eastern Desert of Egypt: A working genetic model and tectonic implications. *Precambrian Res.* 325, 192–216.
- Fabre, S., Nédélec, A., Poitrasson, F., Strauss, H., Thomazo, C., Nogueira, A., 2011. Iron and sulphur isotopes from the Carajás mining province (Pará, Brazil): Implications for the oxidation of the ocean and the atmosphere across the Archaean-Proterozoic transition. *Chem. Geol.* 289 (1–2), 124–139.
- Frei, R., Polat, A., 2007. Source heterogeneity for the major components of ~ 3.7 Ga Banded Iron Formations (Isua Greenstone Belt, Western Greenland): Tracing the nature of interacting water masses in BIF formation. *Earth Planet. Sci. Lett.* 253, 266–281.
- Frei, R., Dahl, P.S., Duke, E.F., Frei, K.M., Hansen, T.R., Frandsson, M.M., Jensen, L.A., 2008. Trace element and isotopic characterization of Neoproterozoic and Palaeoproterozoic iron formations in the Black Hills (South Dakota, USA): Assessment of chemical change during 2.9–1.9 Ga deposition bracketing the 2.4–2.2 Ga first rise of atmospheric oxygen. *Precambrian Res.* 162 (3–4), 441–474.
- Frei, R., Gaucher, C., Poulton, S.W., Canfield, D.E., 2009. Fluctuations in Precambrian atmospheric oxygenation recorded by chromium isotopes. *Nature* 461 (7261), 250–253.
- Frei, R., Døssing, L.N., Gaucher, C., Boggiani, P.C., Frei, K.M., Bech ártíng, T., Crowe, S.A., Freitas, B.T., 2017. Extensive oxidative weathering in the aftermath of a late Neoproterozoic glaciation – Evidence from trace element and chromium isotope records in the Urucum district (Jacadigo Group) and Puga iron formations (Mato

- Grosso do Sul, Brazil). *Gondwana Res.* 49, 1–20.
- Friend, C.R.L., Nutman, A.P., Bennett, V.C., Norman, M.D., 2008. Seawater-like trace element signatures (REE + Y) of Eoarchaeon chemical sedimentary rocks from southern West Greenland, and their corruption during high-grade metamorphism. *Contrib. Mineral. Petrol.* 155 (2), 229–246.
- Fryer, B.J., 1977. Rare earth evidence in iron-formations for changing Precambrian oxidation states. *Geochim. Cosmochim. Acta* 41 (3), 361–367.
- Ghosh, R., Baidya, T.K., 2017. Using BIF magnetite of the Badampahar greenstone belt, Iron Ore Group, East Indian Shield to reconstruct the water chemistry of a 3.3–3.1 Ga sea during iron oxyhydroxides precipitation. *Precambrian Res.* 301 (September), 102–112.
- Gourcerol, B., Thurston, P.C., Kontak, D.J., Côté-Mantha, O., 2015. Interpretations and implications of LA ICP-MS analysis of chert for the origin of geochemical signatures in banded iron formations (BIFs) from the Meadowbank gold deposit, Western Churchill Province, Nunavut. *Chem. Geol.* 410, 89–107.
- Harley, S.L., Kelly, N.M., 2007. Ancient Antarctica: The Archaean of the East Antarctic Shield. In *Earth's Oldest Rocks. Develop. Precamb. Geol.* 15, 149–186.
- Saleh, T.A., Fadillah, G., 2013. Antarctica and supercontinent evolution: historical perspectives, recent advances and unresolved issues. *Geological Society London Special Publications* 383, 1–34.
- Haugaard, R., Frei, R., Stendal, H., Konhauser, K., 2013. Petrology and geochemistry of the ~2.9 Ga Itilliarsuk banded iron formation and associated supracrustal rocks, West Greenland: Source characteristics and depositional environment. *Precambrian Res.* 229, 150–176.
- Haugaard, R., Pecoits, E., Lalonde, S., Rouxel, O., Konhauser, K., 2016. The Joffre banded iron formation, Hamersley Group, Western Australia: Assessing the palaeoenvironment through detailed petrology and chemostratigraphy. *Precambrian Res.* 273, 12–37.
- Hou, K., Li, Y., Gao, J., Liu, F., Qin, Y., 2014. Geochemistry and si-o-fe isotope constraints on the origin of banded iron formations of the yuanjiacun formation, lvliang group, shanxi, china. *Ore Geol. Rev.* 57, 288–298.
- James, L., 1954. Sedimentary facies of iron formation. *Econ. Geol.* 49, 235–293.
- Kamber, B.S., Webb, G.E., 2001. The geochemistry of late Archaean microbial carbonate: Implications for ocean chemistry and continental erosion history. *Geochim. Cosmochim. Acta* 65, 2509–2525.
- Kamber, B.S., Bolhar, R., Webb, G.E., 2004. Geochemistry of late Archaean stromatolites from Zimbabwe: Evidence for microbial life in restricted epicontinental seas. *Precambrian Res.* 132, 379–399.
- Kamber, B.S., Webb, G.E., Gallagher, M., 2014. The rare earth element signal in Archaean microbial carbonate: Information on ocean redox and biogenicity. *J. Geol. Soc. Lond.* 171, 745–763.
- Kamenev, E., Andronikov, A.V., Mikhalsky, E.V., Krasnikov, N.N., Stüwe, K., 1993. Soviet geological maps of the Prince Charles Mountains, East Antarctic Shield,

- Australian Journal of Earth Sciences: An International Geoscience Journal of the Geological Society of Australia. *Aust. J. Earth Sci.* 40, 501–517.
- Klein, C., 2005. Some Precambrian banded iron-formations (BIFs) from around the world: Their age, geologic setting, mineralogy, metamorphism, geochemistry, and origin. *Am. Mineral.* 90, 1473–1499.
- Klein, C., Beukes, N.J., 1989. Geochemistry and sedimentology of a facies transition from limestone to iron-formation deposition in the early Proterozoic Transvaal Supergroup, South Africa. *Econ. Geol.* 84 (7), 1733–1774.
- Klein, C., Ladeira, E.A., 2002. Petrography and geochemistry of the least altered banded iron-formation of the Archaean Carajás formation, northern Brazil. *Econ. Geol.* 97 (3), 643–651.
- Konhauser, K.O., Pecoits, E., Lalonde, S.V., Papineau, D., Nisbet, E.G., Barley, M.E., Arndt, N.T., Zahnle, K., Kamber, B.S., 2009. Oceanic nickel depletion and a methanogen famine before the Great Oxidation Event. *Nature* 458, 750–753.
- Konhauser, K.O., Planavsky, N.J., Hardisty, D.S., Robbins, L.J., Warchola, T.J., Haugegaard, R., Lalonde, S.V., Partin, C.A., Oonk, P.B.H., Tsikos, H., Lyons, T.W., Bekker, A., Johnson, C.M., 2017. Iron formations: A global record of Neoproterozoic to Palaeoproterozoic environmental history. *Earth Sci. Rev.* 172 (April), 140–177.
- Krämer, D., Tepe, N., Pourret, O., Bau, M., 2017. Negative cerium anomalies in manganese (hydr)oxide precipitates due to cerium oxidation in the presence of dissolved siderophores. *Geochim. Cosmochim. Acta* 196, 197–208 Available at. <https://doi.org/10.1016/j.gca.2016.09.018>.
- Krapež, B., Barley, M.E., Pickard, A.L., 2003. Hydrothermal and resedimented origins of the precursor sediments to banded iron formation: Sedimentological evidence from the Early Palaeoproterozoic Brockman Supersequence of Western Australia. *Sedimentology* 50, 979–1011.
- Kreitsmann, T., Lepland, A., Bau, M., Prave, A., Paiste, K., Mänd, K., Sepp, H., Martma, T., Romashkin, A.E., Kirsimäe, K., 2020. Oxygenated conditions in the aftermath of the Lomagundi-Jatuli Event. *Precambrian Res.* 347, 105855 Available at. <https://doi.org/10.1016/j.precamres.2020.105855>.
- Kuhn, T., Bau, M., Blum, N., Halbach, P., 1998. Origin of negative Ce anomalies in mixed hydrothermal-hydrogenetic Fe/Mn crusts from the Central Indian Ridge. *Earth Planet. Sci. Lett.* 163, 207–220.
- Le Wang, C., Zhang, L.C., Lan, C.Y., Dai, Y.P., 2014. Rare earth element and yttrium compositions of the Palaeoproterozoic Yuanjiacun BIF in the Lüliang area and their implications for the Great Oxidation Event (GOE). *Sci. China Earth Sci.* 57 (10), 2469–2485.
- Lechte, M., Wallace, M., 2016. Sub-ice shelf ironstone deposition during the neoproterozoic sturtian glaciation. *Geology* 44 (11), 891–894.
- Liu, X., Zhao, Y., Chen, H., Song, B., 2017. New zircon U/Pb and Hf/Nd isotopic constraints on the timing of magmatism, sedimentation and metamorphism in the northern Prince Charles Mountains, East Antarctica. *Precambrian Res.* 299, 15–33.
- Lottermoser, B.G., Ashley, P.M., 2000. Geochemistry, petrology and origin of Neoproterozoic ironstones in the eastern part of the Adelaide Geosyncline, South Australia.

- Precambrian Res. 101 (1), 49–67.
- Masuda, A., Akagi, T., 1989. Lanthanide tetrad effect observed in leucogranites from China. *Geochem. J.* 23, 245–253.
- Masuda, A., Ikeuchi, Y., 1979. Lanthanide tetrad effect observed in marine environment. *Geochem. J.* 13, 19–22.
- Masuda, A., Kawakami, O., Dohmoto, Y., Takenaka, T., 1987. Lanthanide two mutually tetrad opposite effects types, in nature. *Geochem. J.* 21, 119–124.
- McLennan, S.M., 1989a. Rare earth elements in sedimentary rocks: influence of provenance and sedimentary processes. In: Lipin, B.R., McKay, G.A. (Eds.), *Geochemistry and Mineralogy of Rare Earth Elements*, *Rev. Miner.* 21, pp. 169–200 (Miner. Soc. Am.).
- McLennan, S.M., 1989b. Rare Earth Elements in Sedimentary Rocks: Influence of Provenance and Sedimentary Processes. In: Lipin, B.R., McKay, G.A. (Eds.), *Geochemistry and mineralogy of rare earth elements: Mineralogical Society of America Reviews in Mineralogy*, pp. 169–200.
- Mikhalsky, E.V., Beliatsky, B.V., Sheraton, J.W., Roland, N.W., 2006. Two distinct Precambrian terranes in the Southern Prince Charles Mountains, East Antarctica: SHRIMP dating and geochemical constraints. *Gondwana Res.* 9, 291–309.
- Mikhalsky, E.V., Henjes-Kunst, F., Belytsky, B.V., Roland, N.W., Sergeev, S.A., 2010. New Sm/Nd, Rb/Sr, U/Pb and Hf isotope systematics for the southern Prince Charles Mountains (East Antarctica) and its tectonic implications. *Precambrian Res.* 182, 101–123.
- Mloszewska, A.M., Pecoits, E., Cates, N.L., Mojzsis, S.J., O’Neil, J., Robbins, L.J., Konhauser, K.O., 2012. The composition of Earth’s oldest iron formations: The Nuvvuagittuq Supracrustal Belt (Québec, Canada). *Earth Planet. Sci. Lett.* 317–318, 331–342.
- Möller, P., Bau, M., 1993. Rare-earth patterns with positive cerium anomaly in alkaline waters from Lake Van, Turkey. *Earth Planet. Sci. Lett.* 117 (3–4), 671–676.
- Moon, I., Lee, I., Yang, X., 2017. Geochemical constraints on the genesis of the Algomatype banded iron formation (BIF) in Yishui County, western Shandong Province, North China Craton. *Ore Geol. Rev.* 89 (July 2016), 931–945.
- Peng, Z., Wang, C., Tong, X., Zhang, L., Zhang, B., 2018. Element geochemistry and neodymium isotope systematics of the Neoproterozoic banded iron formations in the Qingyuan greenstone belt, North China Craton. *Ore Geol. Rev.* 102 (August), 562–584.
- Peppard, D.F., Mason, G.W., Lewey, S., 1969. A tetrad effect in the liquid-liquid extraction ordering of lanthanides(III). *J. Inorg. Nucl. Chem.* 31, 2271–2272.
- Phillips, G., Wilson, C.J.L., Fitzsimons, I.C.W., 2005. Stratigraphy and Structure of the Southern Prince Charles Mountains, East Antarctica. *Terra Antarctica* 12, 69–86.
- Phillips, G., Wilson, C.J.L., Campbell, I.H., Allen, C.M., 2006. U-Th-Pb detrital zircon geochronology from the southern Prince Charles Mountains, East Antarctica-Defining the Archaean to Neoproterozoic Ruker Province. *Precambrian Res.* 148, 292–306.
- Pickard, A.L., 2002. SHRIMP U/Pb zircon ages of tuffaceous mudrocks in the Brockman Iron Formation of the Hamersley Range, Western Australia. *Aust. J. Earth Sci.* 49,

- 491–507.
- Pickard, A.L., 2003. SHRIMP U/Pb zircon ages for the Palaeoproterozoic Kuruman Iron Formation, Northern Cape Province, South Africa: evidence for simultaneous BIF deposition on Kaapvaal and Pilbara Cratons. *Precambrian Res.* 41.
- Piegras, D.J., Jacobsen, S.B., 1992. The behaviour of rare earth elements in seawater: Precise determination of variations in the North Pacific water column. *Geochim. Cosmochim. Acta* 56 (5), 1851–1862.
- Planavsky, N., Bekker, A., Rouxel, O.J., Kamber, B., Hofmann, A., Knudsen, A., Lyons, T.W., 2010. Rare Earth Element and yttrium compositions of Archaean and Palaeoproterozoic Fe formations revisited: New perspectives on the significance and mechanisms of deposition. *Geochim. Cosmochim. Acta* 74, 6387–6405.
- Raju, P.V.S., 2009. Petrography and geochemical behaviour of trace element, REE and precious metal signatures of sulphidic banded iron formations from the Chikkasiddavanahalli area, Chitradurga schist belt, India. *J. Asian Earth Sci.* 34 (5), 663–673.
- Rasmussen, B., Meier, D.B., Krapež, B., Muhling, J.R., 2013. Iron silicate microgranules as precursor sediments to 2.5-billion-year-old banded iron formations. *Geology* 41, 435–438.
- Rudnick, R.L., Gao, S., 2003. Composition of the Continental Crust. *Treatise Geochem.* 3, 1–64.
- Sampaio, G.M.S., Enzweiler, J., 2015. New ICP-MS results for trace elements in five ironformation reference materials. *Geostand. Geoanal. Res.* 39, 105–119.
- Schier, K., Bau, M., Münker, C., Beukes, N., Viehmann, S., 2018. Trace element and Nd isotope composition of shallow seawater prior to the Great Oxidation Event: Evidence from stromatolitic bioherms in the Palaeoproterozoic Rooinekke and Nelani Formations, South Africa. *Precambrian Res.* 315, 92–102.
- Schier, K., Bau, M., Smith, A.J.B., Beukes, N.J., Coetzee, L.L., Viehmann, S., 2020. Chemical evolution of seawater in the Transvaal Ocean between 2426 Ma (Ongeluk Large Igneous Province) and 2413 Ma ago (Kalahari Manganese Field). *Gondwana Res.* <https://doi.org/10.1016/j.gr.2020.09.001>.
- Slack, J.F., Grenne, T., Bekker, A., 2009. Seafloor-hydrothermal Si-Fe-Mn exhalites in the Pecos greenstone belt, New Mexico, and the redox state of ca. 1720 Ma deep-seawater. *Geosphere* 5 (3), 302–314.
- Smith, A.J.B., 2007. The Palaeo-environmental Significance of the Ironformations and Iron-rich Mudstones of the Mesoarchean Witwatersrand-Mozaan Basin. University of Johannesburg, South Africa.
- Smith, A.J.B., Beukes, N.J., 2016. Palaeoproterozoic banded iron formation-hosted high-grade haematite iron ore deposits of the Transvaal Supergroup, South Africa. *Episodes* 39 (2), 269–284.
- Smith, A.J.B., Beukes, N.J., Gutzmer, J., 2013. The composition and depositional environments of Mesoarchean iron formations of the West Rand Group of the Witwatersrand Supergroup, South Africa. *Econ. Geol.* 108 (1), 111–134.
- Spier, C.A., de Oliveira, S.M.B., Sial, A.N., Rios, F.J., 2007. Geochemistry and genesis of the banded iron formations of the Cauê Formation, Quadrilátero Ferrífero, Minas Gerais, Brazil. *Precambrian Res.* 152 (3–4), 170–206.

- Stern, R.J., Mukherjee, S.K., Miller, N.R., Ali, K., Johnson, P.R., 2013. ~ 750 Ma banded iron formation from the Arabian-Nubian Shield—Implications for understanding neoproterozoic tectonics, volcanism, and climate change. *Precambrian Res.* 239, 79–94.
- Taylor, S.R., McLennan, S.M., 1985. *The Continental Crust: Its Composition and Evolution*. Blackwell, Oxford, p. 312.
- Toulkeridis, T., Goldstein, S.L., Clauer, N., Kröner, A., Todt, W., Schidlowski, M., 1998. Sm/Nd, Rb/Sr and Pb/Pb dating of silicic carbonates from the early Archaean Barberton Greenstone Belt, South Africa: Evidence for post-depositional isotopic resetting at low temperature. *Precambrian Res.* 92 (2), 129–144.
- Viehmann, S., Hoffmann, J.E., Münker, C., Bau, M., 2014. Decoupled Hf/Nd isotopes in Neoproterozoic seawater reveal weathering of emerged continents. *Geology* 42, 115–118.
- Viehmann, S., Bau, M., Hoffmann, J.E., Münker, C., 2015a. Geochemistry of the Krivoy Rog Banded Iron Formation, Ukraine, and the impact of peak episodes of increased global magmatic activity on the trace element composition of Precambrian seawater. *Precambrian Res.* 270, 165–180.
- Viehmann, S., Bau, M., Smith, A.J.B., Beukes, N.J., Dantas, E.L., Bühn, B., 2015b. The reliability of ~ 2.9 Ga old Witwatersrand banded iron formations (South Africa) as archives for Mesoproterozoic seawater: Evidence from REE and Nd isotope systematics. *J. Afr. Earth Sci.* 111, 322–334.
- Viehmann, S., Bau, M., Bühn, B., Dantas, E.L., Andrade, F.R.D., Walde, D.H.G., 2016. Geochemical characterization of Neoproterozoic marine habitats: Evidence from trace elements and Nd isotopes in the Urucum iron and manganese formations, Brazil. *Precambrian Res.* 282, 74–96 Available at. <https://doi.org/10.1016/j.precamres.2016.07.006>.
- Viehmann, S., Bau, M., Hoffmann, E.J., Münker, C., 2018. Decoupled Hf and Nd isotopes in suspended particles and in the dissolved load of Late Archaean seawater. *Chem. Geol.* 483, 111–118.
- Wang, C., Wu, H., Li, W., Peng, Z., Zhang, L., Zhai, M., 2017. Changes of Ge/Si, REE + Y and Sm Nd isotopes in alternating Fe and Si-rich mesobands reveal source heterogeneity of the ~ 2.54 Ga Sijiaying banded iron formation in Eastern Hebei, China. *Ore Geol. Rev.* 80, 363–376.
- Warchola, T., Lalonde, S.V., Pecoits, E., von Gunten, K., Robbins, L.J., Alessi, D.S., Philippot, P., Konhauser, K.O., 2018. Petrology and geochemistry of the Boolgeeda Iron Formation, Hamersley Basin, Western Australia. *Precambrian Res.* 316 (November 2017), 155–173.
- Webb, G.E., Kamber, B.S., 2000. Rare earth elements in Holocene reefal microbialites: a new shallow seawater proxy. *Geochimica et Cosmochimica Acta* 64, 1557–1565. [https://doi.org/10.1016/S0016-7037\(99\)00400-7](https://doi.org/10.1016/S0016-7037(99)00400-7).
- Zhu, M., Dai, Y., Zhang, L., Wang, C., Liu, L., 2015. Geochronology and geochemistry of the Nanfen iron deposit in the Anshan-Benxi area, North China Craton: Implications for ~ 2.55 Ga crustal growth and the genesis of high-grade iron ores. *Precambrian Res.* 260, 23–38.

A first look at the gallium-aluminium systematics of Early Earth's seawater: Evidence from Neoproterozoic banded iron formation

David M. Ernst^{a*}, Dieter Garbe-Schönberg^b, Dennis Kraemer^c, Michael
Bau^a

^a *School of Science, Constructor University Bremen, Campus Ring 1, 28759 Bremen,
Germany*

formerl Jacobs University Bremen

^b *Institute of Geosciences, Kiel University, Ludewig-Meyn-Straße 10, 24118 Kiel,
Germany*

^c *Federal Institute for Geosciences and Natural Resources, Stilleweg 2, 30655 Hannover,
Germany*

published* in

Geochimica et Cosmochimica Acta

Geochimica et Cosmochimica Acta 355 (2023) 48–61

*The first submission of this PhD thesis contained the preliminary "under review"
version of this manuscript.

* *Corresponding author. Email adress: dernst@constructor.university (D. M. Ernst)*

<https://doi.org/10.1016/j.gca.2023.06.019>

Received 2 February 2023; Accepted 16 June 2023

Available online 19 June 2023

0016-7037/© 2023 Elsevier Ltd. All rights reserved.

6 Gallium-aluminium systematics in the Temagami BIF

6.1 Abstract

Geochemical proxies archived in banded iron formations (BIFs) can provide information on the physico-chemical conditions in the Precambrian atmosphere-hydrosphere system and the element sources to ambient Early Earth's seawater. We here report results of the first investigation of the Ga-Al systematics of BIFs and use adjacent magnetite and metachert bands of the well-studied and very pure 2.7 Ga-old Temagami BIF in Ontario, Canada, in an attempt to test the suitability of the Ga/Al ratio as a geochemical proxy. Due to very low Ga concentrations in BIFs and multiple mass interferences on the stable isotopes ^{69}Ga and ^{71}Ga , we conducted comparative analyses of dissolved samples with sector-field (SF-)ICP-MS and tandem ICP-MS/MS as well as laser-ablation (LA-)SF-ICP-MS on nano-particulate pressed powder tablets (NP tablets). The unexpected results indicate uniform Ga/Al weight ratios between 2.0×10^{-4} and 7×10^{-4} for the Temagami BIF, i.e. Ga/Al ratios that are slightly above those of potential clastic detritus but well below those of modern seawater or marine hydrothermal fluids. Consistent results from solution SF- and ICP-MS/MS and a two-component mixing experiment with BIF reference material IF-G and synthetic pure quartz sand corroborate the high analytical quality of these Ga and Al data. The Ga/Al ratios of the metachert bands show the same range of Ga/Al ratios as the magnetite bands and appear to be dominated by small amounts of finely dispersed Fe oxide particles that were deposited together with the chert. The Ga/Al ratios of the magnetite bands either suggest that (in contrast to other trace elements such as the rare earth elements and Y) Ga and Al were fractionated from each other during scavenging from Archean seawater by Fe (oxyhydr)oxides or that ambient Temagami seawater had significantly lower Ga/Al ratios than modern seawater, possibly due to different weathering, riverine, and estuarine processes in the Archean. While these first results demonstrate the potential of Ga-Al systematics as an additional

geochemical tool for studies of Early Earth, they also reveal the knowledge gaps that still need to be addressed in future investigations.

6.2 Introduction

Gallium and aluminium are two group 13 metals with the same ionic charge and similar atomic radii (Ga 2.33 Å, Al 2.39 Å; Rahm et al., 2016). Due to their almost identical physicochemical properties, Ga and Al are tightly coupled in various geochemical systems and processes and are, therefore, considered geochemical partners. Despite their coherent behaviour and in spite of the considerable interest in their biogeochemistry, only a few studies focus on both Ga and Al, i.e. on the geochemical partners (Ho et al., 2019; Orians and Bruland, 1988a; Shiller, 1988, 1998; Shiller and Frilot, 1996). However, Ga, as an essential material for semiconductors, is on the list of critical raw materials (e.g., European Commission, 2023), and Al is one of the most widely used metals overall. The increasing use and, hence, growing demand for these raw materials and the resulting release (during production, wear and tear and disposal) into the Earth's ecosystems make it crucial to understand better the geochemical behaviour of Ga and Al in the Earth's critical zone.

In geological and geochemical processes, the coupled behaviour of Ga and Al leads to only slight variation of Ga/Al ratios in igneous and clastic sedimentary rocks (e.g., granites, basalts, shales or sandstones; see also Fig. 6.1 and estimates of the Ga/Al ratio of average upper continental crust fall between 1.9×10^{-4} and 4.1×10^{-4} g/g (Ga/Al mass ratios are always given in g Ga per g Al throughout this contribution; data from Chen et al., 2001; Clarke et al., 1989; De Argollo and Schilling, 1978; Fedo et al., 1996; Goodman, 1972; Le Roex, 1985; Li and Schoonmaker, 2014; Liang et al., 2009; Rudnick and Gao, 2003; Shiller and Frilot, 1996). In the following, this narrow Ga/Al range of igneous and clastic sedimentary rocks will be referred to as the “*crustal*” Ga/Al ratio. It is corroborated by published Ga/Al ratios of crustal rocks (igneous and clastic sedimentary rocks), soils, river waters, seawater, hydrothermal fluids and ferromanganese (Fe-Mn) crusts (Fig. 6.1). Additionally, the two geochemical databases of EarthChem (<https://www.earthchem.org/petdb>) and SGP (Sedimentary Geochemistry and Paleoenvironments Project; Farrell et al., 2021) were used to compute two non-screened compilations of Ga/Al ratios in igneous (Fig. 6.2a) and sedimentary rocks (Fig. 6.2b), respectively. Both databases were accessed on 07.12.2022, and all entries containing Ga and Al data were sampled. The respective histograms in Fig. 6.2 further corroborate the rather narrow

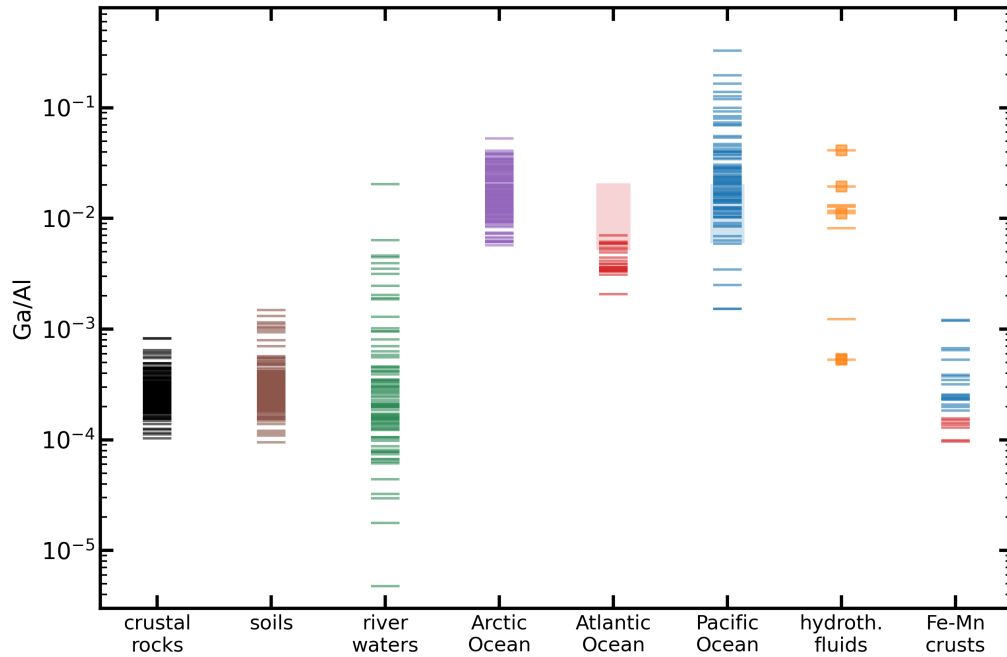


Figure 6.1: Compilation of data for Ga/Al ratios in crustal rocks, soils, river waters, seawaters, hydrothermal fluids and Fe-Mn crusts. The ratios were all transferred into mass ratios [mg/mg]. Data from: (crustal rocks) Breiter et al., 2013; Clarke et al., 1989; De Argollo and Schilling, 1978; Fedo et al., 1996; Goodman, 1972; Le Roex, 1985; McLennan et al., 1983; Sanematsu et al., 2011; Shiller and Frilot, 1996; Tarney et al., 1977; (soils) Chen et al., 2001; Liang et al., 2009; Sanematsu et al., 2011; (river waters) Gaillardet et al., 2013; Pokrovsky and Schott, 2002; Shiller and Frilot, 1996; (seawater) Charette et al., 2020; Ho et al., 2019; Orians and Bruland, 1988; Parker et al., 2016; Shiller, 1988; Shiller and Bairamadgi, 2006; (hydrothermal fluids) Schmidt et al., 2017; (Fe-Mn crusts) Schier et al., 2021.

Ga/Al ratio range for crustal rocks. The igneous rock Ga/Al data show a very smooth and uniform distribution between 1.4×10^{-4} and 4.2×10^{-4} (5 %–95 % percentile; $n = 17,798$) with a median of 2.2×10^{-4} . The sedimentary rock Ga/Al data cover a very similar narrow range between 1.5×10^{-4} and 5.4×10^{-4} (5 %–95 % percentile; $n = 18,868$) and a median of 2.5×10^{-4} . However, the sedimentary data show several individual peaks that probably result from lack of a thorough screening procedure which sort out strongly weathered or metamorphosed lithologies, for example. Furthermore, as discussed below (see Materials and Methods section), Ga can be affected by various mass spectral interferences when analysed with mass spectrometry systems, highlighting the need for verification of data quality with appropriate reference materials.

6 Gallium-aluminium systematics in the Temagami BIF

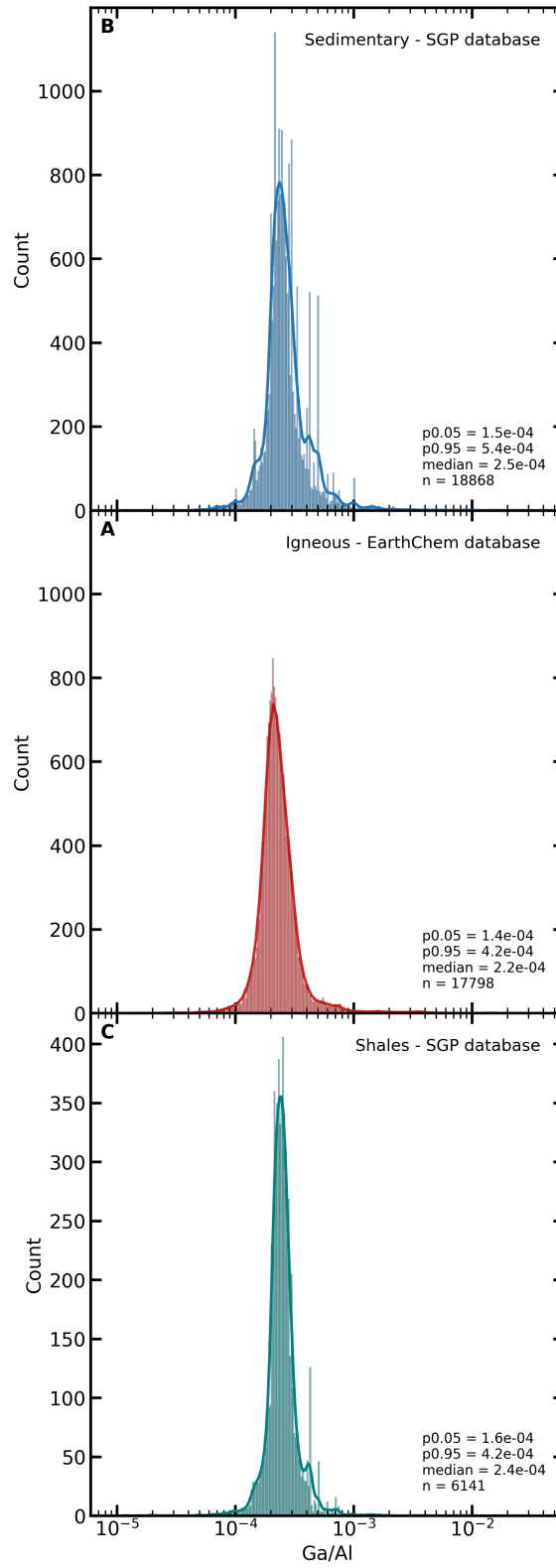


Figure 6.2

Figure 6.2: Histograms and density distribution (bold lines) of Ga/Al ratios in a) igneous and b) sedimentary rocks from the EarthChem (www.earthchem.org/petdb) and SGP (Farrell et al., 2021) databases, respectively. Both datasets were gathered on 07.12.2022. All entries that contained Ga and Al data were sampled. The igneous rocks in (a) comprise the rock types volcanic, plutonic, metamorphic, xenolith, exotic, ore, sedimentary and vein. The sedimentary rocks in (b) comprise the lithology classes shale, siltstone, carbonate, phosphorite, ore, mudstone, lime mudstone, chert, sandstone, dolomicrite, dolomudstone, limestone, conglomerate, dolomite, wackestone, dolograinstone, anhydrite, oil shale, arkose, marlstone, coal, argillite, arenite, gossan, gypsum, greywacke, iron formation, claystone, grainstone, crystalline limestone. The 5 % (p0.05) and 95 % (p0.95) percentile, median value and number of entries (n) are given in both plots. Plot (c) comprises the subset of shales from the sedimentary rocks in (b).

However, Ga and Al behave slightly differently in aqueous systems and hence may fractionate from each other, leading to increasing or decreasing Ga/Al ratios in the dissolved and solid phases. A detailed summary of the currently known behaviour and decoupling of Ga and Al during weathering in river waters and seawater has recently been given by Schier et al. (2021). Without addressing reasons for the observed Ga-Al fractionation yet, it can be summarised that Ga and Al continuously fractionate towards increasing Ga/Al ratios during weathering, transport in river waters and finally, their transit through estuaries into seawater. Hence, river waters show a wide range of subcrustal to supercrustal Ga/Al ratios from about 2×10^{-5} to 8×10^{-3} (Gaillardet et al., 2013; Pokrovsky and Schott, 2002; Shiller and Frilot, 1996). A data compilation for the Orinoco River in South America (Gaillardet et al., 2013) also shows Ga-Al fractionation with even higher Ga/Al ratios (2.04×10^{-2}) in the truly dissolved (< 10 kDa; Da = dalton) fraction compared to the dissolved, i.e. nanoparticles and colloids-bearing fraction ($< 0.2 \mu\text{m}$; Ga/Al = 1.9×10^{-3}), which, however, was not observed in the rivers in NW Russia studied by Pokrovsky and Schott (2002). Reflecting on the elevated Ga/Al ratios of river waters, Shiller and Frilot (1996) reported lower Ga/Al ratios in soils compared to their respective source lithology. This observation suggests the preferred mobilisation of Ga compared to Al during weathering. However, a more recent study by Richardson et al. (2022) described relatively stable Ga/Al ratios along weathering profiles of grey shale without any systematically preferred mobilisation or retention of either Ga or Al. Richardson et al. (2022) also stated that the only study comparable to their results is the one from Shiller and Frilot (1996) and that further in-situ studies are needed to quantify Ga/Al ratios during continental weathering and soil formation.

It is well-documented that open ocean seawater shows higher (supercrustal) Ga/Al ratios between 2×10^{-3} and 8×10^{-2} (Ho et al., 2019; Orians and Bruland, 1988a; Parker et al., 2016; Shiller and Bairamadgi, 2006) when compared to crustal rocks and river waters. Based on currently available data, it appears that Pacific seawater, on average, shows higher Ga/Al ratios (and lower Ga and Al concentrations) than Atlantic seawater (e.g., Schier et al., 2021, and references therein).

To the best of our knowledge, only one study (Schmidt et al., 2017) provides data for Ga and Al in marine hydrothermal fluids. It is, therefore, the only available source for Ga/Al ratios of the hydrothermal flux into modern seawater. Schmidt et al. (2017) investigated black smoker fluids in the Nifonea vent field, New Hebrides back-arc, Vanuatu, SW Pacific. The majority of their samples show supercrustal Ga/Al ratios between 0.8×10^{-2} and 4.1×10^{-2} with two samples showing lower Ga/Al ratios of 5.3×10^{-4} and 1.2×10^{-4} . If this range was in any way representative, the Ga/Al ratios of hydrothermal fluids would be in the same range as those of modern seawater. We caution, however, that the hydrothermal fluids investigated by Schmidt et al. (2017) are all from black smoker-type vents in a back-arc setting and that more data from other hydrothermal vent systems are urgently needed.

Banded iron formations (BIFs) are marine chemical sedimentary rocks consisting of layers of (meta)chert alternating with bands of Fe oxides, carbonates or sulphides (James, 1954). Banded iron formations mainly formed during the Archaean and Palaeoproterozoic and then again during the Neoproterozoic (e.g., Bekker et al., 2010, 2014; Beukes, 1973; Beukes and Klein, 1990; Gole and Klein, 1981; Klein, 2005; Klein and Beukes, 1989; Konhauser et al., 2017; Smith and Beukes, 2016; Trendall et al., 2004; Williams et al., 2004). In the following, only oxidefacies BIFs will be considered. Banded iron formations, and other marine chemical sedimentary rocks, are of great scientific interest for investigations of the palaeoenvironmental conditions on Early Earth, i.e. during the formation and evolution of early life. Numerous studies have shown that BIFs are robust archives for various geochemical proxies, which, in turn, can give insights into the physico-chemical evolution of the Precambrian atmosphere-hydrosphere system (e.g., Bau et al., 2022; Haugaard et al., 2016; Smith, 2007; Smith et al., 2013; Viehmann et al., 2018).

However, although BIFs are used as geochemical archives, details of their actual formation are still a matter of debate, and different models are still discussed (for a review on the formation of BIF, see, e.g. Bekker et al., 2010, 2014). A proxy that was used in the past to examine the provenance of Si deposited in BIFs is the Ge/Si ratio (Alibert

and Kinsley, 2016; Bau et al., 2022; Delvigne et al., 2012; Frei and Polat, 2007; Hamade et al., 2003; Wang et al., 2017). Germanium and Si are geochemical partners similar to Ga and Al. Igneous and clastic sedimentary rocks show similar Ge/Si ratios. At the same time, geochemical processes in aqueous environments may lead to the fractionation of these elements (e.g., Ernst et al., 2022, and references therein). The studies on Ge and Si in BIFs above show that Fe oxide bands have higher Ge/Si ratios than adjacent (meta)chert bands, resulting in a strong positive linear correlation of Ge/Si ratios with the Fe content. There is no consensus yet as to whether the observed Ge-Si fractionation is (i) a primary feature indicating separate element sources (or water masses) for the Fe oxide and (meta)chert bands (Bau et al., 2022; Frei and Polat, 2007; Hamade et al., 2003; Wang et al., 2017), or (ii) whether elevated Ge/Si ratios in the Fe oxide bands might be related to the preferred sorption of Ge onto Fe (oxy)hydroxides during diagenesis and/or metamorphism (Alibert and Kinsley, 2016; Delvigne et al., 2012).

To gain further insights into the distribution and behaviour of Ga and Al in Early Earth's ocean(s), we investigated the Ga-Al systematics of the rather well-studied 2.7 Ga Temagami BIF, Ontario, Canada (Bowins and Heaman, 1991). The Temagami BIF is hosted in volcanic and sedimentary successions of the Temagami Greenstone Belt, which correlates spatially and temporarily with the Abitibi Greenstone Belt further north (Diekrup et al., 2018, Diekrup, 2019 and references therein). The Temagami BIF crops out in two members (~10 km in strike and 60 m to 185 m thickness) close to Temagami town (Diekrup, 2019). Diekrup (2019) stated that the BIF was most likely deposited in an open-ocean setting rather than a restricted basin. The regional metamorphism of Temagami BIF did not exceed greenschist facies (Diekrup, 2019 and references therein). To the best of our knowledge, this is the first study on coupled Ga-Al systematics in Precambrian marine chemical sedimentary rocks. Since reliable literature data for Ga in BIF reference materials are scarce, we performed comparative analyses with three individual analytical methods in two independent laboratories to ensure the analytical quality of the herein presented data.

6.3 Materials and Methods

6.3.1 Wet chemistry and solution ICP-OES and ICP-MS for major and trace elements

In total, four Temagami BIF specimens (TM1, TM2, TM3 and TM4) were investigated. These are the same samples that have been investigated previously (Bau et al., 2022; Bau and Alexander, 2009; Mundl-Petermeier et al., 2022; Schulz et al., 2021; Viehmann et al., 2014). Thirty-seven individual adjacent Fe oxide and metachert bands were subsampled from these specimens (see Fig. 6.3) by micro-drilling (3 to 5 mm diameter). The individual microdrill cores were milled by hand in an agate mortar that was thoroughly cleaned with pure sand (PanReac AppliChem article number 121160.1214), isopropanol and deionised (DI) water between each sample. Of each powdered sample, 100 mg were digested in a PicoTrace DAS Pressure Digestion System, following a 3-acid digestion protocol (conc. HCl, HNO₃, and HF – all of suprapure quality). After overnight digestion at 180 °C in pressure-sealed vials, the dissolved samples were evaporated to incipient dryness in a three-step procedure with two refills of conc. HCl in-between. Finally, the dissolved samples were diluted with 0.5 M HNO₃ and transferred into acid-cleaned PE bottles. Major elements Al, Ca, Fe, Mg, Mn and P were analysed by inductively coupled plasma optical emission spectrometry (ICP-OES, SPECTRO CIROS VISION), and trace elements Li, Be, Sc, Ti, Co, Ni, Rb, Sr, Zr, Cs, Ba, rare earth elements and yttrium (REY), Hf, Ta, W, Pb, Th, and U by quadrupole inductively coupled plasma mass spectrometry (ICP-MS, PerkinElmer NexION 350x). Detailed descriptions of analytical protocols can be found in Dulski (2001) and Alexander et al. (2008). The quality of the entire sample preparation and the analytical procedure was monitored by the BIF Reference Material (RM) IF-G (Isua, Greenland) and blank samples. A comparison of all individual IF-G measurements shows low relative standard deviations (RSD) of <5 % for almost all analysed elements (only P, Zr and Hf show RSDs of <10 %). Very low-abundance elements (Li, Cs, Ba, Ta, U) show RSDs larger than 10 % RSD but always <20 % RSD. Comparison of the measured major and trace elements in the IF-G reference material to published values (Albut et al., 2018; Dulski, 2001; Fabre et al., 2011; Parks et al., 2014; Simons et al., 2016; Viehmann et al., 2016) shows only minor (<7 %) deviations (for further details, see Supplementary Material Table A1). In the following, only data of elements are considered that show <10 % RSD and that are in good agreement with the RM's literature values. We emphasise that our results that deviate more strongly from published values are not necessarily incorrect because, for

some elements, the published values also vary significantly. Moreover, there are issues with different batches of the IF-G RM that show highly variable mass fractions for certain trace elements.

6.3.2 Solution SF- and ICP-MS/MS of Ga and Al

In addition to the major and trace element analyses with ICP-OES and ICP-MS, Ga and Al mass fractions were determined separately. Investigating Ga is challenging because it usually occurs in very small quantities and falls in BIFs within the $\mu\text{g}/\text{kg}$ range. Furthermore, several mass spectral interferences from polyatomic and doubly-charged ion species complicate ICP-MS measurements of Ga in BIFs. Potential interferences with the ^{69}Ga isotope in BIFs originate from polyatomic $^{29}\text{Si}^{40}\text{Ar}^+$, $^{53}\text{Cr}^{16}\text{O}^+$, $^{68}\text{Zn}^1\text{H}^+$ or $^{57}\text{Fe}^{12}\text{C}^+$ and doubly-charged $^{138}\text{Ba}^{++}$. For the ^{71}Ga isotope $^{55}\text{Mn}^{16}\text{O}^+$, $^{70}\text{Ge}^1\text{H}^+$, $^{31}\text{P}^{40}\text{Ar}^+$, $^{54}\text{Fe}^{16}\text{O}^1\text{H}^+$ and doubly-charged $^{142}\text{Ce}^{++}$ and $^{142}\text{Nd}^{++}$ are responsible for interferences (Blokhin et al., 2014). Germanium mass fractions in BIFs are as low as those of Ga (e.g., Bau et al., 2022). Although Mn, Cr, and Zn occur only at trace element levels in BIFs (e.g., Bau and Alexander, 2009), their mass fractions are still much higher than that of Ga. Organic carbon content in Precambrian BIFs is low, and Dodd et al. (2019) measured 0.04 % total organic carbon (TOC) in the Temagami BIF. Silicon mass fractions, however, can be extremely high, especially in the (meta)chert bands, and Ar is plasma gas for ICP. Phosphorus in Temagami BIF can reach around 1500 mg/kg (e.g., Bau and Alexander, 2009) and is much higher than Ga mass fractions. The potential doubly-charged interferences Ba, Ce and Nd generally have very low mass fractions in BIFs of only up to a few tens of mg/kg (e.g., Bau and Alexander, 2009). Besides the low abundance of Ga and potential interferences, the lack of published data on Ga in BIFs go hand in hand with usually relatively poorly defined data for BIF reference materials. There is a high probability that any published data for Ga in BIF obtained by standard quadrupole ICP-MS instruments without reaction cells or other means for proper interference removal are biased. In order to address these issues, each sample was analysed using two independent analytical methods. Measurements with high-resolution sector-field ICP-MS (SF-ICP-MS) and with tandem ICP-MS/MS were performed in different laboratories (Kiel University and Federal Institute for Geosciences and Natural Resources BGR in Hannover, resp.). Both analytical methods are highly precise and accurate and can determine Ga and Al mass fractions in BIFs free from interferences. Combining these two independent analytical methods corroborates the excellent quality of the Ga-Al data presented here.

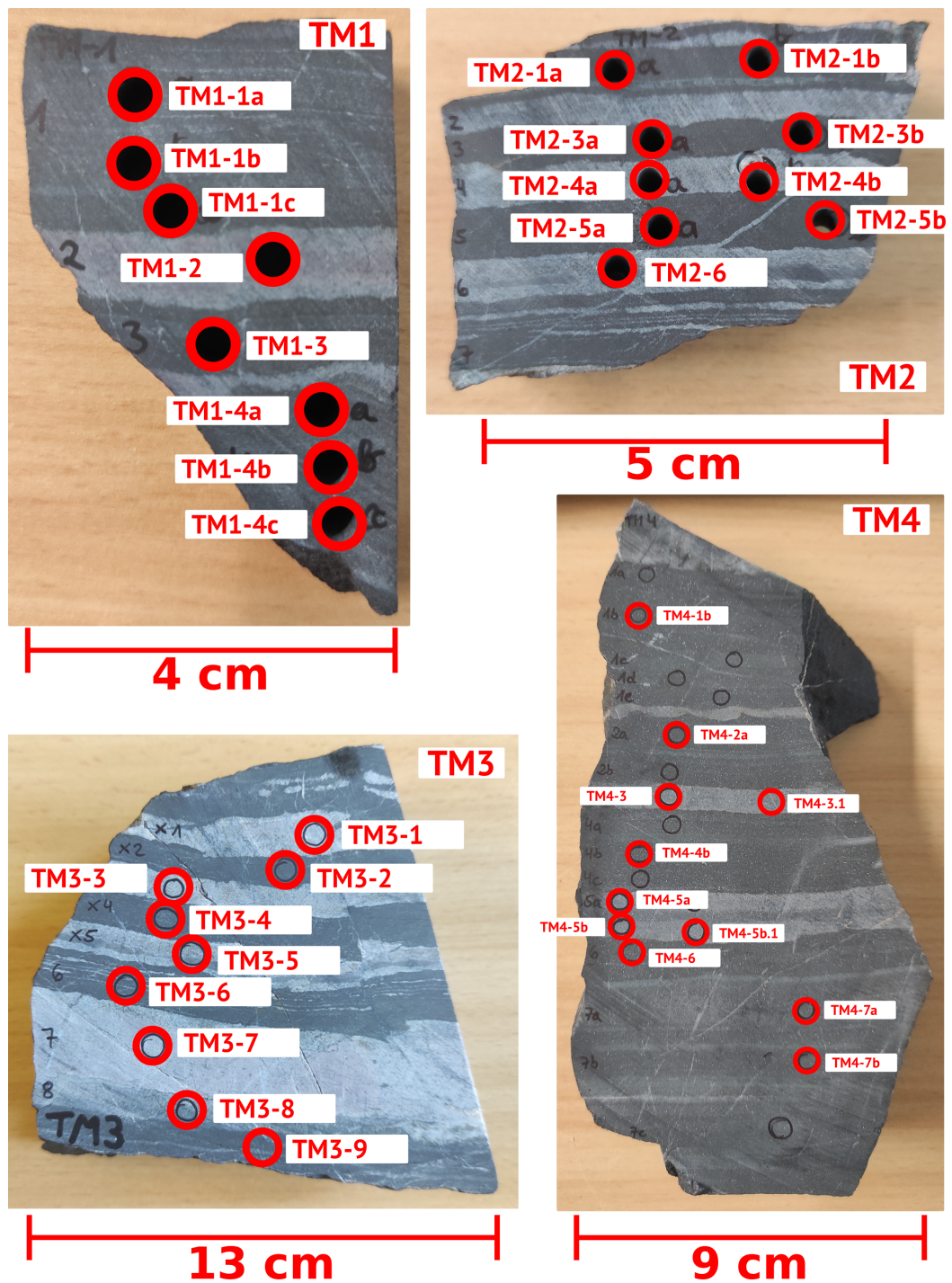


Figure 6.3: Sample specimens TM1, TM2, TM3 and TM4 of the Temagami BIF, Canada. Red circles and sample name labels indicate the locations of micro-drill core samples.

The SF-ICP-MS analyses using a ThermoFisher Element XR at Kiel University were conducted as described by Schier et al. (2021); for further information on calibration procedures for ICP-MS measurements see Garbe-Schönberg (1993). Both Ga (^{69}Ga , ^{71}Ga) and Al (^{27}Al) were measured in high-resolution mode (HR; resolving power $\sim 10,000$) to avoid polyatomic interferences, especially on Ga. Ga with 70.9247 m/z (^{71}Ga) was used for final data evaluation. The analytical quality was monitored with (Fe, Mn)-oxide RMs (IF-G, FeR-3, FeR4, NOD-A1, NOD-P1, and well-characterised basalt BHVO-2), blank samples, and replicate analyses. The measured counts per second (cps) in the blank samples were sufficiently low, and published reference values for Ga and Al in the respective RMs were matched for most RMs (see Table 6.5). Note, however, that for some RMs, the published data for Ga are rather illdefined because most analyses were not performed in high-resolution mode and might have been affected by interferences (for further information, see Schier et al., 2021).

Twenty-five Temagami BIF samples were also measured for Ga and Al by ICP-MS/MS (ThermoFisher iCAP TQ) at the Federal Institute for Geosciences and Natural Resources (BGR) in Hannover. ICP-MS/MS uses reaction cell technology and an additional quadrupole mass filter before the collision/reaction cell to significantly reduce interfering elements and resulting spectral interferences. Hydrogen was used as reaction gas for Ga determination, while Al was measured with oxygen as reaction gas in mass-shift mode as $^{27}\text{Al}^{16}\text{O}$. In contrast to the major interfering elements Fe and Mn, Ga does not react with the H_2 cell gas (Jackson, 2018) and can thus be accurately determined on-mass at 71 m/z (^{71}Ga). Accuracy is demonstrated by the results for the iron-rich RMs FeR-3, FeR-4 and IF-G and the Mn-rich RM NOD-P1 (see Table 6.5). Doubly-charged interferences of $^{142}\text{Ce}^{++}$ and $^{142}\text{Nd}^{++}$ are attenuated in H_2 gas mode (Sugiyama, 2021). The RSDs for each RM and each sample are very low for Ga ($< 5\%$) and sufficiently low for Al ($< 10\%$, except for TM4-3.1: 14.6 %).

6.3.3 Two-component mixing experiment with IF-G and pure SiO_2 sand

In order to further verify the quality of the Ga/Al measurements in Fe oxide and metachert BIF bands, a mixing experiment between the banded iron formation RM IF-G (Isua BIF, Greenland) and pure ($\geq 99.995\%$ SiO_2) quartz sand was prepared. We emphasise that the quartz sand is synthetic (Sigma-Aldrich; CAS number 14808–60-7), and its Ga/Al ratio (5.33×10^{-5}) is not representative of natural materials. In total, nine samples were

prepared with relative amounts of IF-G from 10 % to 90 % and SiO₂ from 90 % to 10 %, respectively, by mixing the respective weights of IF-G and quartz powders in an agate mortar. Before homogenising each sample, the agate mortar and pestle were cleaned with isopropanol and DI water three times. These mixing experiment samples and aliquots of the pure IF-G and quartz endmembers were then dissolved following the same 3-acid pressure digestion procedure described above. ICP-MS and ICP-OES measurements were performed at Constructor University (formerly Jacobs University) in Bremen, and ICP-MS/MS measurements were performed at BGR in Hannover (also see above).

6.3.4 Laser ablation SF-ICP-MS of Ga and Al

Laser ablation ICP-MS allows for the direct in situ analysis of Ga/Al in individual Temagami BIF bands and also of nano-pulverised samples from micro-drilling. Nano-particulate pressed power tablets (NP tablets; for details, see Garbe-Schönberg and Müller (2014) and Jochum et al. (2019) for updated procedures) were prepared for the five Fe oxide bands of TM3 (TM3-0, TM3-2, TM3-4, TM3-6, TM3-9) and the mixed type (Fe oxide and metachert) band TM3-8. Sample TM3-6 (Fe oxide band) was prepared as duplicates (-dup1, -dup2 in Table 6.1). At Kiel University, laser-ablation (LA) SF-ICP-MS analyses were conducted using a GeoLas-HD (Coherent) laser ablation system coupled to the ThermoFisher Element XR. The nano-particulate Temagami BIF samples were mounted with nano-particulate tablet reference materials (RMs) IF-G, FeR-3, FeR-4, NOD-P1, NOD-A1, a milling blank (pure SiO₂), and the glass RM NIST610, into a Zurich-type-large-volume ablation cell. The ablation cell was flushed with 1017 ml/min He carrier gas and 14 ml/min H₂ to reduce oxide formation and increase sensitivity. The laser was operated with a constant fluence of 6 J/cm², a spot diameter of 160 µm, and 400 pulses at 10 Hz on each measurement point. Machine background signal was collected 20 s before the ablation of each sample for 40 s. A 20 s wash-out followed each ablation before moving the ablation cell to the next sample point. The analytical session started and ended with triplicate measurements of each RM and the milling blank. After 30 individual measurements on the actual Temagami BIF samples, the RMs NIST610, IF-G, FeR-3, and FeR-4 were re-measured in triplicate. The measurements of different RMs at the beginning, at the end, and between allowed for monitoring machine drift, and results are used for data evaluation (see the section below). As with solution SF-ICP-MS analyses, Ga/Al ratios were measured in high-resolution (HR) mode with a resolving power of ~10,000. Interferences on ⁶⁹Ga, ⁷¹Ga and ²⁷Al were as described above for the solution SF-IC-MS measurements.

6.3.5 LA-ICP-MS data evaluation

For LA-ICP-MS, only elemental ratios were evaluated. The raw LA-ICP-MS data were pre-processed with LADR (Laser Ablation Data Reduction – version 1.1.02, Norris Scientific). This pre-processing includes time interval selection of background and sampling signal for each measurement and subsequent background subtraction. In turn, the background-subtracted data were further processed manually: (i) Linear calibration lines for $^{69}\text{Ga}/^{27}\text{Al}$ and $^{71}\text{Ga}/^{27}\text{Al}$ were computed with the BIF RMs IF-G and FeR-4 (see Fig. 6.4) because they closely match the sample matrix and show a range of Ga/Al ratios from 7.9×10^{-4} to 2.7×10^{-4} , respectively. Measured Ga/Al [cps/cps] intensity ratios were plotted against the respective reference values for IF-G and FeR-4 using Ga/Al 7.9×10^{-4} and 2.7×10^{-4} , respectively, as determined from solution SF-ICP-MS measurement of digested aliquots described above. Since both IF-G and FeR-4 are BIF RMs prepared as NP tablets, they show similar ablation behaviour to the iron-rich Temagami BIF samples. Unidentified matrix effects should be negligible. The reference values for FeR-3, NOD-P1 and NOD-A1 were taken from: Axelsson et al., 2002; Govindaraju, 1994; Sampaio and Enzweiler, 2015; Terashima et al., 1995. The BIF RM FeR-3 and the two ferromanganese (Fe-Mn) nodule RMs NOD-A1 (Atlantic) and NOD-P1 (Pacific) were used to verify the accuracy of the determined calibration. However, the two Fe-Mn nodule RMs contain large amounts of Mn and, therefore, have a different matrix than the BIF samples. (ii) Final elemental mass ratios of each sample were calculated using the respective calibration equation (see Fig. 6.4). Correction for the natural abundances of ^{69}Ga and ^{71}Ga is not necessary because the two separate calibration equations compensate for that. A correction for variable ablation yield via an internal standard is also not necessary when elemental ratios of Ga and Al are determined.

6.4 Results

Major and trace element data for all samples and RMs can be found in Tables 6.4 and 6.5. A more detailed description of the chemical composition of the Temagami BIF TM1, TM2 and TM3 specimens can be found in Bau and Alexander (2009). Based on the trace element inventory, Bau and Alexander (2009) showed that the investigated Temagami BIF specimens are almost entirely free from clastic detritus. We here also present data for a fourth specimen (TM4; Fig. 6.3), the general chemical characteristics of which are similar to those of the other specimens. Therefore, only a description of the Fe, Ga, Al and Ga/Al ratios are given below.

6 Gallium-aluminium systematics in the Temagami BIF

Table 6.1: Temagami BIF Fe oxide and metachert Fe, Ga and Al mass fractions and Ga/Al ratios measured with SF-ICP-MS and ICP-MS/MS.

Sample	Band type	Fe [% m/m] ICP-OES	Ga [mg/kg] SF-ICP-MS	Al [mg/kg]	Ga/Al [mg/mg] $\times 10^{-4}$	Ga [mg/kg] ICP-MS/MS	Al [mg/kg]	Ga/Al [mg/mg] $\times 10^{-4}$
TM1-1a	Fe oxide	41.51	1.55	5244	2.96			
TM1-1b	Fe oxide	41.68	2.05	8788	2.33	2.367	8785	2.69
TM1-1c	Fe oxide	43.86	1.78	5683	3.13			
TM1-2	metachert	5.53	0.08	368	2.17			
TM1-3	mixed	39.99	2.14	10870	1.97	1.774	10874	1.63
TM1-4a	mixed	39.53	2.04	8106	2.52			
TM1-4b	mixed	34.27	1.47	4466	3.29	1.304	4350	3.00
TM1-4c	mixed	38.85	1.97	6458	3.05			
TM2-1a	Fe oxide	54.22	4.04	9861	4.10	3.868	10249	3.77
TM2-1b	Fe oxide	56.55	3.4	7635	4.45			
TM2-3a	Fe oxide	59.18	2.65	5139	5.16	2.771	5300	5.23
TM2-3b	Fe oxide	58.62	2.72	5218	5.21			
TM2-4a	metachert	3.93	0.09	345	2.61	0.167	354	4.72
TM2-4b	mixed	21.44	0.65	1294	5.02			
TM2-5a	Fe oxide	55.94	2.42	6389	3.79	2.283	6216	3.67
TM2-5b	Fe oxide	54.81	2.39	4945	4.83			
TM2-6	metachert	5.34	0.14	400	3.50	0.177	388	4.56
TM3-0	Fe oxide	52.42	3.82	10143	3.77	3.873	12930	3.00
TM3-1	metachert	3.59	0.22	654	3.36	0.226	634	3.57
TM3-3	metachert	3.50	0.16	548	2.92	0.194	549	3.53
TM3-4	Fe oxide	51.96	1.61	3906	4.12	1.751	4323	4.05
TM3-5	metachert	4.89	0.16	551	2.90	0.202	567	3.56
TM3-6	Fe oxide	44.73	1.25	3430	3.64	1.333	3577	3.73
TM3-7	metachert	3.40	0.059	287	2.06	0.096	302	3.18
TM3-8	mixed	11.85	0.38	792	4.80	0.43	801	5.37
TM3-9	Fe oxide	49.58	2.2	5430	4.05			
TM4-1b	Fe oxide	55.65	2.81	5742	4.89	2.831	5677	4.99
TM4-2a	Fe oxide	55.42	2.55	5037	5.06	2.344	4790	4.89
TM4-3	metachert	3.79	0.03	72	4.17	0.105	75	14.06
TM4-3.1	metachert	3.79	0.02	87	2.30	0.121	95	12.70
TM4-4b	Fe oxide	61.39	2.97	7768	3.82	2.739	8960	3.06
TM4-5a	metachert	3.00	0.01	120	0.83	0.1	119	8.39
TM4-5b	metachert	8.55	0.17	243	7.00			
TM4-5b.1	metachert	5.08	0.06	113	5.31	0.147	117	12.56
TM4-6	Fe oxide	54.58	2.84	5484	5.18	2.7	6468	4.17
TM4-7a	mixed	18.43	0.74	1545	4.79			
TM4-7b	Fe oxide	42.47	2.75	8116	3.39			
median	Fe oxide	54.40	2.60	5584	4.07	2.53	5947	3.78
median	metachert	3.86	0.09	316	2.91	0.16	328	4.64

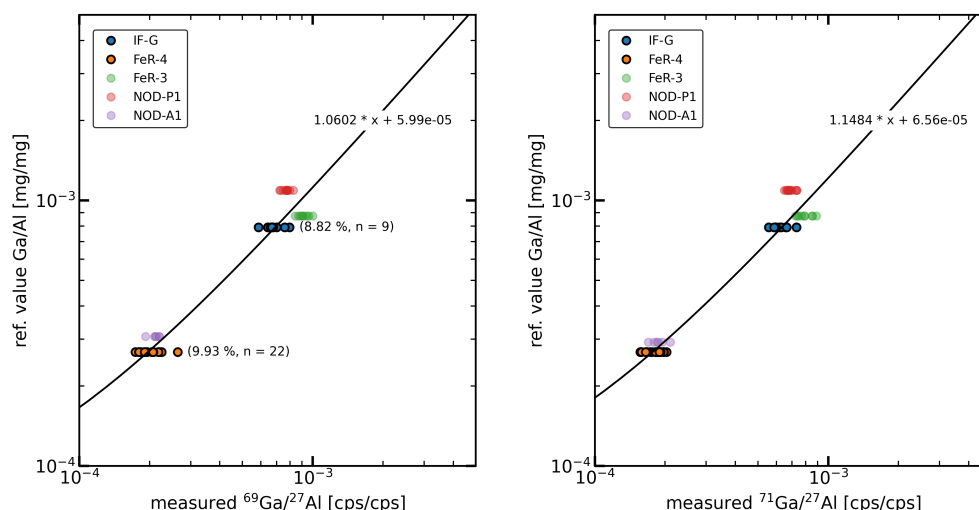


Figure 6.4: Calibration lines for Ga/Al ratios: reference values [mg/mg] plotted against measured intensities [cps/cps]. Solid black lines mark the calculated linear calibration functions, and the respective equations are also given. Reference values for IF-G and FeR-4 taken from solution SF-ICP-MS measurement of digested samples. Reference values for FeR-3, NOD-P1 and NOD-A1 are from Axelsson et al. (2002), Govindaraju (1994). Sampaio and Enzweiler (2015).

6.4.1 Iron

The Fe mass fractions in the Fe oxide bands range from 41.5 % to 61.4 % (m/m), while the metachert bands show very low Fe between 3.0 % and 8.6 %. Bands with more heterogeneous compositions have Fe between 11.8 % and 40.0 %. Although TM2-4b was supposed to be a metachert band sample based on visual inspection (similar to TM2-4a), it also contains material from the adjacent Fe oxide band (TM2-5) due to the micro-drilling.

6.4.2 Gallium and aluminium – A comparison of SF-ICP-MS and ICP-MS/MS data sets

Several samples were measured with two different ICP-MS systems (see Tab. 6.1). Gallium mass fractions range from 0.01 mg/kg to 4.04 mg/kg, and Al mass fractions fall between 72 mg/kg and 12,930 mg/kg. The respective Ga/Al ratios are crustal and range from 2.0×10^{-4} to 7×10^{-4} (TM4-5a outlier excluded; SF-ICP-MS data). Figure 5 directly compares the SF- and ICP-MS/MS results for the TM3 specimen. The two different analytical methods show good agreement for the Ga/Al ratios of both Fe oxide and

metachert bands. Only TM3-7 shows a significant difference ($\sim 54\%$) between the ICP-MS/MS and SF-ICP-MS data, but this sample has the lowest Ga (and Al) of all TM3 samples (0.096 mg/kg Ga measured with ICP-MS/MS; 0.059 mg/kg Ga measured with SF-ICP-MS) which are close to limits of quantification (< 0.007 mg/kg). Also samples TM2-4a, TM4-3, TM4-3.1, TM4-5a, and TM4-5b show differences between the Ga/Al ratios determined by the two ICP-MS methods. However, these are metachert samples with very low Ga (Ga < 0.09 mg/kg for SF-ICP-MS data and Ga < 0.17 mg/kg for ICP-MS/MS data). For all metachert samples, Ga mass fractions measured with ICP-MS/MS are higher than those determined with SF-ICP-MS. Consequently, the resulting Ga/Al ratios determined by ICP-MS/MS are also higher than those calculated from the SF-ICP-MS data, as both methods yield very similar Al mass fractions. Results from both analytical methods agree very well with published Ga and Al data for the RMs (IF-G, FeR-3, FeR-4, NOD-P1 and BHVO-2; Table 6.5). The BIF RMs used (IF-G, FeR-3 and FeR-4) are all rather Fe-rich. However, the largest differences between SF-ICP-MS and ICP-MS/MS data occur in the Fe-poor metachert bands. Since, to the best of our knowledge, there is no chert RM available with reliable Ga-Al data, it cannot be decided which analytical method is more accurate and robust for BIF (metachert) samples. Therefore, for the sake of uniformity, in the following, we will consider the larger dataset determined with SF-ICP-MS.

6.4.3 Analytical quality of Ga-Al data as evaluated from the two-component mixing experiment

The quartz sand used in the mixing experiment shows Ga and Al mass fractions of 0.004 mg/kg and 75 mg/kg, respectively, resulting in a Ga/Al ratio of 5.33×10^{-5} . The Fe mass fraction of the quartz sand is 292 mg/kg. The IF-G reference material shows Ga, Al and Fe mass fractions of 0.59 mg/kg, 883 mg/kg and 410,924 mg/kg, respectively, and a Ga/Al ratio of 6.68×10^{-4} , i.e., significantly higher than the quartz sand.

The mixing of IF-G and synthetic quartz sand results in a measured Ga mass fraction between 0.062 mg/kg and 0.511 mg/kg in the nine mixed samples (Table 3), while their Al mass fraction range between 143 mg/kg and 780 mg/kg. The respective Ga/Al ratios are between 4.34×10^{-4} and 6.55×10^{-4} . The Fe mass fractions of the mixing experiment samples fall between 40,795 mg/kg and 368,619 mg/kg (4.1 % and 37 %, respectively). Figure 6.6b shows these Ga and Al mass fractions plotted against the Fe mass fraction and the calculated binary mixing line between IF-G and quartz sand. All measured mass

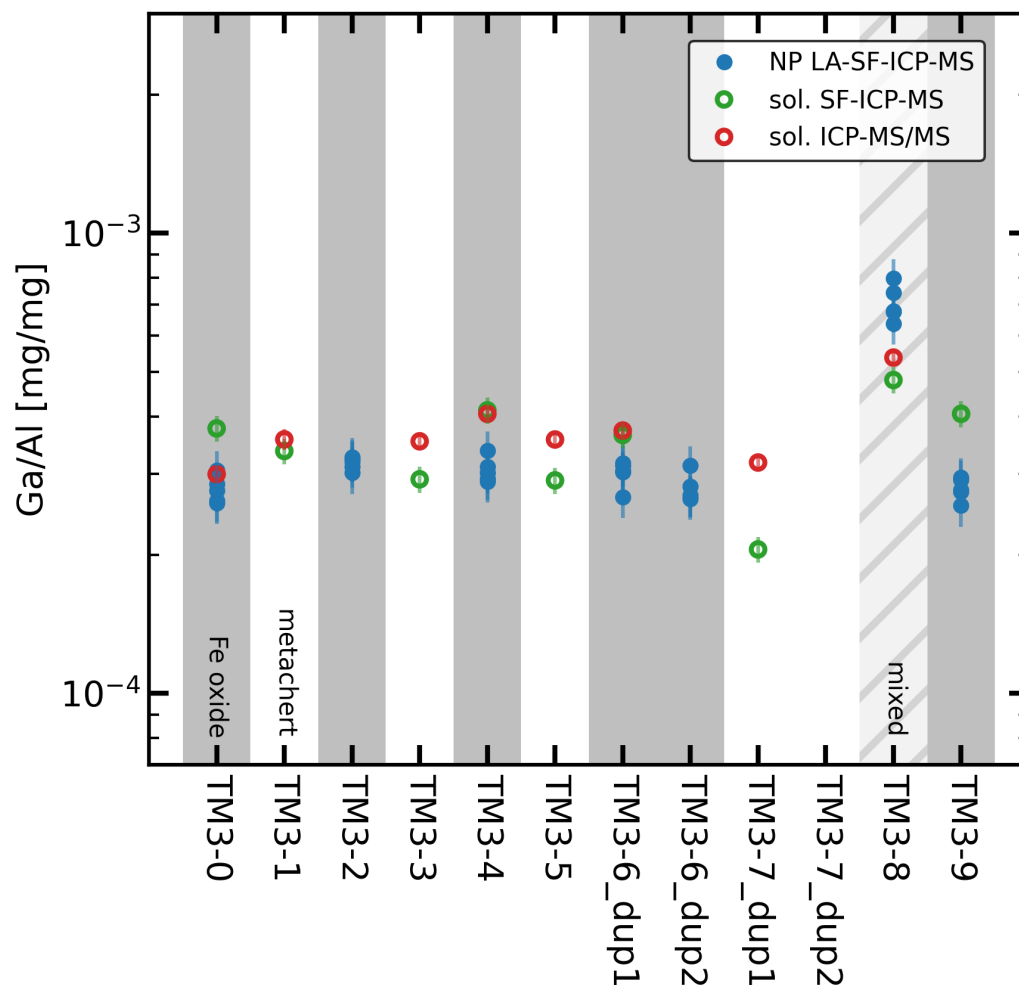


Figure 6.5: Comparison of Ga/Al ratios in the TM3 specimen measured with solution ICP-MS/MS (at BGR Hannover), solution SF-ICP-MS (at Kiel University) and nanoparticulate pressed powder tablets (NP) laser-ablation SF-ICP-MS (at Kiel University). Grey areas mark Fe oxide bands, while white areas mark metachert bands. The grey-hatched area marks the mixed band of TM3-8. The relative standard deviation for ICP-MS/MS data is indicated by green error bars: RSD based on replicate measurements of each sample. The relative standard deviation for SF-ICP-MS data is indicated by red error bars: 6.5 % for metachert bands (based on four times measurement of TM4-5b.1) and 3.0 % for Fe oxide bands (based on four times measurement of TM1-1a). For LA-ICP-MS, the $^{69}\text{Ga}/^{27}\text{Al}$ data (see Fig. 6.4 for calibration) is shown here. The relative standard deviation for LA-SF-ICP-MS is indicated by blue error bars and is based on repetitive measurement of the FeR-4 RM.

Table 6.2: Gallium and aluminium mass fractions and Ga/Al ratios of the solid mixing series (sample 0.1 to 0.9), IF-G and SiO₂ and the used RM FeR-3. The "target" column gives calculated Ga and Al mass fractions based on the mass fraction in the end member IF-G and SiO₂ and their relative proportions in each solid mixing sample.

Sample	Ga [mg/kg] measured	Al [mg/kg]	Ga/Al [mg/mg] $\times 10^{-4}$	Ga [mg/kg] target	Al [mg/kg] target
SiO ₂ _1	0.0055	77	0.71		
SiO ₂ _2	0.0035	73	0.47		
0.1	0.0621	143	4.34	0.0630	155
0.2	0.1195	229	5.22	0.1219	236
0.3	0.1714	296	5.79	0.1809	317
0.4	0.2223	373	5.96	0.2407	399
0.5	0.2517	447	5.63	0.2993	479
0.6	0.3311	543	6.10	0.3575	559
0.7	0.3894	614	6.34	0.4168	640
0.8	0.4750	707	6.72	0.4745	719
0.9	0.5111	780	6.55	0.5344	801
IF-G_1.024_22.i	0.5918	882	6.71		
IF-G_2.024_22.i	0.5958	883	6.75		
FeR-3_1.024_22	0.3488	553	6.31		
FeR-3_2.024_22	0.3756	545	6.89		
IF-G_1.024_22.ii	0.5918	882	6.71		
IF-G_2.024_22.ii	0.5958	883	6.75		

fraction data show good agreement with the calculated mass fractions with deviations <8 %, except for Ga in sample "0.5", which shows a 16 % deviation from the expected Ga mass fraction. Figure 6.6a shows the Ga/Al ratios plotted against the Fe mass fractions of the nine mixing experiment samples and the two endmembers (IF-G RM and quartz sand). The Ga/Al ratios in the mixing experiment samples closely follow the calculated binary mixing between the two endmembers.

The excellent agreement of the measured with calculated mass fractions demonstrates that the employed analytical method can precisely determine even very low mass fractions of Ga and Al in high-iron and high-silica matrices. The mixing experiment is fully compatible with natural BIF samples. It matches the BIF matrices (iron and silica) and the Fe, Ga and Al mass fractions typical of natural BIF samples, with the caveat that the Ga/Al ratio of the quartz sand is not representative of natural chert because it is a synthetic material.

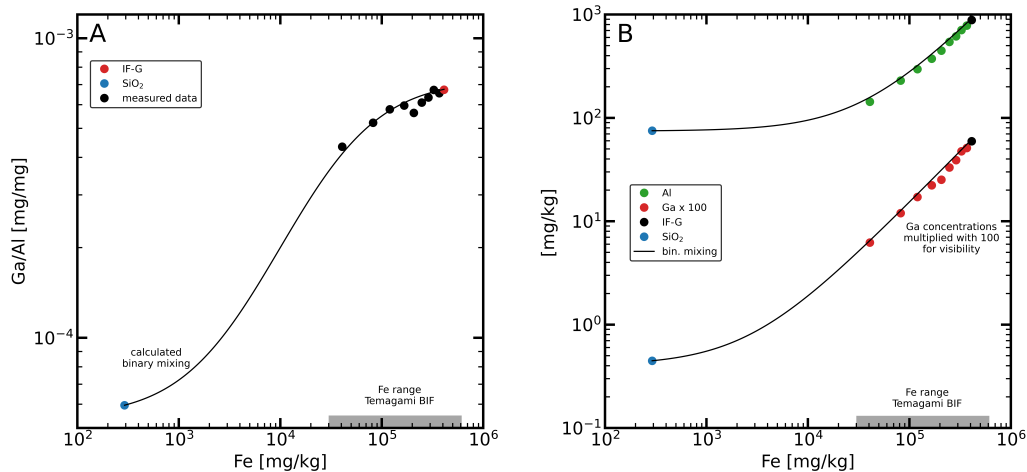


Figure 6.6: (a) Ga/Al ratio against Fe concentration in the solid mixing series samples (black) with the IF-G (red) and SiO₂ (blue) endmembers. The black line indicates the calculated binary mixing between IF-G and SiO₂. (b) Gallium (red) and aluminium (green) against Fe concentrations in the solid mixing series samples. IF-G and SiO₂ endmembers again marked with black and blue and calculated binary mixing indicated by solid black lines. Most uncertainty bars are hidden by the markers.

6.4.4 Gallium and aluminium – comparison of solution and laser-ablation ICP-MS

The micro-drilled and pulverised samples of the TM3 specimen were also analysed with LA-ICP-MS using the same SF-ICP-MS at Kiel University as used for the solution measurements. The Ga/Al ratios determined with LA-ICP-MS (Ga_{LA}/Al_{LA}) range from 2.8×10^{-4} to 3.2×10^{-4} (Tables 6.3 & A6.6). Figure 6.5 also shows the direct comparison with the solution ICP-MS data (Ga_{sol}/Al_{sol}) for the individual bands of the TM3 specimen. The Ga_{LA}/Al_{LA} ratios for the Fe oxide bands match the Ga_{sol}/Al_{sol} ratios reasonably well but are generally lower by 16 %–32 %.

6.5 Discussion

6.5.1 Ga/Al ratios determined with LA-ICP-MS

For pulverised bulk samples of Temagami BIF Fe oxide bands, the LA-ICP-MS measurements of Ga_{LA}/Al_{LA} ratios match those of the solution ICP-MS analysis (Fig. 6.7), demonstrating that LA-ICP-MS of NP tablets is a suitable analytical method for the

Table 6.3: Temagami BIF (TM3) nano-particulate pressed powder tablets raw data [cps/cps] and computed Ga/Al ratios measured with LA-ICP-MS.

Sample		$^{69}\text{Ga}/^{27}\text{Al}$	$^{71}\text{Ga}/^{27}\text{Al}$	$^{69}\text{Ga}/^{27}\text{Al}$	$^{71}\text{Ga}/^{27}\text{Al}$	$^{69}\text{Ga}/^{27}\text{Al}$	$^{71}\text{Ga}/^{27}\text{Al}$	$^{69}\text{Ga}/^{27}\text{Al}$	$^{71}\text{Ga}/^{27}\text{Al}$
LA-ICP-MS	n	median cps ratio	[cps/cps] $\times 10^{-4}$	RSD [%]	RSD [%]	median cps ratio	[cps/cps] $\times 10^{-4}$	RSD [%]	RSD [%]
TM3-0	5	2.04	1.95	8.7	10.9	2.76	2.90	6.8	8.3
TM3-2	5	2.12	1.95	3.8	5.8	2.85	2.90	3.1	4.5
TM3-4	5	2.32	1.95	7.8	15.9	3.06	2.89	6.3	12.5
TM3-6_dup1	5	2.45	1.96	8.2	11.6	3.20	2.91	6.5	9.0
TM3-6_dup2	5	2.45	2.14	9.0	13.8	3.20	3.12	7.1	10.6
TM3-8	5	2.45	2.14	9.8	10.1	3.20	3.12	9.0	9.1
TM3-9	5	2.37	2.05	7.1	3.8	3.11	3.01	5.6	2.9

determination of Ga/Al ratios in Fe oxide bands of BIFs. In contrast, laser ablation analyses of high-SiO₂ materials (cherts, synthetic SiO₂ sand) yielded biased, too high results when compared to solution analyses and are not reported here.

In this study, only nano-particulate tablets (NP) were used, and the application of in-situ LA-ICP-MS Ga/Al measurements in Fe oxide bands on polished sections still needs to be tested. However, the good ablation behaviour of in-situ Fe oxides (Bau et al., 2022) suggests that in-situ LA-ICP-MS measurements of Ga/Al ratios in BIFs should also yield reliable data. Robbins et al. (2019) examined the comparability of LA-ICP-MS measurements on polished slabs with solution ICP-MS measurements of bulk samples for two BIF deposits. Although they only compared bulk analyses with laser ablation analyses on Fe oxide phases (magnetite and hematite), micro-scale heterogeneities are clearly recognisable in the LA-ICP-MS measurements, as is to be expected. The deviations between laser ablation and bulk data are not uniform and can differ within the same sample. The exact reasons for those micro-scale heterogeneities are not well understood but might be controlled by slight differences in the accessory mineral assemblage and/or the trace element influx.

6.5.2 Solution ICP-MS: Uniform Ga/Al in Fe oxide and metachert bands

A recent study (Bau et al., 2022) on Ge/Si ratios, Cr isotopes and Th/U ratios in the Temagami BIF reports differences in these geochemical proxies between adjacent Fe oxide and metachert bands. The Fe oxide bands show high (“hydrothermal”) Ge/Si ratios, unfractionated Cr isotopes relative to Bulk Earth, and unfractionated Th/U ratios relative to Continental Crust. In contrast, the metachert bands show low (“riverine”) Ge/Si ratios, fractionated low Th/U ratios relative to Continental Crust, and are enriched relative to Bulk Earth in heavy Cr isotopes. Furthermore, Fe isotopes (Schulz et al.,

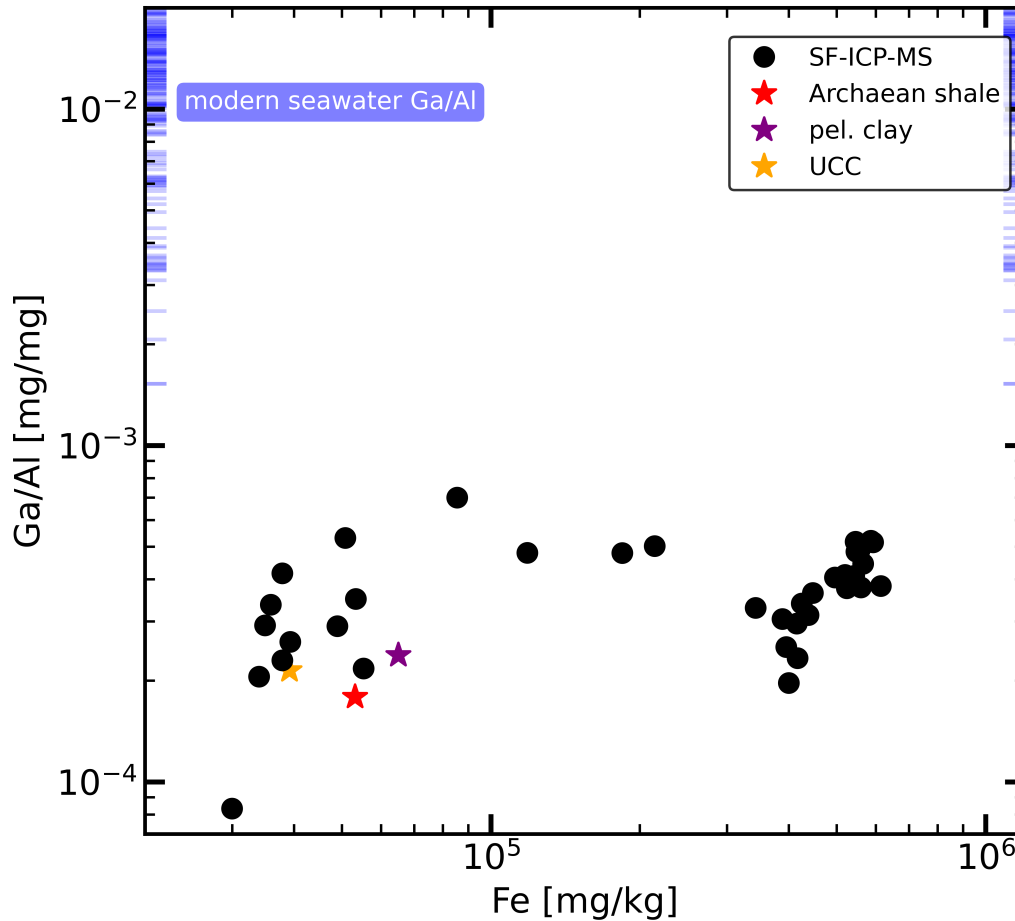


Figure 6.7: Ga/Al mass ratios against Fe mass fractions of the Temagami BIF (TM1, TM2, TM3 and TM4) specimen. Closed circles indicate data measured with solution SF-ICP-MS. Uncertainty bars are hidden by the marker. Star symbols indicate potential detritus: Archean shale - Cameron and Garrels (1980); pelagic clay - Li and Schoonmaker (2014); upper continental crust - Rudnick and Gao (2003). Ga/Al ratios of modern seawater from Charette et al. (2020), Ho et al. (2019), Orians and Bruland (1988), Parker et al. (2016), Shiller (1988), Shiller and Bairamadgi (2006). SGP shale Ga/Al ratio is the median value from Fig. 6.2C.

2021) show distinct differences between adjacent Fe oxide and metachert bands in the Temagami BIF. Bau et al. (2022) conclude, therefore, that the precursors of the Fe oxide and metachert bands precipitated from two distinct water masses in recurring cycles: The Fe oxide bands formed from marine deep-water masses with significant input from hydrothermal fluids, while the metachert bands formed from water masses with a predominantly continental influx. This interpretation also agrees with studies on Ge/Si ratios in other BIFs (see Alibert and Kinsley, 2016; Delvigne et al., 2012; Frei and Polat, 2007; Hamade et al., 2003; Wang et al., 2017). In an actualistic approach, one may expect that Fe oxide and metachert bands also show different Ga/Al ratios, as crustal rocks and modern river waters show lower Ga/Al ratios than modern seawater and hydrothermal fluids (see Fig. 6.1 for references). We emphasise, however, that the Temagami BIF shows uniform Ga/Al ratios across individual bands regardless of the mineralogical and the major element composition of the BIF band. Such behaviour has also been observed for Y/Ho ratios, the rare earth element and yttrium (REY) distribution patterns in general (e. g., Bau and Alexander, 2009; for BIFs in general, see Ernst and Bau, 2021), and for Nd and Hf (Viehmann et al., 2018) and Os isotope ratios (e.g., Schulz et al., 2021). The potential reasons for this striking observation of uniform Ga/Al ratios in the Temagami BIF and their implications will be discussed below.

While Ga and Al *mass fractions* differ between the Fe oxide and metachert bands (Table 6.1), we emphasise that the respective Ga/Al ratios vary only slightly across the sample set: the Temagami BIF shows (crustal to supercrustal) Ga/Al ratios between 2×10^{-4} and 6×10^{-4} (Fig. 6.7), regardless of the BIF band-type (for the very few exceptions see Table 6.1). The purity and pristine nature of the samples from the Temagami BIF were already discussed in great detail in previous publications (e.g., Bau and Alexander, 2009; Diekrup et al., 2018; Mundl-Petermeier et al., 2022; Schulz et al., 2021; Viehmann et al., 2014). Although these studies did not investigate Ga (or Ga/Al ratios), they consistently show for a wide range of different elements that detrital contamination is negligible. This is also supported by our data (Table 6.4). Figure 6.7 shows that potential detritus with a composition like Archean shales (after Cameron and Garrels, 1980) show Ga/Al ratios close to 2×10^{-4} . The median Ga/Al ratio of shales in the SGP database (Farrell et al., 2021) is 2.4×10^{-4} . While this is at the lower end of the Ga/Al range observed in the Temagami BIF samples, most Temagami BIF samples show a distinctly higher Ga/Al ratio compared to such detritus (see, for example, Schier et al., 2021 for a similar approach in their study of Ga/Al ratios in modern Fe-Mn crusts and nodules). Furthermore, the Ga and Al mass fractions are elevated in the Fe oxide bands

compared to the metachert bands, which are more prone to detrital contamination as they have lower trace metal mass fractions. The above demonstrates that the Ga-Al systematics of the Neoproterozoic Temagami BIF are not controlled by detritus but represent the geochemical signature of the marine chemical BIF sediment.

6.5.3 Fe oxide control on the Ga-Al distribution in BIFs

While the banding in the Temagami BIF specimens investigated is well developed with sharp contacts and individual band thicknesses in the range of millimetres to several centimetres, even the purest metachert bands contain about 1 % Fe (Table 6.4; and Bau et al., 2022). This Fe is present as finely dispersed Fe oxide particles that were continuously deposited together with silica during formation of the (meta)chert bands (Diekrup, 2019). The chert-hosted Fe oxide particles should show a rather similar geochemical composition to those that form the adjacent Fe oxide bands and yield much higher trace element mass fractions than the surrounding (meta)chert matrix. Although, to the best of our knowledge, there are no data on Ga mass fractions or Ga/Al ratios of pure BIF (meta)chert bands available, Ga-Fe-Al relationships support this hypothesis. The median Fe mass fraction in the metachert bands (3.86 %) is 7 % of that in the Fe oxide bands (54.40 %), and the median Ga mass fraction (0.09 mg/kg) is approximately 4 % of that in the Fe oxide bands (2.60 mg/kg). Using the ICP-MS/MS Ga results, the Ga median mass fraction in the metacherts (0.16 mg/kg) is 6 % of that in the Fe oxide bands (2.53 mg/kg) and therefore very close to the relative abundance of Fe (7.1 %) in the metacherts compared to the Fe oxide bands. The result is similar for Al, where the metachert bands (316 mg/kg) have, on median, about 6 % of the Al mass fraction of the Fe oxide bands (5584 mg/kg). This corroborates the hypothesis that the observed uniformity in Ga/Al ratios between Fe oxide and metachert bands originates from the absence of significant amounts of Ga in the (meta)chert component and the dominant role of Ga associated with Fe oxide particles in these (meta)chert bands. The chert acts just as a dilution for Fe oxide bands.

Further evidence for the dominant control of Fe oxide particles in the metachert bands comes from the mixing experiment. The nine mixing samples cover the same Fe mass fraction range as the Temagami BIF samples. Also, the Ga/Al values of the mixing experiment samples are within the same range as the natural BIF samples. However, the Ga/Al ratios of the mixing experiment samples only range from 4.34×10^{-4} to 6.55×10^{-4} , while the Temagami BIF samples show a slightly larger range from 1.97×10^{-4} to 7.00×10^{-4} (one low-Ga/Al-outlier excluded). Therefore, the relative difference in

Ga/Al ratios between the highest (0.9) and lowest (0.1) mixing ratio (with respect to the IF-G endmember) is smaller ($\sim 12\%$) than that for the Temagami BIF samples ($\sim 28\%$; one low-Ga/Al-outlier excluded). Figure 6.6a shows that the modelled variation of the Ga/Al ratio across the Fe mass fraction spectrum of the Temagami BIF samples is very small and would only get significant at much lower Fe mass fractions. Only at Fe mass fractions as low as approx. 0.2% (2×10^3 mg/kg Fe), Ga/Al ratios $< 1 \times 10^{-4}$ could be expected (black line in Fig. 6.6a). Therefore, even if there were different Ga/Al ratios in (meta)chert bands relative to the Fe oxide, they would most likely be hidden in the Temagami BIF by the high trace element load of the finely dispersed Fe oxide particles.

The mixing experiment indicates that the Fe mass fractions of BIF (meta-)chert bands must be extremely low to recognise potential differences in Ga/Al ratios. However, no BIF has such homogeneously pure (meta)chert bands. Bau et al. (2022) performed small-scale (160 μm) in-situ laser ablation HR-ICP-MS measurements on the same Temagami BIF samples used in this study. They made over 170 single measurements (four per band) in adjacent Fe oxide and metachert bands. However, only eight of those individual measurements show Fe mass fractions $< 1\%$. If all four clustered measurements of each band are averaged, the lowest Fe mass fraction for a metachert band was still 1.16% (TM2-2) and, therefore, too high to show a potentially different “pure (meta) chert” Ga/Al ratio. This suggests that the Fe oxide particles within the (meta)chert BIF bands are too fine-grained to be avoided even in small-scale laser ablation analyses.

6.5.4 Comparison with the modern marine system and implications for the Temagami seas

All Temagami BIF samples show Ga/Al ratios well below those of modern seawater (see Fig. 6.1 and 6.7). This poses the question of whether Ga and Al were fractionated during scavenging from Archean seawater by the Fe (oxy)hydroxides or whether the Ga/Al ratio of Neoproterozoic seawater was different from that of modern seawater.

The best-documented set of trace elements that are not or only very slightly fractionated during scavenging from Early Earth’s seawater are the REY (Alexander et al., 2008; Alibert, 2016; Bau and Dulski, 1996; Bau and Möller, 1993; Ernst and Bau, 2021; Fryer, 1977; Viehmann et al., 2015a, 2015b). The REY distribution in Precambrian seawater is known from studies of pristine and pure marine sedimentary carbonates, which are known to reproduce the REY distribution of ambient seawater (Bau, 1991, 1999; Elderfield et al., 1988; Elderfield and Greaves, 1982; Kamber et al., 2014; Kamber and Webb, 2001;

Möller and Bau, 1993; Piepgras and Jacobsen, 1992; Schier et al., 2018, 2020). The REY distributions in Early Precambrian BIFs and sedimentary carbonates are very similar to each other, revealing the lack of REY fractionation during the formation and deposition of oxide-facies BIFs. This is in marked contrast to the strong fractionation between modern hydrogenetic ferromanganese crusts and seawater (e.g., Bau et al., 1996; Bau and Koschinsky, 2009). This fractionation, however, is very similar to what is observed in scavenging experiments (e.g., Bau, 1999).

If there was no Ga-Al fractionation during BIF formation, the low Ga/Al ratios observed in the Temagami BIF suggest that Neoproterozoic Temagami seawater was characterised by significantly lower Ga/Al ratios than modern seawater (Fig. 6.7). In the modern marine system, Ga and Al concentrations are dominated by input via aeolian dust as suggested by the elevated Ga and Al concentrations in surface water regions with high dust input (Ho et al., 2019; Hydes, 1979, 1983; Measures et al., 1984; Orians and Bruland, 1985, 1988a; Shiller, 1988, 1998; Shiller and Bairamadgi, 2006). Additional Ga and Al enter the oceans via rivers. However, although river waters show elevated Ga and Al concentrations compared to seawater, large fractions of particle-reactive Ga and Al are removed from the water column in estuaries during salt-induced aggregation and subsequent sedimentation of the nanoparticles and colloids they are associated with (Brown and Bruland, 2009; Ho et al., 2019; Kremling, 1985; McAlister and Orians, 2012; Measures et al., 1984; Morris et al., 1986; Shiller and Frilot, 1996; Takayanagi and Gobeil, 2000; Van Bennekom and Jager, 1978). Anthropogenic influence on modern seawater's Ga/Al ratios is negligible (Shiller, 1988, 1998; Shiller and Bairamadgi, 2006; Shiller and Frilot, 1996). Regardless of the absolute contribution of the aeolian and riverine Ga and Al flux, the Ga/Al ratios of these sources are similar. The Ga/Al ratio of aeolian dust is comparable to that of crustal rocks (Orians and Bruland, 1988b), which shows a median of 2.7×10^{-4} (for references, see Fig. 6.1). Literature data for river waters show a much larger spread in Ga/Al ratios, but mainly cluster in the same range as crustal rocks with a median Ga/Al ratio of 2.0×10^{-4} (for references, see Fig. 6.1). Therefore, in the modern system, Ga and Al must fractionate upon entering seawater which leads to elevated Ga/Al ratios in seawater compared to the aeolian dust and river water sources. Indeed, a higher particle-reactivity of Al than Ga has been suggested, resulting in higher Al removal rates in estuaries and lower Al dissolution rates from dust particles (Orians and Bruland, 1988a; Schier et al., 2021; Shiller, 1988; Shiller and Bairamadgi, 2006).

Potential explanations for lower Ga/Al ratios in Neoproterozoic Temagami seawater could be that (i) the Ga/Al ratios of aeolian dust and river water were lower than

today, (ii) there was no significant fractionation of Ga, and Al in the estuarine and/or marine environment, or (iii) hydrothermal fluids carried lower Ga/Al ratios than modern seawater (or the current database on Ga/Al ratios in modern hydrothermal fluids is biased towards high ratios). Scenario (i) is very unlikely, as the Ga/Al ratio of igneous and epiclastic sedimentary rocks appears to not have changed throughout Earth's history. The Archean (~ 3.0 Ga) shales of Buhwa Greenstone Belt in Zimbabwe (Fedó et al., 1996) have a median Ga/Al of 2.25×10^{-4} , Precambrian (1.6–2.5 Ga) shales of the Superior Province in Canada (Cameron and Garrels, 1980) have a median Ga/Al of 2.24×10^{-4} and modern plagic clay (Li and Schoonmaker, 2014) has a Ga/Al of 2.38×10^{-4} (for further references, see Fig. 6.1). Furthermore, the Ga/Al ratio of the Earth's primitive mantle is assumed to be 2.24×10^{-4} , i.e. identical to that of recent crustal rocks (Lyubetskaya and Korenaga, 2007; McDonough and Sun, 1995; O'Neil and Palme, 1998; Sun, 1982). Scenario (ii) deserves closer consideration as the presence or absence of dissolved organic ligands and organic (nano)particles affects the behaviour of particle-reactive elements in estuaries (e.g., Merschel et al., 2017). Indeed, stability constants for Ga complexes with organic ligands tend to be higher than those for Al complexes (e.g., Schier et al., 2021, and references therein), suggesting they may play a role in modern estuarine Ga-Al fractionation. If organic compounds were largely absent from Neoproterozoic rivers and estuaries, Ga and Al might have remained tightly coupled, and seawater may have shown a crustal Ga/Al ratio. Unfortunately, too little is known about the abundance and hence importance of organic ligands and organic (nano)particles in Neoproterozoic rivers, estuaries and coastal seas to evaluate this possibility seriously (see e.g., Fakhraee et al., 2021).

Scenario (iii) with lower Ga/Al ratios in the ambient seawater of the Temagami BIF could be linked to the Ga/Al ratio of hydrothermal fluids. The presence of positive Eu anomalies in REY distribution patterns and positive ϵNd data (e.g., Alexander et al., 2009; Alibert and McCulloch, 1993; Jacobsen and Pimentel-Klose, 1988; Viehmann et al., 2015a) suggest that hydrothermal fluids dominated the chemical composition of Archean seawater and were the major (though not exclusive) Fe source (e.g., Beukes and Gutzmer, 2008; Bekker et al., 2010; Smith et al., 2013; Smith and Beukes 2023). Hence, Ga and Al of hydrothermal origin may have controlled Archean seawater's Ga/Al ratio and were preserved in BIF Fe oxide particles. However, only a single study provides Ga and Al data measured directly on modern marine hydrothermal fluids (Schmidt et al., 2017). The measured Ga/Al ratios and the estimated endmember Ga/Al ratios for these hydrothermal fluids are mainly in the same range (0.8×10^{-2} – 4.1×10^{-2}) as those of global average seawater, but two samples show lower Ga/Al ratios of 5.3×10^{-4} and 1.2×10^{-4} .

Since these samples (Schmidt et al., 2017) are all from black smoker-type vents in a spatially limited area, more data from different hydrothermal vent systems are needed before sound statements about the Ga-Al systematics in such hydrothermal fluids can be made.

A very different interpretation of the Ga/Al ratios observed in the Temagami BIF would result from the assumption that Neoproterozoic seawater had similar Ga/Al ratios as modern seawater, but that Ga and Al were fractionated during scavenging by the Fe oxides. Such fractionation of Ga and Al during scavenging by ferromanganese (oxy)hydroxides in the modern marine environment was observed and described by Schier et al. (2021). Hydrogenetic Fe-Mn crusts show Ga/Al ratios between 0.18×10^{-3} and 1.20×10^{-3} (Pacific, open ocean) and 0.96×10^{-4} and 1.56×10^{-4} (Atlantic), which are about 1.5 orders of magnitude lower than those of the respective seawater (for references, see Fig. 6.1). The Ga/Al ratios of the Temagami BIF are within the same range as those of modern Fe-Mn crusts at similar Ga and Al mass fractions. Schier et al. (2021) concluded that the Ga-Al fractionation in Fe-Mn crusts might be controlled by the higher particle reactivity of Al, which is also observed in other marine processes. This observation has not been convincingly explained yet, as based on the first hydrolysis constants (Byrne, 2010; Byrne et al., 1988; Evers et al., 1989; Schier et al., 2021; Smith and Martell, 1989), Ga should preferentially be scavenged (Li, 1991). We caution, however, that Fe-Mn crusts cannot be considered straightforward modern analogues to Precambrian BIFs, as they also fractionate those trace elements during their formation that are known to not fractionate during the formation of Precambrian BIFs (e.g., REE, Y-Ho, Zr-Hf-Nb-Ta; Bau et al., 1996, 1998; Bau and Alexander, 2009; Bau and Dulski, 1996; Schmidt et al., 2014).

6.6 Conclusion

We report the first data set on Ga/Al ratios of Precambrian BIFs for samples from adjacent magnetite and metachert bands of the Neoproterozoic Temagami BIF. Furthermore, a two-component mixing experiment of BIF reference material IF-G and synthetic quartz sand was prepared and measured to demonstrate the high analytical quality of the Ga and Al data determined by ICP-MS/MS, SF-ICP-MS, and LA-SF-ICP-MS on nanoparticulate tablets. The LA-ICP-MS method was found to yield accurate data for the Fe oxide bands. The results for the Temagami BIF and for the mixing experiment suggest that fine Fe oxide particles within the (meta)cherts control the Ga-Al distribution. The Ga/Al ratios of the Fe oxides in both the magnetite and the metachert bands provide

valuable information on the geochemistry of ambient seawater during the deposition of the Temagami BIF some 2.7 Ga ago.

The Temagami BIF shows uniform crustal Ga/Al ratios between 2.0×10^{-4} and 7×10^{-4} (*TM4-5a* outlier excluded) in adjacent Fe oxide and metachert bands. Assuming that there was no fractionation of Ga and Al during scavenging from Archean seawater, as is also observed for other elements, this would suggest that Temagami seawater had considerably lower Ga/Al ratios than modern seawater. Lower Ga/Al ratios in Neoproterozoic seawater may have resulted from lack of, or only limited, Ga-Al fractionation during weathering, river transport and estuarine processes in the oxygen- and/or biota-deficient Archean surface environment. Alternatively, it may indicate that Neoproterozoic high-temperature hydrothermal fluids showed unfractionated Ga/Al ratios. Unfortunately, the currently very limited knowledge of Ga-Al distribution and behaviour in the Earth's surface system and in hydrothermal fluids does not allow to address this issue conclusively. Moreover, in spite of the lack of fractionation during marine scavenging observed for other elements, it cannot yet be ruled out that Ga and Al are fractionated during removal from Archean seawater, similar to what is observed in the modern ocean during the formation of hydrogenetic ferromanganese crusts. Nevertheless, it should be remembered that ferromanganese crusts contain large amounts of Mn oxides while BIFs do not. The influence of different minerals on the fractionation of Ga-Al is not fully investigated, and only very few experimental studies on the adsorption of Ga and Al onto Goethite and α -FeOOH exist (e.g., Lövgren et al., 1990; Persson et al., 2006; Yuan et al., 2018). Therefore, the influence Mn oxides on the primary mineralogical composition of ferromanganese crusts and BIFs, which is currently highly debated (see e.g., Sun et al., 2015; Johnson et al., 2018), cannot be assessed yet. However, the surprising results for the Temagami BIF presented here should trigger follow-up studies of other BIFs and chemical sediments as they appear to be a largely untapped source of geochemical information on Early Earth's environments.

6.7 Declaration of Competing Interest

The authors declare that they have no known competing financial interests or personal relationships that could have appeared to influence the work reported in this paper.

6.8 Acknowledgements

We express our gratitude to Ulrike Westerströer from CAU Kiel University for her assistance with operating the LA-ICP-MS and performing the SF-ICP-MS analyses of dissolved samples. We appreciate the valuable discussions with colleagues in the DFG Priority Program SPP-1833 and acknowledge funding from the Deutsche Forschungsgemeinschaft (grant BA-2289/8-1 to MB). Furthermore, we would like to thank the three reviewers Leslie Robbins, Bertus Smith and Andrey Bekker as well as the editor Eva Stüeken for their most helpful feedback and constructive comments.

6.9 Appendix A. Supplementary Material

The Supplementary Material contains three tables with analytical data: (i) the major and trace element data for the Temagami BIF samples measured with ICP-MS and ICP-OES, (ii) the Ga and Al mass fractions in the used RMs measured with solution SF-ICP-MS and ICP-MS/MS and (iii) the individual NP LA-ICP-MS measurements. Supplementary material to this article can be found online at <https://doi.org/10.1016/j.gca.2023.06.019>.

6.9.1 Supplementary Tables

6 Gallium-aluminium systematics in the Temagami BIF

Table 6.4: Major and trace element data for the Temagami BIF samples measured with ICP-MS and ICP-OES.

mg/kg	TM1-1a	TM1-1b	TM1-1c	TM1-2	TM1-3	TM1-4a	TM1-4b	TM1-4c	TM2-1a	TM2-1b
<i>ICP-OES</i>										
Al	4896	8449	5253	343	10757	7917	4405	6449	9952	7282
Ca	6817	9353	4036	659	8762	5043	3407	5370	3820	1985
Fe	415102	416810	438561	55288	399901	395276	342717	388490	542154	565486
Mg	6555	8791	6313	551	8494	7238	5831	7965	8601	6330
Mn	141	163	106		189	123	121	144	136	114
P	1560	2327	855		1701	1362	560	1188	1705	985
<i>ICP-MS</i>										
Li	5.18	6.76	5.37	0.20	6.32	5.98	4.39	6.14	6.63	5.19
Be	1.17	0.90	0.68	0.12	1.02	0.95	0.55	0.74	0.66	1.01
Sc	0.71	0.84	0.60		0.85	0.82	0.61	0.82	1.05	0.90
Ti	234	320	236	28.70	356	274	172	261	475	308
Co		1.01			1.11	1.00		1.00	1.69	1.66
Ni	6.25	4.13	3.19	1.16	3.81	3.94	2.47	3.15	9.37	4.56
Rb	33.41	43.70	30.62	1.18	37.41	32.15	19.91	32.15	0.70	0.78
Sr	115	147	60.89	15.13	164.17	83.61	55.27	84.00	40.41	20.83
Zr	7.88	11.35	5.65	1.65	15.07	11.75	4.98	10.40	19.25	6.24
Cs	7.02	10.07	7.16	0.18	9.12	7.94	5.51	8.55	0.10	0.10
Ba	12.67	16.57	13.42	11.97	17.23	14.15	9.54	10.07	2.59	3.29
La	6.22	11.21	5.07	0.36	10.39	7.88	4.57	8.32	4.51	3.52
Ce	9.48	17.54	8.20	0.65	17.06	13.17	7.53	13.93	9.68	7.24
Pr	1.04	1.92	0.91	0.08	1.90	1.49	0.81	1.51	1.23	0.88
Nd	3.98	7.27	3.34	0.31	7.43	5.72	3.03	5.69	5.19	3.54
Sm	0.72	1.23	0.57	0.06	1.31	1.04	0.50	0.96	1.29	0.78
Eu	0.57	0.92	0.40		0.89	0.75	0.34	0.65	0.93	0.55
Gd	0.90	1.47	0.67		1.56	1.28	0.57	1.15	1.78	1.07
Tb	0.12	0.20	0.09	0.01	0.21	0.17	0.08	0.15	0.27	0.16
Dy	0.78	1.22	0.57	0.10	1.28	1.06	0.47	0.92	1.82	1.03
Y	7.52	11.55	5.05	0.82	12.44	9.67	4.12	8.27	11.51	6.44
Ho	0.18	0.28	0.13	0.02	0.29	0.24	0.10	0.21	0.39	0.22
Er	0.55	0.85	0.41	0.08	0.89	0.73	0.32	0.65	1.23	0.69
Tm	0.08	0.12	0.05		0.12	0.10		0.09	0.18	0.10
Yb	0.49	0.73	0.36		0.75	0.60	0.30	0.56	1.16	0.62
Lu	0.08	0.11	0.06	0.01	0.12	0.09	0.05	0.09	0.18	0.09
Hf	0.22	0.33	0.15	0.06	0.37	0.31	0.14	0.27	0.54	0.20
Ta	0.05	0.05	0.03	0.01	0.06	0.05	0.03	0.04	0.05	0.06
W	0.16	0.20	0.24	0.99	0.13	0.12	0.17	0.13	0.21	0.23
Pb	0.98	0.76	0.85	0.32	0.78	0.66	0.35	0.46	4.92	2.68
Th	0.38	0.72	0.44	0.06	0.89	0.61	0.29	0.53	0.88	0.53
U	0.17	0.13	0.09	0.05	0.19	0.17	0.07	0.11	0.22	0.15

Continued.

mg/kg	TM2-3a	TM2-3b	TM2-4a	TM2-4b	TM2-5a	TM2-5b	TM2-6	TM3-0	TM3-1	TM3-3
<i>ICP-OES</i>										
Al	5110	5079	369	1280	5926	4662	416	11297	638	546
Ca	2460	2208	238	1840	2614	2972	371	1413	578	432
Fe	591815	586205	39334	214372	559406	548063	53352	524235	35895	34965
Mg	4521	4541	521	1239	5205	4260	459	9548	753	657
Mn	98	98			104	92		146		
P	1227	1075		787	1263	1416		766	241	214
<i>ICP-MS</i>										
Li	4.11	4.09		1.30	5.04	3.97		7.59	0.33	0.30
Be	0.95	0.94	0.03	0.24	0.56	0.63	0.03	0.86	0.03	
Sc	0.62	0.58			0.49	0.47		0.94		
Ti	282	251	14.07	67.04	185	194	31.20	417	30.90	23.40
Co	1.16	1.17			0.98	0.99		1.63	0.81	0.45
Ni	4.53	4.68	0.85	2.54	5.58	3.65	0.89	5.65	1.04	1.12
Rb	0.56	0.63	0.70	0.18	0.30		0.41	1.49	0.72	0.83
Sr	24.03	21.93	2.59	16.87	27.17	29.57	4.61	16.30	4.80	4.16
Zr	10.36	6.40	0.86	3.22	5.01	4.78	1.76	20.30	1.56	1.33
Cs	0.07	0.09	0.09	0.04	0.05	0.04	0.07	0.22	0.10	0.10
Ba	2.89	3.03	3.42	1.52	1.63	1.84	4.70	4.55	3.74	23.00
La	9.00	7.63	0.48	3.90	7.43	7.14	0.77	5.09	0.62	0.55
Ce	14.98	12.77	0.85	6.46	12.22	12.08	1.25	9.82	1.25	1.02
Pr	1.67	1.41	0.10	0.71	1.34	1.36	0.14	1.08	0.15	0.12
Nd	6.29	5.37	0.37	2.83	5.14	5.32	0.54	4.03	0.62	0.48
Sm	1.12	0.98	0.07	0.55	0.95	1.03	0.11	0.78	0.15	0.11
Eu	0.76	0.68		0.43	0.70	0.76		0.51	0.11	0.09
Gd	1.40	1.22	0.10	0.75	1.25	1.32	0.13	0.95	0.19	0.14
Tb	0.19	0.16	0.02	0.10	0.16	0.18	0.02	0.15	0.03	0.02
Dy	1.17	1.09	0.11	0.67	1.09	1.18	0.15	1.00	0.21	0.16
Y	9.06	8.36	1.00	5.86	9.48	10.44	1.65	7.02	1.84	1.61
Ho	0.26	0.25	0.03	0.15	0.25	0.28	0.04	0.23	0.05	0.04
Er	0.81	0.74	0.09	0.47	0.79	0.84	0.12	0.75	0.17	0.13
Tm	0.11	0.10		0.06	0.11	0.12		0.11		
Yb	0.72	0.63		0.40	0.66	0.71	0.13	0.79	0.17	0.13
Lu	0.11	0.10	0.02	0.06	0.10	0.11	0.02	0.13	0.03	
Hf	0.26	0.19	0.09	0.12	0.13	0.16	0.10	0.49	0.14	0.10
Ta	0.04	0.04	0.01	0.01	0.04	0.03	0.01	0.07	0.02	
W	0.29	0.32	0.18	0.24	0.40	0.37	0.41	0.41	0.29	0.27
Pb	1.04	0.75	0.64	0.30	0.43	0.58	0.41	4.28	2.87	21.20
Th	0.49	0.42	0.02	0.18	0.36	0.36	0.03	0.93	0.05	0.03
U	0.17	0.14	0.03	0.05	0.10	0.10	0.05	0.24	0.04	0.03

6 Gallium-aluminium systematics in the Temagami BIF

Continued.

mg/kg	TM3-4	TM3-5	TM3-6	TM3-7	TM3-8	TM3-9	TM4-1b	TM4-2a	TM4-3	TM4-3.1
<i>ICP-OES</i>										
Al	4020	600	3556	311	780	6051	5444	4649	92	116
Ca	2706	606	2778	1564	1334	3384	5110	1279	2645	2739
Fe	519561	48942	447276	34005	118478	495757	556461	554217	37879	37902
Mg	3907	724	3089	482	911	5510	4098	2667	588	518
Mn	89		89	104		191	240	80	117	96
P	1292	259	1273		289	1101				
<i>ICP-MS</i>										
Li	4.11	0.30	4.11	0.19	0.85	5.56	3.55	3.35		
Be	0.67		0.57		0.09	0.64	0.37	0.37	0.03	0.04
Sc							0.61	0.53		
Ti	151	25.80	121	15.40	71.00	222	258	198	14	17.69
Co	0.95	0.66	0.84	0.26	0.76	1.62				
Ni	3.26	0.80	2.35	2.16	1.32	2.72	5.30	5.07	3.92	3.84
Rb	0.38	0.77	0.67	0.12	1.15	3.22	0.16	0.08	0.04	0.13
Sr	24.70	5.92	26.10	15.90	13.80	31.00	20.94	6.57	17.06	17.01
Zr	5.98	1.36	3.83	0.16	1.42	8.17	5.23	4.46	0.13	0.15
Cs	0.06	0.09	0.09		0.20	0.56	0.03	0.02	0.01	0.02
Ba	3.18	4.05	27.60	3.00	8.27	4.70	0.72	1.06	1.16	2.68
La	6.46	0.70	5.78	0.49	1.60	2.68	3.52	3.03	0.60	0.55
Ce	10.50	1.20	9.03	0.94	2.78	5.20	6.26	5.19	1.07	1.02
Pr	1.12	0.13	1.00	0.12	0.31	0.63	0.69	0.55	0.12	0.13
Nd	4.37	0.53	3.92	0.51	1.30	2.88	2.47	1.96	0.46	0.51
Sm	0.88		0.77	0.12	0.26	0.69	0.39	0.30	0.10	0.11
Eu	0.69	0.09	0.59	0.07	0.18	0.51	0.18	0.13		
Gd	1.19	0.15	1.00	0.14	0.31	1.01	0.41		0.12	0.15
Tb	0.16	0.02	0.13		0.04	0.13	0.05	0.04	0.02	0.02
Dy	1.09	0.15	0.86	0.13	0.29	0.91	0.32	0.22	0.11	0.14
Y	9.72	1.65	8.71	1.16	2.92	8.96	2.60	2.07	1.00	1.58
Ho	0.25	0.04	0.21	0.03	0.07	0.20	0.07	0.05	0.02	0.03
Er	0.78	0.13	0.62	0.08	0.19	0.63	0.22	0.17	0.07	0.10
Tm	0.10		0.08		0.02	0.08				
Yb	0.66	0.13	0.51	0.07	0.15	0.52	0.21	0.17		
Lu	0.10		0.08			0.08	0.03	0.03	0.01	0.01
Hf	0.14	0.08	0.10		0.06	0.20	0.17	0.15		
Ta	0.03		0.02			0.04	0.07	0.04	0.00	0.00
W	0.43	0.41	0.31	0.37	0.28	0.40	0.45	0.37	0.64	0.57
Pb	6.51	2.46	3.46	68.10	14.10	10.80	0.31	0.23	0.11	0.14
Th	0.33	0.02	0.30		0.13	0.38	0.52	0.40	0.02	0.03
U	0.11	0.05	0.09		0.04	0.13	0.11	0.10	0.03	0.03

Continued.

mg/kg	TM4-4b	TM4-5a	TM4-5b	TM4-5b.1	TM4-6	TM4-7a	TM4-7b	IF-G	IF-G
<i>ICP-OES</i>									
Al	7984	147	275	136	5503	1597	8279	816	816
Ca	5044	1716	1167	517	2402	1597	6780	11048	10951
Fe	613922	29990	85524	50783	545804	184262	424653	403222	400574
Mg	4918	455	292	120	3334	1383	5618	12031	11810
Mn	187				111	105	260	338	335
P	810						935	378	353
<i>ICP-MS</i>									
Li	4.50				4.31	0.95	2.49	0.2143	0.1547
Be	0.45	0.02	0.04	0.02	0.52	0.11	0.12	3.9983	4.0602
Sc	0.83				0.61		0.47		
Ti	223	12.92	26.38	13.51	141	131	179	27.9381	27.5819
Co								3.5619	3.5771
Ni	5.21	3.47	1.35	2.17	3.33	2.45	3.72	27.7510	25.3184
Rb	0.18	0.07				0.41	0.04		
Sr	23.26	10.75	7.73	3.77	11.40	9.23	15.16	3.8743	3.4454
Zr	8.55	0.41	0.39	0.21	5.94	2.22	4.69	0.7541	0.6352
Cs	0.05	0.01			0.04	0.09	0.03	0.0616	0.0559
Ba	0.75	2.30	1.71	1.09	0.90	10.86	0.43	2.9326	2.1363
La	5.99	0.38	1.69	0.72	4.74	2.03	2.88	2.7856	2.6654
Ce	10.52	0.62	2.71	1.08	8.42	3.72	5.42	4.1877	3.9613
Pr	1.18	0.07	0.29	0.11	0.94	0.41	0.64	0.4543	0.4337
Nd	4.54	0.26	1.07	0.43	3.37	1.55	2.54	1.7973	1.7502
Sm	0.85	0.06	0.18	0.08	0.60	0.27	0.53	0.4103	0.3986
Eu	0.47		0.13		0.32	0.16	0.33	0.3761	0.3597
Gd	0.99	0.08	0.25	0.11	0.64	0.28	0.64	0.7276	0.7063
Tb	0.13	0.01	0.03	0.01	0.09	0.04	0.09	0.1174	0.1161
Dy	0.80	0.08	0.23	0.11	0.62	0.23	0.56	0.8525	0.8628
Y	7.53	0.73	2.48	1.14	5.63	1.86	4.50	8.6599	8.7418
Ho	0.18	0.02	0.05	0.02	0.15	0.05	0.12	0.2228	0.2160
Er	0.56	0.05	0.17	0.09	0.49	0.16	0.39	0.6708	0.6829
Tm	0.07				0.07		0.05	0.0948	0.0951
Yb	0.47		0.16		0.45	0.15	0.34	0.5983	0.6111
Lu	0.07	0.01	0.03	0.01	0.07	0.02	0.05	0.0934	0.0914
Hf	0.26				0.19	0.10	0.15	0.0273	0.0218
Ta	0.05	0.00	0.01	0.00	0.03	0.03	0.04	0.0216	0.0147
W	0.57	0.59	1.35	0.57	0.32	0.89	0.32	0.7770	0.7493
Pb	0.32	0.06	0.12	0.12	0.26	0.25	0.18	7.1256	6.5824
Th	0.51	0.02	0.06	0.02	0.38	0.26	0.31	0.0460	0.0462
U	0.16	0.02	0.07	0.03	0.12	0.10	0.08	0.0252	0.0186

6 Gallium-aluminium systematics in the Temagami BIF

Continued.

mg/kg	IF-G	IF-G	IF-G						
<i>ICP-OES</i>									
Al	817	791	804	811	806	796	802	803	801
Ca	11042	11203	11150	11175	11065	11131	11200	11110	11031
Fe	401583	405750	406242	404786	400910	402705	403978	402182	398120
Mg	11715	11821	11802	11735	11697	11846	11737	11858	11782
Mn	328	339	336	330	328	338	333	330	330
P	343	337	313	348	318	309	355	299	299
<i>ICP-MS</i>									
Li	0.1445	0.1341	0.1489	0.1375	0.1412	0.1437	0.1427		
Be	3.9875	3.8830	3.9938	3.9389	3.8897	3.8642	4.0277		
Sc									
Ti	27.4124	26.5155	25.0743	24.9908	24.9983	25.2053	25.5283		
Co	3.5465	3.5087	3.3840	3.4194	3.4304	3.4410	3.4285		
Ni	25.3273	24.8254	23.9670	24.2282	24.1231	24.1587	24.4872		
Rb									
Sr	3.3993	3.3836	3.3829	3.3639	3.3569	3.3624	3.3843		
Zr	0.6235	0.6569	0.6766	0.7247	0.6525	0.6508	0.6547		
Cs	0.0566	0.0589	0.0591	0.0577	0.0641	0.0774	0.0816		
Ba	2.0269	1.9852	1.9432	1.9570	1.9444	1.9836	1.9911		
La	2.6209	2.6694	2.5821	2.5757	2.5673	2.5498	2.5887		
Ce	3.9072	3.9773	3.8846	3.8865	3.8644	3.8649	3.9111		
Pr	0.4291	0.4325	0.4274	0.4168	0.4184	0.4258	0.4163		
Nd	1.7304	1.7735	1.7197	1.7062	1.6995	1.7226	1.6941		
Sm	0.3993	0.4040	0.4040	0.3980	0.3866	0.3833	0.3878		
Eu	0.3619	0.3642	0.3593	0.3607	0.3590	0.3562	0.3588		
Gd	0.7339	0.7183	0.7009	0.7099	0.6995	0.7036	0.7115		
Tb	0.1168	0.1145	0.1109	0.1123	0.1130	0.1080	0.1103		
Dy	0.8447	0.8539	0.8461	0.8534	0.8439	0.8283	0.8437		
Y	8.6671	8.7059	8.5807	8.6172	8.5369	8.6061	8.7088		
Ho	0.2075	0.2102	0.2102	0.2075	0.2032	0.2053	0.2056		
Er	0.6826	0.6855	0.6742	0.6624	0.6679	0.6612	0.6682		
Tm	0.0986	0.0898	0.0932	0.0937	0.0913	0.0937	0.0925		
Yb	0.5974	0.6073	0.5864	0.5952	0.5898	0.5887	0.6004		
Lu	0.0960	0.0933	0.0915	0.0905	0.0899	0.0915	0.0906		
Hf	0.0240		0.0225	0.0259	0.0261	0.0226			
Ta	0.0134	0.0172	0.0197	0.0208	0.0193	0.0203	0.0218		
W	0.7470	0.7525	0.7314	0.7370	0.7436	0.7478	0.7437		
Pb	6.4899	6.5233	6.5814	6.4684	6.5011	6.4652	6.5292		
Th	0.0448	0.0442	0.0447	0.0448	0.0435	0.0477	0.0447		
U	0.0185	0.0154	0.0148	0.0168	0.0153	0.0167	0.0153		

Continued.

mg/kg	IF-G	IF-G	AVG [mg/kg]	RSD [%]	ref. [mg/kg]	meas./ref. [%]	ref. source
<i>ICP-OES</i>			<i>n=13</i>				
Al	819	818	808	1.1	794	1.73	Fabre et al. (2011)
Ca	11184	11084	11106	0.7	11006	0.91	Simons et al. (2016)
Fe	406904	403195	403088	0.6	387774	3.95	Simons et al. (2016)
Mg	11843	11869	11811	0.7	11157	5.86	Simons et al. (2016)
Mn	326	337	333	1.3	325	2.43	Fabre et al. 2011
P	307	385	334	8.7	305	9.56	Simons et al. (2016)
<i>ICP-MS</i>			<i>n=9</i>				
Li			0.1513	16.1079	0.1250	21.04	Viehmann et al. (2016)
Be			3.9604	1.7512	4.0000	-0.99	Parks et al. (2014)
Sc							
Ti			26.1383	4.7012	21.8700	19.52	Albut et al. (2018)
Co			3.4775	2.0550	29.4100	-88.18	Albut et al. (2018)
Ni			24.9096	4.7364	24.5000	1.67	Albut et al. (2018)
Rb							
Sr			3.4392	4.8057	3.5720	-3.72	Albut et al. (2018)
Zr			0.6699	6.3695	0.7013	-4.48	Albut et al. (2018)
Cs			0.0637	14.7209	0.0586	8.66	Albut et al. (2018)
Ba			2.1000	15.1314	1.9950	5.27	Albut et al. (2018)
La			2.6228	2.8260	2.7000	-2.86	Dulski (2001)
Ce			3.9383	2.5765	4.0000	-1.54	Dulski (2001)
Pr			0.4283	2.7447	0.4500	-4.83	Dulski (2001)
Nd			1.7326	2.0111	1.7500	-0.99	Dulski (2001)
Sm			0.3969	2.2912	0.3900	1.76	Dulski (2001)
Eu			0.3618	1.6054	0.3700	-2.22	Dulski (2001)
Gd			0.7124	1.6800	0.7100	0.33	Dulski (2001)
Tb			0.1132	2.8233	0.1110	2.03	Dulski (2001)
Dy			0.8477	1.1341	0.8100	4.65	Dulski (2001)
Y			8.6471	0.7748	9.1000	-4.98	Dulski (2001)
Ho			0.2098	2.9261	0.2030	3.35	Dulski (2001)
Er			0.6729	1.3419	0.6400	5.14	Dulski (2001)
Tm			0.0936	2.6634	0.0910	2.88	Dulski (2001)
Yb			0.5972	1.3970	0.5800	2.96	Dulski (2001)
Lu			0.0920	2.0730	0.0910	1.11	Dulski (2001)
Hf			0.0243	8.7772	0.0230	5.73	Dulski (2001)
Ta			0.0188	16.0592	0.1691	-88.91	Albut et al. (2018)
W			0.7477	1.7030	0.7940	-5.83	Viehmann et al. (2016)
Pb			6.5852	3.1456	2.5000	163.41	Dulski (2001)
Th			0.0452	2.7547	0.0424	6.55	Albut et al. (2018)
U			0.0174	18.5782	0.0208	-16.31	Albut et al. (2018)
Fabre et al. (2011) http://dx.doi.org/10.1016/j.chemgeo.2011.07.019							
Simons et al. (2016) http://dx.doi.org/10.1016/j.lithos.2016.05.010							
Viehmann et al. (2016) http://dx.doi.org/10.1016/j.precamres.2016.07.006							
Parks et al. (2014) http://dx.doi.org/10.1016/j.precamres.2014.02.016							
Albut et al. (2018) https://doi.org/10.1016/j.gca.2018.02.034							
Dulski (2001) http://dx.doi.org/10.1111/j.1751-908X.2001.tb00790.x							

Table 6.5: Gallium and aluminium measured in RMs with SF-ICP-MS and ICP-MS/MS.

Sample	SF-ICP-MS			ICP-MS/MS					Literature values		
	Ga [mg/kg]	Al [mg/kg]	Ga/Al [mg/mg]	Ga [mg/kg]	Al [mg/kg]	Ga/Al [mg/mg]	Ga RSD [%]	Al RSD [%]	Ga [mg/kg]	Al [mg/kg]	Ga/Al
IF-G.i	0.57	807	7.01×10^{-4}						0.61 ⁽¹⁾	793.86 ⁽²⁾	7.68×10^{-4}
IF-G.i_rep	0.58	726	8.05×10^{-4}								
IF-G.ii	0.63	805	7.79×10^{-4}	0.57	732	7.72×10^{-4}	1.1	10.0			
FeR-4	2.58	9725	2.66×10^{-4}	2.52	9283	2.71×10^{-4}	2.4	8.1	2.6 ⁽¹⁾	8467.85 ⁽³⁾	3.07×10^{-4}
FeR-4_rep	2.33	8562	2.72×10^{-4}								
FeR-3	0.19	458	4.21×10^{-4}	0.34	427	7.98×10^{-4}	2.7	5.5	0.37 ⁽¹⁾	423 ⁽³⁾	8.75×10^{-4}
NOD-P1	26.5	24632	1.08×10^{-3}	27.5	23577	1.17×10^{-3}	0.3	6.7	28.1 ⁽⁴⁾	25724 ⁽⁵⁾	1.09×10^{-3}
BHVO-2	24.0	79880	3.00×10^{-4}	22.4	75350	2.97×10^{-4}	1.1	4.2	21.4 ⁽⁶⁾	71739 ⁽⁶⁾	2.98×10^{-4}

(1) Sampaio and Enzweiler (2015) <https://doi.org/10.1111/j.1751-908X.2014.00293.x>(2) Fabre et al. (2011) <https://doi.org/10.1016/j.chemgeo.2011.07.019>(3) Govindaraju (1994) <https://doi.org/10.1046/j.1365-2494.1998.53202081.x-i1>(4) Axelsson et al. (2002) <https://doi.org/10.1039/b105706p>(5) Terashima et al. (1995) <https://doi.org/10.1111/j.1751-908X.1995.tb00160.x>(6) median of all GeoReM values <http://georem.mpch-mainz.gwdg.de/> (accessed on 12.10.2022)

Table 6.6: Individual LA-ICP-MS measurements of the Temagami BIF NP tablet samples.

sample <i>LA-ICP-MS</i>	$^{69}\text{Ga}/^{27}\text{Al}$ [cps/cps]	$^{71}\text{Ga}/^{27}\text{Al}$ [cps/cps]	$^{69}\text{Ga}/^{27}\text{Al}$ mass ratio [mg/mg]	$^{71}\text{Ga}/^{27}\text{Al}$ [cps/cps]	$(^{69}\text{Ga}/^{27}\text{Al}) / (^{71}\text{Ga}/^{27}\text{Al})$ [%]
TM3-0	2.04×10^{-4}	2.03×10^{-4}	2.76×10^{-4}	2.99×10^{-4}	7.8
TM3-0	2.12×10^{-4}	1.95×10^{-4}	2.85×10^{-4}	2.90×10^{-4}	1.6
TM3-0	1.91×10^{-4}	1.65×10^{-4}	2.62×10^{-4}	2.55×10^{-4}	-2.8
TM3-0	1.88×10^{-4}	1.59×10^{-4}	2.59×10^{-4}	2.48×10^{-4}	-4.3
TM3-0	2.32×10^{-4}	1.96×10^{-4}	3.06×10^{-4}	2.91×10^{-4}	-5.2
TM3-2	2.47×10^{-4}	2.15×10^{-4}	3.22×10^{-4}	3.13×10^{-4}	-3.0
TM3-2	2.45×10^{-4}	1.95×10^{-4}	3.20×10^{-4}	2.89×10^{-4}	-10.5
TM3-2	2.51×10^{-4}	2.14×10^{-4}	3.26×10^{-4}	3.12×10^{-4}	-4.7
TM3-2	2.37×10^{-4}	2.28×10^{-4}	3.11×10^{-4}	3.27×10^{-4}	4.8
TM3-2	2.28×10^{-4}	2.05×10^{-4}	3.01×10^{-4}	3.01×10^{-4}	-0.2
TM3-4	2.20×10^{-4}	2.00×10^{-4}	2.93×10^{-4}	2.96×10^{-4}	1.0
TM3-4	2.16×10^{-4}	1.87×10^{-4}	2.89×10^{-4}	2.81×10^{-4}	-2.9
TM3-4	2.28×10^{-4}	2.06×10^{-4}	3.02×10^{-4}	3.03×10^{-4}	0.2
TM3-4	2.62×10^{-4}	2.73×10^{-4}	3.37×10^{-4}	3.79×10^{-4}	11.0
TM3-4	2.37×10^{-4}	2.01×10^{-4}	3.11×10^{-4}	2.96×10^{-4}	-4.9
TM3-6_dup1	2.29×10^{-4}	2.04×10^{-4}	3.03×10^{-4}	3.00×10^{-4}	-0.9
TM3-6_dup1	2.38×10^{-4}	2.19×10^{-4}	3.13×10^{-4}	3.17×10^{-4}	1.4
TM3-6_dup1	1.95×10^{-4}	1.61×10^{-4}	2.67×10^{-4}	2.50×10^{-4}	-6.7
TM3-6_dup1	2.42×10^{-4}	2.15×10^{-4}	3.16×10^{-4}	3.13×10^{-4}	-1.2
TM3-6_dup1	2.31×10^{-4}	2.05×10^{-4}	3.05×10^{-4}	3.01×10^{-4}	-1.4
TM3-6_dup2	1.97×10^{-4}	1.70×10^{-4}	2.69×10^{-4}	2.61×10^{-4}	-3.1
TM3-6_dup2	2.09×10^{-4}	2.19×10^{-4}	2.82×10^{-4}	3.17×10^{-4}	11.1
TM3-6_dup2	1.96×10^{-4}	1.81×10^{-4}	2.68×10^{-4}	2.74×10^{-4}	2.2
TM3-6_dup2	2.39×10^{-4}	2.22×10^{-4}	3.13×10^{-4}	3.21×10^{-4}	2.5
TM3-6_dup2	1.94×10^{-4}	1.68×10^{-4}	2.65×10^{-4}	2.58×10^{-4}	-2.6
TM3-8	6.44×10^{-4}	5.98×10^{-4}	7.43×10^{-4}	7.52×10^{-4}	1.3
TM3-8	5.80×10^{-4}	4.72×10^{-4}	6.75×10^{-4}	6.08×10^{-4}	-11.1
TM3-8	5.83×10^{-4}	5.92×10^{-4}	6.78×10^{-4}	7.45×10^{-4}	9.0
TM3-8	5.44×10^{-4}	5.03×10^{-4}	6.37×10^{-4}	6.43×10^{-4}	1.0
TM3-8	6.96×10^{-4}	5.43×10^{-4}	7.98×10^{-4}	6.90×10^{-4}	-15.7
TM3-9	2.03×10^{-4}	1.92×10^{-4}	2.75×10^{-4}	2.86×10^{-4}	4.0
TM3-9	1.85×10^{-4}	1.79×10^{-4}	2.56×10^{-4}	2.71×10^{-4}	5.5
TM3-9	2.19×10^{-4}	1.91×10^{-4}	2.92×10^{-4}	2.85×10^{-4}	-2.3
TM3-9	2.04×10^{-4}	1.89×10^{-4}	2.77×10^{-4}	2.83×10^{-4}	2.3
TM3-9	2.22×10^{-4}	1.98×10^{-4}	2.95×10^{-4}	2.93×10^{-4}	-0.5

Table 6.7: Individual LA-ICP-MS measurements of the RM NP tablet samples.

reference material <i>LA-ICP-MS</i>	$^{69}\text{Ga}/^{27}\text{Al}$ [cps/cps]	$^{71}\text{Ga}/^{27}\text{Al}$ [cps/cps]	$^{69}\text{Ga}/^{27}\text{Al}$ mass ratio [mg/mg]	$^{71}\text{Ga}/^{27}\text{Al}$ [mg/mg]	$(^{69}\text{Ga}/^{27}\text{Al}) / (^{71}\text{Ga}/^{27}\text{Al})$ [%]
NISTSRM610	3.27E-02	2.93E-02	3.48E-02	3.37E-02	-3.0
NISTSRM610	3.48E-02	3.04E-02	3.70E-02	3.49E-02	-5.9
NISTSRM610	3.37E-02	3.03E-02	3.58E-02	3.49E-02	-2.5
NISTSRM610	3.65E-02	3.30E-02	3.88E-02	3.80E-02	-2.1
NISTSRM610	3.55E-02	3.22E-02	3.77E-02	3.71E-02	-1.9
NISTSRM610	3.77E-02	3.28E-02	4.00E-02	3.78E-02	-5.9
NISTSRM610	3.95E-02	3.58E-02	4.20E-02	4.11E-02	-2.0
NISTSRM610	3.77E-02	3.45E-02	4.00E-02	3.97E-02	-0.8
NISTSRM610	3.92E-02	3.31E-02	4.16E-02	3.81E-02	-9.4
IF-G	6.42×10^{-4}	6.19×10^{-4}	7.41×10^{-4}	7.76×10^{-4}	4.6
IF-G	7.95×10^{-4}	6.57×10^{-4}	9.03×10^{-4}	8.20×10^{-4}	-10.1
IF-G	6.43×10^{-4}	6.29×10^{-4}	7.41×10^{-4}	7.88×10^{-4}	6.0
IF-G	5.85×10^{-4}	5.96×10^{-4}	6.81×10^{-4}	7.50×10^{-4}	9.3
IF-G	6.61×10^{-4}	5.95×10^{-4}	7.61×10^{-4}	7.49×10^{-4}	-1.6
IF-G	7.00×10^{-4}	5.56×10^{-4}	8.02×10^{-4}	7.04×10^{-4}	-13.9
IF-G	6.77×10^{-4}	5.87×10^{-4}	7.78×10^{-4}	7.40×10^{-4}	-5.1
IF-G	7.58×10^{-4}	7.31×10^{-4}	8.64×10^{-4}	9.05×10^{-4}	4.6
IF-G	6.68×10^{-4}	6.63×10^{-4}	7.68×10^{-4}	8.27×10^{-4}	7.2
FeR-3	9.01×10^{-4}	8.53×10^{-4}	1.02E-03	1.04E-03	2.8
FeR-3	8.40×10^{-4}	7.91×10^{-4}	9.50×10^{-4}	9.74×10^{-4}	2.5
FeR-3	8.84×10^{-4}	7.69×10^{-4}	9.97×10^{-4}	9.49×10^{-4}	-5.1
FeR-3	9.46×10^{-4}	7.91×10^{-4}	1.06E-03	9.74×10^{-4}	-9.1
FeR-3	9.62×10^{-4}	7.37×10^{-4}	1.08E-03	9.11×10^{-4}	-18.5
FeR-3	1.00E-03	8.56×10^{-4}	1.12E-03	1.05E-03	-6.9
FeR-3	9.06×10^{-4}	8.91×10^{-4}	1.02E-03	1.09E-03	6.3
FeR-3	8.69×10^{-4}	7.49×10^{-4}	9.82×10^{-4}	9.26×10^{-4}	-6.0
FeR-3	9.20×10^{-4}	7.25×10^{-4}	1.04E-03	8.98×10^{-4}	-15.4

Continued.

reference material <i>LA-ICP-MS</i>	$^{69}\text{Ga}/^{27}\text{Al}$ [cps/cps]	$^{71}\text{Ga}/^{27}\text{Al}$ [cps/cps]	$^{69}\text{Ga}/^{27}\text{Al}$ mass ratio [mg/mg]	$^{71}\text{Ga}/^{27}\text{Al}$ [mg/mg]	$(^{69}\text{Ga}/^{27}\text{Al}) / (^{71}\text{Ga}/^{27}\text{Al})$ [%]
FeR-4	1.74×10^{-4}	1.67×10^{-4}	2.44×10^{-4}	2.57×10^{-4}	4.8
FeR-4	1.80×10^{-4}	1.57×10^{-4}	2.51×10^{-4}	2.46×10^{-4}	-2.0
FeR-4	1.83×10^{-4}	1.56×10^{-4}	2.54×10^{-4}	2.45×10^{-4}	-3.7
FeR-4	2.21×10^{-4}	1.92×10^{-4}	2.94×10^{-4}	2.87×10^{-4}	-2.6
FeR-4	1.90×10^{-4}	1.84×10^{-4}	2.61×10^{-4}	2.77×10^{-4}	5.7
FeR-4	2.64×10^{-4}	2.03×10^{-4}	3.39×10^{-4}	2.98×10^{-4}	-13.8
FeR-4	1.94×10^{-4}	1.65×10^{-4}	2.66×10^{-4}	2.55×10^{-4}	-4.1
FeR-4	2.04×10^{-4}	1.87×10^{-4}	2.76×10^{-4}	2.80×10^{-4}	1.4
FeR-4	2.05×10^{-4}	1.73×10^{-4}	2.78×10^{-4}	2.64×10^{-4}	-5.2
FeR-4	2.05×10^{-4}	1.90×10^{-4}	2.78×10^{-4}	2.83×10^{-4}	2.0
FeR-4	2.07×10^{-4}	1.97×10^{-4}	2.80×10^{-4}	2.92×10^{-4}	4.4
FeR-4	2.25×10^{-4}	1.97×10^{-4}	2.98×10^{-4}	2.92×10^{-4}	-2.3
FeR-4	2.18×10^{-4}	1.91×10^{-4}	2.91×10^{-4}	2.85×10^{-4}	-2.1
FeR-4	2.07×10^{-4}	1.84×10^{-4}	2.80×10^{-4}	2.77×10^{-4}	-1.1
FeR-4	1.92×10^{-4}	1.76×10^{-4}	2.64×10^{-4}	2.67×10^{-4}	1.3
FeR-4	2.06×10^{-4}	1.90×10^{-4}	2.78×10^{-4}	2.84×10^{-4}	2.1
FeR-4	1.95×10^{-4}	1.67×10^{-4}	2.67×10^{-4}	2.58×10^{-4}	-3.4
FeR-4	1.80×10^{-4}	1.58×10^{-4}	2.51×10^{-4}	2.48×10^{-4}	-1.3
FeR-4	1.92×10^{-4}	1.65×10^{-4}	2.63×10^{-4}	2.55×10^{-4}	-3.1
FeR-4	1.80×10^{-4}	1.83×10^{-4}	2.51×10^{-4}	2.76×10^{-4}	9.1
FeR-4	1.90×10^{-4}	1.82×10^{-4}	2.62×10^{-4}	2.74×10^{-4}	4.7
FeR-4	2.07×10^{-4}	1.89×10^{-4}	2.79×10^{-4}	2.83×10^{-4}	1.3
NOD-P1	7.66×10^{-4}	6.59×10^{-4}	8.71×10^{-4}	8.22×10^{-4}	-6.0
NOD-P1	7.81×10^{-4}	6.74×10^{-4}	8.88×10^{-4}	8.40×10^{-4}	-5.7
NOD-P1	7.47×10^{-4}	6.87×10^{-4}	8.52×10^{-4}	8.54×10^{-4}	0.3
NOD-P1	7.74×10^{-4}	6.73×10^{-4}	8.80×10^{-4}	8.39×10^{-4}	-4.9
NOD-P1	7.29×10^{-4}	6.67×10^{-4}	8.32×10^{-4}	8.31×10^{-4}	-0.1
NOD-P1	7.21×10^{-4}	7.32×10^{-4}	8.24×10^{-4}	9.06×10^{-4}	9.1
NOD-P1	7.75×10^{-4}	6.49×10^{-4}	8.82×10^{-4}	8.11×10^{-4}	-8.8
NOD-P1	7.72×10^{-4}	6.90×10^{-4}	8.79×10^{-4}	8.58×10^{-4}	-2.4
NOD-P1	7.71×10^{-4}	6.72×10^{-4}	8.77×10^{-4}	8.37×10^{-4}	-4.8
NOD-P1	8.25×10^{-4}	6.97×10^{-4}	9.34×10^{-4}	8.66×10^{-4}	-7.9
NOD-P1	7.97×10^{-4}	7.23×10^{-4}	9.05×10^{-4}	8.96×10^{-4}	-0.9
NOD-P1	7.75×10^{-4}	7.33×10^{-4}	8.82×10^{-4}	9.08×10^{-4}	2.9
NOD-A1	1.92×10^{-4}	1.70×10^{-4}	2.64×10^{-4}	2.60×10^{-4}	-1.3
NOD-A1	2.14×10^{-4}	1.84×10^{-4}	2.87×10^{-4}	2.77×10^{-4}	-3.3
NOD-A1	2.20×10^{-4}	1.87×10^{-4}	2.93×10^{-4}	2.80×10^{-4}	-4.8
NOD-A1	2.20×10^{-4}	2.11×10^{-4}	2.93×10^{-4}	3.08×10^{-4}	4.7
NOD-A1	2.12×10^{-4}	1.79×10^{-4}	2.85×10^{-4}	2.72×10^{-4}	-4.7
NOD-A1	2.10×10^{-4}	1.95×10^{-4}	2.82×10^{-4}	2.89×10^{-4}	2.3

6.10 Acknowledgements

We express our gratitude to Ulrike Westerströer from CAU Kiel University for her assistance with operating the LA-ICP-MS and performing the SF-ICP-MS analyses of dissolved samples. We appreciate the valuable discussions with colleagues in the DFG Priority Program SPP-1833 and acknowledge funding from the Deutsche Forschungsgemeinschaft (grant BA-2289/8-1).

6.11 References

- Albut, G., Babechuk, M.G., Kleinhanns, I.C., Bengler, M., Beukes, N.J., Steinhilber, B., Smith, A.J.B., Kruger, S.J., Schoenberg, R., 2018. Modern rather than Mesoarchaean oxidative weathering responsible for the heavy stable Cr isotopic signatures of the 2.95 Ga old Ijzermijn iron formation (South Africa). *Geochimica et Cosmochimica Acta* 228, 157–189. <https://doi.org/10.1016/j.gca.2018.02.03>
- Alexander, B.W., Bau, M., Andersson, P., 2009. Neodymium isotopes in Archaean seawater and implications for the marine Nd cycle in Earth's early oceans. *Earth and Planetary Science Letters* 283, 144–155. <https://doi:10.1016/j.epsl.2009.04.004>
- Alexander, B.W., Bau, M., Andersson, P., Dulski, P., 2008. Continentally-derived solutes in shallow Archaean seawater: Rare earth element and Nd isotope evidence in iron formation from the 2.9Ga Pongola Supergroup, South Africa. *Geochimica et Cosmochimica Acta* 72, 378–394. <https://doi.org/10.1016/j.gca.2007.10.028>
- Alibert, C., 2016. Rare earth elements in Hamersley BIF minerals. *Geochimica et Cosmochimica Acta* 184, 311–328. <https://doi.org/10.1016/j.gca.2016.03.026>
- Alibert, C., Kinsley, L., 2016. Ge/Si in Hamersley BIF as tracer of hydrothermal Si and Ge inputs to the Palaeoproterozoic ocean. *Geochimica et Cosmochimica Acta* 184, 329–343. <https://doi.org/10.1016/j.gca.2016.03.027>
- Alibert, C., McCulloch, M.T., 1993. Rare earth element and neodymium isotopic compositions of the banded iron-formations and associated shales from Hamersley, western Australia. *Geochimica et Cosmochimica Acta* 57, 187–204. [https://doi.org/10.1016/0016-7037\(93\)90478-F](https://doi.org/10.1016/0016-7037(93)90478-F)
- Axelsson, M.D., Rodushkin, I., Ingri, J., Öhlander, B., 2002. Multielemental analysis of Mn–Fe nodules by ICP-MS: optimisation of analytical method. *Analyst* 127, 76–82. <https://doi.org/10.1039/b105706p>
- Bau, M., 1991. Rare-earth element mobility during hydrothermal and metamorphic fluid-rock interaction and the significance of the oxidation state of europium. *Chemical Geology* 93, 219–230. [https://doi.org/10.1016/0009-2541\(91\)90115-8](https://doi.org/10.1016/0009-2541(91)90115-8)
- Bau, M., 1999. Scavenging of dissolved yttrium and rare earths by precipitating iron oxyhydroxide: experimental evidence for Ce oxidation, Y–Ho fractionation, and lanthanide tetrad effect. *Geochimica et Cosmochimica Acta* 63, 67–77. [https://doi.org/10.1016/S0016-7037\(99\)00014-9](https://doi.org/10.1016/S0016-7037(99)00014-9)

- Bau, M., Alexander, B.W., 2009. Distribution of high field strength elements (Y, Zr, REE, Hf, Ta, Th, U) in adjacent magnetite and chert bands and in reference standards FeR-3 and FeR-4 from the Temagami iron-formation, Canada, and the redox level of the Neoproterozoic ocean. *Precambrian Research* 174, 337–346. <https://doi.org/10.1016/j.precamres.2009.08.007>
- Bau, M., Dulski, P., 1996. Distribution of yttrium and rare-earth elements in the Penge and Kuruman iron-formations, Transvaal Supergroup, South Africa. *Precambrian Research* 79, 37–55. [https://doi.org/10.1016/0301-9268\(95\)00087-9](https://doi.org/10.1016/0301-9268(95)00087-9)
- Bau, M., Frei, R., Garbe-Schönberg, D., Viehmann, S., 2022. High-resolution Ge-Si-Fe, Cr isotope and Th-U data for the Neoproterozoic Temagami BIF, Canada, suggest primary origin of BIF bands and oxidative terrestrial weathering 2.7 Ga ago. *Earth and Planetary Science Letters* 589, 117579. <https://doi.org/10.1016/j.epsl.2022.117579>
- Bau, M., Koschinsky, A., 2009. Oxidative scavenging of cerium on hydrous Fe oxide: Evidence from the distribution of rare earth elements and yttrium between Fe oxides and Mn oxides in hydrogenetic ferromanganese crusts. *Geochem. J.* 43, 37–47. <https://doi.org/10.2343/geochemj.1.0005>
- Bau, M., Koschinsky, A., Dulski, P., Hein, J.R., 1996. Comparison of the partitioning behaviours of yttrium, rare earth elements, and titanium between hydrogenetic marine ferromanganese crusts and seawater. *Geochimica et Cosmochimica Acta* 60, 1709–1725. [https://doi.org/10.1016/0016-7037\(96\)00063-4](https://doi.org/10.1016/0016-7037(96)00063-4)
- Bau, M., Möller, P., 1993. Rare earth element systematics of the chemically precipitated component in early precambrian iron formations and the evolution of the terrestrial atmosphere-hydrosphere-lithosphere system. *Geochimica et Cosmochimica Acta* 57, 2239–2249. [https://doi.org/10.1016/0016-7037\(93\)90566-F](https://doi.org/10.1016/0016-7037(93)90566-F)
- Bau, M., Usui, A., Pracejus, B., Mita, N., Kanai, Y., Irber, W., Dulski, P., 1998. Geochemistry of low-temperature water–rock interaction: evidence from natural waters, andesite, and iron-oxyhydroxide precipitates at Nishiki-numa iron-spring, Hokkaido, Japan. *Chemical Geology* 151, 293–307. [https://doi.org/10.1016/S0009-2541\(98\)00086-2](https://doi.org/10.1016/S0009-2541(98)00086-2)
- Bekker, A., Slack, J.F., Planavsky, N., Krapež, B., Hofmann, A., Konhauser, K.O., Rouxel, O.J., 2010. Iron Formation: The Sedimentary Product of a Complex Interplay among Mantle, Tectonic, Oceanic, and Biospheric Processes. *Economic Geology* 105, 467–508. <https://doi.org/10.2113/gsecongeo.105.3.467>
- Beukes, N.J., 1973. Precambrian Iron-Formations of Southern Africa. *Economic Geology* 68, 960–1004. <https://doi.org/10.2113/gsecongeo.68.7.960>
- Beukes, N.J., Klein, C., 1990. Geochemistry and sedimentology of a facies transition — from microbanded to granular iron-formation — in the early Proterozoic Transvaal Supergroup, South Africa. *Precambrian Research* 47, 99–139. [https://doi.org/10.1016/0301-9268\(90\)90033-M](https://doi.org/10.1016/0301-9268(90)90033-M)
- Blokhin, M.G., Zarubina, N.V., Mikhailyk, P.E., 2014. Inductively coupled plasma mass spectrometric measurement of gallium in ferromanganese crusts from the Sea of Japan. *J Anal Chem* 69, 1237–1244. <https://doi.org/10.1134/S1061934814130036>
- Bowins, R.J., Heaman, L.M., 1991. Age and timing of igneous activity in the Temagami greenstone belt, Ontario: a preliminary report. *Can. J. Earth Sci.* 28, 1873–1876.

- <https://doi.org/10.1139/e91-167>
- Breiter, K., Gardenová, N., Kanický, V., Vaculovič, T., 2013. Gallium and germanium geochemistry during magmatic fractionation and post-magmatic alteration in different types of granitoids: a case study from the Bohemian Massif (Czech Republic). *Geologica Carpathica* 64, 171–180b. <https://doi.org/10.2478/geoca-2013-0018>
- Brown, M.T., Bruland, K.W., 2009. Dissolved and particulate aluminum in the Columbia River and coastal waters of Oregon and Washington: Behavior in near-field and far-field plumes. *Estuarine, Coastal and Shelf Science* 84, 171–185. <https://doi.org/10.1016/j.ecss.2009.05.031>
- Byrne, R.H., 2010. Comparative carbonate and hydroxide complexation of cations in seawater. *Geochimica et Cosmochimica Acta* 74, 4312–4321. <https://doi.org/10.1016/j.gca.2010.05.001>
- Byrne, R.H., Kump, L.R., Cantrell, K.J., 1988. The influence of temperature and pH on trace metal speciation in seawater. *Marine Chemistry* 25, 163–181. [https://doi.org/10.1016/0304-4203\(88\)90062-X](https://doi.org/10.1016/0304-4203(88)90062-X)
- Cameron, E.M., Garrels, R.M., 1980. Geochemical compositions of some Precambrian shales from the Canadian Shield. *Chemical Geology* 28, 181–197. [https://doi.org/10.1016/0009-2541\(80\)90046-7](https://doi.org/10.1016/0009-2541(80)90046-7)
- Charette, M.A., Kipp, L.E., Jensen, L.T., Dabrowski, J.S., Whitmore, L.M., Fitzsimmons, J.N., Williford, T., Ulfsbo, A., Jones, E., Bundy, R.M., Vivancos, S.M., Pahnke, K., John, S.G., Xiang, Y., Hatta, M., Petrova, M.V., Heimbürger-Boavida, L., Bauch, D., Newton, R., Pasqualini, A., Agather, A.M., Amon, R.M.W., Anderson, R.F., Andersson, P.S., Benner, R., Bowman, K.L., Edwards, R.L., Gdaniec, S., Gerringa, L.J.A., González, A.G., Granskog, M., Haley, B., Hammerschmidt, C.R., Hansell, D.A., Henderson, P.B., Kadko, D.C., Kaiser, K., Laan, P., Lam, P.J., Lamborg, C.H., Levier, M., Li, X., Margolin, A.R., Measures, C., Middag, R., Millero, F.J., Moore, W.S., Paffrath, R., Planquette, H., Rabe, B., Reader, H., Rember, R., Rijkenberg, M.J.A., Roy-Barman, M., Rutgers van der Loeff, M., Saito, M., Schauer, U., Schlosser, P., Sherrell, R.M., Shiller, A.M., Slagter, H., Sonke, J.E., Stedmon, C., Woosley, R.J., Valk, O., Ooijen, J., Zhang, R., 2020. The Transpolar Drift as a Source of Riverine and Shelf-Derived Trace Elements to the Central Arctic Ocean. *J. Geophys. Res. Oceans* 125. <https://doi.org/10.1029/2019JC015920>
- Chen, J., An, Z., Liu, L., Ji, J., Yang, J., Chen, Y., 2001. Variations in chemical compositions of the eolian dust in Chinese Loess Plateau over the past 2.5 Ma and chemical weathering in the Asian inland. *Sci. China Ser. D-Earth Sci.* 44, 403–413. <https://doi.org/10.1007/BF02909779>
- Clarke, D.B., Cameron, B.I., Muecke, G.K., Bates, J.L., 1989. Early Tertiary basalts from the Labrador Sea floor and Davis Strait region. *Can. J. Earth Sci.* 26, 956–968. <https://doi.org/10.1139/e89-077>
- De Argollo, R., Schilling, J.-G., 1978. Ge-Si and Ga-Al fractionation in Hawaiian volcanic rocks. *Geochimica et Cosmochimica Acta* 42, 623–630. [https://doi.org/10.1016/0016-7037\(78\)90007-8](https://doi.org/10.1016/0016-7037(78)90007-8)
- Delvigne, C., Cardinal, D., Hofmann, A., André, L., 2012. Stratigraphic changes of Ge/Si, REE+Y and silicon isotopes as insights into the deposition of a Mesoarchean

- banded iron formation. *Earth and Planetary Science Letters* 355–356, 109–118. <https://doi.org/10.1016/j.epsl.2012.07.035>
- Diekrup, D., 2019. Depositional Pathways and the Post-Depositional History of the Neoproterozoic Algoma-Type BIF in Temagami, ON. University of Ottawa, Ottawa, Canada.
- Diekrup, D., Hannington, M.D., Strauss, H., Ginley, S.J., 2018. Decoupling of Neoproterozoic sulfur sources recorded in Algoma-type banded iron formation. *Earth and Planetary Science Letters* 489, 1–7. <https://doi.org/10.1016/j.epsl.2018.02.022>
- Dodd, M.S., Papineau, D., She, Z.-B., Manikyamba, C., Wan, Y.-S., O’Neil, J., Karhu, J.A., Rizo, H., Pirajno, F., 2019. Widespread occurrences of variably crystalline ^{13}C -depleted graphitic carbon in banded iron formations. *Earth and Planetary Science Letters* 512, 163–174. <https://doi.org/10.1016/j.epsl.2019.01.054>
- Dulski, P., 2001. Reference Materials for Geochemical Studies: New Analytical Data by ICP-MS and Critical Discussion of Reference Values. *Geostandards and Geoanalytical Research* 25, 87–125. <https://doi.org/10.1111/j.1751-908X.2001.tb00790.x>
- Elderfield, H., Greaves, M.J., 1982. The rare earth elements in seawater. *Nature* 296, 214–219. <https://doi.org/10.1038/296214a0>
- Elderfield, H., Whitfield, M., Burton, J.D., Bacon, M.P., Liss, P.S., 1988. The oceanic chemistry of the rare-earth elements. *Philosophical Transactions of the Royal Society of London. Series A, Math. Phys. Sci.* 325, 105–126. <https://doi.org/10.1098/rsta.1988.0046>
- Ernst, D.M., Bau, M., 2021. Banded iron formation from Antarctica: The 2.5 Ga old Mt. Rucker BIF and the antiquity of lanthanide tetrad effect and super-chondritic Y/Ho ratio in seawater. *Gondwana Research* 91, 97–111. <https://doi.org/10.1016/j.gr.2020.11.011>
- Ernst, D.M., Schier, K., Garbe-Schönberg, D., Bau, M., 2022. Fractionation of germanium and silicon during scavenging from seawater by marine Fe (oxy)hydroxides: Evidence from hydrogenetic ferromanganese crusts and nodules. *Chemical Geology* 595. <https://doi.org/10.1016/j.chemgeo.2022.120791>
- Evers, A., Hancock, R.D., Martell, A.E., Motekaitis, R.J., 1989. Metal Ion Recognition in Ligands with Negatively Charged Oxygen Donor Groups. Complexation of Fe(III), Ga(III), In(III), Al (III), and Other Highly Charged Metal Ions. *Inorganic Chemistry* 28, 2189–2195. <https://doi.org/10.1021/ic00310a035>
- Fabre, S., Nédélec, A., Poitrasson, F., Strauss, H., Thomazo, C., Nogueira, A., 2011. Iron and sulphur isotopes from the Carajás mining province (Pará, Brazil): Implications for the oxidation of the ocean and the atmosphere across the Archean–Proterozoic transition. *Chemical Geology* 289, 124–139. <https://doi.org/10.1016/j.chemgeo.2011.07.019>
- Farrell, Ú.C., Samawi, R., Anjanappa, S., Klykov, R., Adeboye, O.O., Agic, H., Ahm, A.C., Boag, T.H., Bowyer, F., Brocks, J.J., Brunoir, T.N., Canfield, D.E., Chen, X., Cheng, M., Clarkson, M.O., Cole, D.B., Cordie, D.R., Crockford, P.W., Cui, H., Dahl, T.W., Mouro, L.D., Dewing, K., Dornbos, S.Q., Drabon, N., Dumoulin, J.A., Emmings, J.F., Endriga, C.R., Fraser, T.A., Gaines, R.R., Gaschnig, R.M., Gibson, T.M., Gilleaudeau, G.J., Gill, B.C., Goldberg, K., Guilbaud, R., Halverson, G.P.,

- Hammarlund, E.U., Hantsoo, K.G., Henderson, M.A., Hodgskiss, M.S.W., Horner, T.J., Husson, J.M., Johnson, B., Kabanov, P., Brenhin Keller, C., Kimmig, J., Kipp, M.A., Knoll, A.H., Kreitsmann, T., Kunzmann, M., Kurzweil, F., LeRoy, M.A., Li, C., Lipp, A.G., Loydell, D.K., Lu, X., Macdonald, F.A., Magnall, J.M., Mänd, K., Mehra, A., Melchin, M.J., Miller, A.J., Mills, N.T., Mwinde, C.N., O'Connell, B., Och, L.M., Ossa Ossa, F., Pagès, A., Paiste, K., Partin, C.A., Peters, S.E., Petrov, P., Playter, T.L., Plaza-Torres, S., Porter, S.M., Poulton, S.W., Pruss, S.B., Richoz, S., Ritzer, S.R., Rooney, A.D., Sahoo, S.K., Schoepfer, S.D., Sclafani, J.A., Shen, Y., Shorttle, O., Slotznick, S.P., Smith, E.F., Spinks, S., Stockey, R.G., Strauss, J.V., Stüeken, E.E., Tecklenburg, S., Thomson, D., Tosca, N.J., Uhlein, G.J., Vizcaíno, M.N., Wang, H., White, T., Wilby, P.R., Woltz, C.R., Wood, R.A., Xiang, L., Yurchenko, I.A., Zhang, T., Planavsky, N.J., Lau, K.V., Johnston, D.T., Sperling, E.A., 2021. The Sedimentary Geochemistry and Palaeoenvironments Project. *Geobiology* 19, 545–556. <https://doi.org/10.1111/gbi.12462>
- Fedo, C.M., Eriksson, K.A., Krogstad, E.J., 1996. Geochemistry of shales from the Archaean (~3.0 Ga) Buhwa Greenstone Belt, Zimbabwe: Implications for provenance and source-area weathering. *Geochimica et Cosmochimica Acta* 60, 1751–1763. [https://doi.org/10.1016/0016-7037\(96\)00058-0](https://doi.org/10.1016/0016-7037(96)00058-0)
- Findlay, J.M., Parrish, R.R., Birkett, T.C., Watanabe, D.H., 1995. U–Pb ages from the Nimish Formation and Montagnais glomeroporphyritic gabbro of the central New Québec Orogen, Canada. *Can. J. Earth Sci.* 32, 1208–1220. <https://doi.org/10.1139/e95-099>
- Frei, R., Polat, A., 2007. Source heterogeneity for the major components of ~3.7 Ga Banded Iron Formations (Isua Greenstone Belt, Western Greenland): Tracing the nature of interacting water masses in BIF formation. *Earth and Planetary Science Letters* 253, 266–281. <https://doi.org/10.1016/j.epsl.2006.10.033>
- Fryer, B.J., 1977. Rare earth evidence in iron-formations for changing Precambrian oxidation states. *Geochimica et Cosmochimica Acta* 41, 361–367. [https://doi.org/10.1016/0016-7037\(77\)90263-0](https://doi.org/10.1016/0016-7037(77)90263-0)
- Gaillardet, J., Viers, J., Dupré, B., 2013. Trace Elements in River Waters, in: *Treatise on Geochemistry*. Elsevier, pp. 195–235.
- Garbe-Schönberg, C.-D., 1993. Simultaneous Determination of Thirty-Seven Trace Elements In Twenty-Eight International Standards By ICP-MS. *Geostandards and Geoanalytical Research* 17, 81–97. <https://doi.org/10.1111/j.1751-908X.1993.tb00122.x>
- Garbe-Schönberg, D., Müller, S., 2014. Nano-particulate pressed powder tablets for LA-ICP-MS. *J. Anal. At. Spectrom.* 29, 990–1000. <https://doi.org/10.1039/C4JA00007B>
- Gole, M.J., Klein, C., 1981. Banded Iron-Formations through much of Precambrian time. *Journal of Geology* 89, 169–183. <https://doi.org/10.1086/628578>
- Goodman, R.J., 1972. The distribution of Ga and Rb in coexisting groundmass and phenocryst phases of some basic volcanic rocks. *Geochimica et Cosmochimica Acta* 36, 303–317. [https://doi.org/10.1016/0016-7037\(72\)90025-7](https://doi.org/10.1016/0016-7037(72)90025-7)
- Govindaraju, K., 1994. 1994 COMPILATION OF WORKING VALUES AND SAMPLE DESCRIPTION FOR 383 GEOSTANDARDS. *Geostandards and Geoanalytical*

- Research 18, 1–158. <https://doi.org/10.1046/j.1365-2494.1998.53202081.x-i1>
- Hamade, T., Konhauser, K.O., Raiswell, R., Goldsmith, S., Morris, R.C., 2003. Using Ge/Si ratios to decouple iron and silica fluxes in Precambrian banded iron formations. *Geology* 31, 35–38. [https://doi.org/10.1130/0091-7613\(2003\)031<0035:UGSRTD>2.0.CO;2](https://doi.org/10.1130/0091-7613(2003)031<0035:UGSRTD>2.0.CO;2)
- Haugaard, R., Pecoits, E., Lalonde, S., Rouxel, O., Konhauser, K., 2016. The Joffre banded iron formation, Hamersley Group, Western Australia: Assessing the palaeoenvironment through detailed petrology and chemostratigraphy. *Precambrian Research* 273, 12–37. <https://doi.org/10.1016/j.precamres.2015.10.024>
- Ho, P., Resing, J.A., Shiller, A.M., 2019. Processes controlling the distribution of dissolved Al and Ga along the U.S. GEOTRACES East Pacific Zonal Transect (GP16). *Deep Sea Research Part I: Oceanographic Research Papers* 147, 128–145. <https://doi.org/10.1016/j.dsr.2019.04.009>
- Hydes, D.J., 1979. Aluminum in seawater: Control by inorganic processes. *Science* 205, 1260–1262. <https://doi.org/10.1126/science.205.4412.1260>
- Hydes, D.J., 1983. Distribution of aluminium in waters of the North East Atlantic 25°N to 35°N. *Geochimica et Cosmochimica Acta* 47, 967–973. [https://doi.org/10.1016/0016-7037\(83\)90164-3](https://doi.org/10.1016/0016-7037(83)90164-3)
- Jackson, B.P., 2018. Low level determination of gallium isotopes by ICP-QQQ. *J. Anal. At. Spectrom.* 33, 897–900. <https://doi.org/10.1039/C8JA00073E>
- Jacobsen, S.B., Pimentel-Klose, M.R., 1988. Nd isotopic variations in Precambrian banded iron formations. *Geophys. Res. Lett.* 15, 393–396. <https://doi.org/10.1029/GL015i004p00393>
- James, H.L., 1954. Sedimentary Facies of Iron-Formation. *Economic Geology* 49, 235–293. <https://doi.org/10.2113/gsecongeo.49.3.235>
- Jochum, K.P., Garbe-Schönberg, D., Veter, M., Stoll, B., Weis, U., Weber, M., Lugli, F., Jentzen, A., Schiebel, R., Wassenburg, J.A., Jacob, D.E., Haug, G.H., 2019. Nano-Powdered Calcium Carbonate Reference Materials: Significant Progress for Microanalysis? *Geostand Geoanal Res* 43, 595–609. <https://doi.org/10.1111/ggr.12292>
- Kamber, B.S., Webb, G.E., 2001. The geochemistry of late Archaean microbial carbonate: implications for ocean chemistry and continental erosion history. *Geochimica et Cosmochimica Acta* 65, 2509–2525. [https://doi.org/10.1016/S0016-7037\(01\)00613-5](https://doi.org/10.1016/S0016-7037(01)00613-5)
- Kamber, B.S., Webb, G.E., Gallagher, M., 2014. The rare earth element signal in Archaean microbial carbonate: information on ocean redox and biogenicity. *Journal of the Geological Society* 171, 745–763. <https://doi.org/10.1144/jgs2013-110>
- Klein, C., 2005. Some Precambrian banded iron-formations (BIFs) from around the world: Their age, geologic setting, mineralogy, metamorphism, geochemistry, and origins. *American Mineralogist* 90, 1473–1499. <https://doi.org/10.2138/am.2005.1871>
- Klein, C., Beukes, N.J., 1989. Geochemistry and Sedimentology of a Facies Transition from Limestone to Iron-Formation Deposition in the Early Proterozoic Transvaal Supergroup, South Africa. *Economic Geology* 84, 1733–1774. <https://doi.org/10.2113/gsecongeo.84.7.1733>

- Konhauser, K.O., Planavsky, N.J., Hardisty, D.S., Robbins, L.J., Warchola, T.J., Haugegaard, R., Lalonde, S.V., Partin, C.A., Oonk, P.B.H., Tsikos, H., Lyons, T.W., Bekker, A., Johnson, C.M., 2017. Iron formations: A global record of Neoproterozoic to Palaeoproterozoic environmental history. *Earth-Science Reviews* 172, 140–177. <https://doi.org/10.1016/j.earscirev.2017.06.012>
- Kremling, K., 1985. The distribution of cadmium, copper, nickel, manganese, and aluminium in surface waters of the open Atlantic and European shelf area. *Deep Sea Research Part A. Oceanographic Research Papers* 32, 531–555. [https://doi.org/10.1016/0198-0149\(85\)90043-3](https://doi.org/10.1016/0198-0149(85)90043-3)
- Le Roex, A.P., 1985. Geochemistry, Mineralogy and Magmatic Evolution of the Basaltic and Trachytic Lavas from Gough Island, South Atlantic. *Journal of Petrology* 26, 149–186. <https://doi.org/10.1093/petrology/26.1.149>
- Li, Y.-H., 1991. Distribution patterns of the elements in the ocean: A synthesis. *Geochimica et Cosmochimica Acta* 55, 3223–3240. [https://doi.org/10.1016/0016-7037\(91\)90485-N](https://doi.org/10.1016/0016-7037(91)90485-N)
- Li, Y.-H., Schoonmaker, J.E., 2014. Chemical Composition and Mineralogy of Marine Sediments, in: *Treatise on Geochemistry*. Elsevier, pp. 1–32. <https://doi.org/10.1016/B978-0-08-095975-7.00701-4>
- Liang, M., Guo, Z., Kahmann, A.J., Oldfield, F., 2009. Geochemical characteristics of the Miocene eolian deposits in China: Their provenance and climate implications. *Geochem. Geophys. Geosyst.* 10, 16. <https://doi.org/10.1029/2008GC002331>
- Lyubetskaya, T., Korenaga, J., 2007. Chemical composition of Earth's primitive mantle and its variance: 1. Method and results. *J. Geophys. Res.* 112, B03211. <https://doi.org/10.1029/2005JB004223>
- McAlister, J., Orians, K., 2012. Calculation of river-seawater endmembers and differential trace metal scavenging in the Columbia River plume. *Estuarine, Coastal and Shelf Science* 99, 31–41. <https://doi.org/10.1016/j.ecss.2011.12.013>
- McDonough, W.F., Sun, S. -s., 1995. The composition of the Earth. *Chemical Geology* 120, 223–253. [https://doi.org/10.1016/0009-2541\(94\)00140-4](https://doi.org/10.1016/0009-2541(94)00140-4)
- McLennan, S.M., Taylor, S.R., Eriksson, K.A., 1983. Geochemistry of Archaean shales from the Pilbara Supergroup, Western Australia. *Geochimica et Cosmochimica Acta* 47, 1211–1222. [https://doi.org/10.1016/0016-7037\(83\)90063-7](https://doi.org/10.1016/0016-7037(83)90063-7)
- Measures, C.I., Grant, B., Khadem, M., Lee, D.S., Edmond, J.M., 1984. Distribution of Be, Al, Se and Bi in the surface waters of the western North Atlantic and Caribbean. *Earth and Planetary Science Letters* 71, 1–12. [https://doi.org/10.1016/0012-821X\(84\)90047-5](https://doi.org/10.1016/0012-821X(84)90047-5)
- Merschel, G., Bau, M., Dantas, E.L., 2017. Contrasting impact of organic and inorganic nanoparticles and colloids on the behavior of particle-reactive elements in tropical estuaries: An experimental study. *Geochimica et Cosmochimica Acta* 197, 1–13. <https://doi.org/10.1016/j.gca.2016.09.041>
- Möller, P., Bau, M., 1993. Rare-earth patterns with positive cerium anomaly in alkaline waters from Lake Van, Turkey. *Earth and Planetary Science Letters* 117, 671–676. [https://doi.org/10.1016/0012-821X\(93\)90110-U](https://doi.org/10.1016/0012-821X(93)90110-U)

- Morris, A.W., Howland, R.J.M., Bale, A.J., 1986. Dissolved aluminium in the Tamar Estuary, southwest England. *Geochimica et Cosmochimica Acta* 50, 189–197. [https://doi.org/10.1016/0016-7037\(86\)90168-7](https://doi.org/10.1016/0016-7037(86)90168-7)
- Mundl-Petermeier, A., Viehmann, S., Tusch, J., Bau, M., Kurzweil, F., Münker, C., 2022. Earth’s geodynamic evolution constrained by 182W in Archaean seawater. *Nat Commun* 13, 2701. <https://doi.org/10.1038/s41467-022-30423-3>
- O’Neil, H.S.C., Palme, H., 1998. Composition of the silicate Earth: Implications for accretion and core formation, in: *The Earth’s Mantle: Structure, Composition, and Evolution*. Cambridge University Press, New York, pp. 3–126.
- Orians, K.J., Bruland, K.W., 1985. Dissolved aluminium in the central North Pacific. *Nature* 316, 427–429. <https://doi.org/10.1038/316427a0>
- Orians, K.J., Bruland, K.W., 1988a. The marine geochemistry of dissolved gallium: A comparison with dissolved aluminum. *Geochimica et Cosmochimica Acta* 52, 2955–2962. [https://doi.org/10.1016/0016-7037\(88\)90160-3](https://doi.org/10.1016/0016-7037(88)90160-3)
- Orians, K.J., Bruland, K.W., 1988b. Dissolved gallium in the open ocean. *Nature* 332, 717–719. <https://doi.org/10.1038/332717a0>
- Parker, C.E., Brown, M.T., Bruland, K.W., 2016. Scandium in the open ocean: A comparison with other group 3 trivalent metals. *Geophys. Res. Lett.* 43, 2758–2764. <https://doi.org/10.1002/2016GL067827>
- Parks, J., Lin, S., Davis, D.W., Yang, X.-M., Creaser, R.A., Corkery, M.T., 2014. Meso- and Neoproterozoic evolution of the Island Lake greenstone belt and the northwestern Superior Province: Evidence from litho-geochemistry, Nd isotope data, and U–Pb zircon geochronology. *Precambrian Research* 246, 160–179. <https://doi.org/10.1016/j.precamres.2014.02.016>
- Piepgras, D.J., Jacobsen, S.B., 1992. The behavior of rare earth elements in seawater: Precise determination of variations in the North Pacific water column. *Geochimica et Cosmochimica Acta* 56, 1851–1862. [https://doi.org/10.1016/0016-7037\(92\)90315-A](https://doi.org/10.1016/0016-7037(92)90315-A)
- Pokrovsky, O.S., Schott, J., 2002. Iron colloids/organic matter associated transport of major and trace elements in small boreal rivers and their estuaries (NW Russia). *Chemical Geology* 190, 141–179. [https://doi.org/10.1016/S0009-2541\(02\)00115-8](https://doi.org/10.1016/S0009-2541(02)00115-8)
- Rahm, M., Hoffmann, R., Ashcroft, N.W., 2016. Atomic and Ionic Radii of Elements 1–96. *Chem. Eur. J.* 22, 14625–14632. <https://doi.org/10.1002/chem.201602949>
- Richardson, J.B., Mischenko, I.C., Mackowiak, T.J., Perdrial, N., 2022. Trace metals and metalloids and Ga/Al ratios in grey shale weathering profiles along a climate gradient and in batch reactors. *Geoderma* 405, 115431. <https://doi.org/10.1016/j.geoderma.2021.115431>
- Robbins, L.J., Konhauser, K.O., Warchola, T.J., Homann, M., Thoby, M., Foster, I., Mloszewska, A.M., Alessi, D.S., Lalonde, S.V., 2019. A comparison of bulk versus laser ablation trace element analyses in banded iron formations: Insights into the mechanisms leading to compositional variability. *Chemical Geology* 506, 197–224. <https://doi.org/10.1016/j.chemgeo.2018.12.036>
- Rudnick, R.L., Gao, S., 2003. 3.01 Composition of the Continental Crust, in: *Treatise on Geochemistry*. Elsevier, pp. 1–64.

- Sampaio, G.M., Enzweiler, J., 2015. New ICP-MS Results for Trace Elements in Five Iron-Formation Reference Materials. *Geostandards and Geoanalytical Research* 39, 105–119. <https://doi.org/10.1111/j.1751-908X.2014.00293.x>
- Sanematsu, K., Moriyama, T., Laochou, S., Watanabe, Y., 2011. Laterization of basalts and sandstone associated with the enrichment of Al, Ga and Sc in the Bolaven Plateau, southern Laos. *Bull. Geol. Surv. Japan* 62, 105–129. <https://doi.org/10.9795/bullgsj.62.105>
- Schier, K., Bau, M., Münker, C., Beukes, N., Viehmann, S., 2018. Trace element and Nd isotope composition of shallow seawater prior to the Great Oxidation Event: Evidence from stromatolitic bioherms in the Palaeoproterozoic Rooinekke and Nelani Formations, South Africa. *Precambrian Research* 315, 92–102. <https://doi.org/10.1016/j.precamres.2018.07.014>
- Schier, K., Bau, M., Smith, A.J.B., Beukes, N.J., Coetzee, L.L., Viehmann, S., 2020. Chemical evolution of seawater in the Transvaal Ocean between 2426 Ma (Ongeluk Large Igneous Province) and 2413 Ma ago (Kalahari Manganese Field). *Gondwana Research* 88, 373–388. <https://doi.org/10.1016/j.gr.2020.09.001>
- Schier, K., Ernst, D.M., de Sousa, I.M.C., Garbe-Schönberg, D., Kuhn, T., Hein, J.R., Bau, M., 2021. Gallium-aluminum systematics of marine hydrogenetic ferromanganese crusts: Inter-oceanic differences and fractionation during scavenging. *Geochimica et Cosmochimica Acta* 310, 187–204. <https://doi.org/10.1016/j.gca.2021.05.019>
- Schmidt, K., Bau, M., Hein, J.R., Koschinsky, A., 2014. Fractionation of the geochemical twins Zr–Hf and Nb–Ta during scavenging from seawater by hydrogenetic ferromanganese crusts. *Geochimica et Cosmochimica Acta* 140, 468–487. <https://doi.org/10.1016/j.gca.2014.05.036>
- Schmidt, K., Garbe-Schönberg, D., Hannington, M.D., Anderson, M.O., Bühring, B., Haase, K., Haruel, C., Lupton, J., Koschinsky, A., 2017. Boiling vapour-type fluids from the Nifonea vent field (New Hebrides Back-Arc, Vanuatu, SW Pacific): Geochemistry of an early-stage, post-eruptive hydrothermal system. *Geochimica et Cosmochimica Acta* 207, 185–209. <https://doi.org/10.1016/j.gca.2017.03.016>
- Schulz, T., Viehmann, S., Hezel, D.C., Koeberl, C., Bau, M., 2021. Highly Siderophile Elements and Coupled Fe-Os Isotope Signatures in the Temagami Iron Formation, Canada: Possible Signatures of Neoproterozoic Seawater Chemistry and Earth’s Oxygenation History. *Astrobiology* 21, 16. <https://doi.org/10.1089/ast.2020.2311>
- Shiller, A.M., 1988. Enrichment of dissolved gallium relative to aluminum in natural waters. *Geochimica et Cosmochimica Acta* 52, 1879–1882. [https://doi.org/10.1016/0016-7037\(88\)90011-7](https://doi.org/10.1016/0016-7037(88)90011-7)
- Shiller, A.M., 1998. Dissolved gallium in the Atlantic Ocean. *Marine Chemistry* 61, 87–99. [https://doi.org/10.1016/S0304-4203\(98\)00009-7](https://doi.org/10.1016/S0304-4203(98)00009-7)
- Shiller, A.M., Bairamadgi, G.R., 2006. Dissolved gallium in the northwest Pacific and the south and central Atlantic Oceans: Implications for aeolian Fe input and a reconsideration of profiles. *Geochem. Geophys. Geosyst.* 7, 14. <https://doi.org/10.1029/2005GC001118>
- Shiller, A.M., Frilot, D.M., 1996. The geochemistry of gallium relative to aluminum in Californian streams. *Geochimica et Cosmochimica Acta* 60, 1323–1328. [https://doi.org/10.1016/0016-7037\(96\)00111-8](https://doi.org/10.1016/0016-7037(96)00111-8)

- [//doi.org/10.1016/0016-7037\(96\)00002-6](https://doi.org/10.1016/0016-7037(96)00002-6)
- Simons, B., Shail, R.K., Andersen, J.C.Ø., 2016. The petrogenesis of the Early Permian Variscan granites of the Cornubian Batholith: Lower plate post-collisional peraluminous magmatism in the Rhenohercynian Zone of SW England. *Lithos* 260, 76–94. <https://doi.org/10.1016/j.lithos.2016.05.010>
- Smith, A.J.B., 2007. The Palaeo-environmental Significance of the Iron- formations and Iron-rich Mudstones of the Mesoarchean Witwatersrand-Mozaan Basin, South Africa. University of Johannesburg, South Africa.
- Smith, A.J.B., Beukes, N.J., 2016. Palaeoproterozoic banded iron formation- hosted high-grade hematite iron ore deposits of the Transvaal Supergroup, South Africa. *Episodes* 39, 16. <https://doi.org/10.18814/epiiugs/2016/v39i2/95778>
- Smith, A.J.B., Beukes, N.J., Gutzmer, J., 2013. The composition and depositional environments of Mesoarchean iron formations of the West Rand Group of the Witwatersrand Supergroup, South Africa. *Economic Geology* 108, 111–134. <https://doi.org/10.2113/econgeo.108.1.111>
- Smith, R.M., Martell, A.E., 1989. *Critical Stability Constants*. Plenum Press, New York and London.
- Sugiyama, N., 2021. Attenuation of doubly charged ion interferences on arsenic and selenium by ICP-MS under low kinetic energy collision cell conditions with hydrogen cell gas. *J. Anal. At. Spectrom.* 36, 294–302. <https://doi.org/10.1039/D0JA00301H>
- Sun, S.-S., 1982. Chemical composition and origin of the earth's primitive mantle. *Geochimica et Cosmochimica Acta* 46, 179–192. [https://doi.org/10.1016/0016-7037\(82\)90245-9](https://doi.org/10.1016/0016-7037(82)90245-9)
- Takayanagi, K., Gobeil, C., 2000. Dissolved Aluminum in the Upper St. Lawrence Estuary. *Journal of Oceanography* 56, 517–525. <https://doi.org/10.1023/A:1011196826709>
- Tarney, J., Saunders, A.D., Weaver, S.D., 1977. Geochemistry of volcanic rocks from the island arcs and marginal basins of the Scotia Arc Region, in: *Island Arcs, Deep Sea Trenches and Back-Arc Basins*. American Geophysical Union, pp. 367–377.
- Terashima, S., Usui, A., Imai, N., 1995. Two New GSJ Geochemical Reference Samples: Syenite JSy-1 and Manganese Nodule JMn-1. *Geostandards and Geoanalytical Research* 19, 221–229. <https://doi.org/10.1111/j.1751-908X.1995.tb00160.x>
- Trendall, A.F., Compston, W., Nelson, D.R., De Laeter, J.R., Bennett, V.C., 2004. SHRIMP zircon ages constraining the depositional chronology of the Hamersley Group, Western Australia*. *Aust J Earth Sci* 51, 621–644. <https://doi.org/10.1111/j.1400-0952.2004.01082.x>
- Van Bennekom, A.J., Jager, J.E., 1978. Dissolved aluminium in the Zaire river plume. *Netherlands Journal of Sea Research* 12, 358–367. [https://doi.org/10.1016/0077-7579\(78\)90039-X](https://doi.org/10.1016/0077-7579(78)90039-X)
- Viehmann, S., Bau, M., Bühn, B., Dantas, E.L., Andrade, F.R.D., Walde, D.H.G., 2016. Geochemical characterisation of Neoproterozoic marine habitats: Evidence from trace elements and Nd isotopes in the Urucum iron and manganese formations, Brazil. *Precambrian Research* 282, 74–96. <https://doi.org/10.1016/j.precamres.2016.07.006>
- Viehmann, S., Bau, M., Hoffmann, E.J., Münker, C., 2018. Decoupled Hf and Nd isotopes in suspended particles and in the dissolved load of Late Archaean seawater. *Chemical*

- Geology 483, 111–118. <https://doi.org/10.1016/j.chemgeo.2018.01.017>
- Viehmann, S., Bau, M., Hoffmann, J.E., Münker, C., 2015a. Geochemistry of the Krivoy Rog Banded Iron Formation, Ukraine, and the impact of peak episodes of increased global magmatic activity on the trace element composition of Precambrian seawater. *Precambrian Research* 270, 165–180. <https://doi.org/10.1016/j.precamres.2015.09.015>
- Viehmann, S., Bau, M., Smith, A.J.B., Beukes, N.J., Dantas, E.L., Bühn, B., 2015b. The reliability of ~2.9 Ga old Witwatersrand banded iron formations (South Africa) as archives for Mesoarchean seawater: Evidence from REE and Nd isotope systematics. *Journal of African Earth Sciences* 111, 322–334. <https://doi.org/10.1016/j.jafrearsci.2015.08.013>
- Viehmann, S., Hoffmann, J.E., Münker, C., Bau, M., 2014. Decoupled Hf-Nd isotopes in Neoproterozoic seawater reveal weathering of emerged continents. *Geology* 42, 115–118. <https://doi.org/10.1130/G35014.1>
- Walker, J.C.G., Schidlowski, M., Schopf, J.W., Stevenson, D.J., Walter, M.R., 1983. Environmental evolution of the Archaean-Early Proterozoic Earth, in: *Earth's Earliest Biosphere, Its Origin and Evolution*. Princeton University Press, New Jersey, pp. 260–290.
- Wang, C., Wu, H., Li, W., Peng, Z., Zhang, L., Zhai, M., 2017. Changes of Ge/Si, REE+Y and SmNd isotopes in alternating Fe- and Si-rich mesobands reveal source heterogeneity of the ~2.54Ga Sijiaying banded iron formation in Eastern Hebei, China. *Ore Geology Reviews* 80, 363–376. <https://doi.org/10.1016/j.oregeorev.2016.06.036>
- Williams, G.E., Schmidt, P.W., Clark, D.A., 2004. Palaeomagnetism of iron-formation from the late Palaeoproterozoic Frere Formation, Earraheedy Basin, Western Australia: palaeogeographic and tectonic implications. *Precambrian Research* 128, 367–383. <https://doi.org/10.1016/j.precamres.2003.09.008>

7 Unpublished work

In this chapter, unpublished Ga and Al data of further BIFs are presented, discussed, and interpreted in the framework of Archaean and Palaeoproterozoic conditions on Earth's surface.

7.1 Ga/Al in Archaean and Palaeoproterozoic BIFs

Apart from the published Ga and Al data for the Temagami BIF (see Chapter 6), further Archaean and Palaeoproterozoic (B)IFs (Isua, Greenland; Marra Mamba, Australia; Mt. Ruker, Antarctica; Kuruman, South Africa; Hotazel, South Africa) were analysed for Ga/Al and Fe/Si ratios with LA-SF-ICP-MS. These measurements were conducted on polished sections, not on NP tablets. Unfortunately, data evaluation of these analyses showed that most of the measurements are unusable due to very irregular measurement signals or intensities indistinguishable from background signals (see Fig 7.1). The sample points with adequate measurement signals ($n=75$) are rather Fe-rich and were evaluated as described in Section 3.3.3. Calibration equations for Ga/Al and Fe/Si ratios can be found in the supplementary material (Fig. 10.1 – Fig. 10.4).

Figure 7.2 shows a compilation of these additional Ga/Al ratios plotted against Fe/Si ratios. Like in the Temagami BIF, the Ga/Al ratios predominantly range from 2×10^{-4} to 1×10^{-3} . The only evaluable measurement point for Mt. Ruker BIF shows an elevated Ga/Al ratio of 3.8×10^{-3} . However, to which extent this is representative of the Mt. Ruker BIF cannot be said. Some BIFs show trends in their Ga/Al vs Fe/Si distributions: (i) The Isua BIF shows strongly increasing Ga/Al ratios with increasing Fe/Si ratios, however, only four data points are available. (ii) The Hotazel IF in drill core *GHEX_97_3* also shows increasing Ga/Al ratios with increasing Fe/Si ratios, but the trend is shallower than that of the Isua BIF. (iii) The Marra Mamba BIF shows very constant Ga/Al ratios (3.0×10^{-4} – 3.8×10^{-4}) over a Fe/Si range of more than one order of magnitude (4–83). Gallium/aluminium ratios of *GHEX_97_6* drill core (Hotazel IF) scatter randomly without a recognisable trend. For Kuruman BIF, only two data points are available.

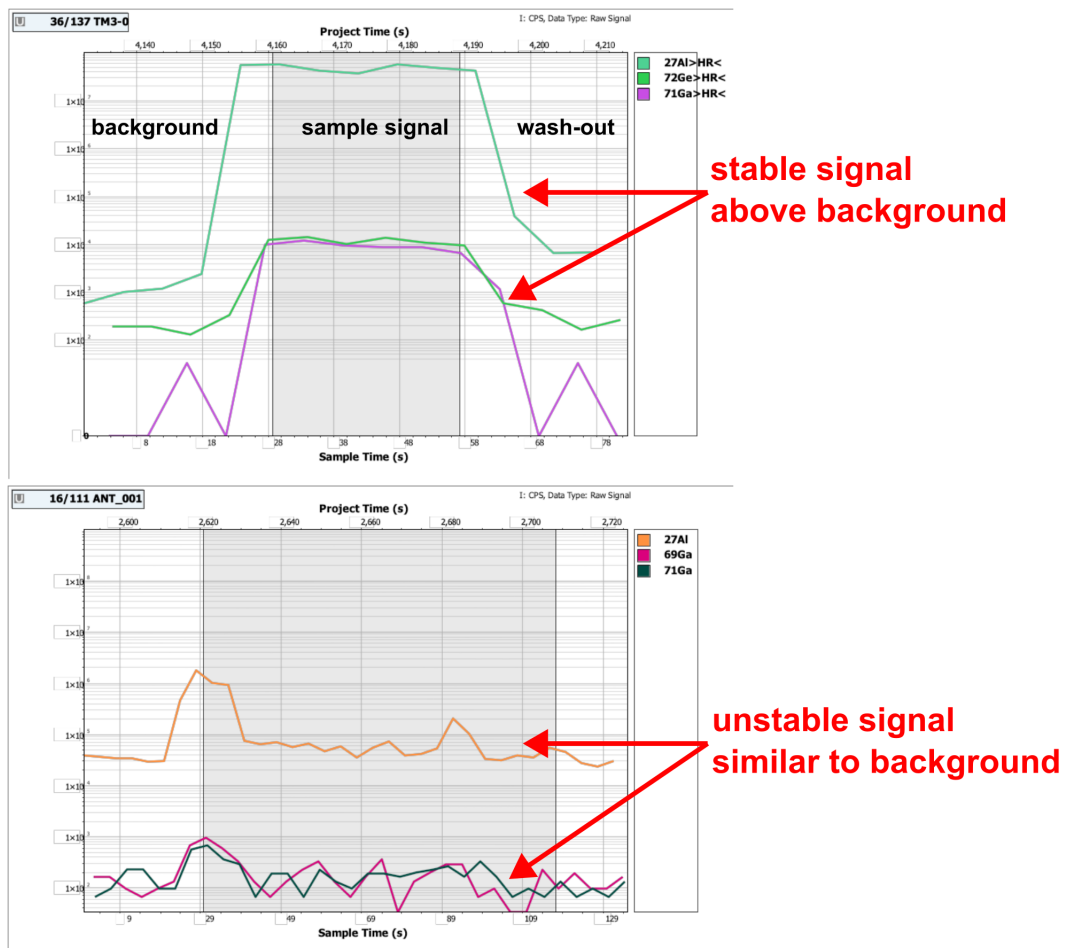


Figure 7.1: Two LA-ICP-MS raw signal sequences as shown in the LADR software. Top: a usable signal that is evaluable due to stable signals clearly above background levels. Bottom: an unusable signal that is not evaluable due to unstable signals indistinguishable from background levels. The measured raw intensities for ^{27}Al , ^{69}Ga and ^{71}Ga are shown in both graphs. The suffix ">HR<" in the top graph is due to the naming in the software. Both measurements were conducted in the high-resolution mode.

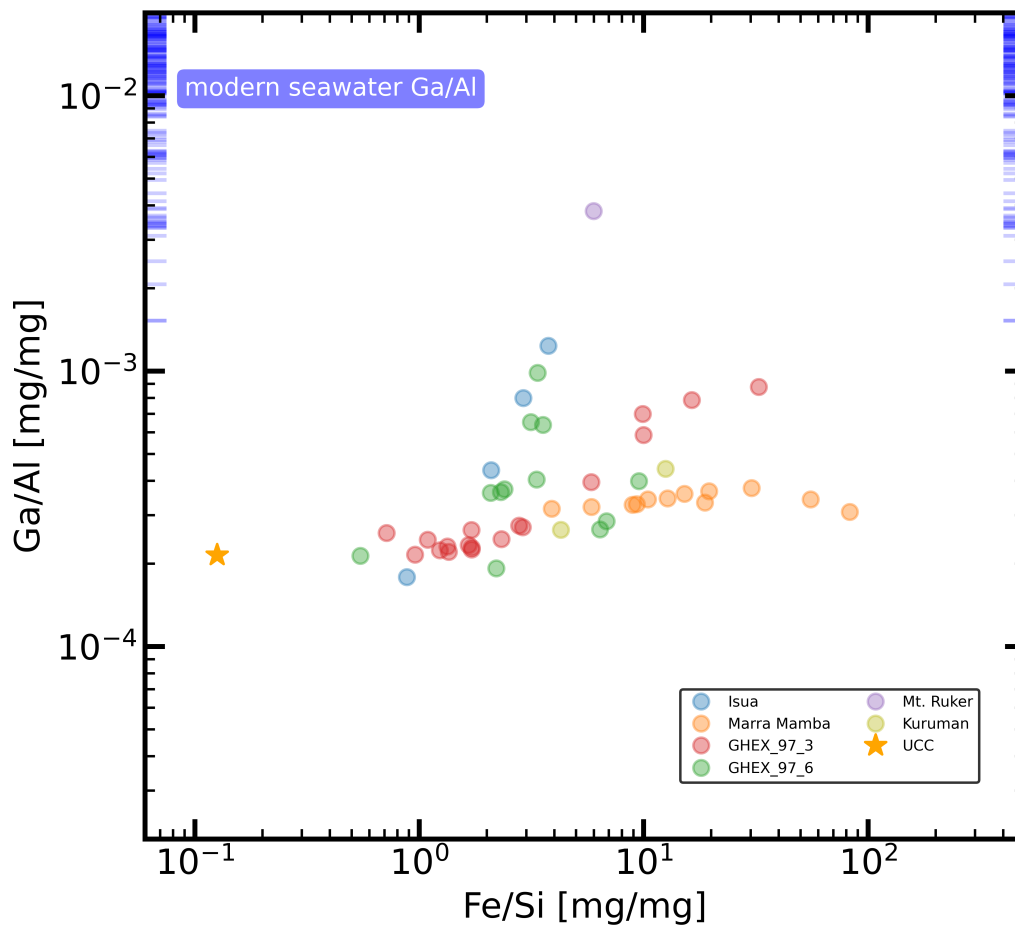


Figure 7.2: Ga/Al ratios against Fe/Si ratios in Isua, Marra Mamba, Mt. Ruker, Kuruman and Hotazel IF. Data from LA-ICP-MS measurements on polished sections. References for *modern seawater* Ga/Al see Fig. 2.2.

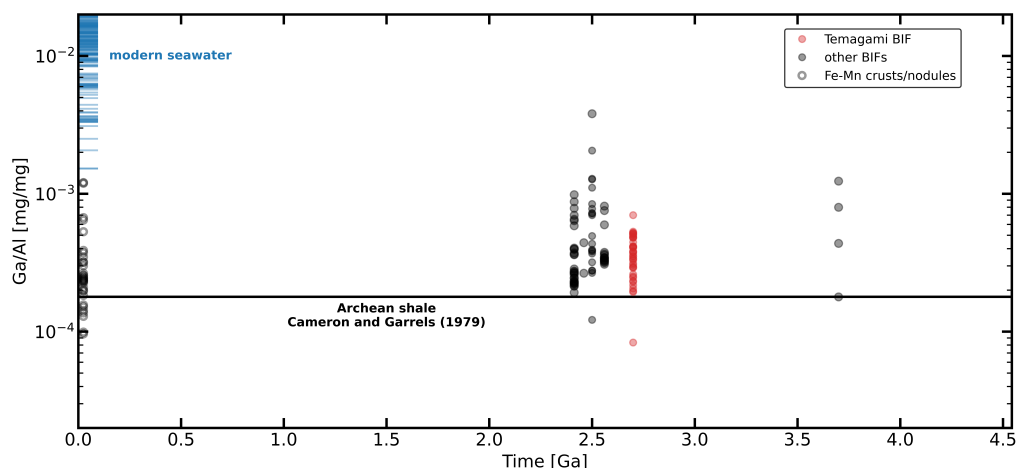


Figure 7.3: Ga/Al ratios in BIFs and modern Fe-Mn crusts (Schier et al., 2021) throughout Earth's history. References for *modern seawater* Ga/Al see Fig. 2.2.

Comparable Ga/Al ratios in these BIFs of different ages (see Fig. 7.3) could indicate an overarching global mechanism that controlled the Ga-Al distribution in Precambrian BIFs. However, the importance of locally and temporally limited processes cannot be estimated yet. They might have resulted in the different Ga/Al ratio trends with respect to the Fe content, as described above. For a comprehensive interpretation of the Ga-Al data, major and trace element data must be considered. While for the two Hotazel IF drill cores (*GHEX_97_3* and *GHEX_97_3*), the Mt. Ruker and Kuruman BIF geochemical data are available (Bau and Dulski, 1996; Schier et al., 2020; Ernst and Bau, 2021), for the investigated Isua, and Marra Mamba BIF samples major and trace elements still have to be determined. Published studies on the Marra Mamba and Isua BIFs indicate that they are rather pure and pristine (e.g., Alibert and McCulloch, 1993; Frei and Polat, 2007). In the following, several ideas are discussed regarding the distribution of Ga/Al ratios with increasing Fe content, i.e., increasing Fe/Si ratios. At this stage, two models are conceivable, as already discussed for the Temagami BIF in Section 6.5.4: (i) BIF Ga/Al ratios represent primary seawater Ga/Al ratios or (ii) Ga and Al were fractionated during BIF formation, diagenesis and/or metamorphism.

The particularly uniform Ga/Al ratios in the Marra Mamba BIF, which are also close to Ga/Al ratios of potential detritus, may indicate a major contribution of the latter. Detrital contamination could be confirmed or rejected by other trace element distributions, e.g., REY, as described for the Mt. Ruker BIF in Chapter 5. Alternatively, the uniform Ga/Al ratios could originate from extremely constant Ga/Al ratios in ambient seawater,

assuming model (i): Ga and Al were not fractionation during BIF formation. This, in turn, would indicate that the variable Ga/Al ratios in other BIFs reflect (temporal) changes of Ga/Al in ambient seawater. Evidence for differences in seawater Ga/Al ratios is given by data from the Atlantic and Pacific oceans (Fig. 2.2), as described in Section 2.4.6. From the published modern seawater Ga-Al data, it might be inferred that seawater Ga/Al ratios increase with increasing age of the respective water mass due to a shorter residence time of Al compared to Ga. Small-scale LA-ICP-MS studies within individual BIF Fe oxide bands could give evidence for such temporal changes.

If, however, the increasing Ga/Al ratios with increasing Fe content are not due to varying Ga/Al ratios in ambient seawater, this would indicate a preferred adsorption of Ga onto the Fe oxides and, hence, strongly argue for model (ii): Gallium and aluminium were fractionation during BIF formation, diagenesis, and/or metamorphism. Preferred Ga adsorption in Precambrian BIFs would be the opposite effect of what is observed in modern hydrogenetic Fe-Mn crusts, which show decreasing Ga/Al ratios with increasing Fe content, as described in Section 4.5.3. The assumption of Ga-Al fractionation during BIF Fe oxide formation would open doors for further interpretations on Ga/Al vs Fe (or Fe/Si) trends.

The uniform Ga/Al ratios in the Marra Mamba BIF could then originate from a rather fast formation and disconnection of the sediment from the seawater source. At the same time, elevated Ga/Al ratios in Fe-rich samples (e.g., Isua or *GHEX_97_3*) would result from longer-term scavenging and prolonged exchange with ambient seawater. A process that is comparable to the accumulation of Ce over time by hydrogenetic Fe-Mn crusts. However, while the Ce accumulation in Fe-Mn crusts is controlled by the surface-oxidation of Ce(III) (Bau and Koschinsky, 2009), Ga and Al are not considered redox-sensitive in the natural environment. Therefore, accumulation of Ga over time in BIFs would more likely be related to and limited by the number of available adsorption sites on Fe oxides. However, following the assumption of Ga-Al fractionation, except for time as a controlling factor, as described above, the depositional setting could also have had a major influence. In an open system with continuous resupply of Ga and Al, BIFs should exhibit constant Ga/Al ratios provided they fractionated Ga and Al with a constant factor ($\Delta_{\text{Ga/Al}} = (\text{Ga/Al})_{\text{BIF}} / (\text{Ga/Al})_{\text{seawater}} = \text{const.}$) from ambient seawater. In a (semi) closed basin, however, preferred incorporation of Al into BIF Fe oxides would lead to increasing Ga/Al ratios in ambient seawater, which, in turn, would finally also lead to elevated Ga/Al ratios in late-stage Fe oxides. The final Fe oxide band will then show increasing Ga/Al ratios from bottom to top. In the case of preferred Ga incorporation,

the opposite (decreasing Ga/Al ratios from bottom to top) would be expected. It is questionable if such trends survived diagenetic or metamorphic recrystallisations.

The important next step is to determine whether BIFs preserved original seawater Ga/Al ratios or Ga and Al were fractionated during BIF formation. An in-depth evaluation of different Ga/Al trends in different BIFs will be an important aspect of future studies on Ga and Al in the Precambrian environment.

7.2 References

- Alibert C. and McCulloch M. T. (1993) Rare earth element and neodymium isotopic compositions of the banded iron-formations and associated shales from Hamersley, western Australia. *Geochimica et Cosmochimica Acta* 57, 187–204.
- Bau M. and Dulski P. (1996) Distribution of yttrium and rare-earth elements in the Penge and Kuruman iron-formations, Transvaal Supergroup, South Africa. *Precambrian Research* 79, 37–55.
- Bau M. and Koschinsky A. (2009) Oxidative scavenging of cerium on hydrous Fe oxide: Evidence from the distribution of rare earth elements and yttrium between Fe oxides and Mn oxides in hydrogenetic ferromanganese crusts. *Geochem. J.* 43, 37–47.
- Ernst D. M. and Bau M. (2021) Banded iron formation from Antarctica: The 2.5 Ga old Mt. Ruker BIF and the antiquity of lanthanide tetrad effect and super-chondritic Y/Ho ratio in seawater. *Gondwana Research* 91, 97–111.
- Frei R. and Polat A. (2007) Source heterogeneity for the major components of ~3.7 Ga Banded Iron Formations (Isua Greenstone Belt, Western Greenland): Tracing the nature of interacting water masses in BIF formation. *Earth and Planetary Science Letters* 253, 266–281.
- Schier K., Bau M., Smith A. J. B., Beukes N. J., Coetzee L. L. and Viehmann S. (2020) Chemical evolution of seawater in the Transvaal Ocean between 2426 Ma (Ongeluk Large Igneous Province) and 2413 Ma ago (Kalahari Manganese Field). *Gondwana Research* 88, 373–388.
- Schier K., Ernst D. M., de Sousa I. M. C., Garbe-Schönberg D., Kuhn T., Hein J. R. and Bau M. (2021) Gallium-aluminum systematics of marine hydrogenetic ferromanganese crusts: Inter-oceanic differences and fractionation during scavenging. *Geochimica et Cosmochimica Acta* 310, 187–204.

8 Review of applied LA-ICP-MS

A major analytical focus of this PhD thesis was the application of LA-ICP-MS on BIF Fe-oxide and (meta)chert bands to determine Ga/Al (and Ge/Si) ratios in situ. In Chapter 6, only the determination of Ga/Al ratios in the Temagami BIF Fe oxide bands by LA-ICP-MS was discussed, and all evaluable measurements in Chapter 7 are Fe-rich. The LA-ICP-MS data for (meta)chert bands was not considered because they could not be confirmed by the *solution-based* measurements in the Temagami BIF samples (Chapter 6.4.4). In the following, potential reasons are discussed.

The first and most obvious reason might be that the trace element mass fractions, especially those of Ga, are extremely low in BIF (meta)chert bands (down to 0.03 mg/kg in *TM4-3*; Chapter 6.4.2). Although the used SF-ICP-MS (ThermoFisher Element XR) is capable of measuring such low mass fractions, the necessary usage of high-resolution mode reduces the measured intensities drastically. Although the LA-ICP-MS raw signal data of the Temagami (meta)chert NP tablet samples were evaluable (above background), the mass fractions of Ga (and Al) might just be too low. Figure 8.1 is an updated version of Fig. 6.5 (Chapter 6), including the Ga/Al ratios for (meta)chert bands determined with LA-SF-ICP-MS. The LA-ICP-MS Ga/Al ratios in the (meta)cherts are all elevated compared to the respective measurements with solution-based SF-ICP-MS and ICP-MS/MS.

As described in Chapter 3.3.7 the largest challenge in LA-ICP-MS analysis is probably signal calibration to obtain quantitative results. Large uncertainty originates from not knowing the exact amount and characteristics (e.g., size distribution) of the ablated material. While there are different data treatments to counteract this uncertainty, e.g., 100 % normalisation, application of internal standards and external calibration, they are not as capable as for solution-based ICP-MS measurements. Also, they cannot entirely make up for *elemental fractionation*. Elemental fractionation describes the different behaviour of elements during the laser-ablation, transport and atomisation process (e.g., Longerich et al., 1996). Although the exact properties that define these groups are yet unknown, they correlate nicely with Goldschmidt's notation of lithophile,

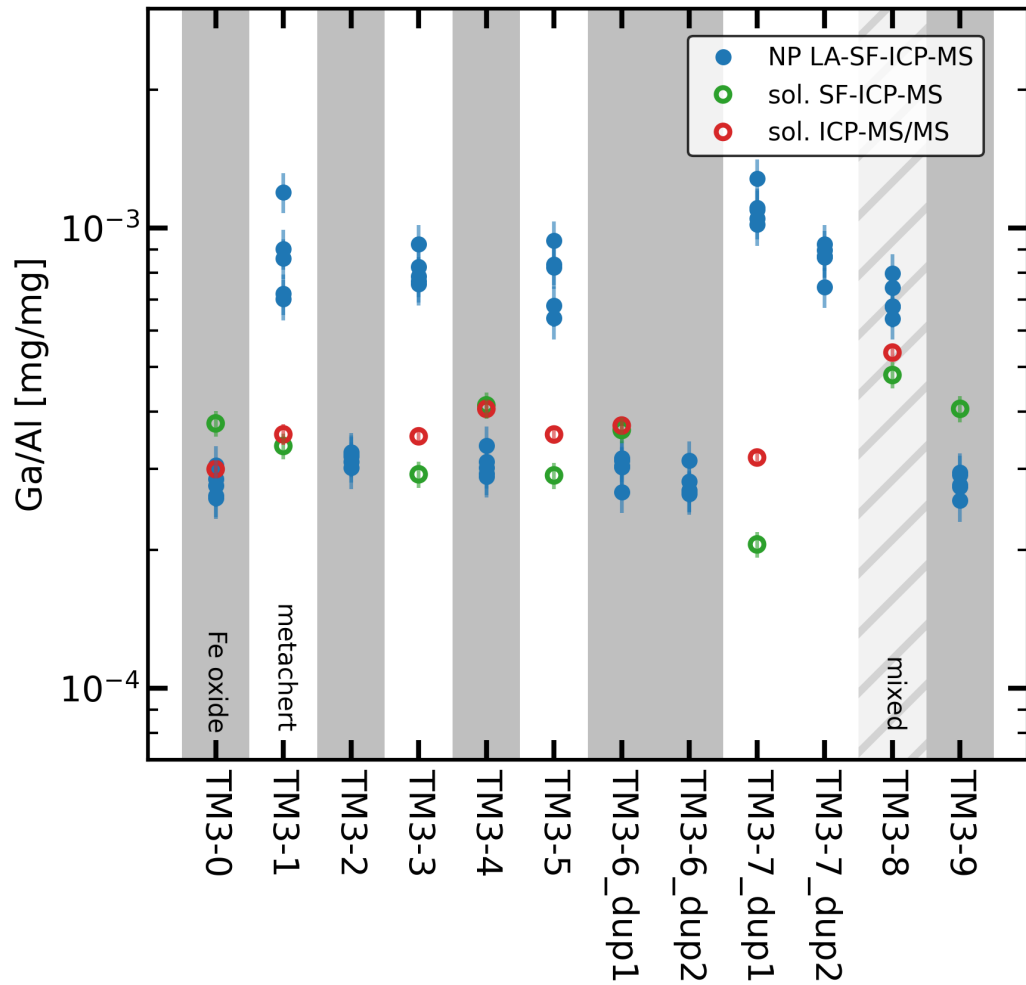


Figure 8.1: Updated version of Fig. 6.5. Comparison of Ga/Al ratios in the *TM3* specimen measured at BGR Hannover (solution ICP-MS/MS) and Kiel University (solution and NP laser-ablation SF-ICP-MS). Grey areas mark Fe oxide bands, while white areas mark metachert bands. The grey-hatched area marks the mixed band of *TM3-8*. The relative standard deviation for ICP-MS/MS data is indicated by green error bars: RSD based on replicate measurements of each sample. The relative standard deviation for SF-ICP-MS data is indicated by red error bars: 6.5 % for metachert bands (based on four times measurement of TM4-5b.1) and 3.0 % for Fe oxide bands (based on four times measurement of TM1-1a). For LA-ICP-MS, the $^{69}\text{Ga}/^{27}\text{Al}$ data (see Fig. 6.4 for calibration) is shown here. The relative standard deviation for LA-SF-ICP-MS is indicated by blue error bars and is based on repetitive measurement of the FeR-4 RM.

chalcophile and siderophile elements (Fryer et al., 1995; Longerich et al., 1996) or the 50 % condensation temperature (Luo et al., 2015). Elements within the same group show similar ablation behaviours and do not fractionate with respect to each other during LA-ICP-MS measurements. However, elements of different groups can show severe differences in their ablation behaviour and, therefore, also in their measured signal ratios compared to their actual compositional ratios. Although these fractionation processes are not fully understood yet, it became clear that one of the major origins of elemental fractionation is related to the formation of differently-sized particles during laser ablation (e.g., Kuhn and Günther, 2004; Limbeck et al., 2015; Luo et al., 2015). Luo et al. (2015) showed that, for example, the lithophile elements are relatively enriched in larger particles and agglomerates, which, in turn, cannot be fully atomised and ionised in the ICP, leading to decreased signal intensities of those elements. In order to prevent strong elemental fractionation during LA-ICP-MS measurements, the production of small and equally sized particles is desirable. Modern laser systems like deep UV Excimer lasers (193 nm and 157 nm wavelengths) or fs-lasers are capable of producing homogeneously small particles in a vast amount of sample materials (Kuhn and Günther, 2004; Shaheen et al., 2012). Especially fs-lasers bear great potential because their very low pulse duration reduces thermal effects and facilitates a much more precise ablation on the spot. Additionally, it was found that the formation of larger particles is time-dependent and predominantly occurs during the first 20–30 s of spot ablation (Kuhn and Günther, 2004; Luo et al., 2015). After approx. 40 s, the produced particles are much more homogeneous, resulting in less elemental fractionation. Therefore, apart from extremely low mass fractions, elemental fractionation might have affected the LA-ICP-MS measurements of BIF (meta)chert samples.

The Fe-oxide and metachert bands of Temagami BIF and other BIFs, consist of Fe-oxide minerals (mainly magnetite) and quartz, respectively. Therefore, laser ablation measurements in adjacent BIF bands must deal with two very distinct sample matrices. Liu et al. (2008) showed that Fe phases generally show excellent ablation behaviour because their high energy absorption potential enables a good coupling of the laser with the sample, which, in turn, facilitates the production of small and equally sized particles. During the LA-ICP-MS measurements for this thesis, it was observed that the laser ablation in Fe-oxide phases created very sharp ablation craters or lines, and irregular breakoff of larger particles from the edges was not observed. For the measurements in the (meta)chert phases, however, the ablation craters and lines were much more irregular, and the breakoff of larger particles was observed during ablation.

In the past years, great progress has been made concerning the optimisation of the ablation process, transport of ablated material, and atomisation and ionisation in the ICP (Günther and Hattendorf, 2005 and references therein). It was shown that ns-lasers with UV wavelengths, like the 193 nm ArF Excimer laser used here, clearly reduce elemental fractionation. In the here presented measurements, He was used as carrier gas which is superior compared to Ar by increasing intensities three to fivefold (Günther and Heinrich, 1999b, a; Horn and Günther, 2003). Therefore, elemental fractionation was minimised as much as possible, which is confirmed by the good results in the BIF Fe-oxide bands. However, the analytical results and the observed irregular ablation behaviour indicate that elemental fractionation might have occurred during LA-ICP-MS measurements of the BIF (meta)chert bands. Comparing LA-ICP-MS (Ga_{LA}/Al_{LA}) with dissolved sample ICP-MS (Ga_{sol}/Al_{sol}) data of the Temagami *TM3* samples shows elevated Ga_{LA}/Al_{LA} ratios compared to Ga_{sol}/Al_{sol} . This might be explained by the particle size-dependent elemental fractionation described by, e.g. Fryer et al. (1995), Longerich et al. (1996), Kuhn and Günther (2004) and Luo et al. (2015). Lithophile elements, including Al, are relatively enriched in larger particles, while Ga is not. Fryer et al. (1995) determined Ca-normalised fractionation factors for 60 elements, including Ga and Al (Fig. 8.2). These fractionation factors compared the signal intensities of the second two minutes (minute 2 to 4) to those of the first two minutes (start to minute 2) of the laser-ablation. Their data show that while Al has a very similar ablation behaviour to Ca (fractionation factor ~ 1), Ga shows a different ablation behaviour (fractionation factor ~ 1.8), more like Cu, P, Sn or Ge. The elevated fractionation factor of Ga indicates that less Ga is ablated at the beginning of laser-ablation (relative to Ca-signal and compared to Al). Although UV ns-lasers generally produce smaller and more homogeneous particles, the formation of larger fragments in certain sample matrices cannot be fully prohibited. The here observed poorer ablation characteristics of (meta)chert compared to Fe oxide phases, resulting in the formation of larger particles due to irregular ablation. While the larger particles are relatively enriched in Al (lithophile elements), they cannot be fully atomised and ionised in the ICP (Günther and Hattendorf, 2005; Shaheen et al., 2012; Luo et al., 2015; Chew et al., 2021) or even "survive" the ICP (Aeschliman et al., 2003). Therefore, the measured signal intensities for Al, and other lithophile elements, are decreased, resulting in an increased measured Ga/Al ratio. A potential explanation for the rather poor ablation behaviour of the BIF (meta)chert bands in this study could be the chosen fluence of 6 J/cm². While the 6 J/cm² are sufficient for Fe-rich phases due to iron's much better energy absorption, it might be too low for SiO₂. Kuhn and Günther

(2004) used a much higher fluence (18.2 J/cm^2) for their LA-ICP-MS measurements on the NIST610 glass with the same 193 nm ArF Excimer laser as in this study. If the fluence is too low, the energy of an individual laser pulse is not strong enough to break the atomic bonds (Shaheen et al., 2012 and references therein). One can think of it as the difference between cutting sharply or tearing off randomly sized parts. Another reason for irregular ablation and formation of larger particles can be metallic impurities in transparent materials (Liu et al., 1997; Shaheen et al., 2012). As previously discussed, BIF (meta)chert bands always contain finely dispersed Fe-oxide particles ($>1 \text{ wt. } \%$). The different ablation behaviour of Fe-oxides compared to the surrounding (meta)chert phase can initiate a local "avalanche ionisation" resulting in irregular ablation (Liu et al., 1997; Lenzner et al., 2000; Hergenröder et al., 2006; Shaheen et al., 2012).

The irregular ablation behaviour of (meta)chert phases was especially strong in the polished sections. However, also the NP tablet Temagami BIF metachert samples showed a "poorer" ablation behaviour compared to the Fe-oxide samples. Due to the partly different ablation behaviours of Ga and Al (and Ge and Si), it is necessary for further LA-ICP-MS studies on (meta)cherts to optimise the laser-ablation parameter with respect to potential elemental fractionation. The first approach could be a higher fluence or usage of a fs-laser system. The measured signals only yield quantitative Ga/Al (and Ge/Si) ratios if sufficiently small particles are produced during the laser ablation. One of the biggest current obstacles are missing appropriate natural chert reference material that could be used for LA-ICP-MS optimisation and calibration. This shortcoming is, of course, due to the very low trace element mass fractions in (meta)cherts. Nevertheless, it should be urgently addressed in the future, as the trace element distribution in (meta)cherts could provide important insights into the past atmosphere and hydrosphere conditions.

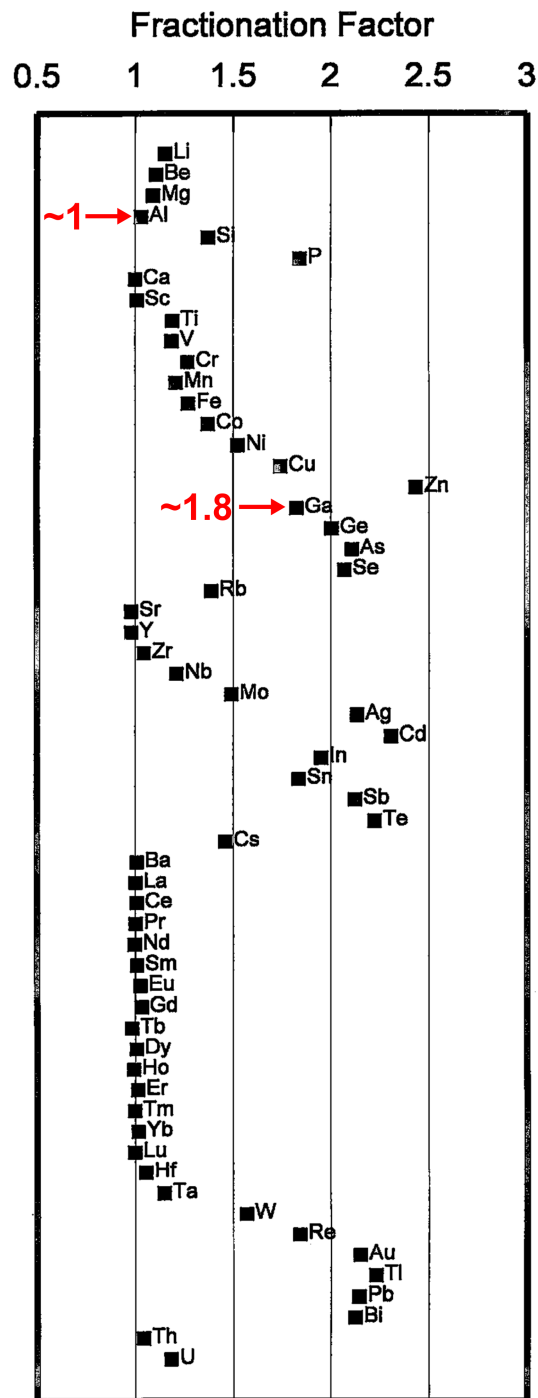


Figure 8.2: Fractionation factors of 60 elements relative to Ca as internal standard. The fractionation factors were determined by comparing the integrated signal of the second two minutes (minutes 2–4) with those of the first two minutes (minutes 0–2) of a laser-ablation measurement of NIST glass 610. Gallium (~ 1.8) and aluminium (~ 1) show clear difference in their fractionation factors indicating that relatively more Ga is ablated during the second two minutes of laser-ablation. Figure modified after Fryer et al. (1995).

8.1 References

- Aeschliman D. B., Bajic S. J., Baldwin D. P. and Houk R. S. (2003) High-speed digital photographic study of an inductively coupled plasma during laser ablation: comparison of dried solution aerosols from a microconcentric nebulizer and solid particles from laser ablation. *J. Anal. At. Spectrom.* 18, 1008.
- Chew D., Drost K., Marsh J. H. and Petrus J. A. (2021) LA-ICP-MS imaging in the geosciences and its applications to geochronology. *Chemical Geology* 559, 119917.
- Fryer B. J., Simon E. J. and Longerich H. P. (1995) The design, operation and role of the laser-ablation microprobe coupled with an inductively coupled plasma - mass spectrometer (LAM-ICP-MS) in the earth sciences. *The Canadian Mineralogist* 33, 303–312.
- Günther D. and Hattendorf B. (2005) Solid sample analysis using laser ablation inductively coupled plasma mass spectrometry. *TrAC Trends in Analytical Chemistry* 24, 255–265.
- Günther D. and Heinrich C. A. (1999a) Comparison of the ablation behaviour of 266 nm Nd:YAG and 193 nm ArF excimer lasers for LA-ICP-MS analysis. *Journal of Analytical Atomic Spectrometry* 14, 1369–1374.
- Günther D. and Heinrich C. A. (1999b) Enhanced sensitivity in laser ablation-ICP mass spectrometry using helium–argon mixtures as aerosol carrier. *Journal of Analytical Atomic Spectrometry* 14, 1363–1368.
- Hergenröder R., Samek O. and Hommes V. (2006) Femtosecond laser ablation elemental mass spectrometry. *Mass Spectrom. Rev.* 25, 551–572.
- Horn I. and Günther D. (2003) The influence of ablation carrier gasses Ar, He and Ne on the particle size distribution and transport efficiencies of laser ablation-induced aerosols: implications for LA-ICP-MS. *Applied Surface Science* 207, 144–157.
- Kuhn H.-R. and Günther D. (2004) Laser ablation-ICP-MS: particle size dependent elemental composition studies on filter-collected and online measured aerosols from glass. *J. Anal. At. Spectrom.* 19, 1158–1164.
- Lenzner M., Krausz F., Krüger J. and Kautek W. (2000) Photoablation with sub-10 fs laser pulses. *Applied Surface Science* 154–155, 11–16.
- Limbeck A., Galler P., Bonta M., Bauer G., Nischkauer W. and Vanhaecke F. (2015) Recent advances in quantitative LA-ICP-MS analysis: challenges and solutions in the life sciences and environmental chemistry. *Anal Bioanal Chem* 407, 6593–6617.
- Liu X., Du D. and Mourou G. (1997) Laser ablation and micromachining with ultrashort laser pulses. *IEEE J. Quantum Electron.* 33, 1706–1716.
- Liu Y., Hu Z., Gao S., Günther D., Xu J., Gao C. and Chen H. (2008) In situ analysis of major and trace elements of anhydrous minerals by LA-ICP-MS without applying an internal standard. *Chemical Geology* 257, 34–43.
- Longerich H. P., Günther D. and Jackson S. E. (1996) Elemental fractionation in laser ablation inductively coupled plasma mass spectrometry. *Analytical and Bioanalytical Chemistry* 355, 538–542.
- Luo T., Wang Y., Hu Z., Günther D., Liu Y., Gao S., Li M. and Hu S. (2015) Further investigation into ICP-induced elemental fractionation in LA-ICP-MS using a local

- aerosol extraction strategy. *J. Anal. At. Spectrom.* 30, 941–949.
- Shaheen M. E., Gagnon J. E. and Fryer B. J. (2012) Femtosecond (fs) lasers coupled with modern ICP-MS instruments provide new and improved potential for in situ elemental and isotopic analyses in the geosciences. *Chemical Geology* 330–331, 260–273.

9 Concluding remarks

The overarching topic of this thesis is the (potential) application of geochemical partner and twin couples as geochemical proxies. The coupled or decoupled behaviour of such geochemical couples can provide information on the physico-chemical conditions that prevail or prevailed in natural systems. The focus of this PhD thesis was placed on the low-temperature marine environment. In order to investigate past atmosphere and hydrosphere, marine chemical sedimentary rocks constitute valuable archives provided they are pure and pristine. Specifically, this means free of detrital contamination and negligible alteration of the target element distribution(s) during diagenesis and metamorphism.

Purity and pristineness are crucial for interpreting geochemical proxies and are not always easy to verify. The application of REY as a powerful tool to assure the integrity of geochemical archives is a topic of Chapter 5. Preservation of seawater-like REY in marine chemical sedimentary rocks, like BIFs, is a first indication of negligible detrital contribution. An even more sensitive indicator is the W-type lanthanide tetrad effect (LTE), which was here described in Precambrian marine chemical sedimentary rocks for the first time (Section 5.5.3). The W-type LTE is characteristic of modern seawater and, as shown by various Precambrian BIFs, also for Archaean and Palaeoproterozoic seawater. Preservation of the W-type LTE in BIFs is clear evidence that they preserved the original and unfractionated seawater REY distribution, as REY distribution of precipitates from Fe-precipitation experiments show the opposite M-type LTE.

Major and trace elements, especially the REY data from the first study of an Antarctic BIF (Chapter 5), show that the investigated Mt. Ruker BIF is pure, pristine, and a promising target for further geochemical studies. The Mt. Ruker BIF might be of special scientific interest as it fills the gap of a BIF from Antarctica, the last continent from which a geochemical BIF study was missing.

For the application and interpretation of a (new) geochemical proxy on the Precambrian environment, it is advantageous if the geochemical behaviour of that proxy in the modern environment is well constrained and understood. Therefore, two coupled studies

were conducted on the behaviour of the Ga-Al and Ge-Si pairs during modern marine hydrogenetic Fe-Mn crust formation. While the study on the Ga-Al systematics in Fe-Mn crusts (and nodules) was part of Katharina Schier's PhD thesis (Schier, 2020), the Ge-Si systematics of the same samples are discussed here in Chapter 4. Both studies reveal fractionation of both couples during scavenging mainly onto Fe oxyhydroxides. While Ge/Si ratios are elevated compared to ambient seawater, Ga/Al ratios of Fe-Mn crusts and nodules are lower than those of modern seawater. Presumably, this is due to the higher particle reactivities of Ge and Al compared to their respective partners. These observations are in accordance with other studies on Ga-Al and Ge-Si systematics in soils, rivers, estuaries, and seawater. To what extent organic material influences the behaviour of Ga-Al (and Ge-Si) in the aqueous environments cannot be assessed yet. However, one can speculate that organic ligands and particles might exert major control due to rather high complexation constants and high abundances of organic particles in many natural systems. In order to capture the entire Ga-Al (and Ge-Si) behaviour in the modern natural environment, future research needs to investigate their interaction with organic substances in more detail. Only if the impact of organic material on the cycling of Ga and Al in the modern system is known, the Ga-Al systematics of Archaean and Palaeoproterozoic systems, depleted in organic material, can be interpreted comprehensively.

In Fe-Mn crusts, all four elements (Ga, Al, Ge and Si) show positive correlations with Fe content indicating adsorption by Fe oxyhydroxide rather than Mn oxide particles during formation. Surprisingly, also Si shows a strong positive correlation with Fe, clearly arguing against an exclusively detrital origin as suggested in previous studies. Oceanic Si concentrations are much higher than those of Fe and Mn, and it is assumed that Precambrian seawaters also had high Si concentrations. In many cases, Si in chemical precipitates is considered of detrital origin, and its adsorption on or coprecipitation with metal (oxyhydr)oxides is barely studied. Therefore, the Fe-Si systematics in hydrogenetic Fe-Mn is a promising target for future studies. It might also provide new insights into the unique coupled occurrence of massive Fe oxide and (meta)chert bands in BIFs.

The studies on Ga-Al and Ge-Si decoupling in Fe-Mn crusts generally point out that more research on the behaviour of these two couples in the natural environment is required. Not only would that improve the interpretation of Ga/Al and Ge/Si ratios as geochemical proxies, but also Ga and Ge are considered critical metals and essential components in several high-tech applications, e.g., components for wireless communication and fibre optics, respectively. The usage of Ga and Ge and, therefore, their anthropogenic

input into natural environments will increase strongly in the near future. A profound understanding of the Ga-Al and Ge-Si couples will help to assess the consequences of such increasing anthropogenic input and might facilitate the exploration of new ore deposits.

As pointed out earlier, there are no modern analogues of BIFs, and although Fe-Mn crusts are Fe-rich marine chemical precipitates, they differ severely from Precambrian BIFs. In Fe-Mn crusts, various geochemical couples and groups are heavily fractionated (e.g., REY, Zr-Hf, Nb-Ta, Ga-Al, Ge-Si). For pure and pristine BIFs, it is generally assumed that they preserved the primary seawater trace elemental — not isotopic — distribution. Surprisingly, Fe-Mn crusts and Fe oxides in BIFs show the same Ga/Al ratios as presented in Chapter 6. At first glance, that might indicate that Ga and Al in BIFs were scavenged and fractionated from a seawater with "modern-ocean" Ga/Al ratios. A closer look reveals a profound difference: while Ga/Al ratios in Fe-Mn crusts decrease with increasing Fe content, Ga/Al ratios increase, remain constant or scatter with increasing Fe content in BIFs. None of the investigated BIFs show decreasing Ga/Al ratios with increasing Fe mass fractions. Therefore, similar Ga/Al ratios in Cenozoic Fe-Mn crusts and Precambrian BIFs might be coincidental. Further data on the Ga-Al distribution in Fe-Mn crusts, nodules, BIFs and marine carbonates (modern and Precambrian) are now required.

An important observation made during the investigation of Ga/Al ratios in the Temagami BIF was that the Ga-Al systematics in the (meta)chert bands is most likely fully controlled by finely dispersed Fe oxide particles as indicated by uniform Ga/Al ratios. It can be assumed that the Ga and Al mass fractions associated with those Fe oxide particles are much higher than those of the surrounding chert matrix. Therefore, they hide the "original" (meta)chert Ga/Al ratio. While it remains unclear how this original (meta)chert Ga/Al ratio looks like, the dominance of Fe oxide particles within (meta)chert may also apply to other trace elements and, therefore, should be considered for the interpretation of geochemical data. To a certain extent, Fe oxide particle dominance could explain similarities in REY distributions, especially positive Eu anomalies, between Fe oxide and (meta)chert bands.

9.1 Relationship between Ga-Al and Ge-Si systematics in BIFs

One of the key aspects of this thesis was to elucidate the relationship between the Ga-Al and Ge-Si systematics in BIFs. Previous studies showed that BIF Fe oxide bands have

9 Concluding remarks

elevated Ge/Si ratios compared to (meta)chert bands (e.g., Hamade et al., 2003; Alibert and Kinsley, 2016; Bau et al., 2022). These differences were previously interpreted as a source proxy for Fe and Si in BIFs (Hamade et al., 2003; Bau et al., 2022) or as evidence for the diagenetic separation of Fe oxide and chert bands from a homogeneous Fe-Si gel (Alibert and Kinsley, 2016). The approach of this PhD thesis was to utilise Ga/Al ratios similar to Ge/Si ratios to prove or falsify one or both models. Surprisingly, the observed Ga-Al systematics in Temagami BIF differ from that of Ge and Si. The interpretations that can be made on the measured Ga/Al ratios are very different from those of the Ge-Si couple. A general relationship of increasing Ge/Si ratios with increasing Fe content is not given for the Ga-Al couple in the Temagami BIF: the Ga/Al ratios in Temagami BIF are uniform regardless of the samples' mineralogy. The most likely explanation is that the Ga and Al content in Temagami BIF (meta)chert bands is dominated by finely dispersed Fe oxide particles and that, with the here applied analytical methods, not the "original" (meta)chert phase Ga/Al ratios were measured. This might raise the question of whether the measured Ge/Si ratios in Temagami BIF (meta)chert bands represent the (meta)chert phase or if finely dispersed Fe oxide particles also dominate at least the Ge content. Figure 9.1 plots Ga/Ge ratios against Fe content in the Temagami BIF samples. The Ga and Fe data are from Chapter 6 and were determined with solution-based SF-ICP-MS and ICP-OES, respectively. The Ge mass fractions originate from the previous publication on Ge/Si ratios by Bau et al. (2022). The plot shows that while Fe oxide bands (high Fe content) show Ga/Ge ratios similar to those of modern seawater (0.27; Bruland et al., 2014), the (meta)chert bands show lower Ga/Ge ratios (down to approx. 2×10^{-2}). If the entire Ga in BIFs is assumed to be associated with Fe oxides, the low Ga/Ge ratios in the (meta)chert samples indicate additional Ge associated with the (meta)chert phase, unlike Ga. This indicates that the Ge distribution in Temagami BIF cannot be entirely dominated by Fe oxides. It should be noted, however, that the here used Ge mass fractions were determined by LA-SF-ICP-MS, which puts certain limitations on the determination of absolute mass fractions, as described in Chapter 8. Two-component mixing experiments, similar to those conducted for Ga and Al in Section 6.3.3 might be appropriate to elucidate whether the trend in Ge/Si ratios is an original and primary feature or if it is an artefact of strong "dilution" with Si in the (meta)chert bands.

Nevertheless, the Ga-Al systematics in Temagami BIF might not be representative of all BIFs, as the additional Ga/Al ratio measurements in other BIF samples (Fig. 7.2) show. While the overall range of Ga/Al ratios in BIFs might be rather uniform, based on the here presented dataset, there are still differences in the actual Ga-Al distribution

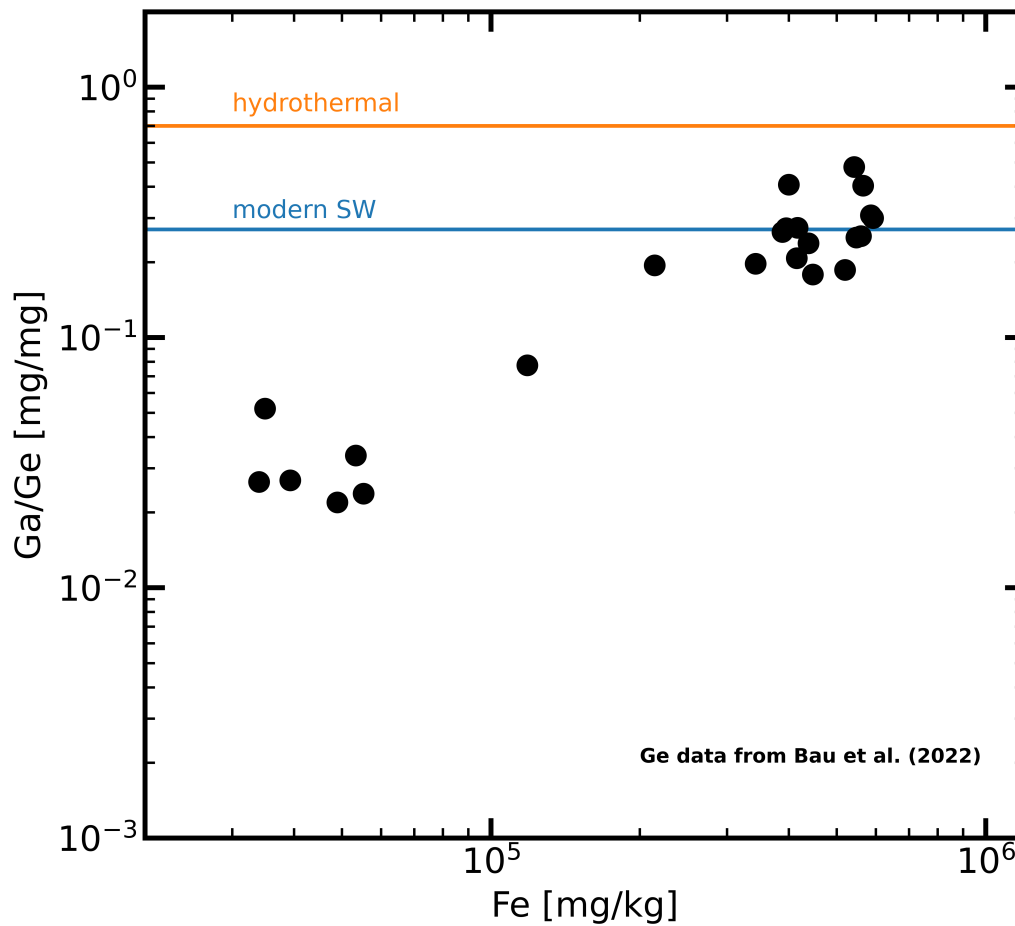


Figure 9.1: Ga/Ge ratios plotted against Fe content in the Temagami BIF samples. The Fe oxide bands show Ga/Ge ratios similar to those of modern seawater (Bruland et al., 2014). The (meta)chert bands show lower Ga/Ge ratios indicating an additional Ge carrier phase besides finely dispersed Fe oxide particles. Gallium and iron mass fractions were determined with solution-based SF-ICP-MS and ICP-OES, respectively. Germanium mass fractions from Bau et al. (2022). Hydrothermal fluid Ga/Ge ratio from Schmidt et al. (2017).

9 Concluding remarks

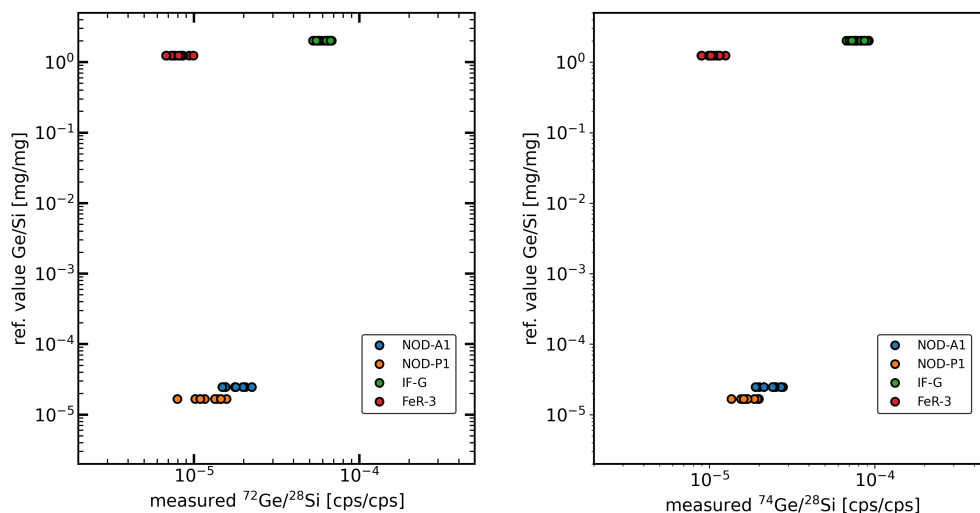


Figure 9.2: Reference Ge/Si values plotted against measured Ge/Si signal for the RMs NOD-A1, NOD-P1, IF-G and FeR-3. Left plot shows $^{72}\text{Ge}/^{28}\text{Si}$ ratios, and right plot shows $^{74}\text{Ge}/^{28}\text{Si}$. Determination of a calibration curve, like for Ga/Al in Chapter 6.3.5 is not possible due to ambiguous calculations with different RMs. Reference values: NOD-A1 (Smith, 1995; Ernst et al., 2022), NOD-P1 (Smith, 1995; Scribner et al., 2006); IF-G (Govindaraju, 1994; van Gerve et al., 2020), FeR-3 (Govindaraju, 1994).

within this “global range” — e.g., increasing Ga/Al ratios with increasing Fe content in Isua and Hotazel drill core *GHEX_97_3*. Unfortunately, determining Ge/Si ratios in those samples was impossible because measurement signal calibration with the RMs IF-G, FeR-3, NOD-A1 and NOD-P1 is ambiguous (example in Fig. 9.2). Therefore, a direct comparison of Ga-Al and Ge-Si systematics is currently only possible for the Temagami BIF samples. Hence, further coupled measurements of Ga/Al and Ge/Si ratios are needed.

Besides comparing Ga-Al and Ge-Si systematics, a comparison with other trace elements might also offer new insights. However, since it is not clear yet whether the Temagami BIF is representative or rather “exotic” in its Ga-Al systematics, such interpretations could be misleading. Figure 10.5 in the appendix shows a compilation of Ga ratios with other trace elements plotted against Fe content, similar to Fig. 9.1 (Ga/Ge vs Fe) described above. Although some trace elements show interesting relationships with Ga in Fig. 10.5, these plots are intended as a starting point for further investigations, and the interpretation of these relationships would be beyond the scope of this thesis.

9.2 Immediate implications

Various starting points for further research are already given in the text above. Therefore, this section gives a more immediate outlook on my own scientific near future.

During this PhD project, it became clear at many points how important the reliability of analytical data is and how difficult or even impossible it is to assess data quality. In the past, typically, the development of a new, more powerful analytical method solved such problems and enabled researchers to answer new questions. However, today we are able to measure extremely small quantities and differences increasingly fast in all kinds of sample types. In some cases, it might be already questionable if the analytical result is even significant for *natural* samples or just caused by random natural variation. On the one hand, massive amounts of analytical data are generated daily. On the other hand, however, the research questions (in geosciences) are becoming increasingly complex. They can already often no longer be answered by individual scientists or working groups. Sharing research data with colleagues and true collaboration becomes crucial and is increasingly done, e.g., via scientific data repositories. However, the huge amount of accessible analytical data is currently not distributed in a uniform manner. Only in the field of geochemistry do numerous data repositories for individual sample types exist. Furthermore, one of the biggest issues for shared data is assessing *data quality*. Nevertheless, the development of data-sharing infrastructure only began, and almost certainly, great progress will be made in the next few years. Therefore, the next big steps (in geochemistry) might not be made due to the development of a new analytical method but due to upcoming advances in the distribution of research data and the resulting linkage of researchers worldwide.

The many hours spent during this PhD thesis to rack one's brain about the reliability of analytical data resulted in the research proposal for *QuARUm* (Quality assessment of analytical data in resource and environmental research). QuARUm aims to develop a software tool that objectively evaluates the quality of self-produced analytical data and data published in articles and data repositories. The German Ministry of Education and Research and the European Union approved and funded the project for three years. The experiences gained and the contacts made during my PhD project will help make QuARUm successful. The results of QuARUm, in turn, will become extremely handy for further investigating Ga-Al and Ge-Si behaviours in natural systems, which of course, will be continued.

9.3 References

- Alibert C. and Kinsley L. (2016) Ge/Si in Hamersley BIF as tracer of hydrothermal Si and Ge inputs to the Paleoproterozoic ocean. *Geochimica et Cosmochimica Acta* 184, 329–343.
- Bau M., Frei R., Garbe-Schönberg D. and Viehmann S. (2022) High-resolution Ge-Si-Fe, Cr isotope and Th-U data for the Neoproterozoic Temagami BIF, Canada, suggest primary origin of BIF bands and oxidative terrestrial weathering 2.7 Ga ago. *Earth and Planetary Science Letters* 589, 117579.
- Bruland K. W., Middag R. and Lohan M. C. (2014) Controls of Trace Metals in Seawater. In *Treatise on Geochemistry* Elsevier. pp. 19–51.
- Ernst D. M., Schier K., Garbe-Schönberg D. and Bau M. (2022) Fractionation of germanium and silicon during scavenging from seawater by marine Fe (oxy)hydroxides: Evidence from hydrogenetic ferromanganese crusts and nodules. *Chemical Geology* 595.
- van Gerve T. D., Neave D. A., Almeev R. R., Holtz F. and Namur O. (2020) Zoned Crystal Records of Transcrustal Magma Transport, Storage and Differentiation: Insights from the Shatsky Rise Oceanic Plateau. *Journal of Petrology* 61, ega080.
- Govindaraju K. (1994) 1994 COMPILATION OF WORKING VALUES AND SAMPLE DESCRIPTION FOR 383 GEOSTANDARDS. *Geostandards and Geoanalytical Research* 18, 1–158.
- Hamade T., Konhauser K. O., Raiswell R., Goldsmith S. and Morris R. C. (2003) Using Ge/Si ratios to decouple iron and silica fluxes in Precambrian banded iron formations. *Geology* 31, 35–38.
- Schier K. (2020) Trace elements and their application as geochemical proxies in marine chemical sediments. Jacobs University Bremen.
- Schmidt K., Garbe-Schönberg D., Hannington M. D., Anderson M. O., Bühring B., Haase K., Haruel C., Lupton J. and Koschinsky A. (2017) Boiling vapour-type fluids from the Nifonea vent field (New Hebrides Back-Arc, Vanuatu, SW Pacific): Geochemistry of an early-stage, post-eruptive hydrothermal system. *Geochimica et Cosmochimica Acta* 207, 185–209.
- Scribner A. M., Kurtz A. C. and Chadwick O. A. (2006) Germanium sequestration by soil: Targeting the roles of secondary clays and Fe-oxyhydroxides. *Earth and Planetary Science Letters* 243, 760–770.
- Smith D. B. (1995) USGS Certificate of Analysis Manganese Nodules. NOD-P1., USGS.

10 Appendix

10.1 Supplementary Figures

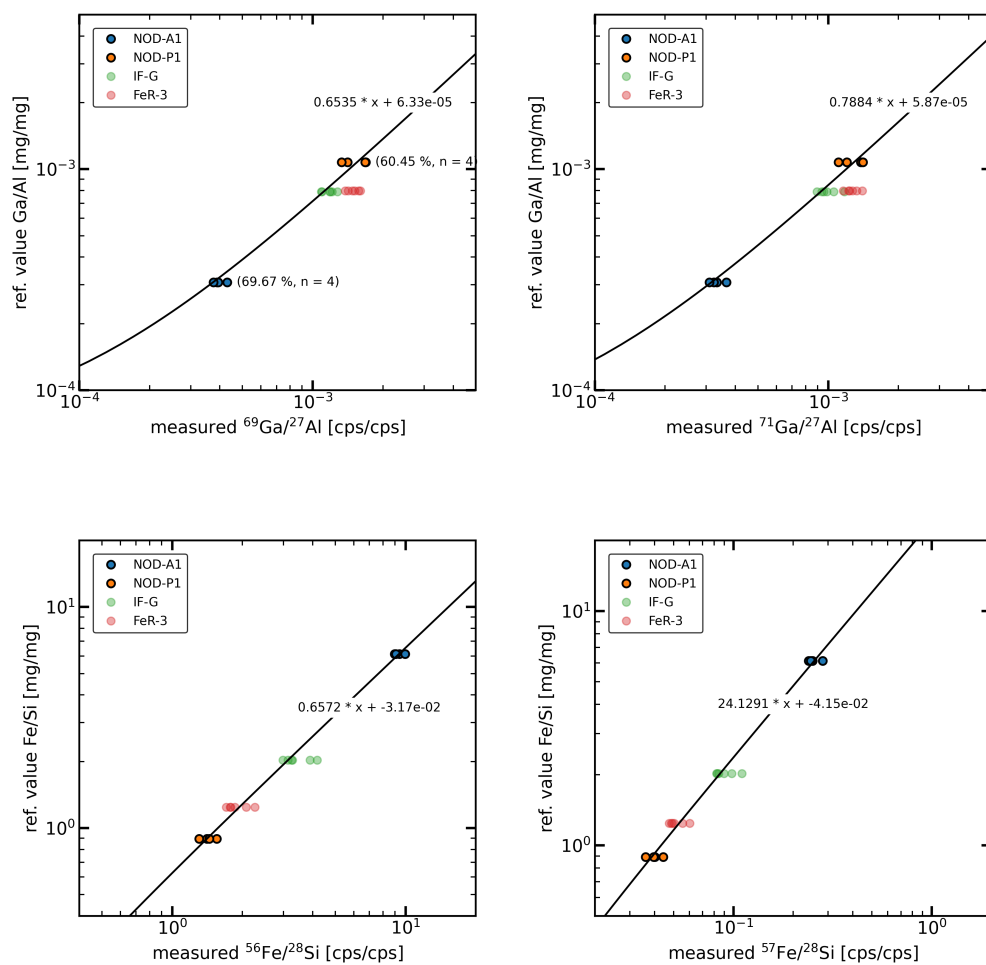


Figure 10.1: Linear calibrations of $^{69}\text{Ga}/^{27}\text{Al}$, $^{71}\text{Ga}/^{27}\text{Al}$, $^{56}\text{Fe}/^{28}\text{Si}$ and $^{57}\text{Fe}/^{28}\text{Si}$ for the Isua BIF samples. Measured on Jul. 3rd, 2019 at Kiel University.

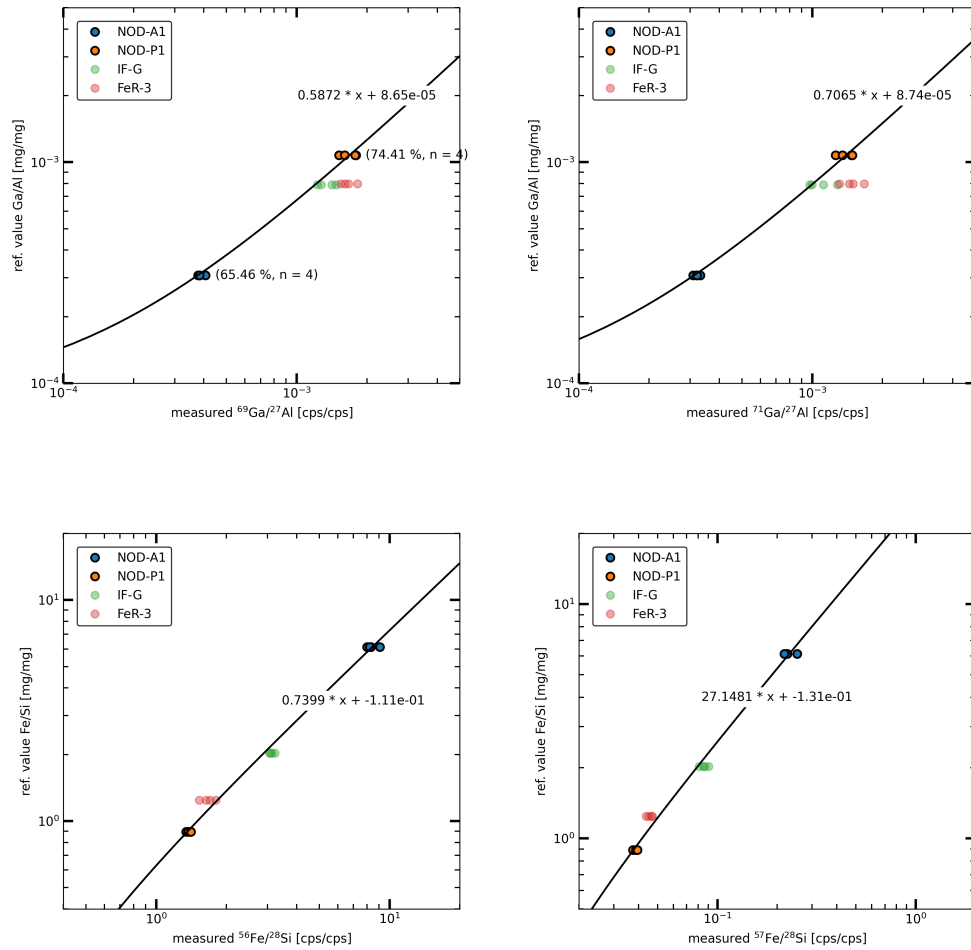


Figure 10.2: Linear calibrations of ⁶⁹Ga/²⁷Al, ⁷¹Ga/²⁷Al, ⁵⁶Fe/²⁸Si and ⁵⁷Fe/²⁸Si for the Marra Mamba BIF samples. Measured on Jul. 5th, 2019 at Kiel University.

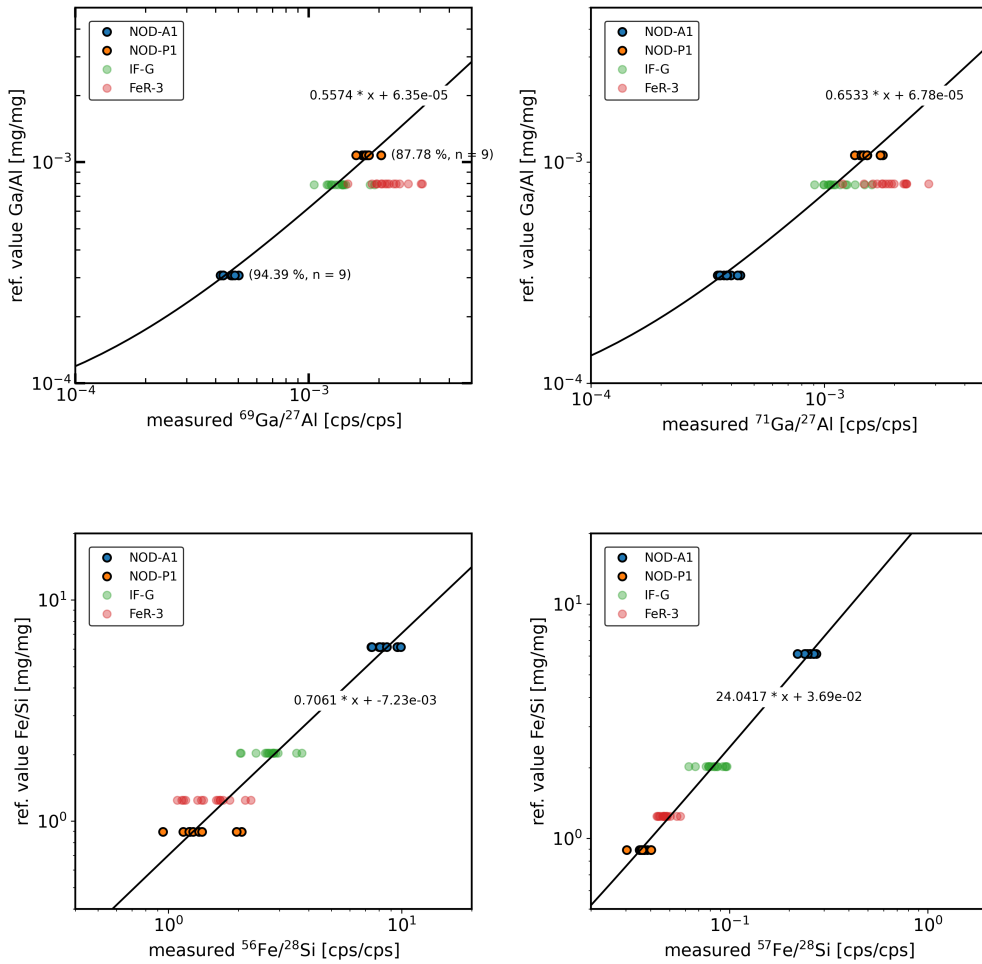


Figure 10.3: Linear calibrations of $^{69}\text{Ga}/^{27}\text{Al}$, $^{71}\text{Ga}/^{27}\text{Al}$, $^{56}\text{Fe}/^{28}\text{Si}$ and $^{57}\text{Fe}/^{28}\text{Si}$ for the Hotazel IF (GHEX drill core) samples. Measured on Nov. 5th, 2019 at Kiel University.

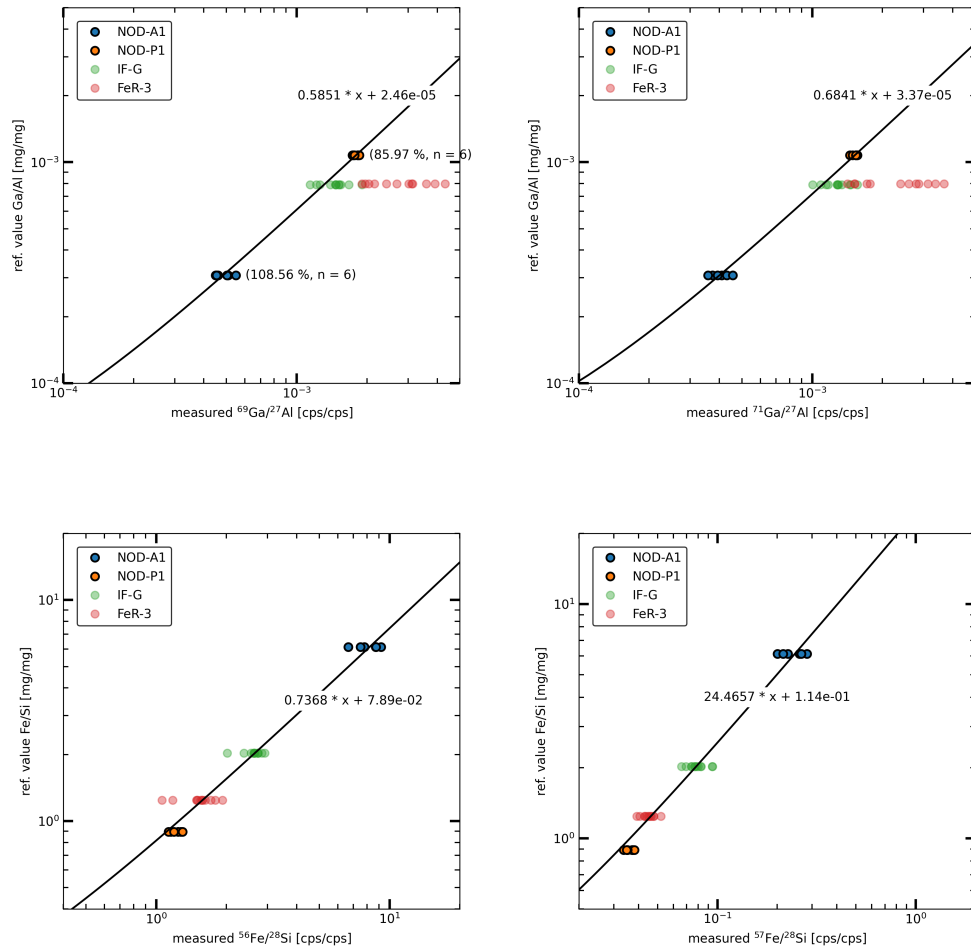


Figure 10.4: Linear calibrations of ⁶⁹Ga/²⁷Al, ⁷¹Ga/²⁷Al, ⁵⁶Fe/²⁸Si and ⁵⁷Fe/²⁸Si for the Mt. Ruker and Kuruman BIF samples. Measured on Nov. 7th, 2019 at Kiel University.

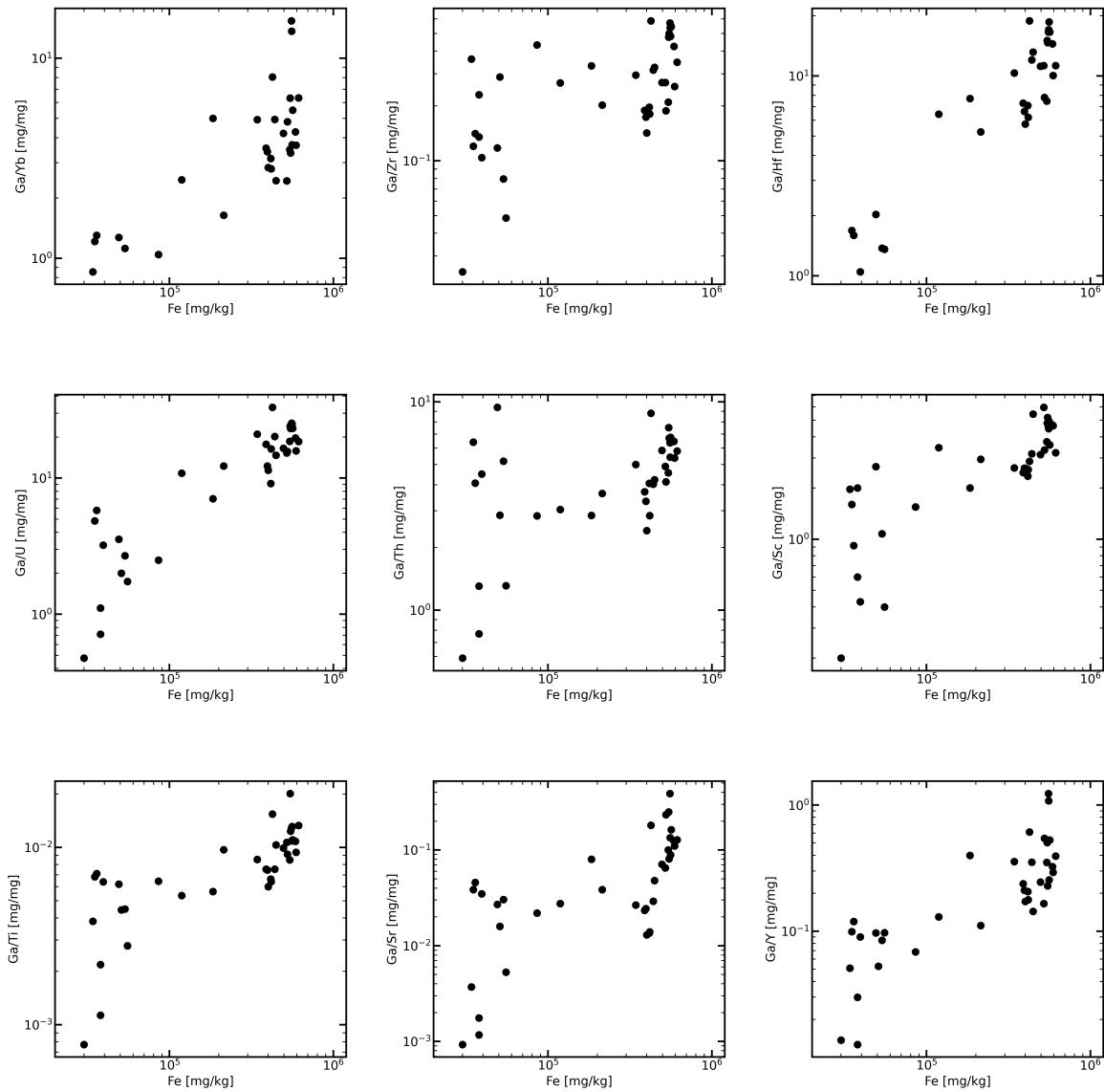


Figure 10.5: Ratios of Ga with other trace elements (TE) plotted against Fe content in Temagami BIF. Solution-based (SF-)ICP-MS from Chapter 6 is used. If assumed that Ga is exclusively bound to Fe oxide particles in BIFs, lower Ga/TE ratios in (meta)chert bands indicate additional carrier phase for that TE. Note the rather different distributions for trace element couples like Zr-Hf or U-Th.

10.2 Supplementary Tables

Table 10.1: Measured Ga/Al and Fe/Si ratios in the Isua BIF. Only evaluable data points are listed here. The Ga/Al ratios were determined with ^{69}Ga and ^{71}Ga isotopes. The Fe/Si ratios were determined with ^{56}Fe and ^{57}Fe isotopes.

sample	$^{69}\text{Ga}/^{27}\text{Al}$	$^{71}\text{Ga}/^{27}\text{Al}$	$^{56}\text{Fe}/^{28}\text{Si}$	$^{57}\text{Fe}/^{28}\text{Si}$
NISTSRM610	3.13×10^{-2}	3.27×10^{-2}	3.36×10^{-2}	4.35×10^{-2}
NISTSRM610	3.09×10^{-2}	3.22×10^{-2}	3.36×10^{-2}	4.35×10^{-2}
NISTSRM610	4.08×10^{-2}	4.20×10^{-2}	3.33×10^{-2}	4.32×10^{-2}
NISTSRM610	4.19×10^{-2}	4.20×10^{-2}	3.34×10^{-2}	4.32×10^{-2}
NISTSRM610	5.42×10^{-2}	5.39×10^{-2}	3.34×10^{-2}	4.32×10^{-2}
NISTSRM610	5.51×10^{-2}	5.71×10^{-2}	3.33×10^{-2}	4.30×10^{-2}
IF-G	8.40×10^{-4}	8.14×10^{-4}	2.78	2.70
IF-G	7.75×10^{-4}	7.65×10^{-4}	2.59	2.41
IF-G	8.53×10^{-4}	8.90×10^{-4}	1.99	2.02
IF-G	7.78×10^{-4}	7.97×10^{-4}	2.09	2.04
IF-G	8.96×10^{-4}	9.84×10^{-4}	2.18	2.20
IF-G	8.37×10^{-4}	8.36×10^{-4}	2.16	2.08
FeR-3	9.91×10^{-4}	1.03×10^{-3}	1.39	1.38
FeR-3	1.11×10^{-3}	9.73×10^{-4}	1.52	1.49
FeR-3	9.63×10^{-4}	1.02×10^{-3}	1.15	1.19
FeR-3	1.09×10^{-3}	1.06×10^{-3}	1.20	1.23
FeR-3	1.03×10^{-3}	1.10×10^{-3}	1.20	1.21
FeR-3	1.05×10^{-3}	1.16×10^{-3}	1.25	1.25
NOD-P1	9.86×10^{-4}	1.01×10^{-3}	1.05	1.11
NOD-P1	9.33×10^{-4}	9.31×10^{-4}	9.58×10^{-1}	1.01
NOD-P1	1.16×10^{-3}	1.15×10^{-3}	8.88×10^{-1}	9.12×10^{-1}
NOD-P1	1.16×10^{-3}	1.17×10^{-3}	9.79×10^{-1}	9.99×10^{-1}
NOD-A1	3.18×10^{-4}	3.22×10^{-4}	6.21	5.82
NOD-A1	3.20×10^{-4}	3.13×10^{-4}	6.57	6.84
NOD-A1	3.09×10^{-4}	3.03×10^{-4}	5.93	6.09
NOD-A1	3.44×10^{-4}	3.47×10^{-4}	6.00	5.97
IS1_LS_001	7.98×10^{-4}	7.94×10^{-4}	2.91	2.75
IS1_LS_002	1.24×10^{-3}	1.29×10^{-3}	3.76	3.67
IS1_LS_005	4.36×10^{-4}	4.16×10^{-4}	2.09	2.09
IS1_LS_006	1.79×10^{-4}	1.85×10^{-4}	8.81×10^{-1}	9.30×10^{-1}
IS1_LS_008	1.39×10^{-4}	1.34×10^{-4}	6.13	6.00
IS1_LS_009	5.71×10^{-3}	6.18×10^{-3}	6.41	6.33
IS1_LS_012	8.05×10^{-3}	9.04×10^{-3}	9.59	9.52
IS1_LS_013	3.87×10^{-3}	4.03×10^{-3}	6.35	6.42
IS1_LS_014	2.06×10^{-3}	2.05×10^{-3}	5.28	5.23
IS1_LS_015	2.28×10^{-3}	2.06×10^{-3}	5.12	5.07
IS1_LS_019	4.17×10^{-3}	3.79×10^{-3}	5.77	5.83
IS1_LS_023	5.45×10^{-3}	5.52×10^{-3}	5.06	5.02
IS1_LS_026	6.85×10^{-4}	6.28×10^{-4}	2.13	2.13
IS1_LS_027	2.24×10^{-3}	2.34×10^{-3}	4.76	4.66

Continued.

sample	$^{69}\text{Ga}/^{27}\text{Al}$	$^{71}\text{Ga}/^{27}\text{Al}$	$^{56}\text{Fe}/^{28}\text{Si}$	$^{57}\text{Fe}/^{28}\text{Si}$
IS1_LS_030	7.07×10^{-4}	5.93×10^{-4}	2.05	2.02
IS1_LS_031	7.66×10^{-3}	7.39×10^{-3}	8.46	8.58
IS1_LS_034	5.86×10^{-3}	6.09×10^{-3}	7.70	7.93
IS1_LS_035	3.67×10^{-3}	4.00×10^{-3}	3.98	3.94
IS1_LS_036	9.06×10^{-4}	8.88×10^{-4}	3.20	3.19
IS1_LS_037	1.56×10^{-3}	1.49×10^{-3}	4.43	4.42
IS1_LS_041	3.35×10^{-4}	3.13×10^{-4}	1.16	1.15

Table 10.2: Measured Ga/Al and Fe/Si ratios in the Marra Mamba BIF. Only evaluable data points are listed here. The Ga/Al ratios were determined with ^{69}Ga and ^{71}Ga isotopes. The Fe/Si ratios were determined with ^{56}Fe and ^{57}Fe isotopes.

sample	$^{69}\text{Ga}/^{27}\text{Al}$	$^{71}\text{Ga}/^{27}\text{Al}$	$^{56}\text{Fe}/^{28}\text{Si}$	$^{57}\text{Fe}/^{28}\text{Si}$
NISTSRM610	3.61×10^{-2}	3.67×10^{-2}		
NISTSRM610	3.51×10^{-2}	3.57×10^{-2}		
NISTSRM610	4.53×10^{-2}	4.57×10^{-2}		
NISTSRM610	4.44×10^{-2}	4.49×10^{-2}		
IF-G	9.18×10^{-4}	8.75×10^{-4}	2.15	2.06
IF-G	8.34×10^{-4}	7.92×10^{-4}	2.28	2.17
IF-G	9.51×10^{-4}	9.92×10^{-4}	2.16	2.32
IF-G	8.05×10^{-4}	7.76×10^{-4}	2.21	2.21
FeR-3	1.16×10^{-3}	1.27×10^{-3}	1.22	1.13
FeR-3	1.07×10^{-3}	1.01×10^{-3}	1.10	1.09
FeR-3	9.93×10^{-4}	1.11×10^{-3}	1.02	1.05
FeR-3	1.03×10^{-3}	1.15×10^{-3}	1.15	1.14
NOD-P1	9.78×10^{-4}	9.77×10^{-4}	0.88	0.89
NOD-P1	1.14×10^{-3}	1.13×10^{-3}	0.92	0.93
NOD-P1	1.03×10^{-3}	1.04×10^{-3}	0.90	0.92
NOD-P1	1.13×10^{-3}	1.14×10^{-3}	0.93	0.94
NOD-A1	3.08×10^{-4}	3.05×10^{-4}	6.04	5.93
NOD-A1	3.12×10^{-4}	3.14×10^{-4}	6.61	6.71
NOD-A1	3.25×10^{-4}	3.22×10^{-4}	5.82	5.98
NOD-A1	3.12×10^{-4}	3.14×10^{-4}	5.97	5.78
MM1_LS_HR_005	3.27×10^{-4}	3.34×10^{-4}	8.93	8.92
MM1_LS_HR_006	3.29×10^{-4}	3.32×10^{-4}	9.33	9.37
MM1_LS_HR_008	3.42×10^{-4}	3.40×10^{-4}	55.49	55.62
MM1_LS_HR_009	3.33×10^{-4}	3.41×10^{-4}	18.78	18.64
MM1_LS_HR_010	3.76×10^{-4}	3.76×10^{-4}	30.30	30.99
MM1_LS_HR_013	3.58×10^{-4}	3.75×10^{-4}	15.21	15.34
MM1_LS_HR_014	3.66×10^{-4}	3.58×10^{-4}	19.59	19.87
MM1_LS_HR_015	3.45×10^{-4}	3.40×10^{-4}	12.80	12.72
MM1_LS_HR_016	3.21×10^{-4}	3.20×10^{-4}	5.85	5.82
MM1_LS_HR_017	3.16×10^{-4}	3.17×10^{-4}	3.89	3.83
MM1_LS_HR_018	3.42×10^{-4}	3.39×10^{-4}	10.45	10.55
MM1_LS_HR_019	3.08×10^{-4}	3.04×10^{-4}	82.91	84.35

Table 10.3: Measured Ga/Al and Fe/Si ratios in the Hotazel (GHEX drill cores) and Dales Gorge BIF. Only evaluable data points are listed here. The Ga/Al ratios were determined with ^{69}Ga and ^{71}Ga isotopes. The Fe/Si ratios were determined with ^{56}Fe and ^{57}Fe isotopes.

sample	$^{69}\text{Ga}/^{27}\text{Al}$	$^{71}\text{Ga}/^{27}\text{Al}$	$^{56}\text{Fe}/^{28}\text{Si}$	$^{57}\text{Fe}/^{28}\text{Si}$
NISTSRM610	3.35×10^{-2}	3.39×10^{-2}		
NISTSRM610	3.27×10^{-2}	3.30×10^{-2}		
NISTSRM610	3.42×10^{-2}	3.48×10^{-2}		
NISTSRM610	3.46×10^{-2}	3.44×10^{-2}		
NISTSRM610	3.64×10^{-2}	3.54×10^{-2}		
NISTSRM610	3.52×10^{-2}	3.52×10^{-2}		
NISTSRM610	3.74×10^{-2}	3.74×10^{-2}		
NISTSRM610	3.60×10^{-2}	3.69×10^{-2}		
NISTSRM610	3.79×10^{-2}	3.76×10^{-2}		
NISTSRM610	3.15×10^{-2}	3.11×10^{-2}		
NISTSRM610	3.10×10^{-2}	3.11×10^{-2}		
NISTSRM610	3.29×10^{-2}	3.29×10^{-2}		
NISTSRM610	5.31×10^{-2}	5.61×10^{-2}		
NISTSRM610	4.74×10^{-2}	4.70×10^{-2}		
NISTSRM610	5.26×10^{-2}	5.15×10^{-2}		
IF-G	8.66×10^{-4}	8.85×10^{-4}	1.91	1.92
IF-G	8.08×10^{-4}	7.19×10^{-4}	2.50	2.14
IF-G	7.31×10^{-4}	7.64×10^{-4}	2.63	2.26
IF-G	8.38×10^{-4}	8.74×10^{-4}	1.83	2.33
IF-G	7.63×10^{-4}	7.54×10^{-4}	1.86	2.05
IF-G	8.48×10^{-4}	8.32×10^{-4}	1.95	2.12
IF-G	8.35×10^{-4}	7.45×10^{-4}	1.99	1.93
IF-G	6.52×10^{-4}	6.62×10^{-4}	1.89	1.95
IF-G	7.57×10^{-4}	7.85×10^{-4}	1.99	1.98
IF-G	8.43×10^{-4}	7.18×10^{-4}	2.03	2.37
IF-G	7.41×10^{-4}	7.98×10^{-4}	1.67	2.07
IF-G	7.87×10^{-4}	7.65×10^{-4}	2.08	2.35
IF-G	1.09×10^{-3}	1.11×10^{-3}	1.44	1.54
IF-G	8.53×10^{-4}	9.53×10^{-4}	1.43	1.66
IF-G	1.13×10^{-3}	1.04×10^{-3}	1.98	1.87
FeR-3	1.25×10^{-3}	1.27×10^{-3}	1.59	1.34
FeR-3	1.43×10^{-3}	1.34×10^{-3}	8.32×10^{-1}	1.25
FeR-3	1.10×10^{-3}	1.23×10^{-3}	1.29	1.14
FeR-3	1.55×10^{-3}	1.54×10^{-3}	1.13	1.08
FeR-3	1.30×10^{-3}	1.52×10^{-3}	1.17	1.19
FeR-3	1.75×10^{-3}	1.53×10^{-3}	7.64×10^{-1}	1.07
FeR-3	1.27×10^{-3}	1.37×10^{-3}	9.92×10^{-1}	1.20
FeR-3	1.16×10^{-3}	1.17×10^{-3}	9.37×10^{-1}	1.16
FeR-3	1.20×10^{-3}	1.22×10^{-3}	1.15	1.16
FeR-3	1.35×10^{-3}	1.30×10^{-3}	9.71×10^{-1}	1.40

Continued.

sample	$^{69}\text{Ga}/^{27}\text{Al}$	$^{71}\text{Ga}/^{27}\text{Al}$	$^{56}\text{Fe}/^{28}\text{Si}$	$^{56}\text{Fe}/^{28}\text{Si}$
FeR-3	1.38×10^{-3}	1.50×10^{-3}	1.17	1.17
FeR-3	1.77×10^{-3}	1.90×10^{-3}	8.14×10^{-1}	1.11
FeR-3	1.15×10^{-3}	1.04×10^{-3}	1.21	1.20
FeR-3	1.21×10^{-3}	1.13×10^{-3}	8.00×10^{-1}	1.16
FeR-3	8.83×10^{-4}	8.50×10^{-4}	1.50	1.10
NOD-P1	1.01×10^{-3}	9.95×10^{-4}	1.45	1.00
NOD-P1	9.53×10^{-4}	9.51×10^{-4}	1.38	9.64×10^{-1}
NOD-P1	1.20×10^{-3}	1.23×10^{-3}	6.64×10^{-1}	7.66×10^{-1}
NOD-P1	1.03×10^{-3}	1.03×10^{-3}	8.69×10^{-1}	9.36×10^{-1}
NOD-P1	1.03×10^{-3}	1.01×10^{-3}	8.13×10^{-1}	8.82×10^{-1}
NOD-P1	1.06×10^{-3}	1.07×10^{-3}	8.61×10^{-1}	9.26×10^{-1}
NOD-P1	1.20×10^{-3}	1.20×10^{-3}	8.94×10^{-1}	1.00
NOD-P1	1.04×10^{-3}	1.03×10^{-3}	9.50×10^{-1}	8.99×10^{-1}
NOD-P1	1.07×10^{-3}	1.06×10^{-3}	9.79×10^{-1}	9.09×10^{-1}
NOD-A1	3.22×10^{-4}	3.28×10^{-4}	6.79	6.64
NOD-A1	3.26×10^{-4}	3.10×10^{-4}	6.75	6.21
NOD-A1	2.97×10^{-4}	2.96×10^{-4}	7.00	6.41
NOD-A1	3.43×10^{-4}	3.53×10^{-4}	5.65	6.15
NOD-A1	3.03×10^{-4}	3.02×10^{-4}	5.23	5.88
NOD-A1	3.26×10^{-4}	3.45×10^{-4}	5.86	6.46
NOD-A1	2.97×10^{-4}	3.01×10^{-4}	5.69	6.01
NOD-A1	3.32×10^{-4}	3.19×10^{-4}	6.09	5.79
NOD-A1	3.03×10^{-4}	3.17×10^{-4}	5.26	5.34
GHEX_97.3.003	2.58×10^{-4}	2.68×10^{-4}	7.16×10^{-1}	7.71×10^{-1}
GHEX_97.3.007	2.75×10^{-4}	2.62×10^{-4}	2.79	2.80
GHEX_97.3.008	2.45×10^{-4}	2.49×10^{-4}	2.33	2.37
GHEX_97.3.009	8.76×10^{-4}	8.84×10^{-4}	32.6	32.6
GHEX_97.3.010	2.25×10^{-4}	2.35×10^{-4}	1.71	1.81
GHEX_97.3.011	2.28×10^{-4}	2.34×10^{-4}	1.71	1.77
GHEX_97.3.013	7.85×10^{-4}	7.59×10^{-4}	16.4	16.5
GHEX_97.3.014	2.65×10^{-4}	2.51×10^{-4}	1.71	1.76
GHEX_97.3.015	5.86×10^{-4}	5.61×10^{-4}	9.99	9.92
GHEX_97.3.016	2.31×10^{-4}	2.39×10^{-4}	1.34	1.40
GHEX_97.3.017	6.99×10^{-4}	7.44×10^{-4}	9.91	10.0
GHEX_97.3.018	2.33×10^{-4}	2.36×10^{-4}	1.66	1.64
GHEX_97.3.020	2.24×10^{-4}	2.19×10^{-4}	1.24	1.29
GHEX_97.3.021	2.71×10^{-4}	2.86×10^{-4}	2.89	2.88
GHEX_97.3.022	2.15×10^{-4}	2.31×10^{-4}	9.57×10^{-1}	1.04
GHEX_97.3.023	2.21×10^{-4}	2.27×10^{-4}	1.35	1.41
GHEX_97.3.024	2.44×10^{-4}	2.31×10^{-4}	1.09	1.18
GHEX_97.3.025	3.95×10^{-4}	4.13×10^{-4}	5.85	6.02
GHEX_97.6.004	2.66×10^{-4}	2.62×10^{-4}	6.40	6.65
GHEX_97.6.005	2.85×10^{-4}	2.81×10^{-4}	6.84	6.91
GHEX_97.6.006	6.38×10^{-4}	5.91×10^{-4}	3.56	3.60
GHEX_97.6.007	6.53×10^{-4}	5.86×10^{-4}	3.14	3.22
GHEX_97.6.008	3.72×10^{-4}	3.83×10^{-4}	2.40	2.23
GHEX_97.6.010	9.86×10^{-4}	9.33×10^{-4}	3.37	3.72
GHEX_97.6.011	3.99×10^{-4}	4.42×10^{-4}	9.53	9.96
GHEX_97.6.013	4.04×10^{-4}	3.81×10^{-4}	3.34	3.23
GHEX_97.6.016	3.64×10^{-4}	3.92×10^{-4}	2.31	2.46

Continued.

sample	$^{69}\text{Ga}/^{27}\text{Al}$	$^{71}\text{Ga}/^{27}\text{Al}$	$^{56}\text{Fe}/^{28}\text{Si}$	$^{56}\text{Fe}/^{28}\text{Si}$
GHEX_97.6_019	2.13×10^{-4}	2.17×10^{-4}	5.47×10^{-1}	6.18×10^{-1}
GHEX_97.6_021	1.92×10^{-4}	1.81×10^{-4}	2.21	2.29
DG_82032.178.31.51_001	2.88×10^{-4}	2.77×10^{-4}	3.89×10^{-1}	4.90×10^{-1}
DG_82032.178.31.51_003	2.52×10^{-4}	2.58×10^{-4}	5.65×10^{-1}	6.72×10^{-1}
DG_82032.178.31.51_006	1.10×10^{-3}	1.08×10^{-3}	7.60	7.43
DG_82032.178.31.51_010	4.01×10^{-3}	3.88×10^{-3}	6.12	6.06
DG_82032.178.31.51_017	5.67×10^{-3}	5.84×10^{-3}	12.6	12.6
DG_82032.178.31.51_018	3.90×10^{-3}	3.38×10^{-3}	6.64	6.56

Table 10.4: Measured Ga/Al and Fe/Si ratios in the Mt. Ruker and Kuruman BIF. Only evaluable data points are listed here. The Ga/Al ratios were determined with ^{69}Ga and ^{71}Ga isotopes. The Fe/Si ratios were determined with ^{56}Fe and ^{57}Fe isotopes.

sample	$^{69}\text{Ga}/^{27}\text{Al}$	$^{71}\text{Ga}/^{27}\text{Al}$	$^{56}\text{Fe}/^{28}\text{Si}$	$^{56}\text{Fe}/^{28}\text{Si}$
NISTSRM610	4.92×10^{-2}	4.99×10^{-2}		
NISTSRM610	5.03×10^{-2}	4.92×10^{-2}		
NISTSRM610	4.96×10^{-2}	5.07×10^{-2}		
NISTSRM610	5.27×10^{-2}	5.28×10^{-2}		
NISTSRM610	5.28×10^{-2}	5.22×10^{-2}		
NISTSRM610	4.86×10^{-2}	5.04×10^{-2}		
NISTSRM610	4.71×10^{-2}	4.65×10^{-2}		
NISTSRM610	5.28×10^{-2}	5.19×10^{-2}		
NISTSRM610	5.63×10^{-2}	5.75×10^{-2}		
NISTSRM610	3.90×10^{-2}	3.93×10^{-2}		
NISTSRM610	3.91×10^{-2}	3.84×10^{-2}		
NISTSRM610	4.01×10^{-2}	3.94×10^{-2}		
IF-G	9.16×10^{-4}	9.10×10^{-4}	2.23	2.14
IF-G	7.60×10^{-4}	9.22×10^{-4}	2.02	2.03
IF-G	7.35×10^{-4}	8.33×10^{-4}	2.09	1.99
IF-G	8.82×10^{-4}	1.03×10^{-3}	2.01	1.92
IF-G	1.00×10^{-3}	1.03×10^{-3}	2.17	2.12
IF-G	1.14×10^{-3}	1.10×10^{-3}	2.01	2.07
IF-G	9.30×10^{-4}	9.12×10^{-4}	1.96	1.81
IF-G	8.40×10^{-4}	9.49×10^{-4}	2.09	2.00
IF-G	8.88×10^{-4}	9.07×10^{-4}	2.09	1.93
IF-G	6.92×10^{-4}	7.20×10^{-4}	1.83	2.42
IF-G	8.85×10^{-4}	7.77×10^{-4}	2.03	2.41
IF-G	9.11×10^{-4}	8.17×10^{-4}	1.56	1.72

Continued.

sample	$^{69}\text{Ga}/^{27}\text{Al}$	$^{71}\text{Ga}/^{27}\text{Al}$	$^{56}\text{Fe}/^{28}\text{Si}$	$^{56}\text{Fe}/^{28}\text{Si}$
FeR-3	1.79×10^{-3}	1.81×10^{-3}	1.24	1.17
FeR-3	2.13×10^{-3}	2.18×10^{-3}	1.19	1.28
FeR-3	1.86×10^{-3}	1.99×10^{-3}	1.22	1.25
FeR-3	1.14×10^{-3}	1.00×10^{-3}	1.17	1.19
FeR-3	1.18×10^{-3}	1.07×10^{-3}	1.27	1.07
FeR-3	1.21×10^{-3}	1.21×10^{-3}	8.59×10^{-1}	1.21
FeR-3	1.29×10^{-3}	1.07×10^{-3}	1.40	1.24
FeR-3	1.60×10^{-3}	1.67×10^{-3}	9.45×10^{-1}	1.17
FeR-3	1.44×10^{-3}	1.25×10^{-3}	1.24	1.11
FeR-3	2.32×10^{-3}	2.55×10^{-3}	1.49	1.22
FeR-3	2.55×10^{-3}	2.34×10^{-3}	1.18	1.28
FeR-3	1.85×10^{-3}	1.94×10^{-3}	1.34	1.38
NOD-P1	1.09×10^{-3}	1.09×10^{-3}	1.02	1.02
NOD-P1	1.10×10^{-3}	1.09×10^{-3}	9.94×10^{-1}	1.03
NOD-P1	1.11×10^{-3}	1.10×10^{-3}	1.03	1.05
NOD-P1	1.04×10^{-3}	1.03×10^{-3}	9.32×10^{-1}	9.76×10^{-1}
NOD-P1	1.05×10^{-3}	1.05×10^{-3}	9.11×10^{-1}	9.36×10^{-1}
NOD-P1	1.06×10^{-3}	1.09×10^{-3}	9.57×10^{-1}	9.66×10^{-1}
NOD-A1	3.22×10^{-4}	3.14×10^{-4}	6.85	7.03
NOD-A1	2.87×10^{-4}	2.89×10^{-4}	5.82	5.66
NOD-A1	3.18×10^{-4}	3.28×10^{-4}	6.50	6.46
NOD-A1	3.46×10^{-4}	3.46×10^{-4}	6.51	6.60
NOD-A1	2.94×10^{-4}	2.78×10^{-4}	4.98	5.03
NOD-A1	2.90×10^{-4}	3.02×10^{-4}	5.61	5.36
ANT.009	3.81×10^{-3}	3.94×10^{-3}	5.99	5.71
Kuruman.009	2.65×10^{-4}	2.60×10^{-4}	4.28	4.15
Kuruman.012	4.42×10^{-4}	4.52×10^{-4}	12.5	12.8